THE UNIVERSITY *of* EDINBURGH

Instrumentation development to study candidate materials for an organic piezoelectronic transistor

Sergejs Afanasjevs

THE UNIVERSITY
of EDINBURGH

Doctor of Philosophy – The University of Edinburgh – 2021

Abstract

High pressure (HP) is a powerful tool which is used to modify the material's physical properties. The work described in this thesis is dedicated to the development of new or adaptation of the existing HP instrumentation which is capable of producing *in situ* conductivity (γ) measurements on the test materials to identify the most promising candidates for the organic piezoelectronic transistor (OPET). OPET is a concept of a new transistor which overcomes limitations of the currently employed transistor technology because it utilizes piezoelectric transduction rather than the electric field to propagate digital logic signals. This, in turn, implies small driving voltages, higher processing speeds and denser integration/scaling capabilities.

The OPET device concept utilizes a piezoelectric actuator which, when the voltage (V) is applied to it, expands and, as a result, uniaxially compresses the thin layer of piezoresistive (PR) material within the rigid system. The employed PR materials need to have high pressure-dependent resistivity (ρ) to turn from the insulator/semiconductor into the conductor and, therefore, to pass the electric signal further within the ambient and 3 gigapascals (GPa) (pressure within the suitable range for OPET application). Among a wide variety of materials, organics were selected as PRs due to the high interest which they attracted in the recent decades by the worldwide multidisciplinary research in the electronic materials and because molecular organics are much more compressible than inorganic lattices.

Although the OPET device concept implies the uniaxial compression, on the initial project stages it is rationally and economically viable to first characterise the PRs in the single crystal or the compressed powder form before their deposition into thin films. The characterisation implies the variable pressure (P) and variable temperature (T) ρ studies which resulted in necessity in developing double-layer autofrettaged piston-cylinder cell (PCC). The PCC is capable of reaching 3 GPa and is equipped with the feedthrough plug which introduces the probe wires into the HP environment to monitor sample resistance (R) and P changes *in situ*.

To achieve P beyond the 3 GPa the DAC of the Merrill Bassett type was adapted for the electric γ measurements. DAC is equipped with 0.8 mm in diameter diamond

culets and the NiCrAl seats to allow safe exploitation up to the 10 GPa to characterise those PR materials which failed to metallise within the desired *P* range but still are having a good ρ - *P* tendency which might find an application in the future OPET devices when better performance piezoelectric actuators will be made.

Designs of both: PCC and DAC were analytically verified and validated using finite element analysis (FEA) as well as experimentally tested to indeed survive the *P* extremes with no yielding in the employed materials. Both cells were made to fit the required sample geometry with the necessary optimal probe contact separation which is the important prerequisite for the precise *R* into ρ conversion. In the case of the DAC the special sample loading techniques, gasket (a mechanical seal and a sample chamber between two opposed diamonds) preparation and insulation, as well as the gold sputtering of the probe contacts procedures, were implemented to achieve experimental success.

Another HP cell which is reported in this thesis is the uniaxial high-pressure cell (UHPC). It was designed to produce both: static and dynamic *P* experiments to mimic the OPET device concept to study those PR materials which were deposited into the thin films. The performance of the above-mentioned *P* cells within this project is illustrated in the form of the project related outcomes.

Among selected for the study materials, the hydrostatic HP measurements were performed on the platinum and iridium complexes with organic ligands, Magnus salts (organic-inorganic hybrids) as well as on the gold dithiolene complexes. The achieved results showed that some candidate materials indeed are promising for an application in the OPET device due to high *P* dependence on the electronic properties within the above-mentioned *P* range. For instance, the gold radical with (4-(4-chlorophenyl)-1,3-dithiolene) ligand and the $Pt(bqd)_2$ materials were found to undergo 3 and 7 orders of magnitude change in ρ respectively between ambient pressure (*Pamb*) and 2 GPa at room *T*. The latter material was also deposited into the thin film form and exposed to the uniaxial HP. The produced measurements showed that the sample *R* gradually decreases from 600000 Ohm (Ω) at *Pamb* to 35 Ω at 0.11 GPa and values stay consistent between *P* cycles.

Declaration of originality

I declare that this thesis has been composed by myself and that the presented work is entirely my own, except where otherwise indicated by reference or acknowledgement.

Sergejs Afanasjevs

Acknowledgements

I would like to dedicate this section to thank those who helped me through the course of this PhD. First of all, I would like to thank my supervisor, Prof. Konstantin Kamenev, for his guidance, support and patience. Not only he offered me the funded PhD but also opened my eyes to the beautiful world of HP science and its small details.

I would also like to thank Dr Xiao Wang for sharing experience and exchanging ideas throughout this PhD and technician Mr David McCabe for bringing complex 3D concepts into the reality and, sometimes, introducing suggestions before manufacturing.

I am also grateful to Dr Michael Kepa and Dr James Cumby for all early project discussions and valuable advice when they still were part of CSEC family.

I would also like to thank my project group members, Dr Benjamin Helen and Prof. Neil Robertson for always being helpful and easy to reach.

I have to express my gratitude to all my CSEC colleagues and other residents for a friendly and supportive atmosphere.

Last but most importantly, I owe infinitely to my parents Viktorija and Genadijs Afanasjevs and my partner Kristine Kravcenko for their love and support.

Contents

List of figures

List of tables

Acronyms and abbreviations

HP	High pressure
OPET	Organic piezoelectronic transistor
PR	Piezoresistive
PCC	Piston cylinder cell
DAC	Diamond anvil cell
FEA	Finite element analysis
UHPC	Uniaxial high-pressure cell
CSEC	Centre of science at extreme conditions
IT	Information technology
CPU	Central processing unit
FET	Field-effect transistor
PET	Piezoelectronic transistor
PE	Piezoelectric
BG	Bandgap
PVD	Physical vapour deposition
MGS	Magnus green salts
DMM	Digital multimeter
MM	Montgomery method
FEM	Finite element method
PTFE	Polytetrafluoroethylene
PTM	Pressure transmitting medium
CPP	Compressed powder pellet
WC	Tungsten carbide
SST	Stainless steel
PVC	Polyvinyl chloride
CCR	Closed cycle refrigerator
PPMS	Physical property measurement system

Nomenclature

V	Voltage	r_e	External radius
T	Temperature	r_2	Common radius
$Troom$	Room temperature	θ	Angle
$Televated$	Elevated temperature	σ_r	Radial stress
γ	Conductivity	σ_t	Tangential stress
P	Pressure	σ_a	Axial stress
$Pamb$	Ambient pressure	u	Displacement
R	Resistance	ε_r	Radial strain
ρ	Resistivity	ε_t	Tangential strain
I	Current	ε_a	Axial strain
ℓ	Length or thickness	E	Young's modulus
h	Height	σ_e	Von Misses stress
w	Width	σ_1	Maximum principal stress
A	Area		
H	Contact separation ratio	σ_2	Middle principal stress
Z	Effective pellet thickness	σ_3	Minimum principal stress
F	Force	δ	Interference fit
R_0	Resistance at $Pamb$		
λ	Wavelength		
d	Diameter		
ID	Inside diameter		
OD	Outside diameter		
σ_y	Yield strength		
UTS	Ultimate tensile strength		
Pi	Internal pressure		
Pc	Common pressure		
r	Radius		
r_1	Internal radius		

Chapter 1

Introduction

This first chapter introduces the reader to the transistor, its role in information technology (IT), and its fundamental limitations. The chapter then introduces the new transistor concept which overcomes limitations of the conventional transistor and answers question why and how it can be improved. Also, the link between the new transistor concept and HP is established. The purpose and aims of this PhD project are described at last along with the thesis layout.

1.1 Technological need and devices

IT is a set of methods and tools used for collecting, storing, processing and distributing information. IT optimizes and, in many cases, automates information processes, which are becoming even more prevalent in modern human activity life. It is accepted to evaluate the progress of humankind by its achievements in the scientific and technological fields and this progress can be driven by formations of new sciences. For example, at the end of the 20th century, computer science appeared growing rates of which were so high, that it provoked the information revolution, resulting in microprocessor technology development [1].

It has been about 20 years since mankind has stepped into the 21st century and now we are surrounded by smart technology: laptops and tablets, phones and watches with cameras, flying drones with camcorders etc. All these smart electronic devices are equipped with central processing unit (CPU), the electric "brain" that runs billions of tasks, performance of which is directly related to the number of transistors sitting on it. The more of them we have on the CPU, the more tasks it can run simultaneously. The smaller transistors are, the faster the On/Off switch operates within them.

Transistors can also be found on other devices such as graphics processing unit (GPU), dynamic random-access memory (DRAM), static random-access memory (SRAM), read-only memory (ROM), flash memory, etc. In these devices, transistors are assembled into various groups which are responsible for numerous gate operations allowing for digital logic language to exist. A classic example is a number 0 for an "Off" state and number 1 – for an "On" state.

All conventional transistors are built with complementary metal-oxide-semiconductor (CMOS) process technology (See figure 1.1). In the "On" state, the *V* potential is applied at the gate and the positive electric field builds up which attracts electrons on the positively doped layer/region of the silicon substrate. Silicon dioxide which acts as an insulator prevents further electron movement, so electrons are forced to occupy the upper layer of silicon substrate allowing *I* to flow from Source to Drain. Substrates which are made of elements from the carbon group (e.g. with 4

valence electrons) can be doped positively using ion implantation of elements from the boron group (e.g. with 3 valence electrons) or negatively with elements from the nitrogen group (e.g. with 5 valence electrons) [2].

It can be concluded that the performance and functionality of electronics technology are driven by two scalings: transistor and Dennard [3]. The former is associate with Moore's empirical observation regarding the exponential rise in transistor density with time [4]. This observation stays to be true as nowadays microprocessor transistors have reached 7 nanometres in width (w) [5] (this w was twice as bigger in 2016 when I just started my PhD) and there are no known manufacturing obstacles for their further reduction in size [6]. The latter implies that with a decrease in the size of the transistor increases the processor's clock speed and, hence, the processor's performance [3], however, the maximum clock rate has not increased much since 2005 (See figure 1.2) because the further reduction in the size of the transistor leads to the unacceptable heat production which occurs inside of the chips (when electrons are passing smaller and smaller silicon circuits with the same speed the circuits heat up) [7].

The Dennard scaling of the conventional field-effect transistors (FET) cannot be restored by any engineering solution due to the operating principle of FET. There is a minimum gate V change needed to switch the transistor from an "Off" or low-I state to and "On" or high-I state. It is set by thermal excitation of carriers in the "Off" state [8, 9].

The lowest line V value required to gate a single carrier electrostatically with high fidelity or 10^{-4} On/Off R ratio is about 1 Volt (V) in practice. Values below 1 V are leading to dramatic slowing down and inadequate On/Off ratios (e.g. poor performance of the device) while values above 1 V are leading to high thermal excitation of carriers in the "Off" state – electrical instability of device [3, 10, 11, 12, 13].

This line V value was reached back in 2005 and it is defined by charge and T according to the equation 1.1 and consequently, it does not scale with device dimensions.

$$V_T = kT/q \tag{1.1}$$

Where V_T is the thermal voltage, k – Boltzmann constant, T – the temperature of the p-n junction and q – charge.

If the device is to be scaled further there will be an excessive leakage I in the "Off" state, or low I (slow) in the nominally "On" state [12]. In other words, the fundamental physical speed limit of the FET transistors has been reached back in 2005, marking the end of the highly desirable "Dennard scaling" era [7].

Since then, microprocessor manufacturers decided to limit heat generation inside of the chips by setting the speed limit for electrons (e.g. no clock rate increasements) and, to "somehow" go along with Dennard's tendency, manufacturers introduced multi-core chips which, in theory, are promising (eight 250 MHz cores = one 2 GHz core assuming simultaneous operation), but, in practice, many algorithms cannot be broken into several pieces becoming bottlenecks for one of the 250 MHz cores of the chip [7].

The worth mentioning improvement of the FET technology took place back in 1998 when the first FinFET concept [14] was presented by professor Chenming Hu and his team (See figure 1.1). In the 2013 FinFET [15] fully replaced CMOS when major semiconductor manufacturing foundries like TSMC [16] and Sk Hynix [17] first utilised FinFET designs [18, 19].

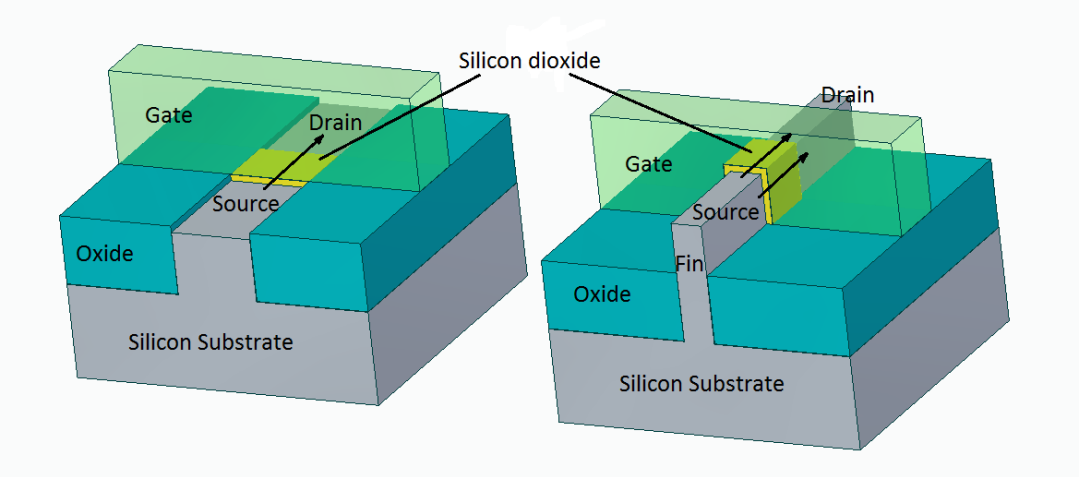

Figure 1.1: Planar MOSFET on the left and FinFET on the right. The arrow shows the direction of the current.

FinFET architecture improved CMOS technology performance in terms of many aspects among which are higher transductance and reduction of leakage or idle *I*. At first glance, it looked as if scaling problem was solved or, at least, postponed, however new architecture of source (e.g. addition of fin) made model much complex and previously not considered mechanical stress of the source had to be modelled to avoid malfunctions. Also, further scaling of finFET brought new problems: random fluctuations of dopant and roughness of line edge resulting in device performance deterioration [20, 21, 22].

There are many other types of FET [23, 24, 25, 26], however, all of them and any further modifications/improvements of FinFET were way below the desired performance of transistors that Dennard predicted in terms of the clock speeds.

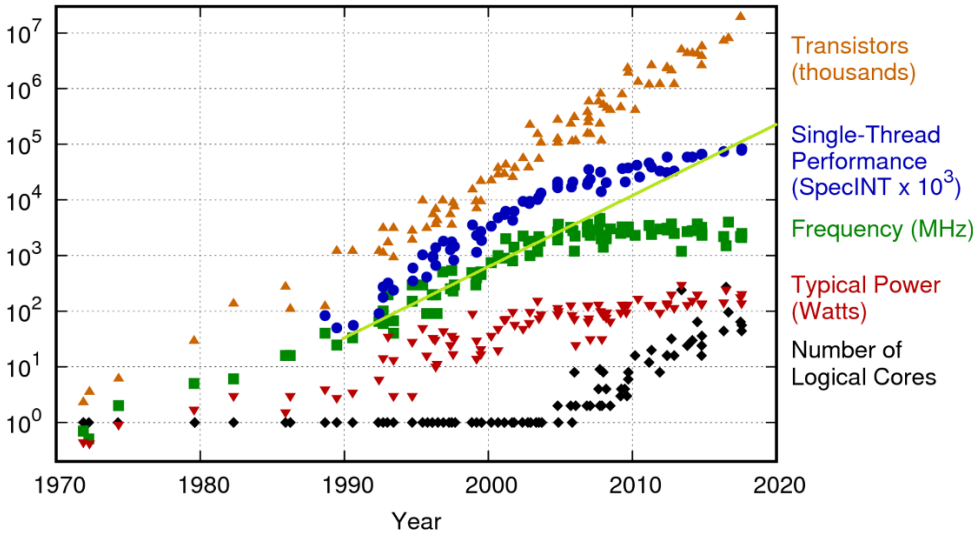

Figure 1.2: Key performance indicators of microprocessors versus time. Orange data represents transistor count and, as it can be seen, they continue to follow Moore's law while green data – the clock rate frequency shows no grow since 2005. The light green line shows the extrapolation of the previously observed trend or expected Dennard scaling [27].

Clock speeds of modern CPUs, for instance, cannot go above 4 GHz without professional cooling systems. The commercially available CPUs are having base clock speed (the speed at which CPU works by default) and boost clock speed (the maximum speed that CPU can reach when overclocked without any damage to components). When conventional cooling uses fans and heat sinks, the professional uses liquid as a cooler. The affordable liquid coolers use distilled water and these allow to push the CPU to "limits" (4.5 GHz max), however, if higher frequencies are of an interest the coolants such as liquid nitrogen and/or liquid helium should be

employed. There is, however, no manufacturing guarantee that the device will work properly over the promised by the manufacturer life-span of CPU. The highest overclocked CPU speed was achieved in 2011 when Advanced Micro Devices (AMD) company used both liquid nitrogen and liquid helium to reach 8 GHz [28]. Although this greatly maximises the speed, by observing the frequency trend in figure 1.2, it can be noted that 8 GHz value is still below Dennard's expectations (in 2011 rate should be at around 11 GHz). Moreover, the trade-off between performance and cost must be considered and with liquid coolants like nitrogen and helium, this trade-off is inadequate and unprofitable.

To restore Dennard's scaling, it is required to develop a novel device which would be able to operate at low *V* and high frequencies using the new unconventional method. Just like nature uses transduction to distribute signals in bioorganisms [29], the transduction can be used to propagate digital logic in between input and output electronic signals of the transistor by the means of the displacement of the intermediate form [30]. Among the transduction devices like spintronics [31] and nanoelectromechanical (NEM) relay [32], the International Business Machine Corporation (IBM) proposed new device concept – piezoelectronic transistor (PET) (See figure 1.3) which appears to be challenging but a promising technological solution since piezoelectric actuation requires much less driving *V* allowing PET to have denser integration and, therefore, further scaling [33].

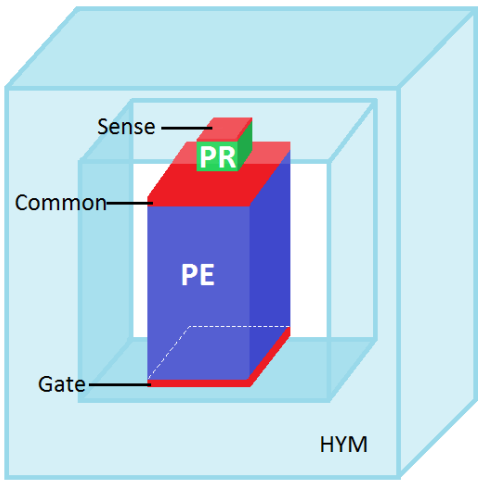

Figure 1.3: The PET concept showing key components. The piezoelectric (PE) material in between Gate and Common and piezoresistive (PR) element in between Sense and Common. The whole device, as shown, is to be surrounded by a high yield material (HYM) [34].

The idea behind the operation of the device is as follows: the high-performance PE actuator (e.g. previously mentioned as an intermediate form) [35] receives an input *V* from Gate and expands along the vertical axis while delivering acoustic pulse to Common. Expansion of the PE element results in a PR element compression within the rigid HYM. The PR element, which has a high pressure-dependent ρ, as a result, undergoes an insulator-to-metal transition and converts pulse back to *V* in between Common and Sense [34]. The lack of thermionic emission, which is present in the form of charge carriers over a barrier in the regular FET transistors, and transduction physics of PET are promisingly leading to a low-*V* and fast operation device which bypasses limitations of the Dennard scaling [36] as well as appears to be centenarian in comparison to NEM relay [32] which has a limited cycling life [30].

IBM reports PET transistors which can operate at around 150 mV line voltages while delivering 10^{-4} On/Off *R* ratios while giving around 10 GHz clock speeds (See figure 1.4 – C) by simulating the known materials [34, 37].

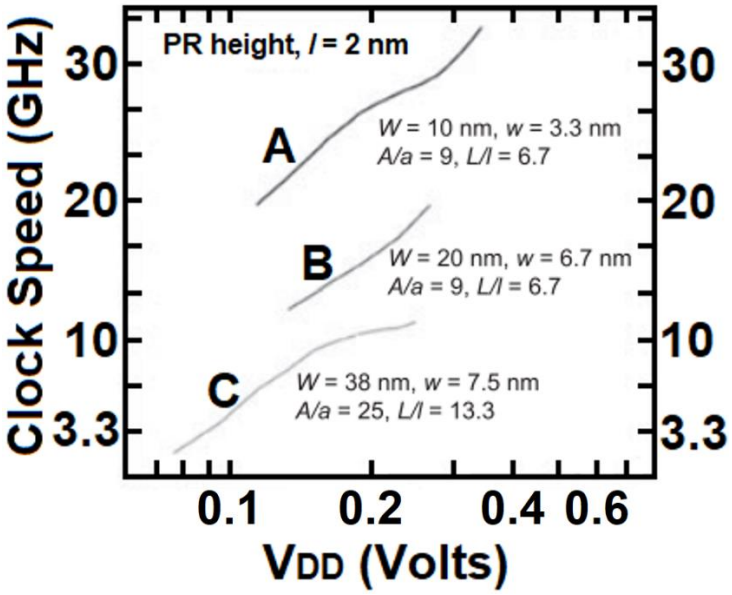

Figure 1.4: The PET performance simulation. Left & right-hand scales represent clock speeds in GHz. Bottom scale is line voltages. A, B and C represent three different geometries with dimensions as shown next to the lines. Please note that *W* – width of PE, *w* – width of PR, *A* – area of the PE, *a* – area of the PR, *L* – the thickness of the PE and *l* – the thickness of the PR. Adapted from [34].

As it can be seen in figure 1.4, the further device dimensional scaling (e.g. simulated B and A curves) are leading to the even higher clock speeds with small line voltages (V_{DD}), making Dennard scaling applicable to PET.

1.2 Suitable materials

The first step towards the PET realization is a selection of the appropriate materials. At present, PET devices (See figure 1.3) are built up from a stack of five materials (Gate, PE, Common, PR and Sense) with a rigid yoke which is in contact with Gate (at the bottom) and Sense (at the top). The international collaborative research which is led by IBM is working towards PET realisation [36, 37, 38] and materials for Gate, Common and Sense do not require deep research because these can be chosen among many metals with good electrical conduction properties and selection criteria would be mainly dependent upon scaling feasibility/price/cycle loading simulations.

The PE actuator, as its name suggests, uses the piezoelectric effect, which is present in crystals of tourmaline, quartz and other natural crystals, as well as many artificially grown crystals which are dielectrics [39]. This effect is widely used in modern technology and can be found in operation principle of hand watches, headphones, microphones, lighters, etc.

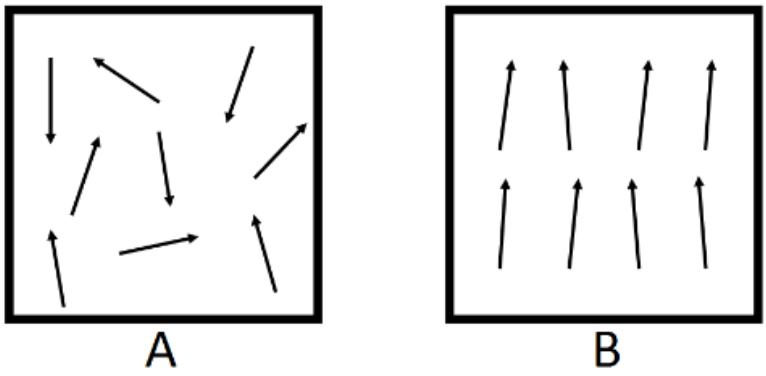

Figure 1.5: Alignments of electric dipoles. A – the unpoled material with random dipole orientation. B – dipole alignment after poling. Arrow pointer indicates positive charge with a negative charge at the tail. Adapted from [40].

Based on thermodynamic considerations, there is a direct piezoelectric effect, when an electric charge is induced on the surface of a crystal under the mechanical deformation (for example compression), and a reverse piezoelectric effect, when a crystal deforms under the influence of an external electric field [41]. The latter applies to the desired actuator operation principle for PET (e.g. linear movement which leads to PE extension as a result of the applied *V*), inside of which polarized

piezo crystals that can be formed into any structural shape are placed in between plate electrodes. Polarization is important as it aligns positive and negative charges of dipoles in the direction of interest (See figure 1.5) using a strong magnetic field, which improves the piezo sensitivity and, hence, the extension capabilities of piezo materials.

PE's closest analogue in terms of operation principle is a capacitor with an exception that it does not change its volume and this volume change is only the difference between materials these two electric components use.

The suitable PE materials for PET were found to be the relaxor ferroelectric ceramics [42]. They are having ultrahigh strains and, hence, enough performance to drive PET [37] providing big PE expansion at the low driving *V* [33].

From figure 1.4, it can be noted that scaling of PE is also an important step to realize PET, however, such a PEs with the high piezo response already exist and function at nanoscale dimensions [43, 44, 45] due to the fact that ferroelectricity is persistent down to unit cell volume [38, 42].

Although the developmental PET devices and their simulations are very promising as a new post-CMOS digital logic with fast switching speeds and low power consumption due to the combined use of high-performance PR and PE materials, the former is considered to be the bottleneck on the pathway towards PET realisation because the currently employed PR candidates are rare earth material compounds such as SmXEu1-XS [46] and SmSe [47] which require several GPa of *P* to make the Common-Sense channel conductive. Also, there are known manufacturing issues that occur when trying to bring concept design into fully integrated standalone PET device due to several reasons among which are PET fabrication process, chemical incompatibility between PE and PR and oxidation of latter (SmSe material is unstable in the air) [37, 38, 48]. Moreover, practical experiments with fully integrated PET device are having higher line *V* than these observed in the simulations [42] (See figure 1.4). Among the two possible solutions, scientists suggest innovative PR materials being found/made/used [36].

In recent decades, worldwide multidisciplinary research in electronic materials has been galvanised by the study of organic light-emitting diodes (OLEDs), organic field-effect transistors (OFETs) and organic photovoltaics (OPVs) [49]. Organic materials started to slowly substitute inorganic analogues in the commercial domain due to many reasons among which are the flexibility, affordability, power efficiency [50] and ability to be synthesised rather than mined from bowels of the earth. The synthesis also allows varying chemical and electronic properties of organics which makes them being promising candidates for the PR material. Just like in Lego where different building blocks can be assembled into the desired shape, the material molecules of organics can be built according to the required chemical and electrical properties [51, 52].

Based on literature precedent, the promising class of PR materials was identified with potential in large ρ change between ambient and *Pelevated*. Just like in PET concept, these materials are expected to undergo insulator/semiconductor to metal transition at room temperature (*Troom*) during uniaxial compression. Please refer to the 2nd chapter for more details regarding PR materials and their relevant properties.

1.3 Why high pressure

High pressure (HP) is a powerful tool which is used to modify the material's physical properties. These modification studies produce significant contributions towards the development of many technological and scientific fields such as biology, chemistry, geophysics, astrophysics, material science and food industry [53, 54]. The HP application can cause dramatic changes in the material's behaviour by producing first and/or second-order phase transitions within it by the means of compression that leads to change in materials volume as a result of the change in interatomic (intermolecular) distances. The HP first-order phase transitions are generally liquid into crystals (a classic example is water which turns into the ice when subjected to HP [55]) and gases into metals (for example nitrogen gas into fluid metal [56]). The second-order HP induced phase transitions are generally associated with changes in structural, magnetic and electronic properties of matter without changes in its state [53]. Both, 1st and 2nd order phase transitions are also sometimes followed by

necessity in the change of another thermodynamic parameter – *T*, in order to be successful.

HP can be achieved statically and dynamically. The former method has no time constraints but can reach smaller *P* compared to the latter which goes beyond tera pascal range [54]. PET concept has dynamic operation principle but does not require/ may have ultra-high *Ps* to achieve high On/Off ratios. Beforehand, PR materials will be tested statically for an accurate picture of their physical nature, more precisely, their electronic properties that will be presented in the form of ρ - *P* charts. These charts will be used to identify if the sample is promising or not. Promising candidates would be those that are having reversible insulator/semiconductor to conductor transition within the ambient and 3 Gpa *P* range at *Troom*.

It is expected that HP application, will transform PR material from insulator or semiconductor into the conductor. This work is therefore focused on systematic ρ studies on different PR materials at variable *P* and *T* as well as the development of the HP instrumentation required to accomplish this.

This research is novel and important as it may lead to the new electronic device which will significantly improve the performance of the current transistor technology in terms of the increased clock speeds using new device concept – organic piezoelectronic transistor (OPET) which overcomes fundamental limitations of conventional FET allowing denser transistor integration on a chip, has low *V* switching capabilities and utilizes new organic PR materials which are not having limitations of the currently employed continuous lattice materials in the PET concept. Please refer to the 2nd chapter for more information.

1.4 Objectives

The general aims of this thesis are to develop or adapt HP instrumentation to produce the variable *T* and/or variable *P* - *R* measurements on the selected PR materials to determine the most promising candidates for the OPET device as well as to develop UHPC design which would allow producing both: static and dynamic *P* conditions for *R* measurements on the thin film samples. The following are the specific objectives:

- To develop PCC which is capable of reaching 3 GPa for *in situ R* measurements while having a big enough reaction chamber to fit the suitable compressed powder pellet (CPP) and to precisely allocate probing contacts on it.
- To adapt the opposed DAC for *in situ R* measurements which is capable of reaching 10 GPa. This objective, therefore, involves the development of methods and techniques for insulation of metallic cell parts, for sample loading, for gasket preparation and the introduction of probe wires into the reaction chamber.
- To determine the precise method for *R* into ρ conversion which is suitable for the anisotropic nature of PR materials and yields consistent results when deployed in PCC and DAC.
- To produce variable *T* and/or variable *P* measurements utilizing PCC and DAC and based on the acquired data to select the most promising PR candidates.
- To design UHPC for *in situ R* measurements on the thin film samples. The cell must be able to produce both: static and dynamic *P* applications.

1.5 Thesis layout

This thesis consists of nine chapters outlined below:

Chapter 1: Introduction

This chapter describes problems of the conventional transistor and limitations of the PET concept. It also suggests how these may be overcome, answers how HP is related to the device operation and talks about the suitable PR materials. At last, the project objectives and thesis layout are provided.

Chapter 2: Literature review – materials.

This chapter reviews the chemistry of selected materials for PR and contains the key material information and properties which will be used to characterize them with the crystal and/or molecular structure illustrations.

Chapter 3: Literature review – HP techniques.

This chapter reviews the relevant electronic terms, techniques and employed for *R* measurements devices. The chapter also reviews the HP devices, *P* measurement techniques, different pressure transmitting medium (PTM) and contains general thoughts on electrical *R* measurements in the selected HP devices.

Chapter 4: Development of PCC for *R* measurements.

In this chapter, the author describes how he develops the PCC for *R* measurements providing the driving parameters of the design as well as the employed theories. By utilizing the computer-aided design and FEA the compound cylinder was studied for relevant stresses and, at the end of the chapter, was presented along with the experimental testing. The PCC is capable of reaching 3 GPa of *P* and is equipped with the feedthrough plug for *R* measurements on the sample material as well as on the Manganin coil to probe *P in situ*.

Chapter 5: Adaptation of DAC for *R* measurements.

This chapter starts with the requirements and reasoning for the DAC which are followed with design considerations and applied method for gasket's insulation. Further, the FEA of the backing discs is provided based on which the material the disc is made of is selected. Lastly, the manufacturing, assembly and experimental testing of the DAC are provided. The adapted DAC is capable of reaching 10 GPa of *P* while producing *R* measurements on the sample material.

Chapter 6: Development of UHPC for *R* measurements.

This chapter starts with the requirements and reasoning for the UHPC which are followed with design considerations based on which the final design was developed which allows both: static and dynamic *P* applications depending on the employed components. Lastly, the manufacturing, assembly and experimental testing of the UHPC are provided.

Chapter 7: HP measurements.

This chapter provides the full experimental details regarding the *R* and *T* experiments along with the employed techniques, methods and instrumentation.

Chapter 8: Discussion.

This chapter contains the experimentally derived data on the PR materials from the 2nd chapter using techniques which are outlined in the 7th chapter in the form of the *R* - *T*, BG - *P* and ρ - *P* charts with details and analysis.

Chapter 9: Conclusions and future directions.

This chapter provides a summary of the completed work and outlines future potential directions of the project.

Chapter 2

Literature review – materials

This chapter reviews the chemistry of selected materials for PR, highlights the desired for OPET application properties, introduces bandgap (BG) theory and the significance of the variable *T* analyses. Lastly, but most importantly, the chapter identifies known and new promising PR candidates, illustrates the crystal and/or molecular structures and mentions the relevant material properties for which they were chosen.

2.1 Chemistry of materials

Organic materials show a tremendous diversity of electric properties including metallics [36], superconductors [57] and semiconductors [58]. The compressible nature of (neutral) organic solids is due to the relatively weak Van Der Waals interactions between the molecules in the solid-state. One such example is the π-stacking arrangement (See figure 2.1 – A) which yields high *P* dependence on properties, compared to continuous lattice materials such as SmSe (See figure 2.1 – B), where intramolecular interactions are strong and result in high intermolecular repulsion when molecules are pressed closer (See figure 2.2).

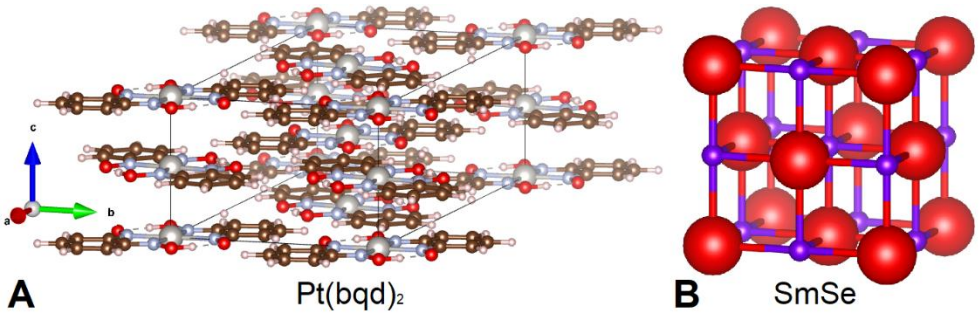

Figure 2.1: Unit cells. A – Example of the molecular solid unit cell (grey, red, blue, brown and pink spheres represent platinum, oxygen, nitrogen, carbon & hydrogen respectively) [59]. There are many variations of possible molecular structures and chains with different geometrical complexity levels, where the molecules are bound to each other with weak intermolecular forces, while the atoms within each molecule are held together with strong covalent bonds. B – ionic solid unit cell (red & purple spheres represent cations & anions respectively). Conventional rock salt structure [34, 60]. In an ionic bond, atoms are held electrostatically.

There are several organic materials that metallise under the applied *P* [61]. Nearly all, however, are multiple-component, charge-transfer salts or other doped systems [62]; they generally show the metallisation effect at low *T* and are often brittle single crystals with no clear route to being deposited in the thin film form (the PET prerequisite) [63]. Therefore, PR candidates should be single-component undoped materials for ease of (vapour or solution) processing which, ideally, are affordable in terms of price and abundance and nonreactive with air or other PET components they are in direct contact with (to avoid problems as in the case with SmSe).

Transition metal complexes with organic ligands were chosen as a promising material class for the PRs. This class constitutes of assemblies of a central transition metal ion which is bonded to a group of surrounding organic molecules (ligands)

[64]. Ligands have a relatively high symmetry surrounding the central metal ion which has the incomplete shell of d-electrons [65]. This material class can contain highly-tunable candidates for PR due to the existence of weak bonding of d-orbitals which indicates the possibility of narrow BG (See figure 2.4). It is expected that the *P* application to these materials will strengthen their intermolecular interactions (See figure 2.2) resulting in the broadening of the bands and a decrease in the BG. For piezoresistive applications, it is also required to have the conducting pathway/axis of the PR material to be the same as the axis along which the uniaxial compression takes place (See figure 1.3) to maximise the *P* - *R* response.

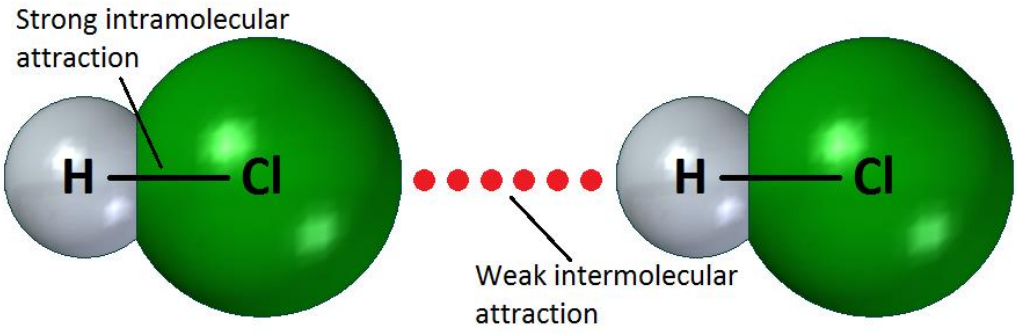

Figure 2.2: Intermolecular vs intramolecular interactions. On the hydrogen chloride (HCl) example it can be noted that the intramolecular attraction is formed within the molecule with H and Cl atoms while the intermolecular attraction originates between molecules. Generally, intramolecular forces can be metallic, covalent (shown) or ionic while intermolecular can have hydrogen bonding, dipole-dipole attractions (shown) and London dispersion forces. Adapted from [64].

2.2 Properties of materials

2.2.1 General considerations

To determine the fundamental properties and the performance of new PR materials for the OPET a systematic material study is required to produce adequate selection and differentiate between promising and non-promising candidates across a broad canvas of possibilities. A selection of appropriate materials with varying properties is essential to enable devices with differing options for dimensions, operating speed and power, appropriate for different applications. Some key properties are specified below and these provide a basis for new PRs' assessment:

- Semiconductor/insulator to conductor change between ambient pressure (*Pamb*) and 3 GPa (*P* within the suitable PET application range) at *Troom*.
- The associated structural change should be whether continuous with no phase transition whether reversible if phase transition exists. The goal is to have consistency in ρ in response to the applied *P* during cyclic *P* applications.
- The material should be soluble and/or volatile to enable solution and/or vapour processing and, therefore, the ability to be deposited into the thin film form.

2.2.2 Electrical properties

As stated above, one of the essential criteria for PRs' functionality is the high ρ change within the aforementioned *P* range. Such a tangible change is a must to maintain a high On/Off ratio.

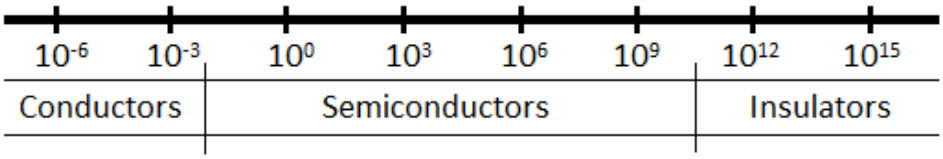

Figure 2.3: Rough ρ scale. Units are Ωm [66].

In figure 2.3 the rough ρ scale is illustrated to show how big the numerical change should be to treat material which was an insulator or semiconductor at *Pamb* as a conductor when subjected to *Pelevated.*

2.2.3 BG theory

In BG theory conduction and valence bands (See figure 2.4) represent allowed energy bands with quasi-continuous energy levels. In semiconductors and insulators at absolute zero *T* (e.g. at $T = 0°$ K) these bands are separated with the forbidden region (e.g. BG) where electrons cannot exist. The valence band is a region which is filled with electrons, whereas the conduction band is a region which is either partially filled with electrons or empty. For example, in conductors, the valence orbital is free given the fact that it is not filled with electrons completely (e.g. it has

free energy levels for electrons to jump onto). In semiconductors and insulators, the valence band is filled entirely.

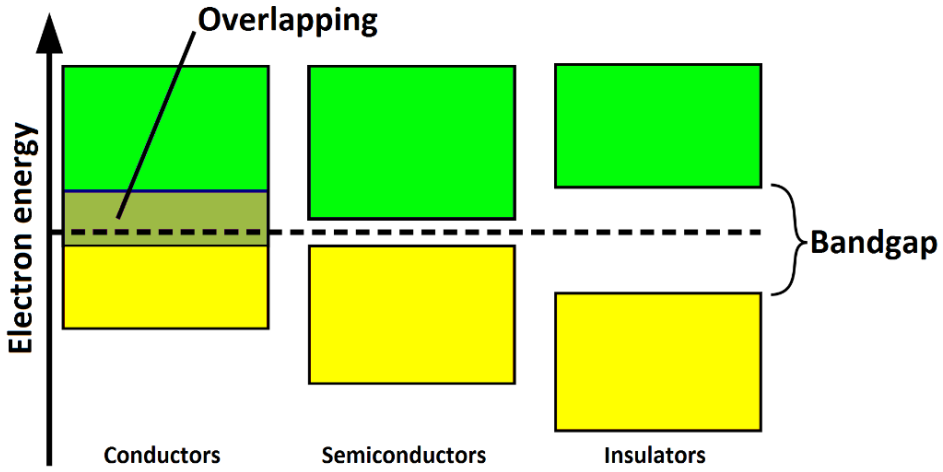

Figure 2.4: BG theory. Green & yellow rectangles are representing conduction and valence bands respectively. The dashed line represents the Fermi level. The band theory is used to explain the electrical γ in conductors, semiconductors and insulators from a unified point of view [67].

Therefore, in conductors, at absolute zero T (e.g. at $T = 0°$ K), valence and conduction bands are partially filled with electrons and, since there are free energy levels in the conduction band to which electrons can go, conduction and valence bands overlap each other, indicating/ illustrating that conductors are having high γ. Whereas in semiconductors and insulators, at T = 0° K, the valence band is entirely filled with electrons while the conduction band has none and, hence, no energy levels for electrons to go to, resulting in the illustrated gap between valence and conduction bands which can be small for semiconductors and big for insulators, denoting their electrical γ potentials [68, 69].

For semiconductors, depending on the doping, the allowed energy bands are shifted from the fermi level. For negatively doped semiconductors fermi level lies closer to the conduction band and for positively doped it's closer to the valence band. For undoped semiconductors, the Fermi level lies almost in between the allowed energy bands [70].

The BG itself is the energy difference between the top of the valence band and the bottom of the conduction band or the energy required to be overcome by an electron

from the valence band to get into the conduction band. The higher is the BG value which has the Electronvolt unit (eV) – the higher energy is required to overcome it. Semiconductors are those materials with BG width in between 0 & 3 eV and insulators are those above 3 eV [71]. Both: *T* and *P* can alter the electron energy. While the former parameter is rather unwanted in the transistor applications the latter is well suited for the PET operation concept. It is expected that increases in *P* will remove the BG in PR's material (e.g. transform it from insulator/semiconductor into conductor).

2.2.4 Role of temperature

T is another thermodynamic parameter which can tune the electrical properties of the matter (See figure 2.5), however, one of the OPET prerequisites is *Troom* operation. In spite of that, it is a common practice to include *T* analysis for *P* studies as it helps to identify the electronic phase of the material at a given *P* and calculate the BG.

In semiconductors, with an increase in the *T*, some electrons acquire energy that is sufficient to overcome the BG. This results in a sharp decrease in ρ and, therefore, an increase in γ. However, in conductors with increasing *T*, the electrical γ falls (negative *T* coefficient of electrical γ). Thus, the fundamental difference between conductors and semiconductors lies in the different *T* dependence of electrical γ [72]. Knowing that the only difference in BG theory between semiconductors and insulators is the width of the forbidden region, this semiconductor *T* - ρ behaviour is also applicable to insulators.

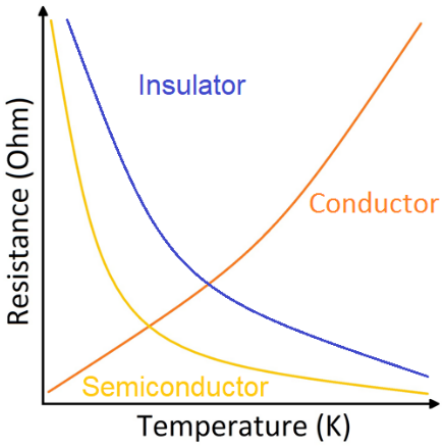

Figure 2.5: Common *R* - *T* dependence for conductors, semiconductors and insulators.

This work is therefore focused on systematic studies of different PR materials at variable *Ps*. If *P* - ρ behaviour looks promising (e.g. has high ρ change in between *Pamb* and 3 GPa), the measurements would be extended to include the *T* analysis at different *P* points to determine materials' electronic phase as well as to calculate the BG.

2.2.5 BG calculations

Generally, there are two approaches to calculate BG and, therefore, to understand materials' electronic behaviour: computational and experimental. The former approach is composed of several methods which are mainly united with the solution of the density function theory (DFT) equations (also called Kohn-Sham equations) while the latter uses experimentally acquired data [73]. It is a common knowledge that experimentally obtained BGs are more precise rather than DFT which uses numerous assumptions, approximations and simplifications during modelling and, therefore, experimentally derived BGs are preferred more on condition that the collected data can be undoubtedly interpreted.

The experimental way to calculate BGs is directly related to the use of Arrhenius equation – the mathematical expression of the *T* dependence of the rate of a chemical reaction [74].

$$k = Ae^{-Ea/RT} \tag{2.1}$$

Where *k* is the rate constant at *T*, *A* – pre-exponential factor, *Ea* – activation energy in Joules, *T* – the temperature in K and *R* – the energy gas constant (molar equivalent to the Boltamann's constant).

When dealing with electrical properties the equation is modified to be as follows:

$$\gamma = Ae^{-Ea/KbT} \tag{2.2}$$

Where γ is the conductivity in 1/Ωcm, *A* – pre-exponential factor, *Ea* – activation energy in eV, *T* – the temperature in K and *Kb* – the Boltzmann's constant in eV/K.

Compared to equation 2.1, in equation 2.2 the γ is taken as an inverse of ρ [75] – the experimentally derived value and the gas constant is replaced with Boltzmann's

constant as we are not dealing with moles anymore but with molecules. Activation energy and Boltzmann's constant are now expressed with electronvolt unit as it is more preferred when dealing with electron energy and BG theory.

To calculate a BG value and, therefore, to identify PRs' electronic status it is required to produce T - ρ measurements at any P point of interest. Points of interests are the P points and each BG will be corresponding to the P point during which the T - ρ experiment was performed. Thus, it is expected to see a decrease in BG's value with an increase in P.

It is a common practice to rearrange and take the natural log of equation 2.2:

$$ln(\gamma) = \frac{Ea}{Kb} * \frac{1}{T} + ln(A) \tag{2.3}$$

Considering the number of collected Ts and ρs (any quantity of points), this allows to get a straight-line plot and, therefore, slope with x-axis to be ln(γ) and y-axis to be 1/T. The activation energy can then be found by multiplication of slope with Boltzmann's constant [76].

For intrinsic (undoped/pure) semiconductors, the Fermi level lies almost in between conduction and valence bands because the quantity of excited electrons in the conduction band is the same as the number of electron holes in the valence band and, therefore, activation energy is assumed to be = ½ BG [71, 77, 78].

$$BG = 2Ea \tag{2.4}$$

2.3 Preparations and forms

To investigate the electronic behaviour of transition metal complexes with organic ligands it is necessary to obtain them in a form that allows them to be measured. Depending on the material the synthesis methods differ, and development details will be omitted due to complexity level, individual processing steps for each material as well as the unrelated to the author contribution as these specialities are beyond the project scope. The final physical forms include single crystals (needles), crystalline powder and amorphous powder (plates/flakes). These physical forms allow

producing a total of three different ρ studies: single crystal (if the size of grown monocrystal allows probe wire attachments), CPP (powders are usually compressed into a tablet/pellet geometry) and thin films (thin layer of material on a substrate). The first two studies require no advance technology or instrumentation to produce them while the formation of the last (e.g. thin films) requires a set of knowledge in the field of the thin film technology. Being an OPET prerequisite (See figure 1.3 & 1.4), where PR thickness must follow the transistor scaling and shrink further, the solubility and/or volatility were named as a key property the PR materials must have to enable solution and/or vapour processing to produce thin films.

Looking ahead, there was no solution processing done on the PR materials as those that can be solution-processed were found to be non-promising in terms of the metallisation *P* and, therefore, were not further studied as thin films. Instead, the vapour processing in the form of physical vapour deposition (PVD) was employed. High-vacuum evaporation was used as it provides great purity of the coatings [79]. Vacuum deposition of thin films consists of three main processes: 1) the transition of a substance from a condensed phase to a gaseous phase; 2) vapour transfer in a vacuum from the evaporator to the substrate; 3) vapour condensation on the substrate [80]. The system which was built is shown in figure 2.6.

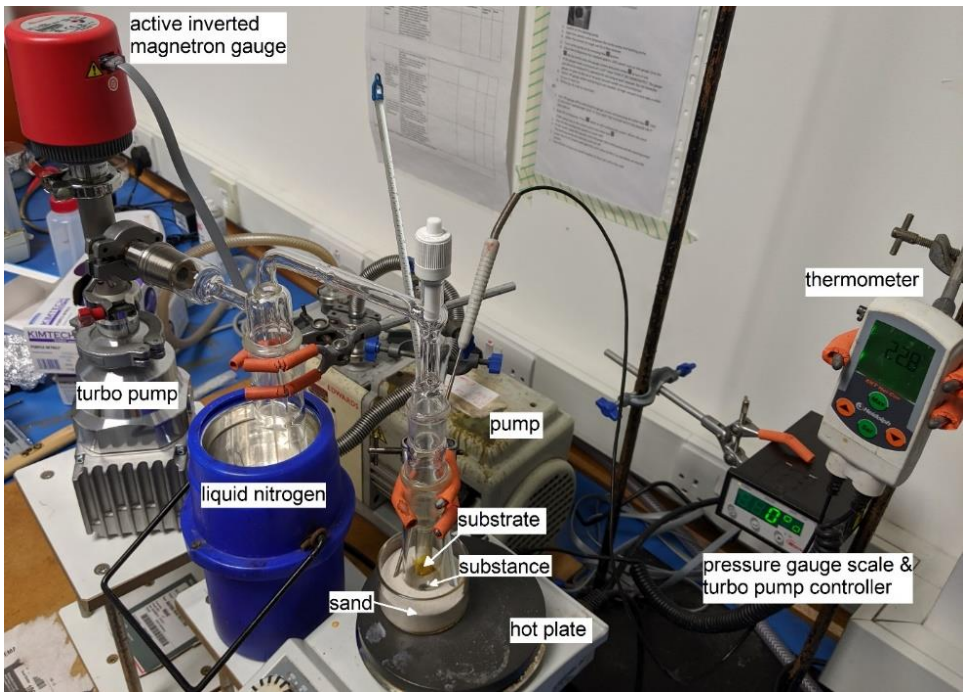

Figure 2.6: High vacuum evaporation station with key instrumentation and components.

The conventional pump creates a low vacuum and turbopump creates high vacuum environment which is supported with a liquid nitrogen trap. The active inverted magnetron gauge is reliable *P* gauge and controller which is connected to the turbopump [81]. Its digital reading and control are done with *P* gauge scale & turbo pump controller device. The substance in the form of a powder sits at the bottom of the glass chamber facing the substrate. The glass chamber is immersed into the sand bath which is heated with the hot plate. The thermometer is used to probe *T* at different sand depths but is mainly emerged to the same depth as a substance material to more precisely monitor its *T*. The sand is used to translate the heat from the hot plate to the glass since it provides better/uniform contact area with the chamber.

2.4 Known and new materials

2.4.1 Platinum complexes

The previously mentioned prerequisite for a PR material was found to be high *R* change that occurs as a result of applied *P* and this sort of behaviour was already reported for some d-metal complexes with organic ligands in literature. For example, the Bis(1,2-Dione Dioximato) platinum(II) complexes are known for their tendency to form linear chains of metal complexes in the solid-state, and under the application of *P* members of the family display interesting conductive properties. Platinum bisbenzoquinonedioximato (or $Pt(bqd)_2$) undergoes an insulator-to-metal transition with the metallic state being reached at 0.8-1.4 GPa; this corresponds to 4 orders of magnitude *R* change between *Pamb* and the above-mentioned value [82, 83, 84]. Such a tangible change is associated with BG reduction, which at *Pamb* equates to 0.25-0.52 electron volts (eV) and in between 0.8 and 1.4 GPa approaches 0 eV indicating electron free transfer between conduction and valence bands [59, 83] because *P* strengthens/increases intermolecular attraction by the means of Pt-Pt atom distance shortening (See figure 2.7) [59, 82].

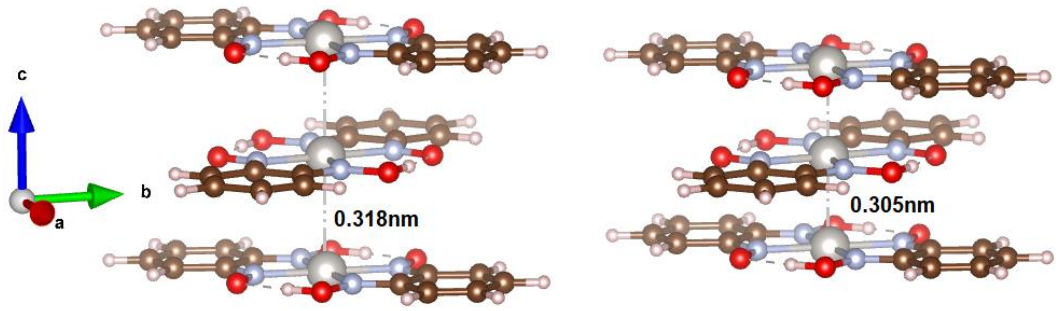

Figure 2.7: One-dimensional molecular stacking of $Pt(bqd)_2$ along the c-axis. Semiconductor on the left and metallic on the right. Atoms are coloured: Pt (grey), O (red), N (blue), C (brown) and H (pink). *P* application shortens Pt-Pt atom distances as shown with a numerical value (e.g. 0.318 nanometres on the left and 0.305 nanometres on right). Adapted from [59]. Molecules alternate along the stacking axis with neighbouring molecules related by an approximate 90º rotation.

Generally, the smaller is the primordial numerical values of BG at *Pamb*, the faster they would reach zero and, hence, metallic state with the applied *P*. This general rule arises from the comparison of $Pt(bqd)_2$ with another member of the Bis (1,2-Dione Dioximato) platinum (II) family – platinum dimethylglyoximato (or $Pt(dmg)_2$). Both materials at *Pamb* are having nearly identical short Pt-Pt distances [85, 86] however $Pt(dmg)_2$ has *Pamb* BG to be 1.44 eV (compared to 0.25-0.52 eV of $Pt(bqd)_2$) [59] and, thus, metallises only at 5 GPa [87] – *P* outside of OPET operation range and, hence, the material is beyond interest. Given the above, it becomes obvious that the main difference in electrical behaviour in response to the applied *P* arises from the distinction of the structural configuration of ligands. Therefore, it can be concluded that BG not only represents the Pt-Pt distances but also the Pt-ligand.

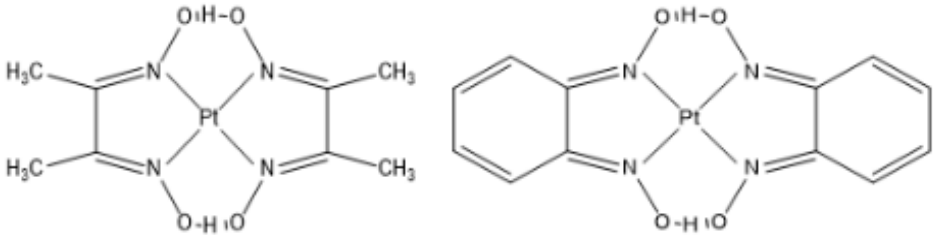

Figure 2.8: The difference in molecular structure. $Pt(dmg)_2$ (on the left) encompasses the N, O, C, H-containing chelate [87], while in $Pt(bqd)_2$ (on the right) the conjugation extends to include the benzene rings [83].

The *P* - γ behaviour of $Pt(bqd)_2$ combined with easy processing into thin films [88] makes this complex type ideal for study. Therefore, this known organic

semiconductor will be further investigated to refurnish the previously reported literature [83] and, also, used as an example material with the promising molecular pattern based on which new Pt analogues (See figure 2.9) will be synthesised. For example, the aromatic framework of $Pt(bqd)_2$ can be extended and supplemented with heteroatoms (atoms other than hydrogen or carbon), which may result in higher γ.

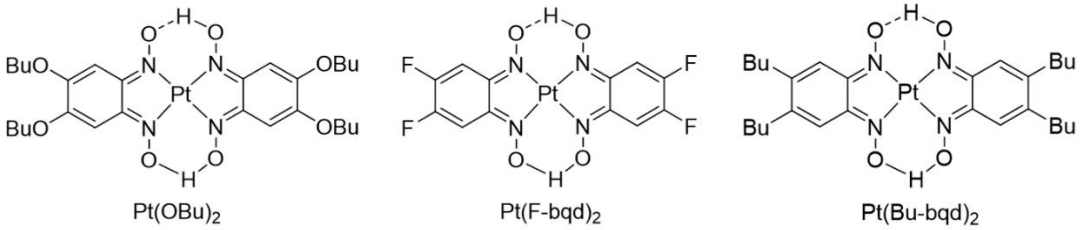

Figure 2.9: $Pt(bqd)_2$ analogues. The original aromatic framework of $Pt(bqd)_2$ was extended to have chelates with butyl oxide (BuO) on the left, fluorine (F) in the middle and butyl (Bu) on the right.

The fluorinated $Pt(F\text{-}bqd)_2$ was synthesised in a hope to lower the *Pamb* value of the BG and, hence, achieve metallic state under *P* earlier than the original $Pt(bqd)_2$. Fluorine is known for its electronegativity and its addition to the benzene ring should, in theory, lower the energy level of ligand and, thus, lower the *Pamb* BG value. Therefore, if $Pt(F\text{-}bqd)_2$ will have identical to the $Pt(bqd)_2$ Pt-Pt stacking and compressibility (See figure 2.7), the lower *P* would be required to close its BG.

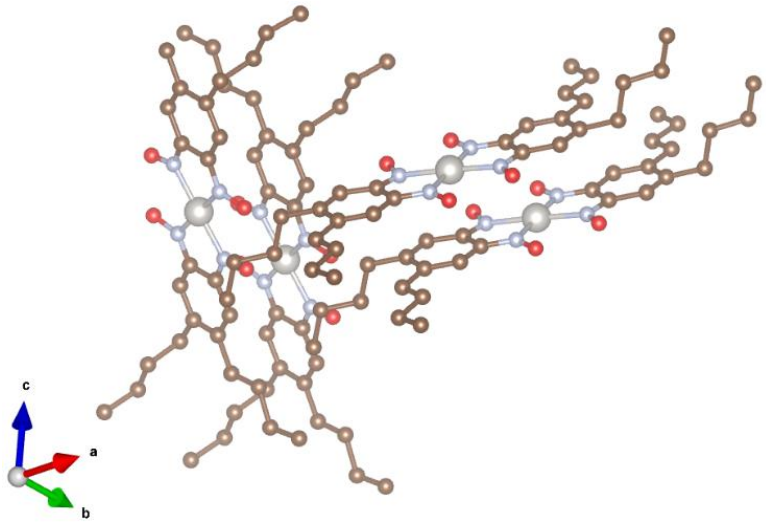

Figure 2.10: Crystal structure of $Pt(Bu\text{-}bqd)_2$. Atoms are coloured: Pt (grey), O (red), N (blue), C (brown). Molecules stack along b-axis with alternating in terms of molecular directionality layers along the c-axis. In respect to each other layers look perpendicular. Pt atom has the shortest connection with C atom in the benzene ring.

The $Pt(bqd)_2$ is completely insoluble which limits processing methods to vacuum deposition only [89, 90]. The butyl (See figure 2.10) and butyl oxide analogues were mainly synthesised to increase the solubility of the parent compound and, therefore, to simplify characteristics and physical working with the materials.

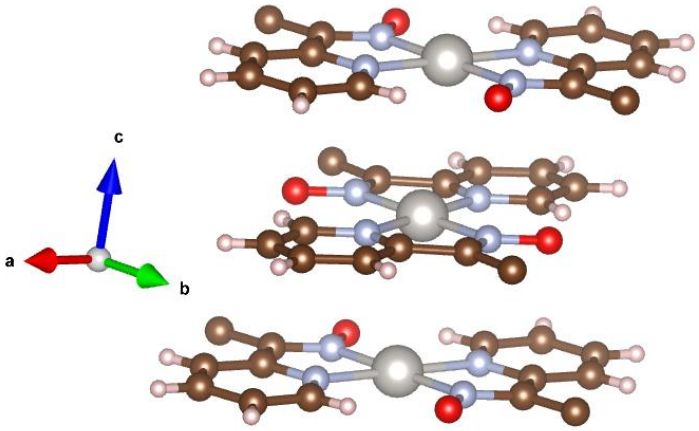

Figure 2.11: Crystal structure of PTC1. Atoms are coloured: Pt (grey), O (red), N (blue), C (brown) and H (pink). Molecules stack and alternate along c-axis with neighbouring molecules related by an approximate 30° rotation. Pt-Pt atom stacking.

The other Pt complexes which are worth mentioning are Pt complex 1 (PTC1) [91] (See figure 2.11), PTC2 and PTC3 (See figure 2.12). The former is known semiconductor at *Pamb* with Pt-Pt distance of 0.336 nm [91] – this is only 0.018 nm more than the Pt-Pt distance in the $Pt(bqd)_2$ but, unfortunately, no BG information on this material exists and no P - ρ studies were carried out. This limited information makes this material suitable for research.

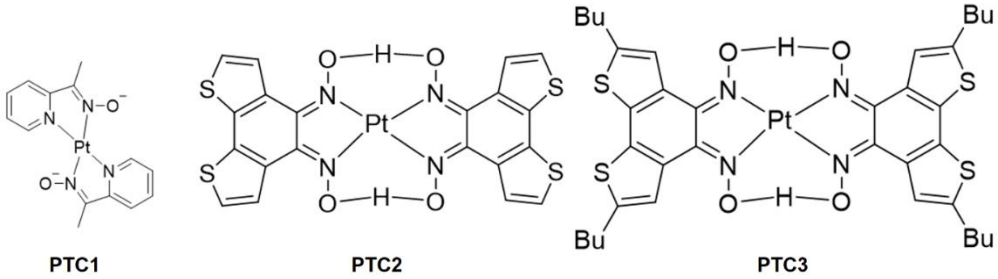

Figure 2.12: Other Pt complexes.

The last two are novel. The PTC2 has the aromatic framework which was adapted from thiophene-fused phenazine [92]. It is expected that thiophene ligand will improve the γ of the whole molecule due to the excellent electronic properties of thiophenes which are well known in organic electronics [93, 94]. The PTC3 has the

Bu extensions that, as it was previously discussed, may improve the solubility of the parent material (e.g. extend processing methods).

2.4.2 Magnus salts

The Magnus salts are coordination complexes (organic-inorganic hybrids) [95] with columnar Pt-Pt stacking [96]. The Magnus green salt (MGS) is a known semiconductor at *Pamb* with the increase in γ with an applied *P* and it has many analogues with no performed HP studies. Although MGS (See figure 2.13 & 2.14) and its analogues are known and have some preliminary measurements done [96], one of the analogues does look promising and requires *P* effect investigation on the electrical properties due to reported low *Pamb* BG.

Figure 2.13: The Magnus salts. With parent MGS on the left and its analogue on the right.

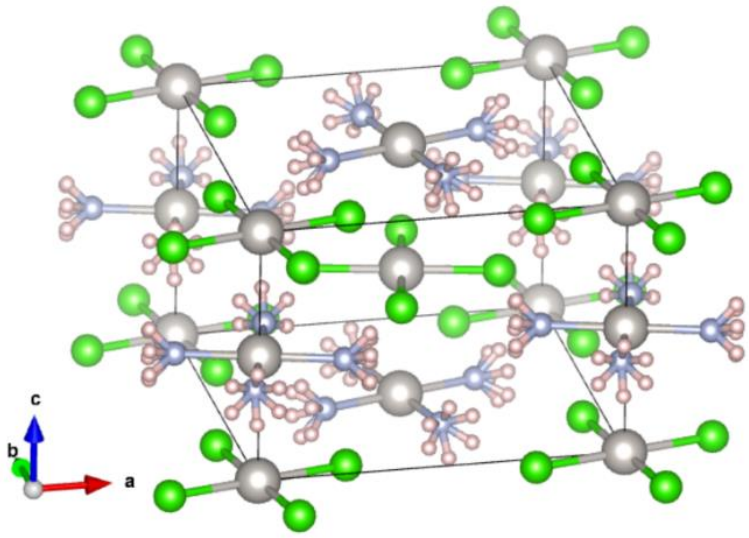

Figure 2.14: Crystal structure of $Pt(NH_3)_4PtCl_4$. Atoms are coloured: Pt (grey), Cl (green), N (blue) and H (pink). Note the unit cell and how neighbouring molecules alternate each other. Pt-Pt stacking occurs along the c-axis.

2.4.3 Copper and cobalt complexes

Both copper (Cu) and cobalt (Co) complexes (See figure 2.15) are novel, and they have no literature information. The Cu complex which was made from the same ligand as $Pt(bqd)_2$ was found to be a networked crystalline structure which is made of two coordinate environments: A and B (in a 50:50 ratio) (See figure 2.16). In one environment the ligand binds through both N atoms (just like in the case of $Pt(bqd)_2$) while in the other it binds through N and O atoms. The Cu material was selected as a central atom for the budgetary reasons since Cu is much cheaper than Pt and is a good conductor.

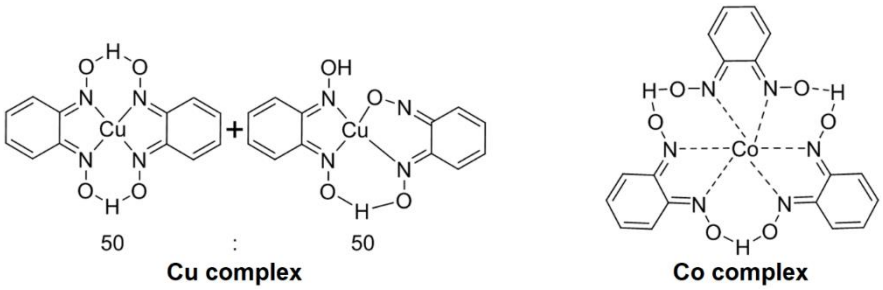

Figure 2.15: Copper and Cobalt complexes.

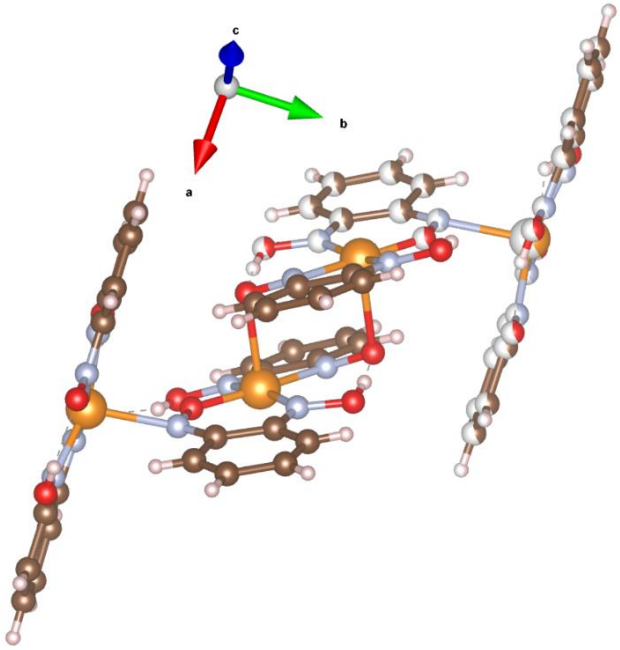

Figure 2.16: Crystal structure of Cu complex. Atoms are coloured: Cu (orange), O (red), N (blue), C (brown) and H (pink). Note the half-white atoms which represent disorder in the crystal structure. The less occupied positions were deleted by an author for a clearer picture. Stacking occurs along a-axis with a repetitive pattern of a 4x bound molecule (with Cu-O and C-N stacking as shown). Metal-chelate interactions.

The Co is another cheaper (if compared to Pt) material, and it was decided to employ it for the same reason – e.g. to reduce costs and see if the electronic behaviour of the whole compound (See figure 2.17) would be found promising. The ligand as with Cu complex was adapted from $Pt(bqd)_2$ with the only difference that there are 3 ligands around the metal atom rather than only two. There were meant to be only two, however, it was found that Co oxidised in the solution.

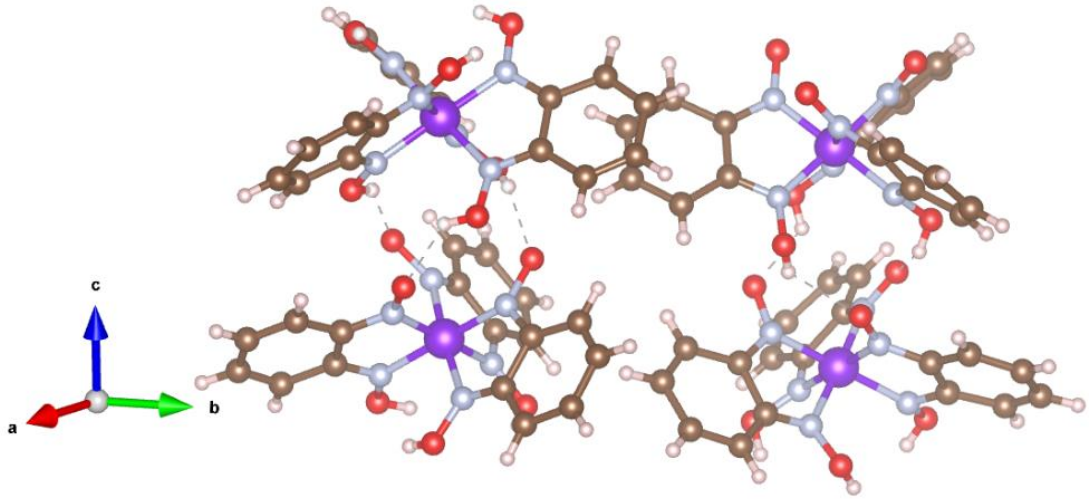

Figure 2.17: Crystal structure of Co complex. Atoms are coloured: Co (purple), O (red), N (blue), C (brown) and H (pink). Co-Co Stacking and rotational alternation of layers occur along and around c-axis respectively with lots of inter and intramolecular hydrogen bonding interactions.

2.4.4 Iridium complexes

Just like MGS, Iridium (Ir) complexes (See figure 2.18) are stacking in columns along with metal atoms in chains [97] and *P* application should be able to decrease atomic spacing and increase the overlap of molecules and, therefore, increase γ [98].

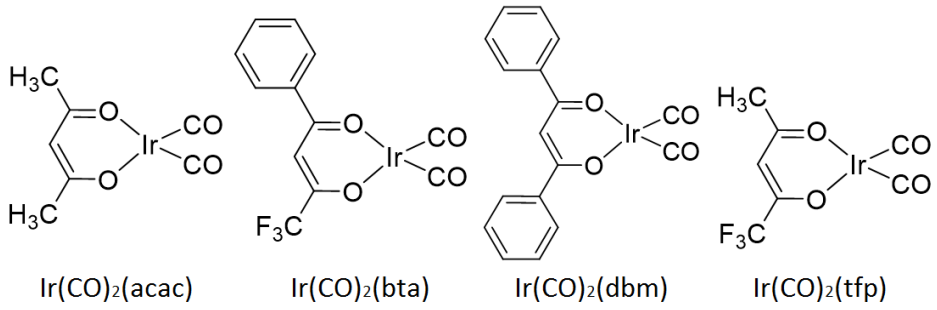

Figure 2.18: Iridium complexes. With known $Ir(CO)_2$(acac) [97] and $Ir(CO)_2$(dbm) [99] and new bta & tfp $Ir(CO)_2$ analogues. The acronyms are explained in table 2.1.

Table 2.1: Acronyms of ligands.

Acronym	*The ligand used in the synthesis of $Ir(CO)_2X$*
acac	Acetylacetone
bta	4,4,4-trifluoro-1-phenyl-1,3-butanedione
dbm	1,3-Diphenyl-1,3-propanedione
tfp	1,1,1-trifluoro-2,4-pentanedione

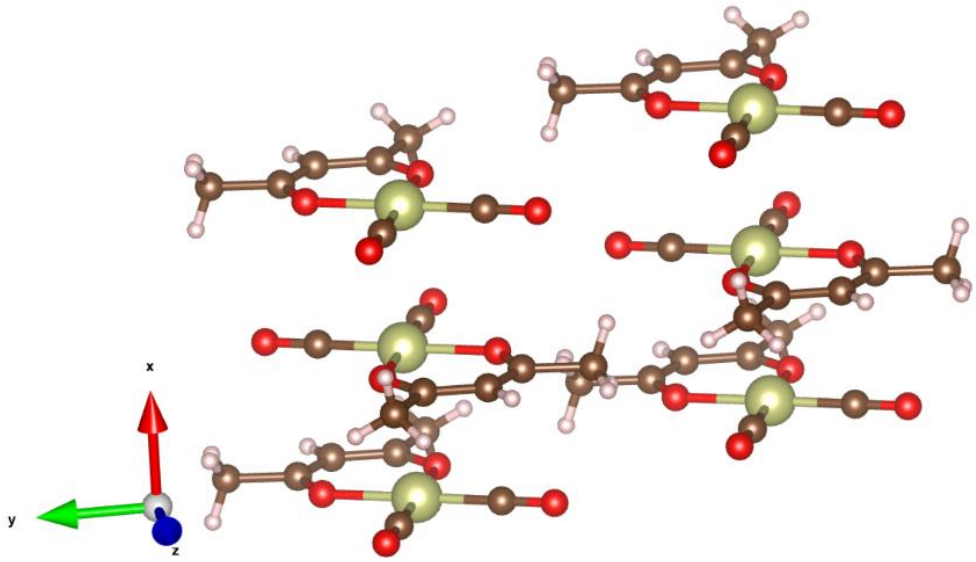

Figure 2.19: Crystal structure of $Ir(CO)_2$(acac). Atoms are coloured: Ir (green), O (red), C (brown) and H (pink). The unit cell has 2x molecules with Ir-Ir stacking along the x-axis and intermolecular O-H interactions.

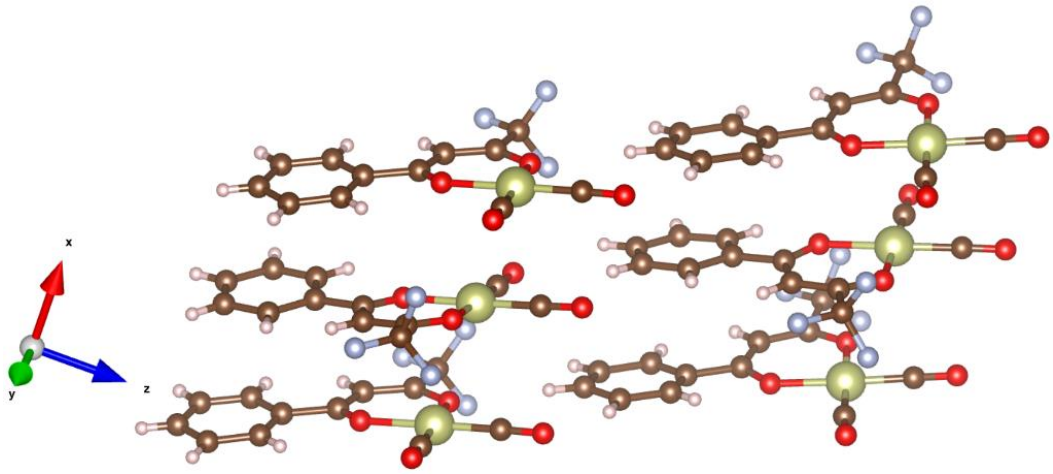

Figure 2.20: Crystal structure of $Ir(CO)_2$(bta). Atoms are coloured: Ir (green), O (red), C (brown), F (blue) and H (pink). The unit cell has 8x molecules with slipping Ir-Ir stacking along the x-axis and intermolecular H-F interactions.

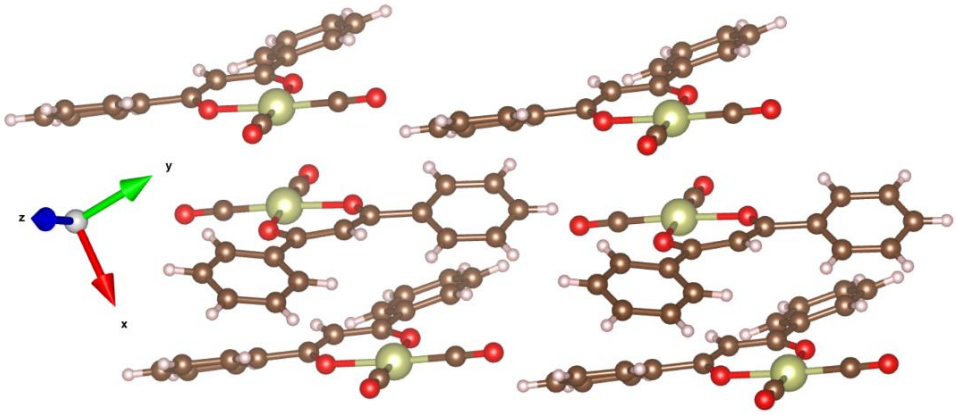

Figure 2.21: Crystal structure of $Ir(CO)_2$(dbm). Atoms are coloured: Ir (green), O (red), C (brown) and H (pink). The unit cell has 4x molecules with Ir-Ir interaction more of a dimer type rather than stacking.

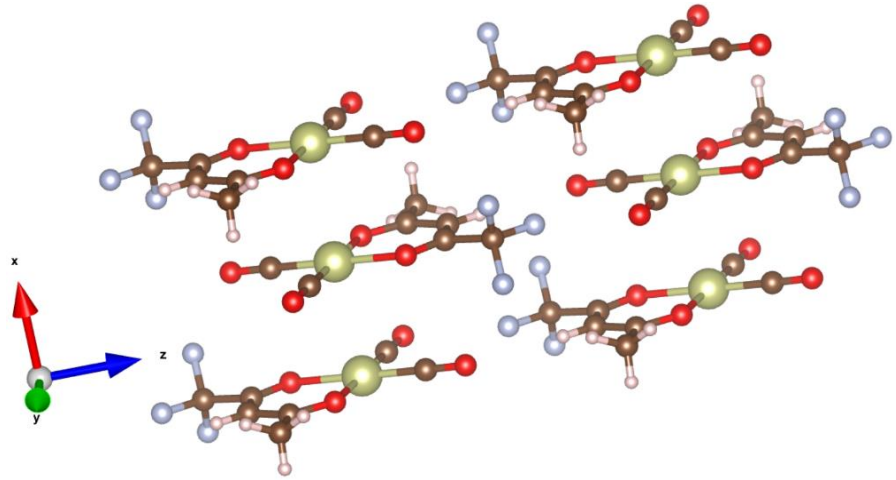

Figure 2.22: Crystal structure of $Ir(CO)_2$(tfp). Atoms are coloured: Ir (green), O (red), C (brown), F (blue) and H (pink). The unit cell has 2x molecules with Ir-Ir stacking along the x-axis with some F-O covalent character.

The $Ir(CO)_2$(acac) complex was reported to have five orders of magnitude change in γ in between *Pamb*, where it acts as a semiconductor, and 14.5 GPa – materials metallic state [97]. Obviously, this *P* range is not acceptable for the OPET device operation, however, the X-ray analysis showed small atomic distance at *Pamb* for Ir-Ir atoms to be 0.321 nm [98] pointing that the compressibility can be greatly improved if different ligand was used.

The synthesis of $Ir(CO)_2$(dbm) complex exists [99] however there was no performed study about the P - ρ. The new bta and tfp analogues have no literature behind them and were synthesised in a hope that their electrical properties under *P* would be better than those reported for their parent compound. The further reported findings

regarding *Pamb* BGs for $Ir(CO)_2(acac)$ and $Ir(CO)_2(bta)$ which are ranging in between 1 & 1.3, 1 & 1.2, 1.5 & 2 eV respectively [100], only strengthened the need to produce set of practical experiments and investigate electronic behaviours of these complexes to identify if *Pelevated* would have a high impact on the reported BGs within the *Pamb* – 3 GPa range.

2.4.5 Gold radicals

Gold dithiolene complexes (See figure 2.23) are other promising material examples in the class of planar transition metal complexes. Some of the gold dithiolenes were already reported to have potential applications in electronic systems such as quantum computing [101], resistive random-access memory (ReRAM) devices [102] and FETs [103].

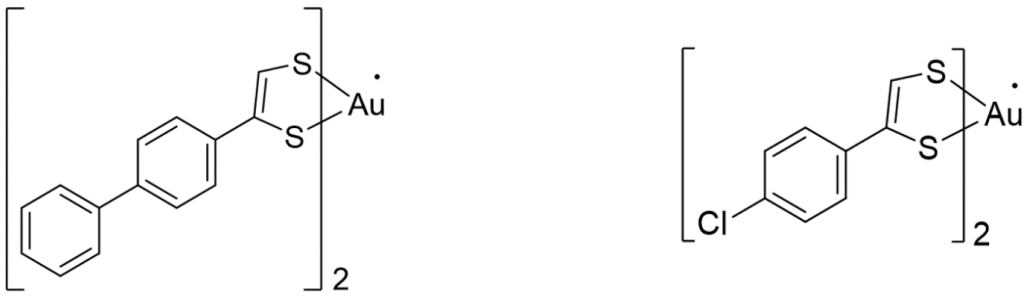

Figure 2.23: Gold dithiolene complexes. With (1-((1,1-biphenyl)-4-yl-)-ethylene-1,2-dithiolene ligand (GDC1) [103] on the left and (4-(4-chlorophenyl)-1,3-dithiolene) ligand (GDC2) [104] on the right.

The GDC1 complex (See figure 2.24) can be treated as both: known and new. It was reported by our collaborators to behave as a semiconductor with *Pamb* BG of 0.11 eV [103], however, the material was not subjected to any *Pelevated*. Moreover, this complex was found to have polymorph modifications with the main difference in how the molecules are packed in the crystal structure. Since polymorphism is not always a thing that can be controlled, for now, only two forms were isolated to produce studies on them.

The GDC2 material was reported to acts as a semiconductor at *Pamb* with a BG of 0.5 eV [104]. It was decided to investigate how *Pelevated* would affect its electronic behaviour.

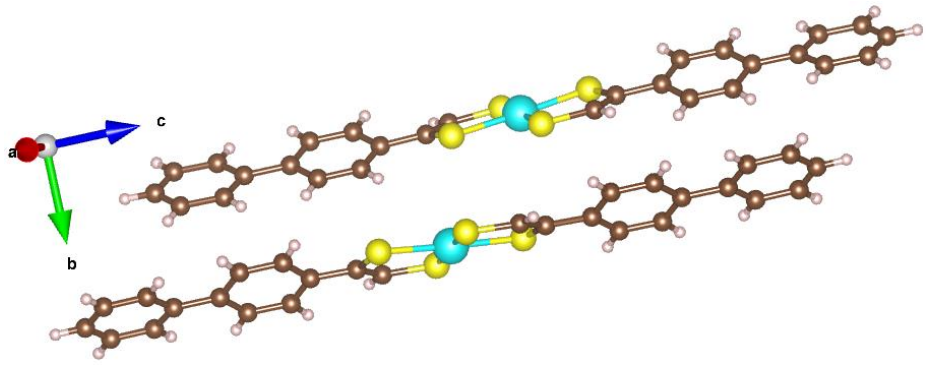

Figure 2.24: Crystal structure of GDC1. Atoms are coloured: Au (navy), S (yellow), C (brown) and H (pink). The unit cell has 4x Au molecules with strong S-S stacking along a-axis and the weak ≈ 30° C-H stacking along b-axis.

Although the mechanism of γ in these two gold compounds is different to the previously mentioned materials in this section due to nonexistence of metal-metal stacks, there are reported studies with gold dithiolene species that metallise under *P* [105] and their solution processing ability as well as interesting electron configuration of the central gold atom which has single unpaired electron [104] could mark these materials as potential candidates for the PRs. Both materials belong to the class of Mott-Hubbard insulators and information regarding their conduction mechanism can be found in the following literature [106, 107].

2.5 Summary

Among broad canvass of candidate materials for the PR in PET's concept it was decided to work with organics due to the high interest which they attracted in the recent decades by the worldwide multidisciplinary research in the electronic materials and because molecular organics are much more compressible than inorganic lattices. The existing literature allowed to identify some known candidates with the necessary change in electronic behaviour as a result of the applied *P* (e.g. insulator/semiconductor to metal transition) and also hinted at what could be a possible explanation for such electronic behaviour – one dimensional stacking of aromatic molecules. The in-house synthesis allowed to alter ligands of the known candidates by extending their aromatic frameworks which resulted in new materials being made and, therefore, the necessity in new *Pelevated* studies.

Chapter 3

Literature review – HP techniques

The first part of this chapter reviews the electronic terms along with the techniques and instrumentation that are required to produce the *R* measurements using the most relevant method to evaluate intrinsic properties out of extrinsic for different sample geometries. The second part of this chapter reviews the HP devices which can be combined with *R* measurements, the relevant for those devices *P* measurement techniques, suitable PTM and general thoughts on how to produce electrical *R* measurements in them.

3.1 Resistance and resistivity

3.1.1 Basics

In the 1st and 2nd chapters, an author used to speak about things like resistance (*R)*, resistivity (ρ) and conductivity (γ) without any definitions of these terms and how they are related to each other to avoid distracting the reader from what was emphasized at that time. In this chapter, an author will raise those terms again and explain them to the reader.

Resistance (R), current (I) and voltage (V) are related by Ohm's law [108]:

$$R = V/I \tag{3.1}$$

The base unit of the electric I in the International System of units (SI system) is Ampere (A). One A is an electric I corresponding to a stream of 1 / (1.602 176 634 x 10^{-19}) elementary charges per second. The V in the SI system has units of Volts (V) and is defined as the potential difference between two points of a wire which is carrying 1 A current with 1-watt power dissipation between points. Lastly, the R has units of Ohm (Ω) in the SI system. The Ω is the electrical R between two conductor points which would produce 1 A of electric I if 1 V of potential difference would be applied to these points [109].

The physical nature of R is as follows: imagine free electrons that are moving in the conductor. These electrons collide in their path with positive ions, atoms and molecules of the material from which the conductor is made, thereby are transferring part of their energy to them. Therefore, the energy of moving electrons as a result of these collisions is partially released and dissipated in the form of heat resulting in T raises in the conductor. The R, as the name suggests, is what free electrons are facing during their transfer through the conductor when they are slowed with the particle collisions.

Given the above, changes in material shape or size would affect its total R which makes R to be extrinsic property dependent upon the mass of material presented. The electrical property of material alone is called resistivity (ρ). It is independent of the

size of a conductor and is therefore of higher interest for material scientists as it is an intrinsic property [110].

Please note that the word conductor in this context is not representing an electrical behaviour of the material and has nothing to do with BG theory. In this context, a conductor is any material that is subjected to *V* or electric *I*.

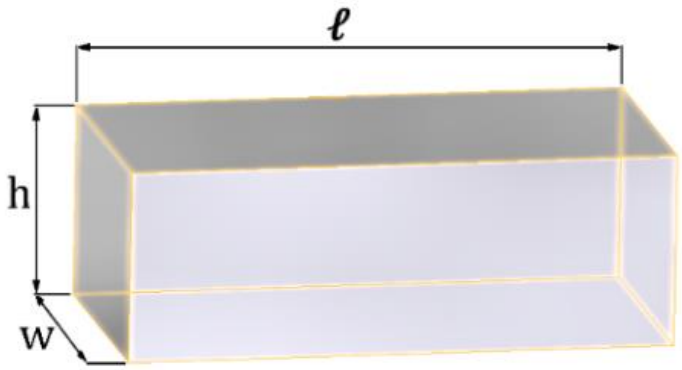

Figure 3.1: Material specimen with cuboid geometry. With: ℓ – length or thickness, *h* – height and *w* – width.

Assuming isotropic and homogeneous nature of the material specimen above its ρ will be given as follows for the probe contacts which are separated with ℓ:

$$\rho = R\frac{A}{\ell} \tag{3.2}$$

Where *A* is the cross-sectional area, and for the geometry in figure 3.1, it is a product of *h* and *w*.

3.1.2 Two-probe and four-probe methods

It is important to note that probe contacts themselves are physical objects and, although they are often made of very conductive materials such as Au, Pb or Cu, the experimental measurement accuracy drops since some level of *R* exists beyond the system of interest.

To avoid measurement inaccuracies which can be very critical, especially when the sample material is the superconductor and small *R* of contact probes adds up to the total *R* (which is then converted to ρ using equation 3.2) resulting in incorrectness, the two-probe method is replaced with the four-probe method.

To differentiate between these two methods let's consider the electric circuit diagrams in figure 3.2.

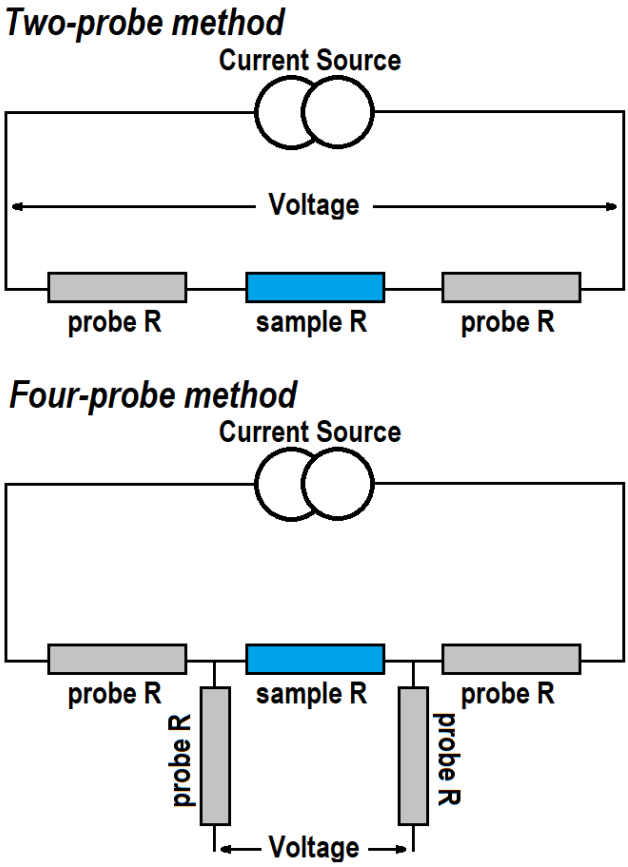

Figure 3.2: Two-probe and four-probe methods. *Rs* are coloured: probe wires are grey, and the sample is blue. Note the Voltage probing shift.

In the two-probe method, there are only two probes which are used for both: application of *I* and measurement of potential difference which results in probe wire *Rs* being added to the *R* of the sample. In the four-probe method, there are four probes across the sample with outer probes for passing the *I* through them and inner probes for measuring the potential difference. This way the probe wire *Rs* are in a parallel arrangement and are cancelled [110, 111].

3.1.3 Resistance monitoring devices

The *R* measurements in this thesis were undertaken with the help of the KEITHLEY® 2002 digital multimeter [112] as well as the KEITHLEY® 6517A electrometer [113]. The former instrument is well suited for measuring *Rs* which are lower than 1.05 GΩ and is capable of producing four-probe measurements in the 0 -

2.1 MΩ range. The latter instrument extends the measurable *R* range up to the 1 MΩ – 200 TΩ and, therefore, is well suited for high *R* measurements of PR materials. The electrometer has no four-probe method capability since *Rs* of probe wires can be neglected for the materials which are having *R* above 100 Ω [114]. The circuit diagrams of how *R* is calculated in digital multimeter (DMM) is illustrated in [114] for both: two-probe and four-probe methods.

In DMM the constant *I* is passed through the material under test and measures *V* across it, which allows using equation 3.1 to calculate *R* but when it comes to the high *R* measurement where materials are insulators the constant *V* method is more preferred [115] where the *I* source is replaced with the constant *V* source.

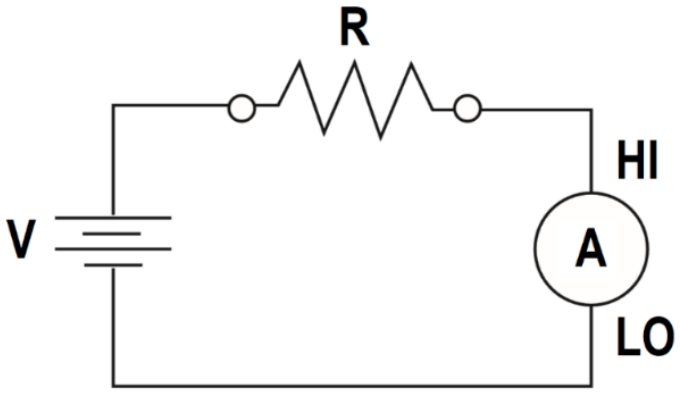

Figure 3.3: The constant voltage method. With the voltage source (*V*) in series with an unknown resistance (*R*) and an ammeter (A).

Due to the negligible *V* drop across the ammeter, all the *V* appears across the unknown *R* (material under test) which allows measuring the resulting *I* with the ammeter and, therefore, the *R* using equation 3.1. Although this method allows producing precise results for the volume and surface ρ measurements, it requires to consider things like humidity, good insulation of probe wires and *T* [116].

Electrometer allows setting any constant *V* (up to 400 V) and monitor sample *R* with the varying *I*. The *I* can be automatically adjusted using an auto-range feature within programmed recommended limits and ranges or controlled manually [113]. The general trend for the constant *V* method is that the higher is the *R* of the material then the lower *I* is required to display it. If controlled manually, then special care must be taken to avoid sample heating via probe wires which would result in inadequate *R* readings being collected which are way lower than they should be (See figure 2.5).

3.1.4 Sample material, geometry and method

Sample material itself is known to exist in two fundamental forms in nature – powder and crystal. Some materials cannot be obtained as crystals but yet for making physical property measurements they need to be made as large solid pieces – usually in the form of a CPP. Looking ahead, there were no single-crystal measurements undertaken due to the high fragility and/or short size of the grown crystals which resulted in whether single crystal fracture during probe contact attachments whether lack of free space for contact allocation. Instead, *R* measurements on CPPs as well as the thin films were performed.

In ideal case scenario the testing specimen is both homogeneous (same properties everywhere) and isotropic (same properties in all directions) however this is not always the case and, therefore, for ρ to be scalar it is important to choose the relevant technique/method for it's measuring.

Among popular within the material science community techniques (for measuring electrical ρ) such as Four-Point Probe method [117], Van Der Pauw method [118] and Montgomery method (MM) [119] the last method was chosen as it suits best for the materials which were outlined in the 2nd chapter since it was assumed that complex ligands with one-dimensional stacking cannot have the same properties in all directions and, therefore, these materials are having anisotropic nature [120].

The MM suggest producing measurements on a uniform thickness material with probe contacts to be distributed near the edges. For the CPP which is in the form of a disc such a probe contact distribution results in a circumferential pattern (See figure 3.4).

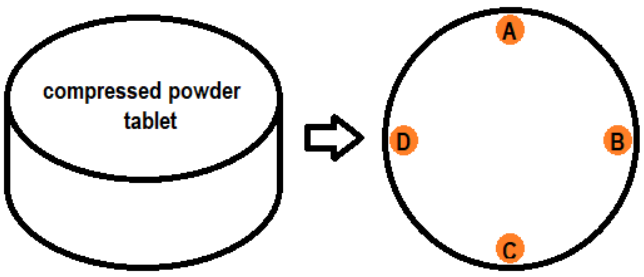

Figure 3.4: Tablet for Montgomery method. With ISO view on the left and top view on the right showing circumferential contact distribution for four-probe measurements in the form of an ABCD rectangle.

The MM equation for R into ρ conversion is as follows:

$$\rho = HZR \tag{3.3}$$

Where H is the function of contact separation AB to contact separation BC distances and for the rectangular distribution, this function's ratio would always be equal to 1 which gives a constant value of H to be 4.531 (H would always be equal to this value for any rectangular contact distribution according to [119] source). Z is the effective pellet thickness in mm which can be found using figure 3.5 in which the AB/BC ratio curve is used to link together the relationships between the normalized actual thickness of the tablet (the real thickness) on the x-axis versus normalized effective thickness of the tablet on the y-axis. Normalization implies the actual and effective thicknesses as dividends and AB contact separation as the divisor. The R is the resistance in Ω. Thereby, ρ units are Ω*mm.

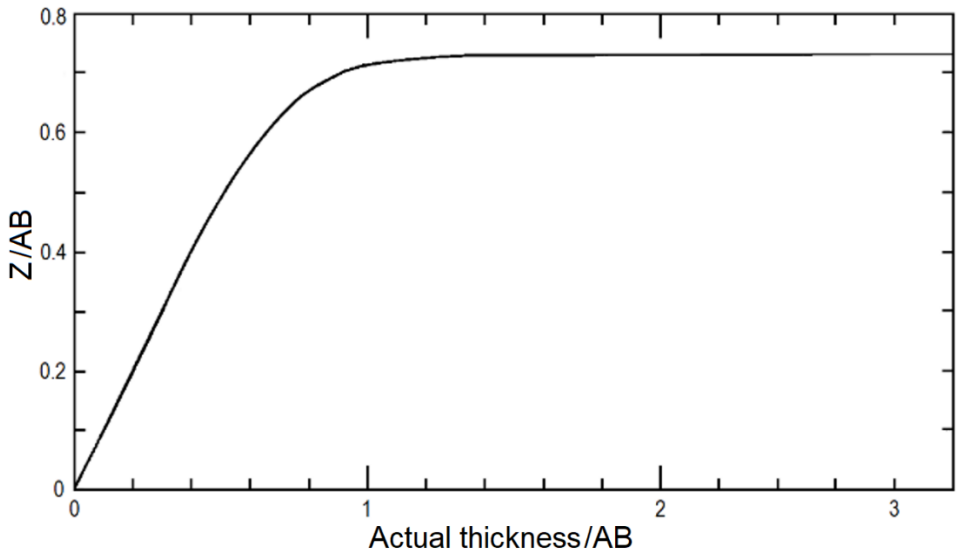

Figure 3.5: A graph to determine the effective pellet thickness. Adapted from [119] and simplified in accordance with figure 3.4.

3.1.5 Thin film resistivity

For the thin film samples, as per the OPET device concept, it is required to measure ρ through the thin layer of PVDed on the substrate material (See figure 3.6). This means that both probe contacts must be those that participate in uniaxial compression (See figure 3.7). By sputtering gold layer on a substrate first, the bottom contact might be attached on a side to the gold layer on the substrate which is not uniaxially

compressed and acts as an insulation layer in between the bottom metallic surface of a hydraulic press (worktable plate) and the deposited on the substrate gold. The top probe contact could become the indenter if it is made of good conducting material. This way, the top and bottom contacts would be separated with a thin layer of PVDed PR material which can be uniaxially compressed as per OPET prerequisite without any damage to contacts and ρ can then be calculated using equation 3.2 with ℓ being the thickness of a thin layer of the PR material and A being the cross-section of the indenter's head.

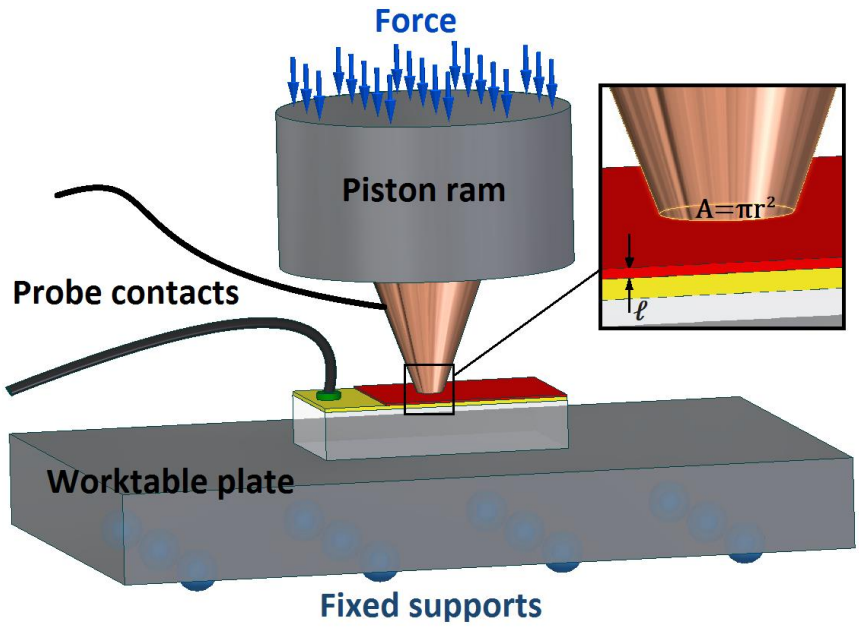

Figure 3.6: Thin film uniaxial compression concept. Components are coloured: white – transparent glass, yellow gold, red PR material, green silver paste (conductive glue) and brown indenter. Other components are named on the figure with ℓ – thickness of the PR material and A – the cross-section area of the indenter's head.

3.2 HP instrumentation

3.2.1 Types of pressure cells

In the 1st chapter, an author explained the principle of OPET device operation as well as answered why HP is required to achieve the 2nd order phase transition in candidates for PR materials. HP science is dealing with two P environments: hydrostatic and uniaxial. The former environment implies P which surrounds

material from every side while the latter, as its name suggests, produces *P* in a single axis.

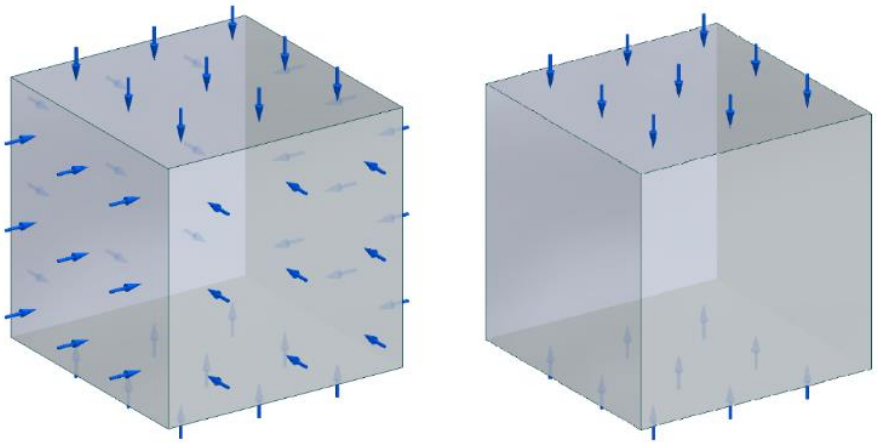

Figure 3.7: Pressure environment. Cube and blue arrows are representing the sample material and *P* application respectively. The hydrostatic environment on the left and uniaxial on the right.

Devices for the static HP generation can be roughly divided into two groups if the amount of working volume is the basis: small and large volume apparatuses. The former group is based on small anvils such as diamond anvil cells (DAC) [121], where the sample is squeezed in between the two opposed anvils with polished tips. DAC technique was invented back in 1958 by Valkenburg [122] and continues to improve instrumentation over time in terms of the maximum attainable experimentally *P*. According to the recent advances in the HP field, the DAC technique allowed to achieve extremes of 770 GPa of *P* [123] which is roughly 2.5 times bigger than those *P* conditions of the Earth's inner core [124]. The latter group includes such instrumentation as piston-cylinder cell (PCC), multi-anvil and Paris-Edinburgh devices. Compared to DACs these devices are not capable of such *P* extremes, for instance: highest attainable to date *P* in piston-cylinder cell is 4.6 GPa [125], multi-anvil press – 65 GPa [126] and the Paris-Edinburgh cell reached 40 GPa [127], however, the large volume of these instruments allows to produce an accurate synthesis of novel materials with high homogeneity of *P* and *T* [128] as well as to produce a comprehensive study about crystallisation, decomposition and polymerization of the sample material/materials [54, 129].

From the physics point of view, the pressure (*P*) is defined by the amount of force (*F*) acting per unit area (*A*):

$$P = \frac{F}{A} \tag{3.4}$$

This is a fundamental equation for the HP engineer as it tells that HPs can be achieved by generating higher *Fs* and/or by reducing the unit *A*. However, knowing that product of *P* and volume has units of energy, the more adequate question during HP design process would be not how much *F* or *A* to increase or reduce but how much energy can be stored and held within the operating volume. This is the main reason why HP devices were divided into small and large volume apparatuses as when it comes to the material selection for HP device, its mechanical properties must adhere and how much *F* would they survive without yielding is the question when dealing with hydrostatic conditions and complex 3D stress states.

For an author, particular interest arises with DACs and PCCs as these are widely employed in HP ρ studies [130 – 135] and are capable of reaching the project related *P* ranges. To produce such a ρ study, it is required to "somehow" introduce the electric probe wires to the HP environment of these cells which is not a straightforward task as it requires both: engineering adaptation of existing instrumentation (if possible) and a lot of labour patience due to physical working complexity on a small scale.

3.2.2 The piston-cylinder cell

In PCC (See figure 3.8), the *P* is generated by the means of a piston/pistons which is/are penetrating the cylinder inside walls (cell body). The *P* can be applied with the help of screws, clamps, or hydraulic press. Compression occurs along the cylinder axis resulting in *P* elevation within the sample volume. The sample volume consists whether of a solid sample/samples which is/are surrounded by a PTM whether of a liquid sample. Both scenarios are accompanied by leakage problems that can be solved by the introduction of the sealing elements such as copper rings (nearby piston/pistons) [136] and/or the polytetrafluoroethylene (PTFE) capsule which

contains whole sample volume [134]. Materials for sealing elements are generally selected based on their yielding.

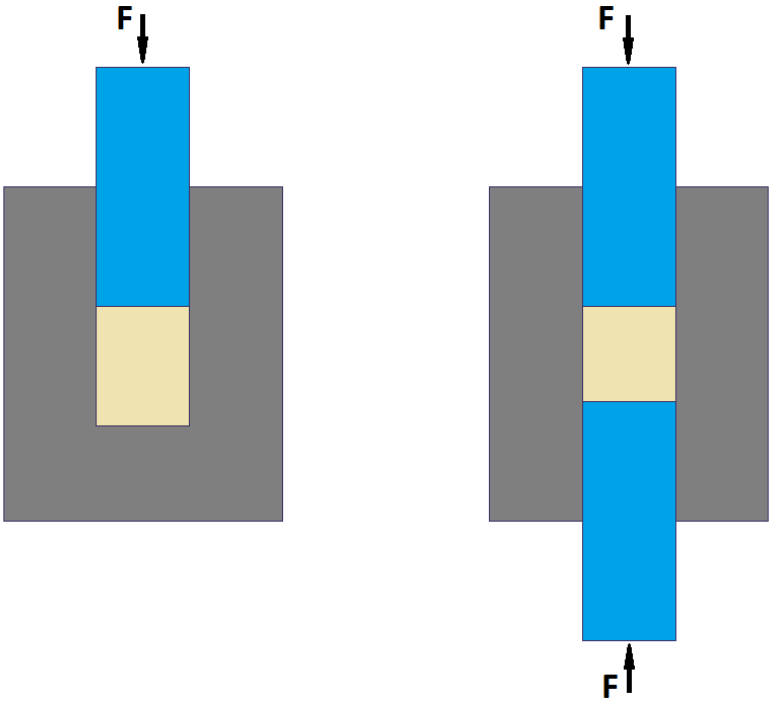

Figure 3.8: Schematic view of the piston-cylinder cell. With closed-end cylinder on the left and the open end on the right. Components are coloured: blue – piston, grey – cylinder, light yellow – sample volume [54].

The PCC underwent various modifications depending on the experiment preferences throughout the 20th century [53] with an open-end system type being employed more often since it allows to access the sample from both sides and if the piston (which is responsible for *P* generation within sample volume during pistons penetration into the cylinder) gets jammed into the bore, the sample can be accessed from the other end by ejecting the static piston (which is often made in the form of a plug that can be grabbed).

Probe wires for *R* measurements in PCC are generally introduced through the bottom of the cell since it is usually made to be static. This allows reducing the contact bending/short-circuiting probabilities. The part which introduces the leads into HP environment is called feedthrough plug (See figure 3.9) and it is a common practice to hold it with the bottom locking nut. Both, the feedthrough plug, and the bottom locking nut are having the hollow cavities along the vertical axis and in case of a plug, the cavity is filled with the epoxy once wires are introduced through it.

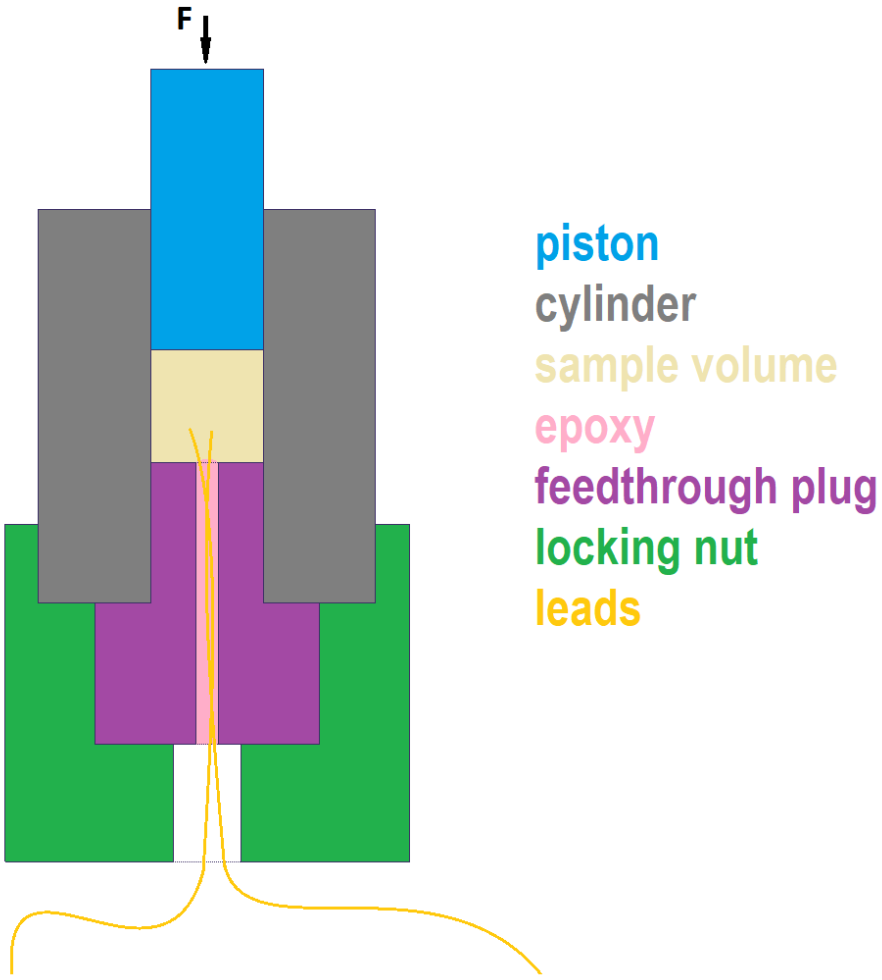

Figure 3.9: Simplified schematic view of PCC with leads. Component names are shown on the right and are having the corresponding colours. Please note that the locking nut can be used as a base on the worktable plate if it has the side slot for leads exit [53, 133, 134].

3.2.3 The diamond anvil cell

In DAC, the *P* on a sample is generated in between two polished tips of the diamonds – inside of the gasket (See figure 3.10). The gasket is a metal disk with two main functions: 1) to make sure that sample experiences hydrostatic *P* and 2) to prevent diamond fracture. If there is no gasket, the culet outer edges of the diamonds are becoming the first contact point in between two diamonds because of diamond deformation as a result of the applied *P*. In other words, under HP, the flat cullet faces are becoming concave. Thereby, the gasket which is made of a much softer material than the diamond deforms first, preventing diamond culet outer edges contact and altering the *P* distribution [53, 137].

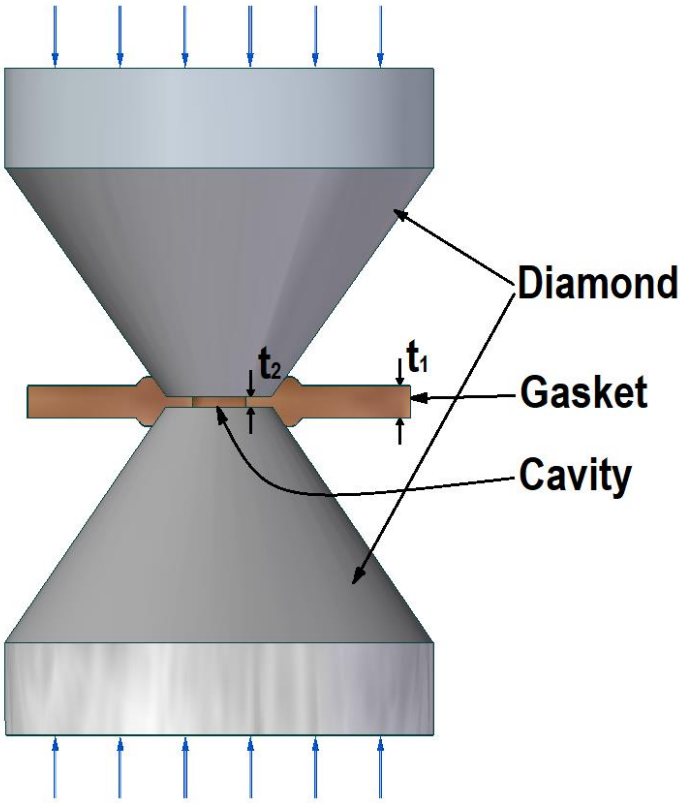

Figure 3.10: The basic design of DAC with a section view of the gasket. Blue arrows represent locations and directions of force which is then translated to the cavity. The cavity is a drilled in the centre of the gasket hole which contains a sample, hydrostatic medium and HP gauge. The hole can be made using conventional hand drilling, laser drilling or electric discharge machining [138]. Please note that gasket thickness t_1 is bigger than t_2. This is called pre-indentation of the gasket.

The pre-indentation of the gasket gives the following advantages compared to non-pre-indented gaskets: gasket thickness choice, gasket's active area is work hardened and simplified positioning on the diamond when it is time to load the gasket with the sample (as most of the diamonds are having sides instead of conical shape). The only disadvantage of gasket pre-indentation is the diamond breakage risk. When the gasket is being pre-indented it is subject to the same load which is necessary for the future experiment, which results in high tensile stresses on the diamond during gasket pre-indentation [139].

Diamonds are not only acting as *P* generators but also as an optical window which allows sample visual access after cells' closure as well as spectroscopic access to probe the *P* the sample is subjected to. There are various DAC designs for different kinds of experiments [140 – 143] and, therefore, different mechanisms to bring together the culets but the overall idea of device operation is similar.

Since 1950 when the first DAC device concept was proposed [144], the DAC underwent various kinds of improvements such as the introduction of bevel/bevels that reduce stress concentration on the cullet edges [145], designs of diamond seats/backing plates, threads, materials used as well as manufacturing technology [146].

It is important to note that with the reduction of working area (e.g. culets) the higher *Ps* are obtained at a cost of a complexity level of physical working with the cell assembly. One of the key steps to succeed is the diamond alignment process where two cullet faces of opposed anvils must be precisely aligned with respect to each other (when they are mounted in the cell along the loading direction of the force) since this alignment process increases the stability of the cell. The other important aspects include preparation of gasket, sample and HP gauge loading and selection of the most suitable for the experiment PTM [54].

When it comes to the ρ measurements metallic parts such as cell body and, most importantly, the gasket must be insulated to avoid short-circuiting through them. Although insulation of the cell body can be done relatively easy, insulation of the gasket, especially at the contact area with the diamond, is a rather difficult task. This is since the only pathway for probe wires into the HP environment is a diamond surface and contact leads should follow its geometrical curves. Probe wires themselves are thus, the thinner the better, and among various techniques can be gold-sputtered [147] – this requires a special mask to be made to cover non-preferrable for the sputtering areas, lithographically probed with focused ion beam [132] or can be made by hand [148].

3.3 HP measurement techniques

When producing the experiment, it is important to know the current *P* inside of the cell not only to collect the corresponding data of interest but also to avoid exceeding the yielding point of the materials the cell is made of. Depending on the apparatus used, experiment type, *P* range and the corresponding accuracy there are several techniques which can be employed for HP measurements. Along with a wide variety of HP instrumentation an author has already marked two HP apparatuses which are

most commonly used for *R* measurement studies and, therefore, only *P* measurement techniques which are relevant to them will be described.

3.3.1 Manganin as the HP gauge

For the piston-cylinder type device that has no optical access to the sample volume, it is a common practice to use Manganin coil as the HP sensitive sensor. This HP gauge requires lead wires to be introduced into HP environment (See figure 3.9) which are then soldered to the tips of the Manganin coil which sits inside sample volume. Manganin wire must have insulation to be wound into a coil as the coil body is more compact and safer to use rather than free wire which is not attached to anything and just drifts inside of the sample volume. Manganin wire works as the *R* manometer which electric *R* changes almost linearly against *P* up to the 2.5 GPa at *Troom* if properly seasoned [54, 149]. Seasoning implies the necessity of removal of the thermal stress and hysteresis in the Manganin wire by the means of a *T* cycling between 295 and 78° K as well as *P* cycling between *Pamb* and *Pelevated* and, also, the necessity of reduction of residual stress of coil which can be achieved with heat-treatment for 100 hours at 150° C providing microstructure stabilization [150, 151].

Pamb R of Manganin wire is used to calibrate the *R* - *P* scale using the equation below:

$$P\ (GPa) = \frac{(\frac{R}{Ro} - 1)}{0.0234} \tag{3.5}$$

Where *P* is pressure in GPa, *R* – current resistance of the coil & *Ro* – resistance of coil at *Pamb* [150].

Elevated and low *T* slightly affect the *R* of the Manganin [152, 150, 153] and, therefore, the equation must be corrected accordingly. For instance, for *Televated* the constant in equation 3.5 must be changed to acquire precise *P* probes:

$$P\ (GPa) = \frac{(\frac{R}{Ro} - 1)}{0.0246} \tag{3.6}$$

3.3.2 Ruby fluorescence technique

For the DAC the most common and sensitive method for *P* determination within the sample volume is based on the displacement observed in the ruby (Al_2O_3:Cr^{3+}) fluorescence given that the ruby piece sits inside of the cavity and can be optically accessed through the transparent diamond. This technique was introduced back in 1972 [154] and since then had various calibrations and revisions [155 – 158]. The principle of this technique is that when the high-intensity light source such as laser hits the ruby chip, ruby molecules become excited and emit two fluorescent peaks R1 (at the 694.2 nm) and R2 (at the 682.8 nm) at the *Pamb* [54]. The R1 fluorescence peak became widely employed to calculate the *P* inside of the cell from the wavelength shift $\Delta\lambda$:

$$P\ (GPa) = \frac{1904}{B}\left[\left(1 + \frac{\Delta\lambda}{694.2}\right)^{B} - 1\right] \qquad (3.7)$$

Where *P* is pressure in GPa, $\Delta\lambda$ is the shift of ruby R1 wavelength in nanometres, and *B* is a value which at non-hydrostatic conditions = 5 and for hydrostatic = 7.665 [157, 159].

The *Televated* are affecting the R1 and R2 wavelengths and, therefore, it is advised to use R2 instead of R1 as it is often found to be more intense and sharper [160]. For the low *Ts*, down to 10° K, there is no need to produce corrections to the equation 3.7 as the low *T* study shows that *P* dependence of R1 shift is identical to the one which is observed at *Troom* [161].

It is a common practice to measure the ruby piece at *Pamb* before loading it into the cell. This practice helps to calibrate the employed spectroscopic system which is used for the fluorescence measurement as well as the numerical fitting analysis of the spectra on the computer. It is also worth to mention that the geometry of the employed ruby piece can also affect the measurement accuracy. It is advised to prefer spherical rubies to the randomly cut chips from the bulk crystal because the spherical form provides homogenous luminescence characteristics [54, 162]. This becomes especially important when the ruby size is bigger than the diameter of the laser beam.

3.3.3 Pressure transmitting medium

The maximum possible achievable in the cell value of *P*, its distribution within the reaction volume/the cavity, the efficiency and the service life of the HP cell are largely defined by the choice of the PTM since it reduces the stress gradient within the sample chamber [54]. The main role of the PTM is to create the hydrostatic environment around the sample (See figure 3.7) and, therefore, the key property of interest about any PTM is its hydrostatic limit – the maximum *P* and/or *T* after which PTM starts to solidify which results in pseudo or quasi hydrostatic conditions that entail some spatial inhomogeneity. Such conditions might affect the experiment quality, especially for anisotropic materials [163]. Another important property which must be adhered is chemical inertness to avoid any reactions with the sample material. It is important to make sure that PTM and sample are compatible to produce a measurement of interest unless these two are intended to participate in the synthetic or reactivity studies [54].

The PTM substances exist in all aggregation states: solid, gas and liquid. The solid PTMs can be soft: potassium bromide (KBr), sodium chloride (NaCl) and caesium iodide (CsI) or hard: aluminium oxide (Al_2O_3) and magnesium oxide (MgO) which are not capable of producing any hydrostaticity and are employed if thermal insulation is required. The initially hydrostatic and, therefore, more preferred in HP experiments mediums are gas and liquid. The gas PTMs provide the best hydrostaticity due to higher, in terms of their solidification limit, *Ps* compared to liquid PTMs. For instance: the helium (He) and dihydrogen (H_2) remain highly hydrostatic up to 11.6 GPa and 5.7 GPa respectively with a quasi hydrostatic limit of around 50 GPa [163]. The obvious disadvantage of gas PTMs is their loading difficulty as they require special installations for gas to be injected into the reaction volume/the cavity which cannot always be available for the given HP cell design. Drawbacks of solid and gas PTMs make liquid PTMs being employed more often within the HP community. The popular instances include oils: Daphne oils (7373 and 7474) [164 – 167], alcohol mixtures: methanol-ethanol (ME) and methanol-ethanol-water (MEW) [163, 165] as well as the chemical mixtures such as Fluorinert 84/87 [166, 168] and n-pentane isopentane [165, 169].

Table 3.1: Liquid PTM and their hydrostatic limits.

PTM	*Ratio*	*Solidification P*	*Reference*
Daphne 7373	N/A	2.2 – 2.4 GPa	164, 165
Daphne 7474	N/A	3.7 GPa	165, 167
Methanol-ethanol	4:1	10.4 – 10.5 GPa	163, 165
Methanol-ethanol-water	16:3:1	14	163
Fluorinert 84/87	1:1	2.3 GPa	166, 168
n-pentane isopentane	1:1	7 – 7.3 GPa	165, 169

According to the table 3.1, ME, MEW and n-pentane isopentane provide the highest solidification *Ps*, however, these are highly volatile substances which require fast operation (cell closure) which is not advantageous when reaction volume/the cavity also contains probe wires for *R* measurements. On the contrary, all actions should be slow and accurate to avoid probe damage. Also, in some cases, these mediums can react with or dissolve the sample and ME & MEW are not advised when doing electronic transport measurements that require conductive paste such as silver, carbon or gold [167].

Daphne oils which are trademarks of Idemitsu Kosan Co., Ltd., [170] are synthetic non-conductive lubricants which are widely preferred in the PCCs to other PTMs due to their not too high change in *P* with *T* which is almost independent of *P* making these mediums to be ideal for *T* analyses [171] which are key for BG calculation (See 2.2.5 section in the 2nd chapter).

3.4 General thoughts

Electrical ρ measurements at HP is a complex delicate work which requires patience and accuracy. The experimenter's most common problem is associated with electrical leads that can tear off and/or short circuit during *P* application or even preparation for the experiment (e.g. cell assembly). In PCC (See figure 3.9) electrical leads can easily lose their protective insulation layer during their passing process through the feedthrough plug. Any sharp metallic edge is a potential hazard for

electrical leads. Once the feedthrough canal is filled with epoxy (a Stycast mixed with catalyst) it becomes impossible to visually access/check if the probe wires are fine. Before employment of such a feedthrough plug in the HP experiment, it will be required to produce the *R* tests of all lead wires to make sure that electronic signal exists for a particular wire and does not cross with others. This might not be the case at ambient conditions when epoxy rests but under applications of *P*, there might be issues caused by small shrinkage in the epoxy and/or its stretching during *P* release. Therefore, it is important to apply and release *P* slowly however it might not help if epoxy used is poorly mixed or badly applied which can result in trapped inside of the feedthrough plug air and friction in between leads and cylinder walls [53]. The short circuit problems may be spotted only at *Pelevated* and disappear when *P* is released. Therefore, it is important to produce checks during the experiment conduction.

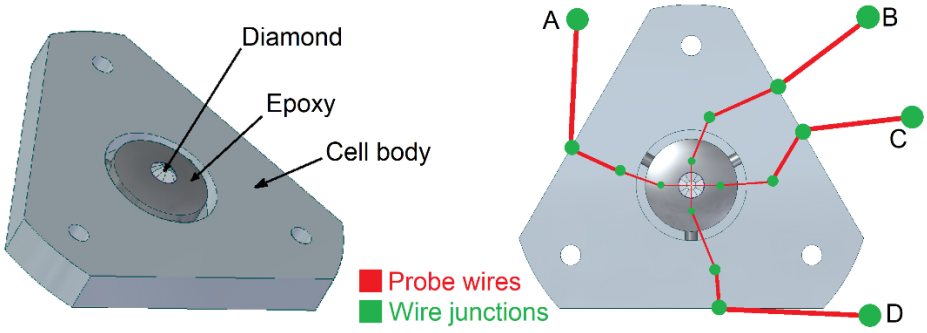

Figure 3.11: Probe wires and wire junctions on DAC. With ISO view on the left with key component names and top view on the right with electrical leads assembly concept. Note the thickness change of the probe wires with thinnest nearby diamond and thickest outside of the cell body boundary where contact ends are represented with A, B, C & D for probing *R*. The general DAC design idea was adapted from the Merrill Bassett cell [172].

To produce electrical ρ measurements on a CPP (See figure 3.4) the need to follow specific method based on the materials directional inhomogeneity was identified (e.g. MM) in which pellet geometry needs to be calculated in accordance with figure 3.5. Unquestionably, the bigger is the size of the CPP, the more precise contact allocation would be and, therefore, the more accurate results would be collected. When the material is subjected to extremes of *P* in PCC it is a common practice to use the conductive paste to make sure that leads/probe wires would stay in contact with the sample during the experiment [134, 173].

While for PCC it is required to use an external device to produce a tablet – a tablet compress which can be made to produce any required for the experiment CPP to fit it

into PCC, in DAC the CPP is made inside of the cavity during powder loading process when handfuls of powder are compacted into the drilled in the gasket hole. Unlike in the PCC where scale allows to use thick wires with insulation, in DAC wires used are often thin and non-insulated to simplify working with them at a small scale which results in a necessity to insulate areas they adjoin.

If the design of DAC allows, the electrical leads can be allocated on one of its cell bodies as it is shown in figure 3.11, while the gasket with the sample can be assembled on another identical cell body. It is important to have wire junctions as safety stations which, in case of the accidental wire pulling, would prevent further damage to the wire assembly – especially nearby the delicate areas such as diamond. Wire junctions can be made of a mechanical character (e.g. twisted ends) since wires used are non-insulated or can be soldered or even glued with a conductive paste to improve the connection strength.

3.5 Summary

Lack of the commercially available HP apparatuses which are specially designed to produce *R* measurements dictates the need in the development of the new or, if possible, adaptation of the existing instrumentation. Since the size of the CPP was mentioned to affect the experiment quality in terms of contact allocation precision due to the employed MM, it is reasonable to first consider the large volume devices such as PCC. For the OPET application, the PR's metallization is expected to happen in the *Pamb* – 3 GPa range which was mentioned in the 2nd chapter and such a *P* range is achievable in the PCC which will be therefore developed. To characterise those PR materials which failed to metallise within the desired *P* range but still are having an interesting ρ - *P* tendency the DAC will be adapted which will extend the achievable *P* up to the 10 GPa. The 10 GPa value was selected as an upper *P* limit to allow to employ as big as possible diamond cullets and, therefore, to fit as big as possible CPP. The DAC adaptation is more rational than the development of new since some DAC designs already exist which can be adapted to produce *R* measurements and it is therefore required to select the most suitable one in terms of the probe wire access to the sample and visual access to the ruby.

Chapter 4

Development of PCC

The first part of this chapter starts with the requirements and reasoning for the PCC which are followed with design considerations. Further, the Lame's and distortion energy theories are provided and explained since these were used in the PCC's design. The second part of this chapter provides a brief description of the finite element method (FEM), has single-cylinder simulation with analytical validation of the model to access the quality of the employed software, and, lastly, the compound PCC design and analysis of relevant stresses. In the end, the manufacturing, assembly and experimental testing of the compound PCC which is capable of reaching 3 GPa and is equipped with feedthrough plug for *R* measurements on the sample material and Manganin coil (e.g. HP sensor) *in situ* are provided.

4.1 Requirements and reasoning

4.1.1 Pressure limit

The maximum attainable *P* in PCC is highly affected by the size of the reaction volume. The bigger is the internal diameter (*ID*) which should fit the CPP (See figure 3.4), the more advanced the design of the PCC will be to hold the 3 GPa – the upper limit of *P* within the suitable OPET application range (See 3.4 section in the 3rd chapter). Design advances can be attributed to the introduction of the additional cylinder and/or autofrettage which allows to extend the maximum attainable *P* inside of the PCC and to go beyond the yielding point of the materials employed in the design without causing the permanent deformations in them [53]. With 3 GPa as a *P* limit, the most suitable PTMs are Daphne oils (See table 3.1) which stay highly hydrostatic at this *P* range and are non-conductive, inert and non-volatile.

4.1.2 Sample dimensions

To determine the required diameter of the reaction volume for PCC it is first required to find the optimum CPP geometry in accordance with the MM. By drawing straight vertical and horizontal axis lines on the graph (See figure 3.5) it can be found that the actual thickness would stay identical with the effective pellet thickness (*Z*) in case if the normalised axis values would not go above certain value when they meet the AB/BC ratio curve. This equal dependency will be complied up to the value of 0.3 which is also well supported by Yadunath Singh, who in his report [120], where he reviews different electrical measurement techniques, states that the thickness of the pellet for the MM must be as follows:

$$CPP\ thickness \leq 0.3\sqrt{AB^2} \tag{4.1}$$

Where AB is the contact separation and, as it can be seen, the equation above does not have the diameter character involved and, therefore, it is required to determine it based on the optimal contact separation value. It was practically determined that to securely attach one copper (Cu) contact to the CPP it is required to add silver paint of such a quantity that the resulting occupied surface on the CPP would equate to roughly 0.4 mm in diameter circle which should be placed near the CPP's edge.

Silver paint is required to produce a conductive secure connection between CPP and Cu probe wire end over the experiment duration. To produce four-probe measurements it is required to have 4 of these circles which are precisely distributed in the form of ABCD rectangle on the CPP's surface. The 0.4 mm value could have been smaller however the used in the PCC Cu contacts, which work as a pathway in between *Pamb* and HP environment (See figure 3.9) must be insulated and relatively thick (≈ 0.1 mm or more) to prevent short circuits and accidental discontinuities which otherwise would become inevitable even with the careful exploitation of the PCC.

Knowing how important the precision in contact distribution for accurate *R* into ρ conversion is, the value of space required for Cu wire and silver paint (e.g. 0.4 mm circle) and the equation 4.1 which brings the relationship of thickness to contact separation, the final geometry of CPP can be determined.

By having A, B, C & D circles as a constant 0.4 mm in diameter circles it was found that the optimal outside diameter (*OD*) of the CPP equates to 3 mm which gives a value of 1.44 mm to be the contact separation and 0.43 mm to be the thickness.

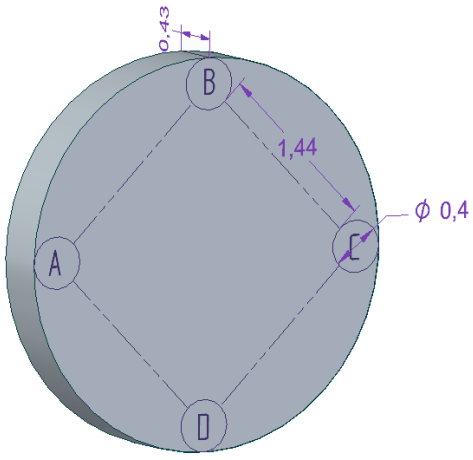

Figure 4.1: Compressed powder pellet geometry for the piston-cylinder cell. Four-point contacts on the top surface of the pellet are arranged in the form of ABCD rectangle. The 0.4 mm in diameter A, B, C & D circles are representing contact areas which will be occupied with Cu wires and silver paint. 1.44 mm distance represents contact separation in between A & B, B & C, C & D and D & A. Please note the thickness to be 0.43 mm.

On the one hand, the increase in the *OD* would highly simplify the working/handling, however, on the other hand, it would also affect the maximum attainable *P* in PCC. On the contrary, the lower *ODs* for CPP would improve the PCC capabilities,

however, these *OD* decreases would also be followed with necessity in decreasing the contact separation as well as the pellet thickness in accordance with equation 4.1. The experience shows that even the contact separation of 1.44 mm (See figure 4.1) was hard to measure due to small scale and non-uniform surface (when the silver paint is applied to the CPP it forms protrusions since A, B, C & D blobs are containing Cu probe ends).

For instance, if the CPP's *OD* was selected to be 2 mm, the contact separation would be shortened to 0.73 mm and, therefore, the CPP's thickness becomes 0.219 mm. The thickness value of 0.219 mm is unacceptable for the CPP due to the empirical observations when it was determined that CPP snaps during ejection from tablet press device or process during which the CPP is brought to such size. Not to mention the high probability of failure during hydrostatic *P* application and release in the PCC where the thicker size of CPP would provide more reliability and, therefore, it was decided to stick to the geometry which is shown in figure 4.1.

Although the PR material candidates are all insulators at *Pamb* which means that *R* can be measured using the two-probe method (See figure 3.2) the final geometry (See figure 4.1) takes into account the probability of a change in electrical properties of PR candidates under extremes of *P* and, therefore, all CPPs must be equipped with a reasonable amount of probe wires (e.g. four) which are adequately allocated in the form of ABCD rectangle for the four-probe method to be employed if needed. This approach would not only prepare for any experiment outcome in terms of change of electrical properties of the test materials but would also allow determining if the contact separation equalities of AB, BC, CD and DA are complied as per MM. This can be achieved with the conduction of two-probe *Pamb R* measurements to collect a total of four *Rs*: R_{AB}, R_{BC}, R_{CD} and R_{DA} which in turn will allow checking if *R* values converge. Convergence is also highly affected with the quality of the CPP, so special care must be taken during work with it, not to mention CPP's extraction from the tablet press device (See figure 4.2) to avoid crack and microcrack propagations as these would greatly increase observable *Rs*.

The final *ID* of the PCC should be able to contain the 3 mm in *OD* CPP, which should be mounted on a special table (a non-metallic component which allows

placing a CPP on it so it won't float in PTM). The size of such a table must be > 3 mm (*OD* of CPP) to allow Cu wires to reach the CPP's edges for *R* monitoring. Also, the CPP and a table with all Cu leads as well as the Manganin coil must fit into the PTFE capsule to minimize leakage issues (See 3.2.2 section in the 3rd chapter).

By looking ahead, the optimum *OD* for the table was found to be 3.8mm because of the thicknesses of the employed Cu wires. The PTFE capsule with 3.8 mm *ID* and the wall thickness of 0.5 mm was selected. The *OD* of the PTFE was then reduced to 4.5 mm with the sandpaper. Any further wall thicknesses reductions were found to be unreliable since cracks started to propagate on the tubes. Therefore, the *ID* of the PCC's cylinder should be at least 4.5 mm in diameter to fit the 3 mm in *OD* CPP.

4.1.3 CPP press

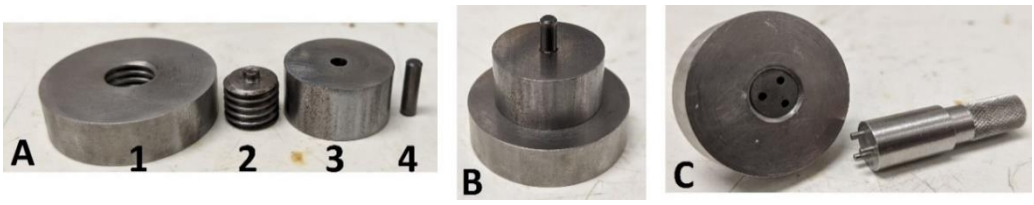

Figure 4.2: CPP press. Where A – disassembled press with 1 – press base with internal thread, 2 – plug with external thread, 3 – cylinder and 4 – piston, B – assembled press and C – bottom view of B with the tool for plug insertion & extraction.

The idea of press operation is as follows: well-grinded powder particles are poured into the cylinder hole to occupy 2/3 of its volume without any physical *P*, the piston is then injected into the cylinder as in B and this assembly is put under the hydraulic press which forces piston into the bore and compresses the CPP. The threaded parts simplify CPP extraction. They allow to slowly lift cylinder out of the press base (1) by rotating parts 2, 3 and 4 using the tool from C. The appearing gap in between parts 1 and 3 allows to gently detach part 2 out of part 3 using the flat screwdriver as a crowbar. Once parts 2 and 3 are detached, it is required to extract CPP out of part number 3 by utilizing the part number 4 (which is stuck into part 3) and the hydraulic press. Part 1 which has bigger *ID* than part 3 is then employed as a stand, in between worktable plate and the part 3 to avoid CPP's pushing into the worktable plate which can happen due to fact that part 4 is longer than part 3. To avoid contamination and to make sure that the tablet won't fall and break, soft and clean sheets can be placed

inside of part 1, however, the practise shows that CPP stays attached to the piston even after its full ejection from the cylinder so there are no risks of crack propagations and gentle side push allows to disjoin CPP out of the piston's head.

Parts 1, 2, 3 and tool for insertion/extraction are made of silver steel as it has high wear resistance and is easy to be machined while part 4 is made of tungsten carbide to avoid any deformation of the piston during the pellet compression process. All parts must be kept clean to avoid sample contamination and, after each pellet compression, must be cleaned in the ultrasonic bath while submerged into the suitable media to avoid rust formation. It is important to note that the value of *P* which is required to make the CPP may vary depending on the sample material. This value can be found empirically after careful visual examination of the CPP for dints and cracks. Also, such a method is not suitable for materials which are not having reversible nature because compression of powder may already incur permanent changes in material and its properties. Luckily, material reversibility is one of the key properties which were previously outlined (See 2.2.1 section in the 2nd chapter) which makes this powder compression method suitable for employment.

4.2 Design considerations

4.2.1 Feedthrough plug for lead wires

The feedthrough plug for lead wires is an essential component in PCC that allows *in situ P* measurements and electrical measurement on the sample. The feedthrough canal should be wide enough to be able to let though itself 12 Cu wires with 4 wires for 4-probe *R* measurements on CPP, 4 wires for 4-probe *R* measurements on a Manganin coil (*P* sensor) and 4 wires to be there as spare ones considering the labour intensity and high-probability of wire failures such as bending etc. etc. On the bottom side of the feedthrough plug which is open to the atmosphere, 12 Cu wires should sit inside in the protective plastic tube to provide additional protection from the sharp edges of the bottom locking nut and its thread. On the upper side of the feedthrough plug which leads to HP environment, Cu wires should be circumferentially evenly distributed with the help of a cone knob with 12 grooves. The conical contact geometries in between feedthrough plug and cone knob would improve/increase the

contact surface area in between those parts and, therefore, evenly distribute stress when the cell is subjected to HP. The grooves in the cone knob would separate Cu wires so they do not cross and do not rub each other under HP. The existence of the cone knob also improves the sealing of the PCC since there are less unoccupied by the physical materials space and, therefore, less epoxy is required to fill in the hollow cavity resulting in a more reliable hitch and reduced probability of wire discontinuities at high loads. Also, the cone knob can be designed in such a way that its geometry would allow wounding of a Manganin coil around its body by introduction of the rod concept on top of the conical shape. Moreover, another end of the rod might be used as a connection with the table which can be used to precisely mount the CPP [136]. Some of the dimensions for the sample table such as *OD* were discussed earlier and table must be designed in such a way so it would be able to protect Cu and Manganin wires against PTFE tube, has a narrow rod for unused Cu wires to be wound around it and circular disk on the top for the CPP mounting. Whole tables' geometry should also have 4 cut-in grooves which are circumferentially allocated at the 90-degree angles with respect to each other. These grooves should act as a protected pathway for 4 Cu wires to be in a reach with the contact regions of the CPP (See figure 4.1). It is a must to protect wires in order to avoid probe breakage or short-circuiting. Both adverse scenarios exist due to the likelihood of inward bending of the hollow PTFE capsule when the piston penetrates the inner cylinder of the PCC as a result of *P* application. The small thread such as M1.6 can be used to connect table and cone knob. Given that the interest of measurements has the electrical character, parts which are physically connected with the CPPs (in this case it is a table component) must be made of a non-conductive material. The Polyetheretherketone (PEEK) being chemically resistive with exceptional insulation properties and high-temperature tenacity (good for *Televated* analyses) becomes ideal candidate material for the table while the feedthrough plug and cone knob components should be made with beryllium copper (BeCu) because of its high yield strength ($\sigma_y \approx 1.4$ GPa) and the high thermal diffusivity observed over a wide *T* range (for *T* analyses), whilst BeCu remaining non-magnetic down to low *T* [174, 175]. The most suitable epoxy for the cone knob and feedthrough canal sealing is the LOCTITE Stycast 2850FT which has electrical insulative properties

and good physical strength when mixed with a suitable catalyst [176] and is blended with diamond powder (grain size approx. 1 μm) [177]. It is important to suck any air out of the black epoxy before its application to the parts. Small air bubbles arise during mixture process of the catalyst with the Stycast and diamond powder. Also, considering the small size of the cone knob grooves (as Cu wires are ≈ 0.1 mm in diameter) it is a must to produce negative *P* inside of the hollow cavity on the bottom side of the feedthrough plug during black epoxy curing so epoxy gets into the grooves. This can be achieved with the help of a conventional pump.

Table 4.1: The mechanical properties of the hardened BeCu [178].

Mechanical property and units	*Numerical value*
Tensile yield strength – σ_y (MPa)	1400
Tensile ultimate strength – UTS (MPa)	1500
Poisson's ratio – ν	0.3
Young's modulus – E (GPa)	130

Another promising alloy for the HP instrumentation is the $Ni_{57}Cr_{40}Al_3$ (NiCrAl) which is also known as the Russian alloy. Such a sobriquet was given to this material since it was previously available only in the former Soviet Union until it was reproduced in Japan in 2002 [179]. The NiCrAl alloy can achieve the optimum mechanical properties during the ageing process and was previously employed in the PCCs development [133, 134, 179] due to low magnetic background properties [179], high σ_y and UTS. The mechanical properties of this material were provided by the supplier and the technical datasheet can be found in Appendix A.

Table 4.2: The mechanical properties of the hardened NiCrAl (See figure A.1 & A.2).

Mechanical property & units	*Numerical value*
Tensile yield strength – σ_y (MPa)	2000
Tensile ultimate strength – UTS (MPa)	2200
Poisson's ratio – ν	0.3
Young's modulus – E (GPa)	300

4.2.2 Manganin coil

The *R* of the Manganin depends on its length and it is a common practice to have a segment of such a length which would correspond to 100 Ω. Once the Manganin is properly seasoned (See 3.3.1 section in the 3rd chapter) and epoxy is cured on the feedthrough plug and the cone knob, Manganin with removed from the wire ends insulation can be wound around the cone knob's rod. It must be wound in such a way so that the overall width would not become bigger than the available in the PTFE capsule space which also contains 12 Cu wires that should go nearby the coil. In order to keep the coil static, it might be necessary to use the weak non-conductive glue such as GE Varnish. It is important to keep an eye on the non-insulated wire ends and to make sure that they stay within physical access. When the GE Varnish dries out, each Manganin end must be soldered with 2x Cu wires. It might be necessary to choose the closest for the Manganin Cu wires, shorten them with accordance with Manganin end positions and remove 0.5 mm of their insulation at the ends. Prior to soldering, relative wire ends must be carefully and lightly tied to each other to simplify the soldering process which must be done at as low as possible *T* at which solder melts, to prevent accidental removal of wire insulation where it is not desired. The soldered blobs must be as small as possible so they would still fit into the PTFE capsule and the bottom part of the table.

4.2.3 Clamp-design

The PCC should be utilized with a hydraulic press. The top of the hydraulic press (the ram) operates dynamically which would allow translating the vertical force to the upper part of the PCC (e.g the piston) resulting in its penetration into the cylinder and, therefore, to the *P* increases in the reaction's volume. The force can be controlled during the experiment as well as the speed at which it is applied. The bottom part of the hydraulic press is static and is called the worktable plate. For the PCC which at the bottom is equipped with the feedthrough plug, this is a safe non-dynamic environment where the Cu contacts which are open to the atmosphere and interconnected with the suitable *R* monitoring devices would not bend, snap or wind around the PCC.

By introducing additional component to the simplified schematic view of the PCC (See figure 3.9) such as the upper locking nut, the PCC could be clamped/locked at any achieved *P* with the full release of the force from the hydraulic press if needed. This might be handy for long experiments that involve *T* analyses. Depending on the piston design, the locking concept also requires the introduction of other component/components: the pusher if the piston is of a T-shape [136, 180] or, in addition to the pusher, the spacer component is required if the piston is of a rod shape (See figure 4.3) [181].

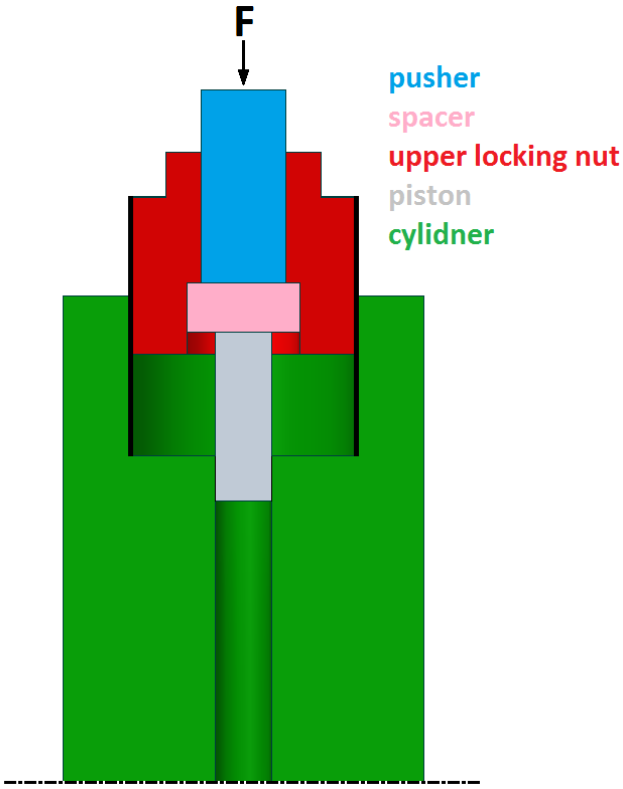

Figure 4.3: The upper locking nut concept. Component names are shown on the right and are having the corresponding colours. The upper locking nut and the cylinder are having external and internal threads respectively for the engagement purposes. The piston and spacer could be made as a single piece resulting in the T-shape piston.

The *P* in the PCC with the upper locking nut concept (See figure 4.3) should be applied once the nut is sufficiently engaged into the cylinder (up until it becomes hard to turn it). This can be achieved by creating a hexagon geometry on the top of the nut during machining so this is still one unit (this also can be applied to the bottom nut). Hexagon geometry would allow to employ the hand spanner and, therefore, to simplify the engagement process of the upper locking nut into the cell

body. This, however, must be done with care to avoid premature *P* increases. To minimise such a risk, it is required to first fully engage the bottom locking nut into the PCC and start monitoring the HP gauge for changes in its *R*. To further improve the nut engagement process, the cylindrical cell body might be equipped with slots nearby the cylinder ends so these could be clamped into the conventional vice. Moreover, the threads can be covered with a lubricant which may improve engagement at higher *Ps*.

The cylinder slots might be also found useful during low *Ps* to prevent PCC's rotation around the axis of *P* application (e.g. vertical) when trying to close the upper locking nut. Rotation is unwanted as to keep the bottom part and, therefore, Cu contacts static.

4.3 Lame's theory for thick cylinders

The state of the loaded PCC can be well described by the Lame's theory for thick wall cylinders [182] which allows to analytically determine the maximum *P* the PCC's materials can withstand before yielding. The cylinder is regarded as thick if the ratio of wall thickness to the *OD* is greater than 1/20 indicating that more complex compared to thin cylinders 3D stress state exists in the cylinder wall.

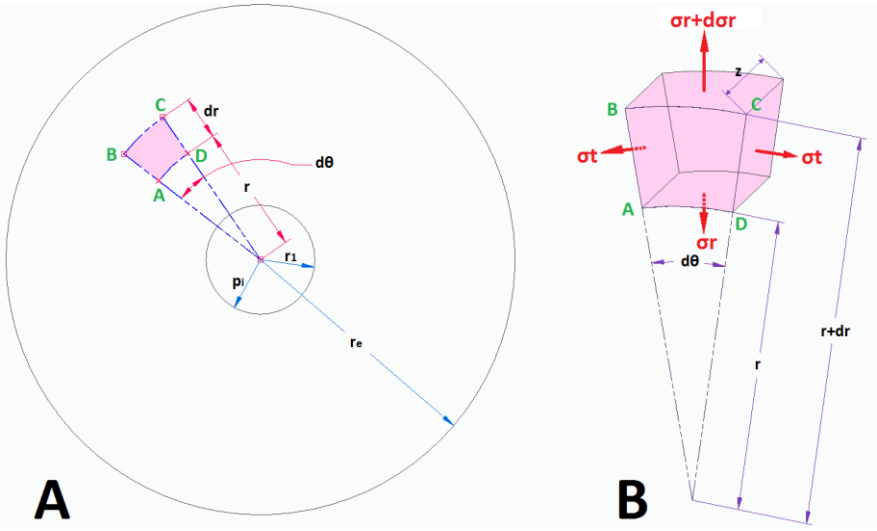

Figure 4.4: The thick-walled cylinder subjected to internal pressure. With: A – cross-section view and B – cut out element.

Assuming infinitely long cylinder with length (ℓ), homogeneity and isotropy of the material it is made of as well as that the stresses due to internal pressure (*Pi*) do not

exceed the yield stress of that material, it can be concluded that stresses generated in the cylinder will only depend on the radius (r) and will have nothing to do with an angle $d\theta$.

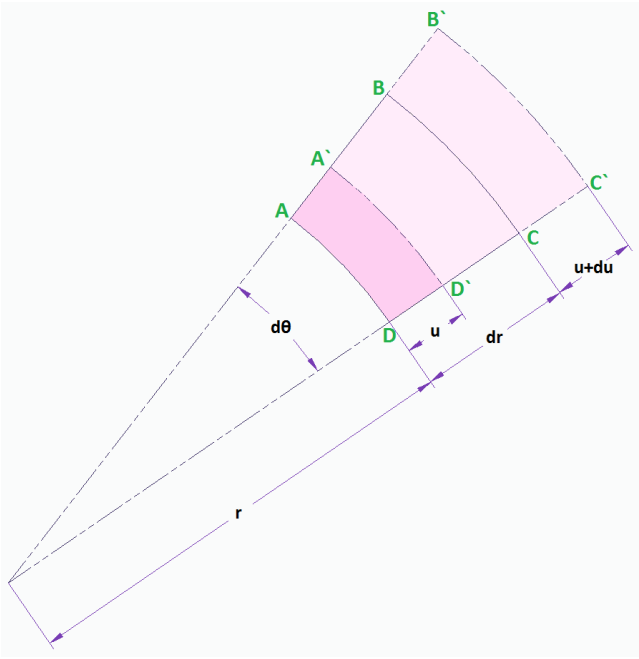

Figure 4.5: The cut-out element from figure 4.4. Translation of ABCD nodes due to *Pi* to A`B`C`D` nodes.

The shape of the A`B`C`D` element is maintained without distortion due to the uniformly distributed *Pi* (another important assumption and the reason why PTMs must be taken in accordance with PCC capabilities and be hydrostatic) and, as a result, there are no shears on radial or tangential planes. This results in three principal stresses which are mutually perpendicular: radial stress (σ_r), tangential stress (σ_t) and axial stress (σ_a). While the first two greatly vary in value along the cylinder walls (e.g. dependent upon the r), the last is assumed to be constant and independent on the wall thickness as long as there are no thermal stresses involved.

The only possible deformation is therefore radial, and thus, the displacement (u) relates only to the radius (r). When the edge of the element AD moves to A`D`, the tangential strain (ε_t) can be calculated as follows:

$$\varepsilon_t = \frac{\overline{A`D`} - \overline{AD}}{\overline{AD}} = \frac{(r + u - r)d\theta}{rd\theta} = \frac{u}{r} \tag{4.2}$$

And as expected, the $d\theta$ angle cancels itself. Another important relation which can be derived from figure 4.5 is the radial strain (ε_r), which can be calculated as follows:

$$\varepsilon_r = \frac{\overline{A`B`} - \overline{AB}}{\overline{AB}} = \frac{(u + du + dr - u) - dr}{dr} = \frac{du}{dr} \qquad (4.3)$$

These relations help to understand what happens with stresses (See figure 4.4 – B). The deformational direction is indicating the direction for stresses which will be equal but with an opposite direction for σ_t which acts from AB and CD surfaces. The σ_r, as it was previously said, varies depending on the wall depth and there is an increment $d\sigma_r$ on the surface BC [183].

For the radial equilibrium of the element (See figure 4.4 – B & 4.5):

$$(\sigma_r + d\sigma_r)(r + dr)d\theta - \sigma_r d\theta r - 2\sigma_t dr \cdot sin\frac{d\theta}{2} = 0 \qquad (4.4)$$

For small angles (in radians):

$$sin\frac{d\theta}{2} \approx \frac{d\theta}{2}$$

And, if 2nd order small quantities are neglected:

$$rd\sigma_r + \sigma_r dr = \sigma_t dr \;\; \therefore \;\; \sigma_r + r\frac{d\sigma_r}{dr} = \sigma_t$$

Which can be written as follows [184]:

$$\sigma_t - \sigma_r = r\frac{d\sigma_r}{dr} \qquad (4.5)$$

Three principal strains ε_t, ε_r and ε_a are also related to principal stresses σ_t, σ_r and σ_a in the linear elasticity condition where they follow the Hook's law [183, 184]:

$$\varepsilon_t = \frac{1}{E}[\sigma_t - v(\sigma_r + \sigma_a)]$$

$$\varepsilon_r = \frac{1}{E}[\sigma_r - v(\sigma_t + \sigma_a)] \qquad (4.6)$$

$$\varepsilon_a = \frac{1}{E}[\sigma_a - v(\sigma_r + \sigma_t)]$$

Where *v* is the Poisson's ratio and *E* is the modulus of elasticity of a given material.

Since ε_a and σ_a are constant (at points remote from the cylinder ends) as well as *v* and *E*, the third relation from equation 4.6 can be simplified to:

$$\sigma_r + \sigma_t = constant = 2A \;\; \therefore \;\; \sigma_t = 2A - \sigma_r \tag{4.7}$$

Where 2A is an arbitrary chosen constant.

By substituting equation 4.7 to equation 4.5, the σ_t becomes eliminated:

$$2A - \sigma_r - \sigma_r = r\frac{d\sigma_r}{dr} = 2A - 2\sigma_r$$

Multiplication through by *r* and rearrangement gives:

$$2r\sigma_r + r^2\frac{d\sigma_r}{dr} - 2Ar = 0 \tag{4.8}$$

Integration of 1st and 3rd term of equation 4.8 with respect to *r* gives:

$$\frac{\sigma_r dr^2}{dr} + \frac{r^2 d\sigma_r}{dr} - \frac{dAr^2}{dr} = 0$$

Where $\frac{d\sigma_r}{dr}$ is a constant and, therefore, a zero if differentiated, which gives:

$$\frac{d}{dr}(r^2\sigma_r - Ar^2) = 0$$

If $r^2\sigma_r - Ar^2$ is further integrated as a constant (say –B), it can be obtained that:

$$r^2\sigma_r - Ar^2 = constant = -B$$

Finally, by dividing by r^2 it can be obtained that:

$$\sigma_r = A - \frac{B}{r^2} \tag{4.9}$$

And, from equation 4.7:

$$\sigma_t = A + \frac{B}{r^2} \tag{4.10}$$

These two equations (e.g. equation 4.9 & 4.10) are known as Lame's equations and they give radial and tangential stresses at any *r* in terms of two constants A & B which are usually referred as Lame's constants.

It is important to note that if the vessel is subjected to *Pi* only – the *P* is considered as negative radial stress since it leads to thinning of the cylinder wall and the Lame's constants can be found using the following boundary conditions:

$$at\ r = r_1, \qquad \sigma_r = -Pi$$

$$at\ r = r_e, \qquad \sigma_r = 0$$

Where *r* is the radius, r_1 is the internal radius and r_e is the external radius.

And, therefore, Lame's constants can be found using:

$$A = \frac{Pir_1^2}{r_e^2 - r_1^2}\ \&\ B = \frac{Pir_1^2 r_e^2}{r_e^2 - r_1^2} \tag{4.11}$$

If A and B from the equation 4.11 are then plugged into the equations 4.9 and 4.10, the principal stresses can be expressed through the radiuses and the *Pi* only [183] (See figure 4.4 – A for the reference):

$$\sigma_r = \frac{Pir_1^2}{r_e^2 - r_1^2}\left(1 - \frac{r_e^2}{r^2}\right)$$

$$\sigma t = \frac{Pir_1^2}{r_e^2 - r_1^2}\left(1 + \frac{r_e^2}{r^2}\right) \tag{4.12}$$

Therefore, if trying to calculate the principal stresses, at the internal radius: $r = r_1$ and at the external radius $r = r_e$. If in the equation 4.12 all inputs are kept constant except the value of *r* which alters within $r_e \geq r \geq r_1$ relationship, the principal stresses are yielding the following stress distribution in the thick cylinder which is subjected to *Pi* only:

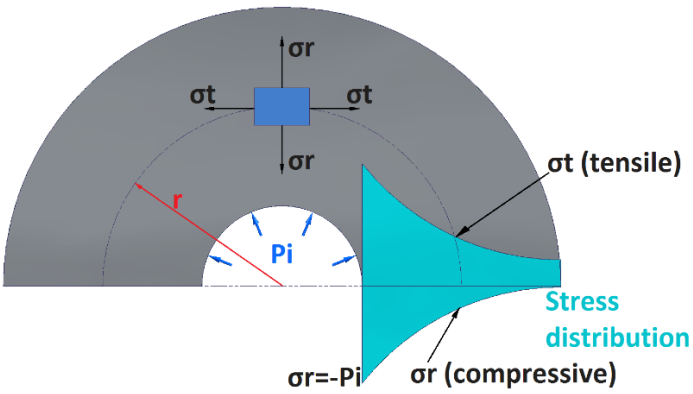

Figure 4.6: Radial and tangential stress distribution in the thick vessel subjected to *Pi* [53, 183, 184]. The vessel is shown with a cross-sectional view and grey colour while the element of interest and the stress distribution are shown with blue and cyan colours respectively.

As it can be noted in figure 4.6 the maximum stress is the radial stress which is highly concentrated at the bore (e.g. only a thin layer around the r_1 experiences the highest stress while the rest of the wall is, roughly speaking, unloaded). This stress distribution explains why the thick cylinders are limited in terms of maximum attainable *P* with material properties rather than their amount and further increases in wall thickness of the cylinder is a waste of the material as they won't expand the HP scope.

The σ_a, if there are no thermal stresses involved, is calculated based on the longitudinal equilibrium conditions resulting in two cases: cylinder with open ends (ends of the internal bore are not subjected to *Pi*) and cylinder with closed ends. For the cylinder subjected to the *Pi* only, the first case gives:

$$\sigma_a = 0$$

While the second case leads to [183]:

$$\sigma_a = \frac{Pir_1^2}{r_e^2 - r_1^2} = A \tag{4.13}$$

4.4 Distortion energy theory – von Mises stress

All three principal stresses (e.g. σ_t, σ_r & σ_a) must be considered in the design process of the PCC to avoid material's failure due to *Pi*. The von Mises stress deals with three-dimensional stress cases and belongs to distortion-energy theory (the most

preferred failure theory in the industry). The distortion energy theory states: "*A machine member under the multiaxial state of stress fails when the distortion energy per unit volume becomes equal to or exceeds the distortion energy per unit volume at the time of failure in a simple uniaxial stress test using a specimen of the same material*". In other words, the theory states that the material specimen would yield and, therefore, fail when its equivalent stress (σ_e) exceeds the materials yield strength (σ_y) [183].

$$\sigma_e = \sqrt{\frac{1}{2}[(\sigma_1 - \sigma_2)^2 + (\sigma_2 - \sigma_3)^2 + (\sigma_3 - \sigma_1)^2} \tag{4.14}$$

Where $\sigma_1 = \sigma_t$, $\sigma_2 = \sigma_a$ & $\sigma_3 = \sigma_r$.

$$Pi(\max) = \frac{r_e^2 - r_1^2}{r_e^2}\frac{\sigma_y}{\sqrt{3}} \tag{4.15}$$

Also, it is worth to note that the hydrostatically stressed materials can go beyond their ultimate tensile strength without failing because the hydrostatic stress reduces the volume of the specimen without changes in its shape [185]. This, however, is more relevant to the testing materials rather then the HP devices which are required to contain them.

4.5 Thick cylinders beyond yielding

Introduction of design advances such as autofrettage and/or component cylinders can be employed to increase the maximum value of the σ_e and to postpone the failure of the materials employed in the PCC's design and, therefore, to increase the maximum attainable *P* without yielding failure.

4.5.1 Autofrettage

The autofrettage method is a widely employed technique to go beyond initial yielding. If a certain load is exerted on the metal, which exceeds the yield strength of it, then the stresses will arise and after the *P* is removed, the material will be deformed. In the case of the repeated "loading", the plastic deformation ability of this

material will decrease, and its yield strength will increase to the value of the stresses that arose earlier. Therefore, the material will become stronger and it will be necessary to apply higher loads to further produce permanent changes in materials shape.

In the thick cylinder, the *Pi* of such a value is applied that internal bore experiences plastic deformations while the outer portion of the cylinder remains in the elastic region. When *Pi* is released, the outer portion tries to go back to the original location but the permanently deformed internal portion does not allow this to happen, resulting in the following principal stress distribution:

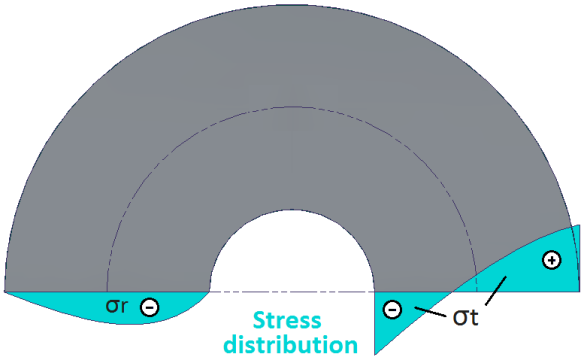

Figure 4.7: Radial and tangential stress distribution due to autofrettage [53]. Vessel and stress distributions are grey and cyan colour respectively. Compressive and tensile stresses are marked with the corresponding symbol in the white circle.

There are several methods available to produce autofrettage [183] and those won't be covered in this thesis as well as the analytical component of the technique [53, 183] due to the limited space.

4.5.2 Compound cylinder

Another technique which allows going beyond initial yielding incorporates double or multi-cylinder layers. In the double layer concept, the *OD* of the inner cylinder is a little bit bigger than the *ID* of the outer cylinder. This diametrical difference is called an interference fit (δ) (See figure 4.8). Cylinders can be brought to the same common radius (r_2) using whether force-fit technique (requires a press and, preferably, a tapered pattern to simplify the process), whether the shrinking technique in which the outer cylinder is heated (widens in *ID*) and the inner cylinder is cooled (shortens in *OD*). These two techniques can be combined to facilitate the task. In case of

successful fitting/shrinking the cylinders would gain the r_2 which will be subjected to the induced common pressure (*Pc*). This *Pc* would create the similar to the autofrettage principal stress distribution (See figure 4.7). If the cylinder is then subjected to *Pi* the compressive σ_t would cancel some of the tensile σ_t at the internal bore where it is at maximum (See figure 4.6), thus, expanding the maximum *Pi* scope.

Just like in the autofrettage method and for the same reason the analytical component of the component cylinders will be omitted in this thesis and the detailed calculations can be found in the literature [53, 183].

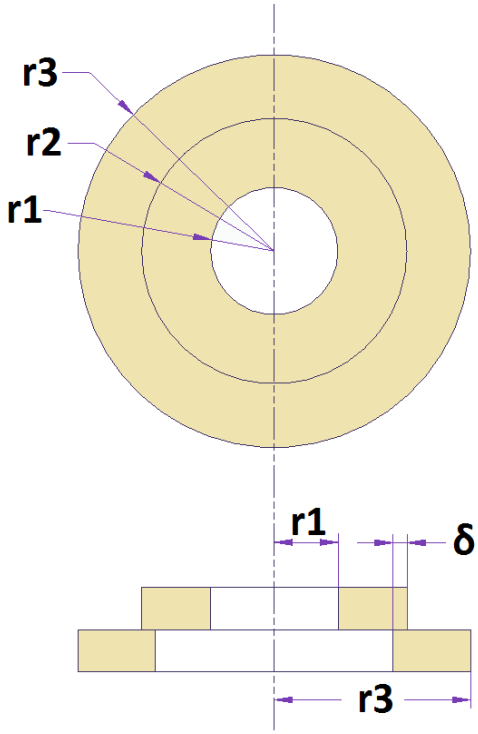

Figure 4.8: Compound cylinder. The cross-section view at the top with r_1, r_3 & r_2 representing the internal radius of the inner cylinder, the *OD* of the outer cylinder and common radius of two cylinders respectively and, interference fit (δ) concept at the bottom prior to force-fitting or shrinking procedure.

The multilayer compound technique works on the same principle however is more rarely employed as brings the limiting *P* to almost the same result as in the double-layer technique [53]. It is worth to mention that the component cylinder and autofrettage methods can be combined, however, special care must be taken with autofrettage as it comes with a high risk of fracture during the autofrettage process which compared to the double layer technique goes beyond elastic region.

4.6 Finite element method

Prior to making the PCC, it is required to virtually test the design to evaluate stresses and deformations under the work to determine if the design is meeting the requirements in terms of maximum achievable *P*. The virtual test implies the use of the engineering computer software for simulation and optimisation such as ANSYS [186] or others which can implement the finite element analysis (FEA). The FEA is a numerical technique which is based on the finite element method (FEM) and is used for solving complex problems of engineering and mathematical physics. The FEM is not limited to structural analysis and can be used to simulate and analyse heat transfer, fluid flow, mass transfer and electrodynamics problems. These problems can be represented by mathematical models which are governed by differential equations. These equations can become too complex to be solved directly so the FEM is employed to offer an approximate solution using integral formulations. The method approximates an unknown function by region. To solve the given problem, it divides the large system into smaller, simpler parts called finite elements. The simple equations which are modelling these finite elements are then assembled into a larger system of equations which are used to model the entire problem [54, 187].

The FEA if undertaken in ANSYS Workbench can be roughly broken into the three main stages:

1) The pre-processing:

The pre-processing includes the selection of the analysis system, design of the geometry/model, assignment of material to it with the relevant mechanical properties, creation of connections in between parts (if applicable), meshing (e.g. dividing the system into smaller elements), application of boundary conditions such as force, *P*, etc.

2) Solving:

The solving stage implies the process during which the equations are solved based on the pre-processing inputs. If unsuccessful, there must be something wrong with the pre-processing inputs.

3) The post-processing:

The main goal of the post-processing is to achieve the physical quantities of interest such as stresses, strains and deformations.

Once the post-processing is complete it is worth to validate results (if possible, from the analytical point of view) to determine if the observable physical quantities are reasonable. Therefore, the post-processing stage may not be final. If something looks wrong, it is a must to go back to the pre-processing stage to alter some of the inputs. ANSYS Workbench provides a wide variety of editable fields and controls during the pre-processing stage to be changed if needed such as analysis setting, selection of element type & size [188] (which can be refined better at a specific location of the geometry), quantity and directionality of the analysis-related system inputs etc. These details will be omitted as they are beyond the theme of this thesis.

The validated model can be further studied within the ANSYS software with the application of many other analysis systems such as DesignXplorer [189] which allows producing sensitivity and optimisation studies by marking some of the geometrical or structural inputs such as dimensions and/or *Ps* as parameters/variables.

Since 1982 it is a common practice to use FEA in the construction of the HP instrumentation [190] to study how stresses affect cullet of the diamond or the diamond seats in DACs [191, 192], optimise the geometry of the double-toroidal anvils [193], estimate the maximum attainable *P* in the compound PCC [194] etc.

All simulations which are reported in this thesis have been performed with the static structural analysis system with 2D type because the axial symmetry of the geometry allows saving time during the computation. The simulated geometries were drawn using DesignModeler [195] and simulated with accordance to the three-stage process.

4.7 Single-cylinder simulation with analytical validation

This section exists to illustrate that the FEA within the ANSYS software can be applied to thick cylinders which are subjected to *Pi* as well as analytically validated

using principal stresses and the von Mises stress criteria (See equation 4.14). Please consider the single cylinder which is made of BeCu (See table 4.1 for properties) and has an r_1 = 2.25 mm and is required to withstand 700 MPa of ***Pi***.

First, it is required to determine the minimum r_e of the cylinder so it would stay within the elastic region once the 700 MPa of ***Pi*** will be applied to the bore. This can be done using equation 4.15:

$$Pi(\max) = \frac{r_e^2 - 2.25^2}{r_e^2}\frac{1400}{\sqrt{3}}$$

Solving for r_e gives:

$$r_e^2 - 5.0625 = 0.8660254038$$

$$r_e = \sqrt{\frac{5.0625}{0.1339745962}} = 6.1471 \approx 6.15\ mm$$

Therefore, using equations 4.12 and 4.13 it can be obtained that:

At the $r = r_1$ (e.g. at the bore):

$$\sigma_r = \frac{700 \times 2.25^2}{6.15^2 - 2.25^2}\left(1 - \frac{6.15^2}{2.25^2}\right) = -700\ MPa$$

$$\sigma_t = \frac{700 \times 2.25^2}{6.15^2 - 2.25^2}\left(1 + \frac{6.15^2}{2.25^2}\right) = 916.346\ MPa$$

$$\sigma_a = \frac{700 \times 2.25^2}{6.15^2 - 2.25^2} = 108.173\ MPa\ (closed\ ends)$$

$$\sigma_a = 0\ MPa\ (open\ ends)$$

And, at $r = r_e$ (e.g. at the outside portion):

$$\sigma_r = \frac{700 \times 2.25^2}{6.15^2 - 2.25^2}\left(1 - \frac{6.15^2}{6.15^2}\right) = 0\ MPa$$

$$\sigma_t = \frac{700 \times 2.25^2}{6.15^2 - 2.25^2}\left(1 + \frac{6.15^2}{2.25^2}\right) = 216.346\ MPa$$

$$\sigma_a = \frac{700 \times 2.25^2}{6.15^2 - 2.25^2} = 108.173\ MPa\ (closed\ ends)$$

$$\sigma_a = 0\ MPa\ (open\ ends)$$

Now, the von Mises maximum and minimum stress values can be calculated using equation 4.14:

$$\sigma_e(max)$$

$$= \sqrt{\frac{1}{2}[(916.346 - 108.173)^2 + (108.173 - -700)^2 + (-700 - 916.346)^2}$$

$$= 1399.7967\ MPa\ (closed\ ends)$$

$$\sigma_e(max) = \sqrt{\frac{1}{2}[(916.346 - 0)^2 + (0 - -700)^2 + (-700 - 916.346)^2}$$

$$= 1403.97\ MPa\ (open\ ends)$$

$$\sigma_e(min) = \sqrt{\frac{1}{2}[(216.346 - 108.173)^2 + (108.173 - -0)^2 + (-0 - 216.346)^2}$$

$$= 187.361\ MPa\ (closed\ ends)$$

$$\sigma_e(min) = \sqrt{\frac{1}{2}[(216.346 - 0)^2 + (0 - -0)^2 + (-0 - 216.346)^2}$$

$$= 216.346\ MPa\ (open\ ends)$$

To simplify the modelling, the PCC geometry was set to the axisymmetric 2D behaviour and, therefore, only the wall thickness of the cylinder was drawn (See figure 4.9). Although the cylinder was drawn with the open ends, it needs to be treated as the cylinder with closed ends since the ***P*** was applied to the whole internal bore. With the r_e being found as a 6.15 mm, the length of the cylinder was assumed to be 20 mm (immaterial value), leading to the geometry which is illustrated in figure 4.9. Please note that the H1 value is the r_1 value and it translates the geometry from the Y-axis in A to allow the axisymmetric 2D behaviour to be selected in the project settings and mimic the cylinder analysis. The axisymmetric 2D behaviour allows reducing computation time for simple geometries such as cylinders. The shown in figure 4.9 geometry in A and structural conditions in B are key pre-processing inputs

and by assigning BeCu material with relevant properties (See table 4.1) the geometry meshing can be performed to allow moving onto next stages which are solving and post-processing.

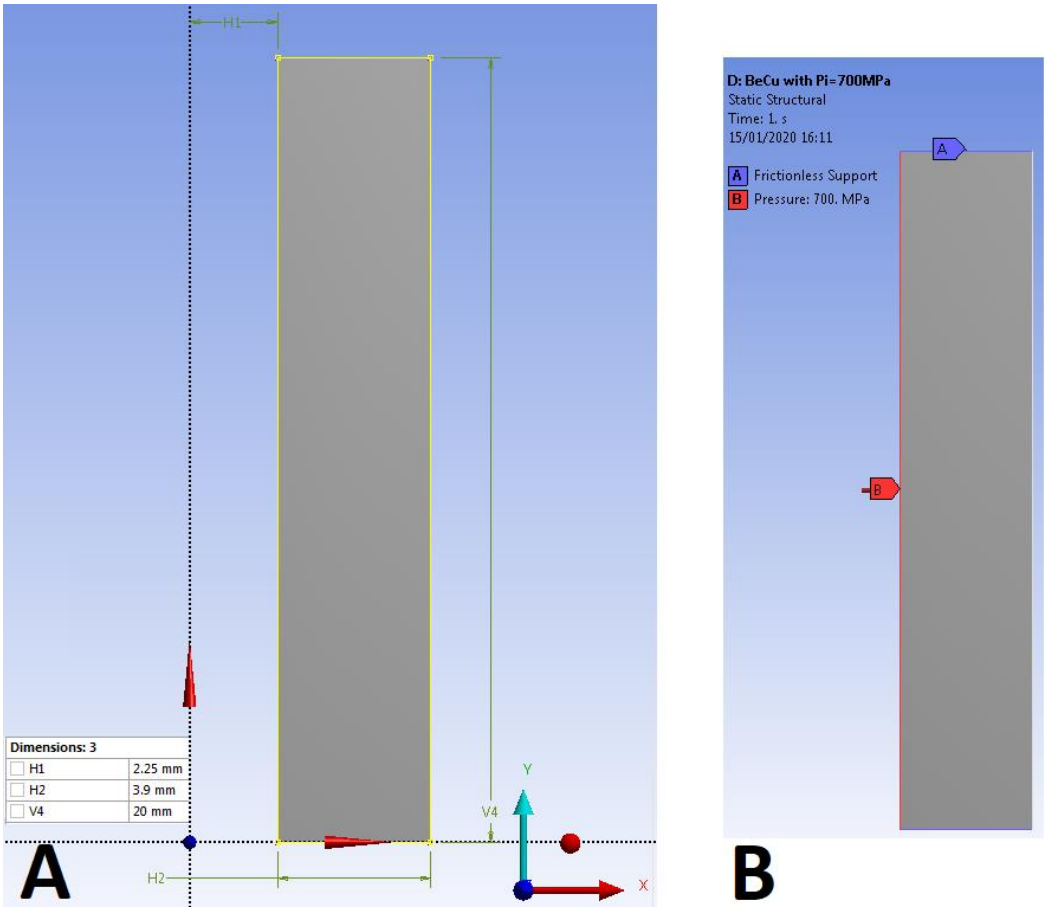

Figure 4.9: 2D geometry of BeCu cylinder. With: A – relevant dimensions and B – structural conditions. The frictionless supports were introduced as constraints to prevent rigid body motion of the model.

Knowing the theoretical stress distribution (See figure 4.6) it was decided to mesh the cylinder with a high concentration of elements near the bore. This is a common practice which allows obtaining finer results at the areas of interest while saving computational time by producing coarser mesh on the rest of the model.

By solving the model it was found that the highest von Mises stress occurred along the internal bore (See figure 4.10) – as expected, and its value is close to the σ_y of the BeCu material (See table 4.1) for the given geometry in figure 4.9 and in accordance with equation 4.15. The magnitudes of the principal stresses and how they change along the cylinder's depth are shown in figure 4.11.

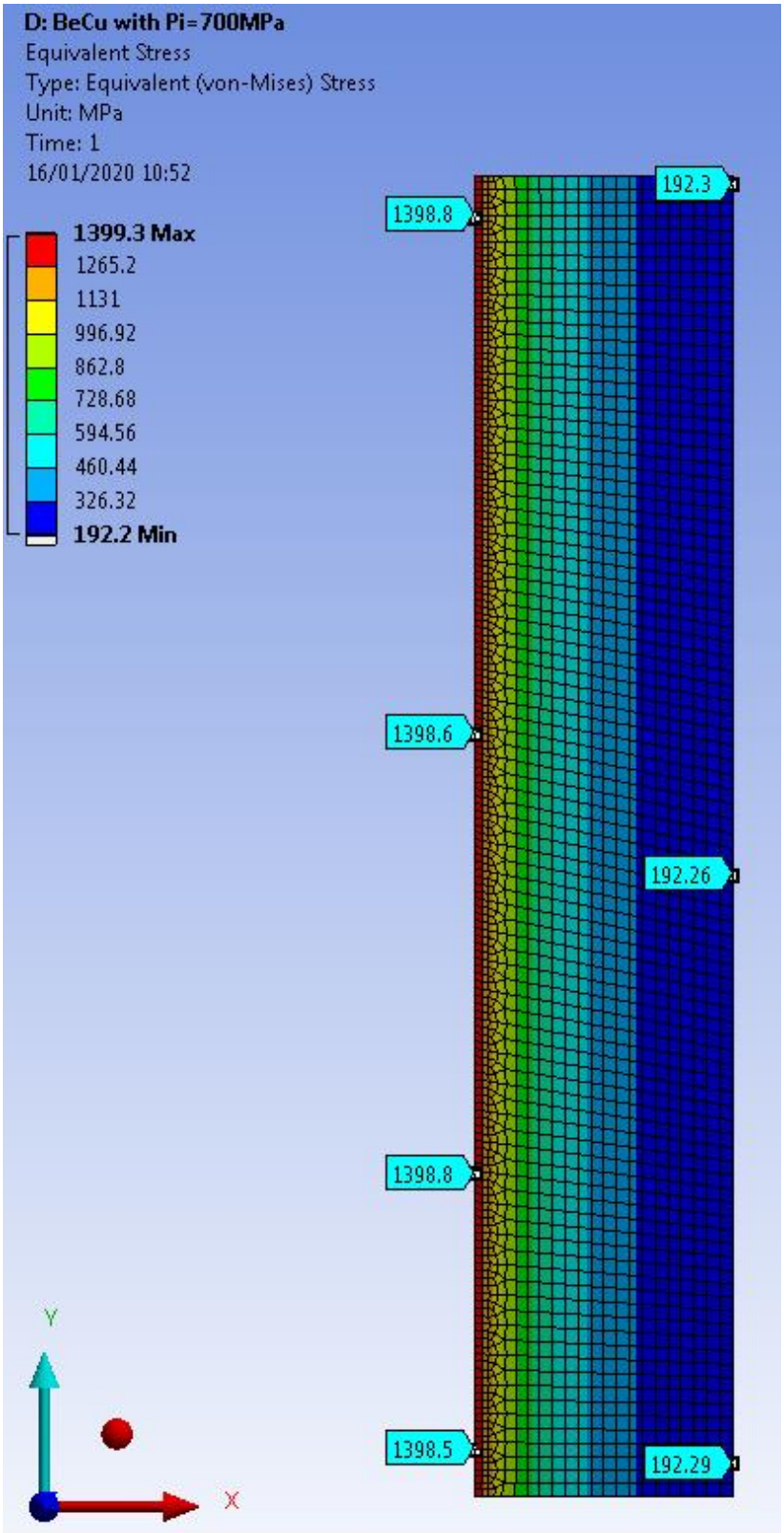

Figure 4.10: Von Mises stress in the BeCu cylinder under *Pi*. The coloured scale represents the maximum (red) and minimum (blue) stress values in the cylinder with units as specified. The probes of stresses (labels with cyan colour) were taken to demonstrate the similarity of numerical values along the vertical axis.

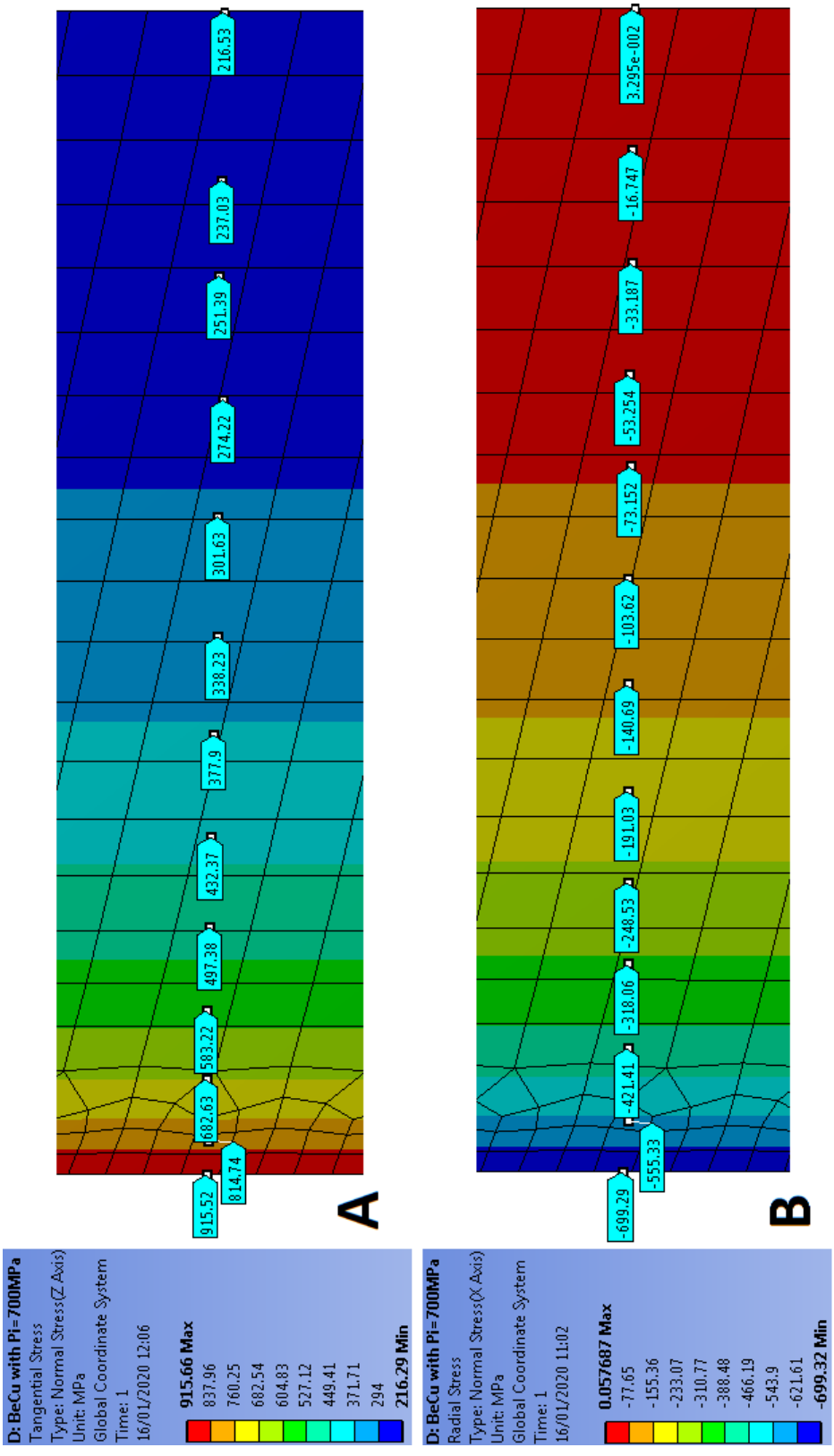

Figure 4.11: Principal stresses in the BeCu cylinder under *Pi*. With: A – tangential stress distribution through the wall and B – radial stress distribution through the wall. The similar tendency for both stresses was observed along the vertical axis and, therefore, only the zoomed-in sections are provided to show, with the help of stress probes, the stress variations.

The observed principal stress behaviour is well illustrated in figure 4.6 with σ_t being the highest nearby the bore and lowest at the outer portion of the cylinder. Also, the σ_r, as per theory, equates to the negative *Pi* as this stress is compressive and leads to the thinning of the cylinder wall and approaches 0 at the outer portion of the cylinder.

Table 4.3: Comparison of analytical and simulated values.

	Analytical (MPa)	*Simulation (MPa)*
σ_r *(at* $r=r_1$*)*	-700	-699.32
σ_r *(at* $r=r_e$*)*	0	0.057687
σ_t *(at* $r=r_1$*)*	916.346	915.66
σ_t *(at* $r=r_e$*)*	216.346	216.29
σ_e *(at* $r=r_1$*)*	1399.7967	1399.3
σ_e *(at* $r=r_e$*)*	187.361	192.2

By comparing the analytical and simulation values (See table 4.3) it can be noted that the numerical difference is small which means that simulations are in good agreement with theory indicating the competence of the selected FEA software and that the model can be further used for more advanced designs. The biggest numerical difference belongs to the σ_e (at $r = r_e$) and can be neglected because the main interest is associated with stress concentration at the bore (e.g. at the $r = r_1$) since this area is subjected to higher stresses which are nearby the σ_y value of the employed material while the outer portions of the PCC are barely stressed (e.g. won't yield for sure).

Having obtained evidence that ANSYS is a suitable FEA software for analysing, modelling and studying the behaviour of thick cylinders which are subjected to *Pi*, it will be further used in this thesis to highlight the relevant stress values in the PCC without repeated analytical evidence of the software's correctness.

4.8 Compound cylinder design and analysis

The design presented in figure 4.12 was drawn in accordance with the required *P* limit (e.g. 3 GPa), minimum bore size (e.g. 4.5 mm due to CPP, table, Cu wires and

PTFE capsule) and other considerations which were mentioned earlier in this chapter, by considering concepts in figure 4.3 & 3.9.

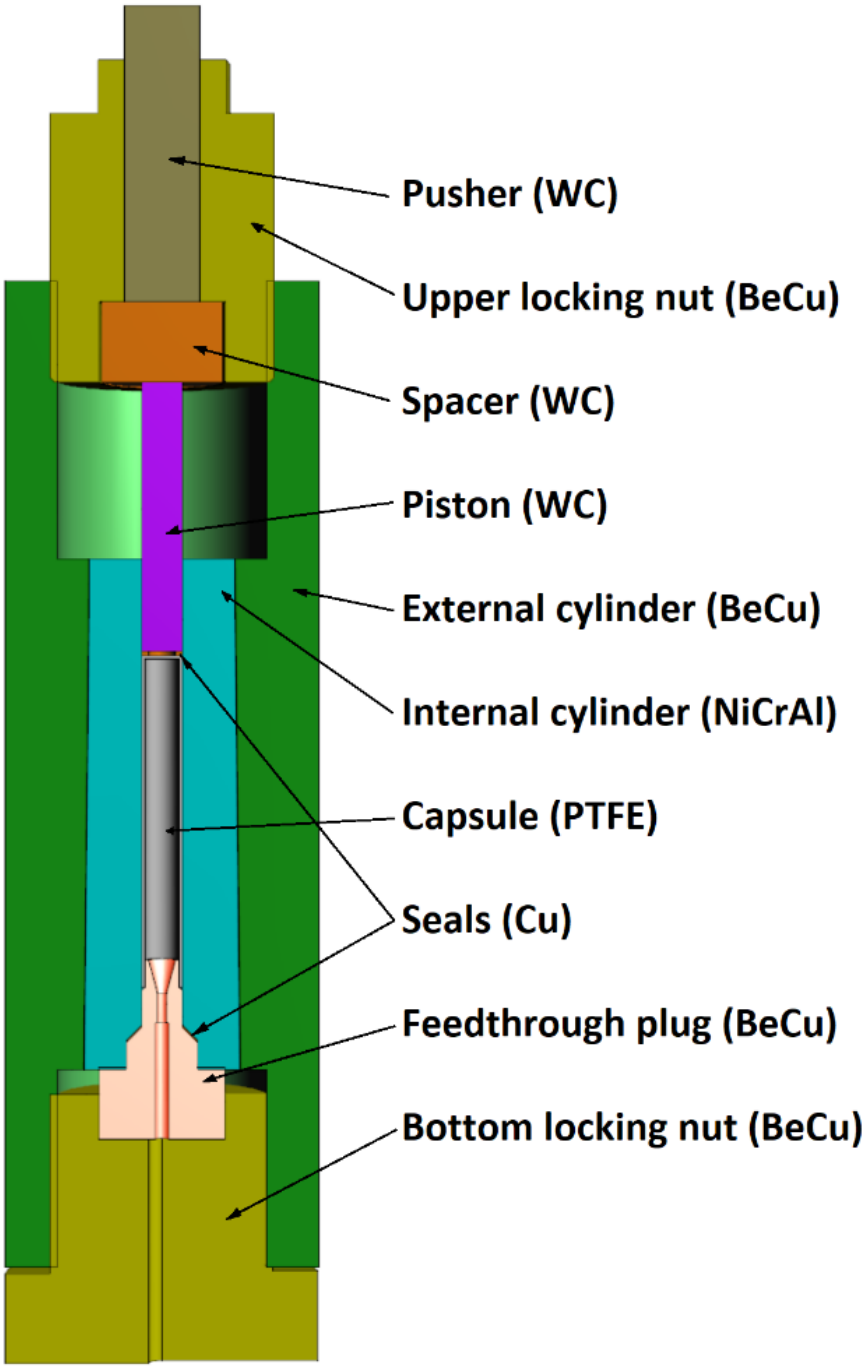

Figure 4.12: Section view of the PCC. This design is made with accordance to design considerations. Please note that the seal which is nearby the feedthrough plug was drawn deformed to keep the integrity of the image. The component materials are shown in brackets.

As previously, the 2D model was created to simulate the behaviour of the compound cylinder in response to the applied *P* with dimensions as in figure 4.13.

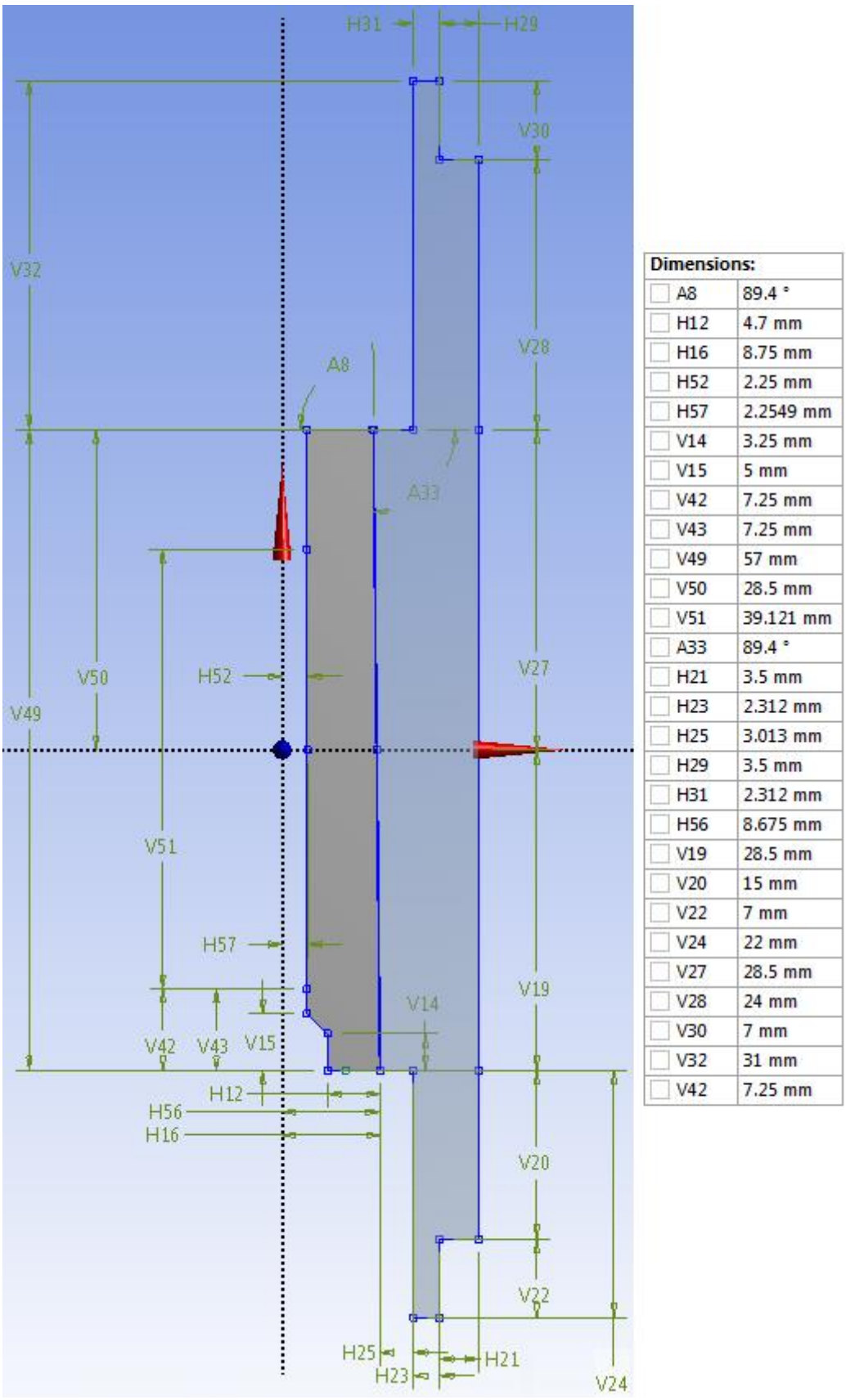

Figure 4.13: 2D geometry of compound cylinder. All dimensions are present.

Please note the dimensions A8 & A33 in figure 4.13 which are indicating the angular dimensions. The 89.4° angle is required to allow force-fitting of the inner cylinder into the outer which, according to the model can be done from the bottom side of the external cylinder by introducing the upper portion of the inner cylinder into it. The value of the angle was empirically derived and translated into the simulation resulting in the following key dimensions to be highlighted: H52 = 2.25 mm (r_1 of an inner cylinder), H21+H23+H25+H56 = 17.5 mm (r_e of an outer cylinder), H16 = 8.75 mm (r_e of inner cylinder at the bottom) which due to 0.6° tilt over the V49-V15 length result in r_e of the inner cylinder at the top to be 8.1531 mm and H56 = 8.675 mm (r_1 of the external cylinder at the bottom) which due to 0.6° tilt over the V49 length result in r_1 of the external cylinder at the top to be 8.0781 mm. Which means that the top of the inner cylinder can easily fit into the bottom of the external cylinder (e.g. 8.1531 mm vs 8.675 mm). Once cylinders are fully engaged the resulting diametrical interference (See figure 4.8) would equate to 0.15 mm and this value was empirically found during numerous attempts to achieve the full engagement of cylinders. Another important dimension to note is V51 which equates to 39.121 mm. It was made in between special nodes which were placed to mimic the endpoints of the feedthrough plug and piston (See figure 4.12). The V51 was further used to allow to select a specific region in the bore, to apply *P* to it as it can be noted in figure 4.14.

Figure 4.14: Structural conditions of the compound cylinder.

The displacement of 0 mm in the Y direction was added for the same purpose as the frictionless supports in figure 4.9 – B – to constrain the model. The C component of the static structural (e.g. the force of 47713 N magnitude) corresponds to the 3 GPa of *P* exerted on the cross-sectional A of the piston (e.g. 15.904 mm^2) which was calculated using the equation 3.4. This force was applied to mimic the device operation where the piston translates the force to the upper locking nut in the Y direction to investigate if such a magnitude can lead to any consequences.

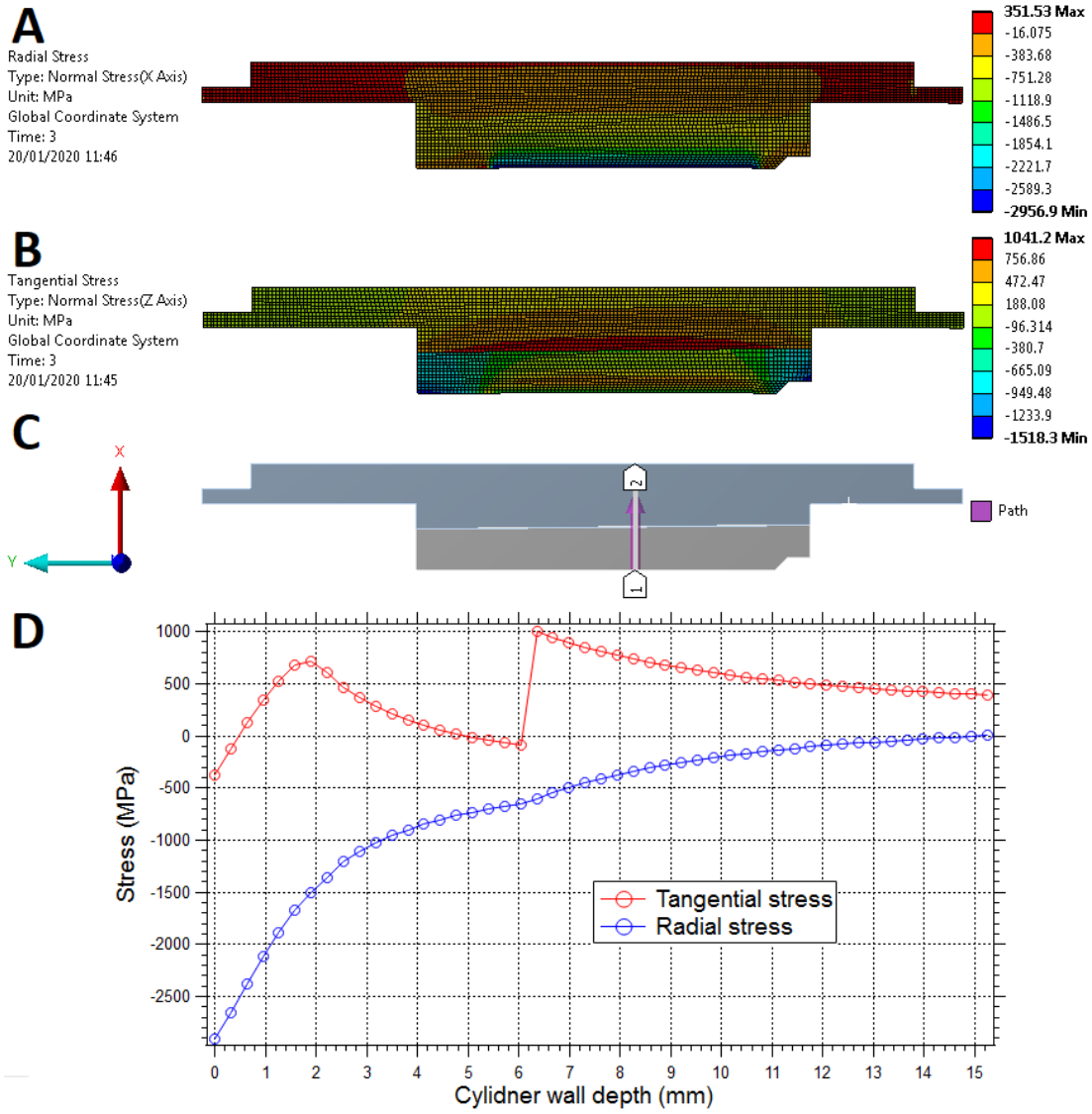

Figure 4.15: Principal stresses in the compound cylinder under *Pi*. With: A – radial stress, B – tangential stress, C – selected path for study and D – principal stresses vs cylinder wall depth along the path in C. Numerical data available in the figure A.3.

Please note that the x-axis limit for chart D in figure 4.15 is 15.25 mm which is the sum of internal and external cylinder walls. To better understand which portion of the compound cylinder is referenced with the cylinder wall depth number (e.g. x-axis), the value of the 2.25 mm (e.g. the r_1 of the inner cylinder) should be added to the provided in the x-axis values and compared with the original dimensions (See figure 4.13).

The σ_r in the compound cylinder slightly resembles the σ_r in the BeCu single cylinder (See figure 4.11) with an almost imperceptible pit at the 6 mm wall depth which can be noted by carefully observing the chart in D. As before, the highest σ_r concentrates

at the bore of the internal cylinder and is numerically close to the *Pi* but with a negative sign to mark this stress as a compressive and, the lowest values of σ_r can be found at the r_e of the outer cylinder as in D where it is approaching the 0.

The σ_t in the compound cylinder shows how the interference fit affects the highest principal stress distribution through the wall. According to the chart in D and the stress distribution in B, the highest σ_t occurs at the bore of the external cylinder while the lowest σ_t can be observed nearby the r_e of the internal cylinder emphasising that internal cylinder has better mechanical properties (See table 4.1 & 4.2). The jump from the negative value to the positive after 6 mm of wall depth indicates the material change and, therefore, by adding more points to the chart in D, the real common radius (r_2) of both cylinders can be found for the path C.

Since the simulated geometry is not as symmetric and of an infinite length as the BeCu cylinder (See figure 4.9), the outer cylinder ends which are responsible for holding upper and bottom locking nuts (See figure 4.12) are having different distribution and values of stresses which can be seen in A & B – indicating the bending profile in which the distant parts of the cylinder are striving for the sphere of influence – *P* which is distributed at a specific location rather than the whole internal bore.

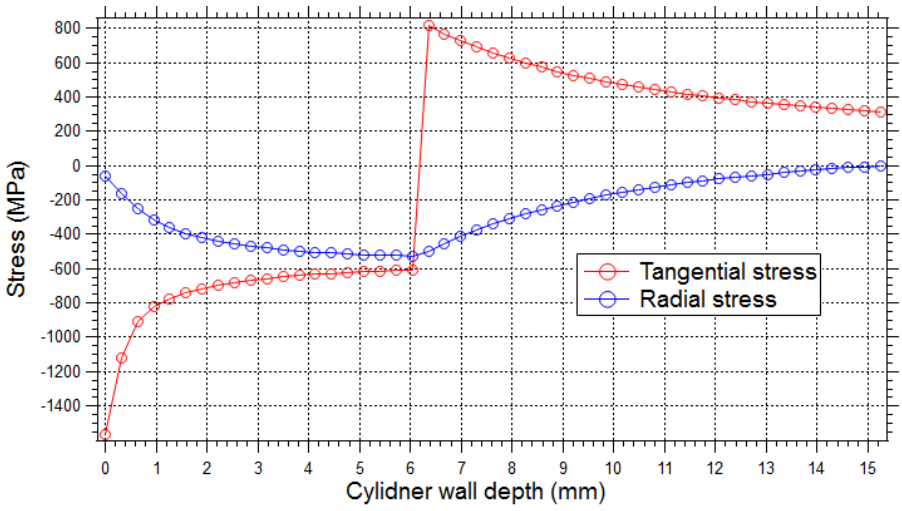

Figure 4.16: Principal stresses in the compound cylinder with no *P*. Points were collected along a similar path as in figure 4.15 – C. The numerical data is available in figure A.3.

It is worth to note that by producing simulation with suppressed force on the thread, the achieved results were identical to those presented. Also, by producing simulation

with *Pi* = 0 MPa, the stress distribution in the cylinders (See figure 4.16) was found to be in a close agreement with the stress distribution of an autofrettage cylinder (See figure 4.7) where σ_r is equal to 0 at the internal and external radius ends while is also compressive through the wall and σ_t starts with negative value at the bore of the internal cylinder, approaches zero at the end of the internal cylinder and becomes tensile when it hits external cylinder (highest value) which slowly falls towards the end of the cylinder's external radius.

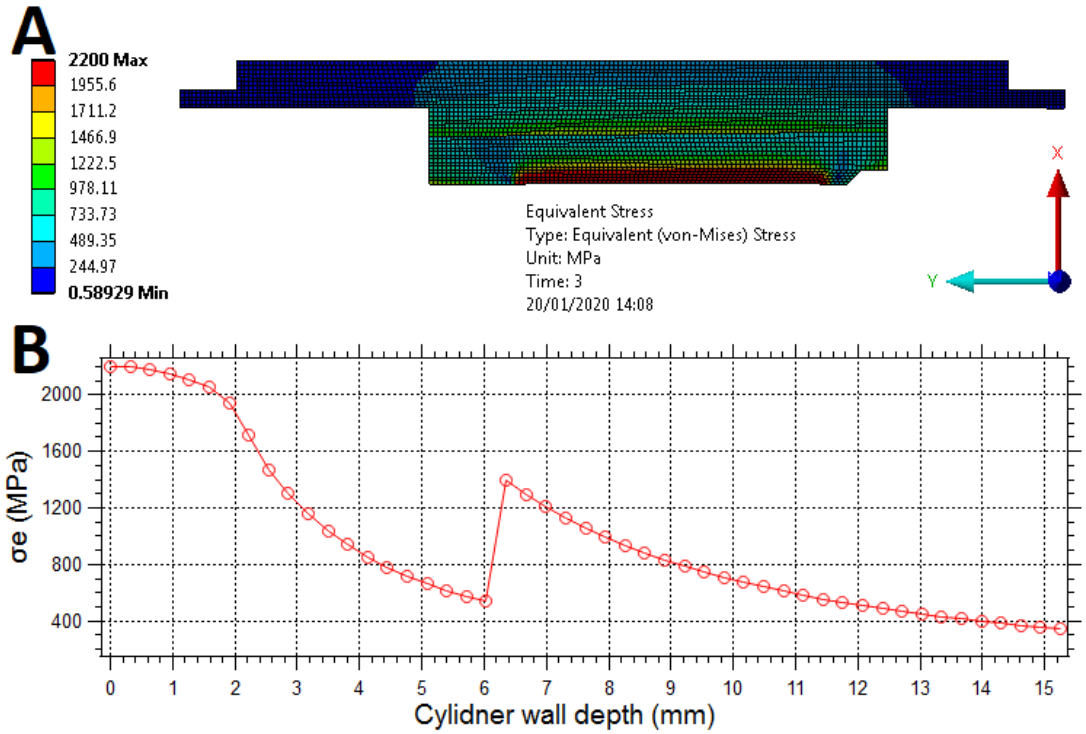

Figure 4.17: Von Mises stress in the compound cylinder under *Pi*. With: A – von Mises stress of the whole geometry & B – von Mises stress of the specific profile (See figure 4.15 – C). The numerical data is available in figure A.3.

As expected, the maximum value of the σ_e appears at the bore of the internal cylinder where it meets the *Pi* (See figure 4.17). Please note that the maximum value of σ_e which is shown as a 2200 MPa is beyond the yield point of the inner cylinder (e.g. NiCrAl) by 200 MPa while the outer cylinder (e.g. BeCu) stays within the elastic region with highest σ_e being found as a 1395 MPa at 6.3542 mm. This means that this PCC if build to dimensions (See figure 4.13) could reach the 3 GPa of *P*, however, this may lead to plastic deformations in the internal bore. At this stage, it was decided to stick to the dimensions and to build the PCC to test its capabilities. Although the produced simulation indicated the yielding of the inner bore of NiCrAl

cylinder it was decided to rely on autofrettage. It implied the development of additional 3rd cylinder which would act as a protective layer and absorb the flying elements of the PCC in case of the explosion.

4.9 Manufacturing process

All parts of the compound PCC (See figure 4.12) were made using a conventional machining process. To achieve the double-layer configuration both, shrink and force-fitting techniques were combined. In the former technique, the liquid nitrogen was employed, and the inner cylinder was submerged into the 77° K bath. The *T* difference between liquid nitrogen and NiCrAl cylinder was accompanied with bubble formation and, the end of such a formation marked the end of the treatment's duration, during which the cylinder shrank in size and only then was inserted into the outer cylinder which was of a *Troom*. As it was previously said, the latter technique resulted in the necessity of producing the tapered pattern with 89.4° angle (See figure 4.13). Force fitting was undertaken with the help of the conventional hydraulic press and, to achieve best results, was done right after the employment of the former's technique (e.g shrink). Another important aspect was the final length of the bore which was decided to be 57 mm (See figure 4.13). To achieve the exact value, both cylinders were on purpose made longer with the outer cylinder to be 60 mm and inner – 65 mm. This was required to allow some material removal once the double-layer configuration was achieved which resulted in the necessity to keep the tapered profiles along the above-mentioned lengths as well as to mark to which extend inner cylinder should be pushed to achieve the required interference fit of 0.15 mm. Once both cylinders became a single unit they started to be treated accordingly and in the further sections of this thesis are referred to as a cell body.

The Cu seals were annealed with a heat gun until the dark red colour to make them softer and, therefore, to make them yield at lower *P* while the PTFE capsule was decided to be made of two parts: the hollow rod and cap (because it is much easier to find and buy a hollow rod and make a cap for it rather than a closed profile piece of the required shape). The tight fit of PTFE and bore was achieved with slow polishing process of the PTFE with sandpaper. Cu seals which are nearby piston were made to have the 45° draft to improve their involvement into the PTFE cap during low *P*.

The manufacturing of small parts such as cone knob and sample table (See figure 4.18) was also performed using conventional machining tools but had to be hand-finished to achieve better surface quality due to the small scale. Parts were filed and sandpapered to get rid of the sharp edges at the grooves of the cone knob and to achieve the deep enough grooves in the sample table to fit Cu wires.

The cone knob and the feedthrough plug were connected with the help of the black epoxy mixture details of which were previously discussed in this chapter.

4.10 Assembly and disassembly

Before accessing the full cell assembly, it was required to finalize the assembly of the small parts:

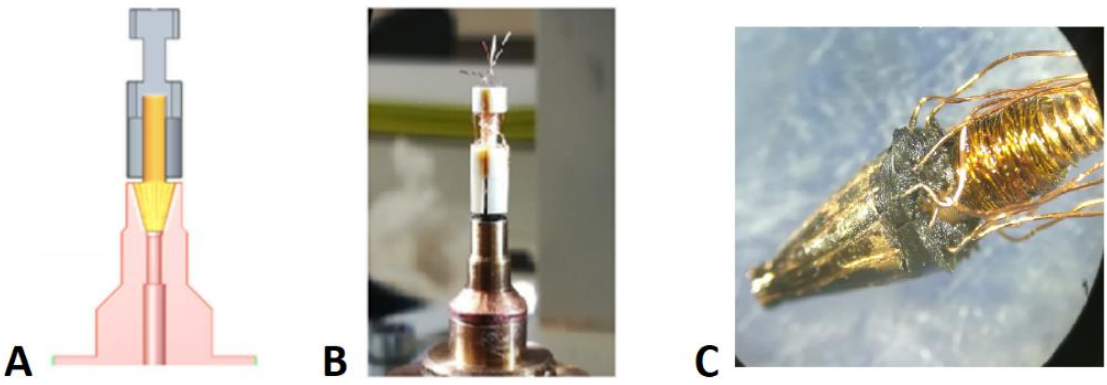

Figure 4.18: The assembly of small parts. With: A – a cross-section of geometry from CAD, B – the real-life image with all wiring & C – the ejected cone knob. Parts are coloured: feedthrough plug is pink; cone knob is yellow and the sample table is grey. Dimensions of parts can be found in Appendix A.

Please note that in figure 4.18 – B the Cu sealing ring can be found. It sits on the feedthrough plug and follows the curvature of the feedthrough plug's 45° draft as in figure 4.12. The ejected cone knob in C demonstrates how Cu wires are sitting inside of its grooves while surrounded with black epoxy. This particular cone knob was ejected form the feedthrough plug since it did not work and had short-circuiting issues. It took a total of five attempts to produce the working piece. The more detailed process, as well as the order of stages, can be noted by observing figure 4.19.

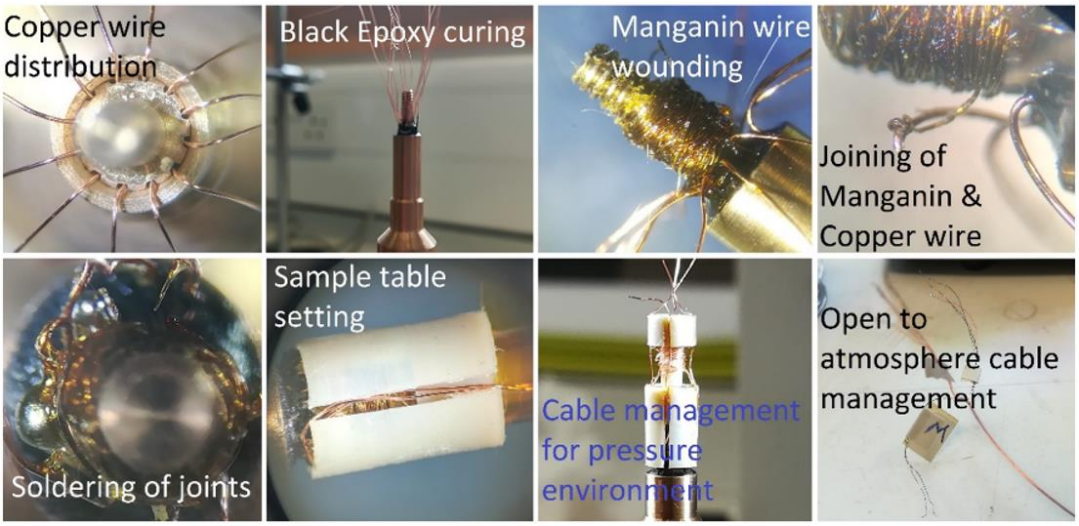

Figure 4.19: The comprehensive assembly of small parts. Detailed preparation of figure 4.18 – B. Left to right, top to bottom stages with corresponding comments.

The cone knob was first glued with small amounts of superglue which was applied in between grooves into the feedthrough plug to make these components static and to prevent accidental movement/rotations during Cu contact introductions into the cone knob's grooves. A total of 12 Cu wires were first cut to be of the same lengths and, although the sharp edges on the cone knob were polished, the contacts were additionally covered with an insulation layer – nail polish to improve their insulation thickness. Contacts were then slowly introduced from the top through the cone knob's grooves and the feedthrough plug. It was then required to bent contacts to the sides as it is shown in the top left image in figure 4.19 to simplify the application of the black epoxy mixture. While the epoxy mixture was still runny the contacts were then lifted back which allowed this mixture to get around the contacts and into the grooves of the cone knob. There is not much to be said regarding the other stages which were comprehensively discussed earlier in the design considerations section of this chapter, however, it can be noted in figure 4.19 – "Soldering of joints" that the soldering amount should be as small as possible as to fit into the sample table. To achieve such a small solder blob, the *T* of the soldering iron was set to be 190° C – the melting *T* of the employed soldering alloy. Once these parts (e.g. cone knob, sample table, all wiring and feedthrough plug) became a single unit they started to be treated accordingly and in the further sections of this thesis are referred to as the "cable guys".

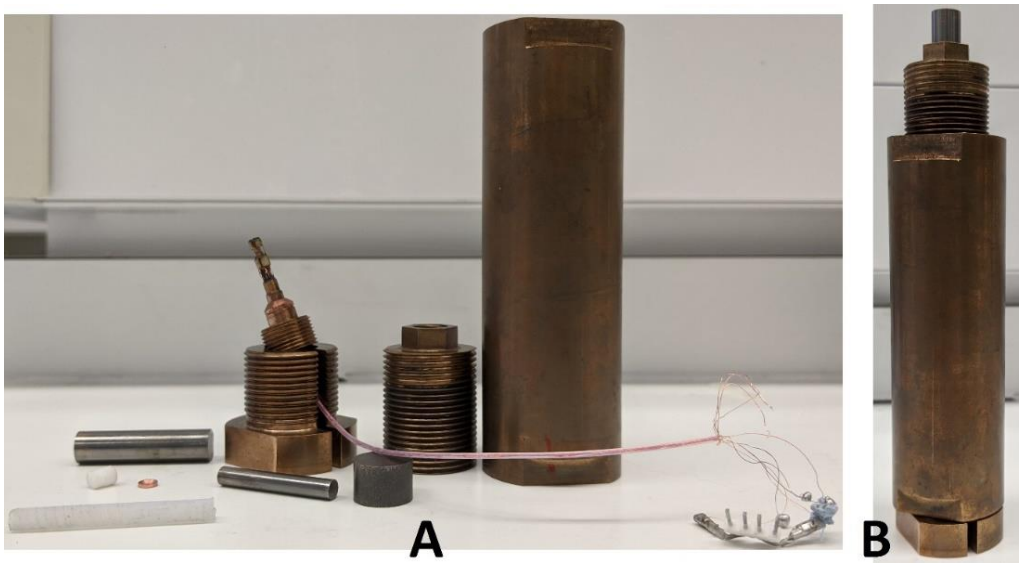

Figure 4.20: Compound piston-cylinder cell. With: A – disassembled and B –assembled. Part names can be found in figure 4.12. Dimensions of parts can be found in Appendix A.

The whole PCC (See figure 4.20) was assembled in the following order:

1) The bottom Cu seal was deformed to stay whether on the "cable guys" (See figure 4.18 – B) whether in the cell body. This was achieved by placing seal in between the "cable guys" and the cell body and closing the bottom locking nut until fully engaged. Once was done the parts were disassembled.

2) The PTFE hollow rod was put on the "cable guys" and fulfilled with the relevant PTM. This was done outside of the cell body to be able to check for air bubble formation which was unwanted.

3) The 2nd stage was introduced into the cell body's bore and, the lost during the introduction, PTM was added (≈ two small droplets).

4) The bottom locking nut was carefully closed with hand spanner while the cell body was locked in the vice in the upside-down position and, once fully engaged, the PCC was brought back to the normal standing position.

5) The PTFE cap was then introduced into the bore to close the PTFE capsule and the Cu seal was then added on top of it with sharp edges of the Cu pointing towards the PTFE cap.

6) The piston and spacer were then introduced into the cell with the spacer being covered with grease on all surfaces.

7) The PCC was closed with the not fully engaged upper locking nut and the pusher was finally introduced to complete the assembly.

It is worth to note that the further upper locking nut engagement into the PCC must be done with care to avoid changes in *Pi*. It is, therefore, reasonable to monitor Manganin *R* at all times and to compare its value prior to cell closure with after the cell closure. Both must be the same and, if a small difference of (+/– 0.02 Ω) is present, it can be accounted for small *T* changes and neglected. Else, based on the situation, the proper actions should be employed.

Generally, the disassembly of the PCC is inversely proportional to the assembly process with an exception that the piston might become stuck in the bore (especially if PCC was exposed to *Pi* above 500 MPa). If this is the case, the "cable guys" are also becoming stuck and, to carefully extract them out of the cell body it is required to employ additional tools (See figure 4.21 – A). These tools were specially designed to grip the external thread on the bottom portion of the feedthrough plug and, using the twist and pull technique, pull the "cable guys" out of the cell body in the vertical direction which also highly minimises damage to the CPP and leads if the directional extraction is produced slowly and without wobbling. The piston can then be easily ejected by pushing it out from the just-opened side of the bore.

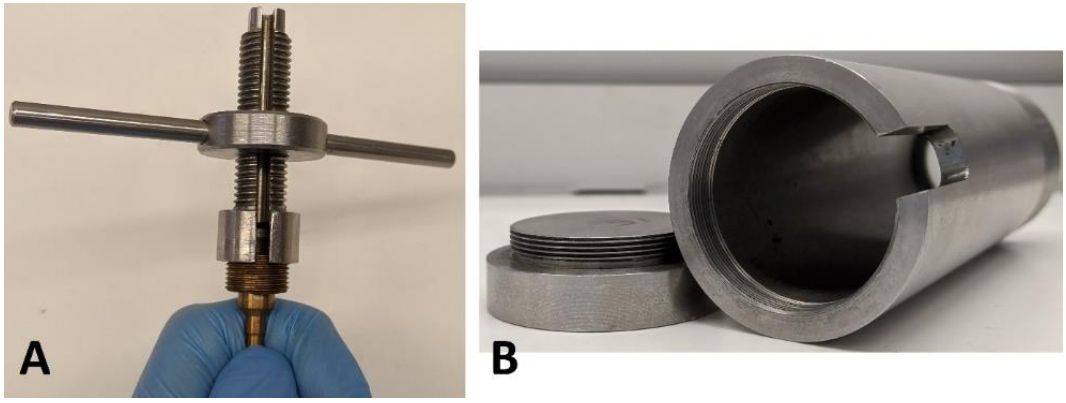

Figure 4.21: Additional tools. With: A – extraction tools and B – protective cylinder. Both additional tools were made of stainless steel (SST). Please note that A has the feedthrough plug which is engaged into the tool for demonstration purposes. Dimensions of parts can be found in Appendix A.

Since it was required to reach 3 GPa in PCC, simulation of which gave σ_e to be higher than the σ_y (See figure 4.17), it was required to produce an autofrettage and, to keep the working environment safe, an additional protection layer was utilised – the protection cylinder (See figure 4.21 – B) which was designed to fit the compound PCC inside of it and, in case of the fracture, would absorb the flying elements of the compound cylinder.

The protection cylinder was also designed to fit all the necessary heating elements such as the resistive panel as well as the layers of Kapton tape to hold them firmly on the surface of the PCC. Also, both additional tools are having special notches for lead wires which are coming from the bottom side of the feedthrough plug to be fed through them.

4.11 Experimental testing

The experimental testing of the PCC was first employed to investigate if the cell was able to reach the required *P* (e.g. 3 GPa) without failing and if the "cable guys" would be able to survive these *P* extremes with no short circuits in the Manganin wire. Once the PCC had reached the 3 GPa it was brought back to *Pamb* to examine the internal bore which did not reveal any deformations which meant that the cylinder was successfully autofrettaged and now can be safely exploited in the *Pamb* – 3 GPa *P* range.

It took in total 5 "cable guys" assemblies being tested until the last, which is described in this thesis did work up until the required *P*. The previous four used to fail on the short-circuiting issues for all 12 Cu wires. Along with PCC's testing, the set of Manganin coils was subjected to *P* cycles to season them (See 3.3.1 section in the 3rd chapter).

The second set of the experimental testing involved the experiments on the CPPs to investigate if the "cable guys" would be able to survive these *P* extremes with no short circuits in the Cu wires which are connected to the CPPs. The CPPs were made per sample dimension requirements and measured using the electrometer while the Cu wires which are interconnected with Manganin wire were measured using DMM as per the *R* ranges.

Once all experimental tests showed no issues the presented PCC was concluded to be successfully made to be able to safely operate in the required *P* range while is capable of producing *R* measurements both on samples and on Manganin wire to probe the *Pi*. The *R* measurements can be performed on the CPPs which are 3mm in *OD* and potentially (this was not checked yet) the long needle-shaped samples because the size of the PCC's reaction volume allows this.

Chapter 5

Adaptation of DAC

This chapter starts with the requirements and reasoning which are followed with design considerations of the desired DAC based on which the most suitable existing DAC was selected that can be adapted for *R* measurements. Further, the method for gasket's insulation is provided as well as the FEA of the backing discs which are made of two non-magnetic materials to determine the most suitable one which won't yield under the applied *P*. Lastly, the manufacturing, assembly and experimental testing of the DAC which can routinely go up to the 10 GPa in *P* while is capable of producing *R* measurements on the sample material and is equipped with the visual and laser access to access the quality of the contacts and to probe the *P* using the ruby fluorescence technique are provided.

5.1 Requirements and reasoning

5.1.1 Pressure limit

The DAC is another suitable HP device for measuring electrical properties of sample materials (See 3.2.3 section in the 3rd chapter). The small reaction volume of DAC makes it difficult to exploit the HP cell (especially if measurement interest lies upon electrical properties) however, it also becomes an advantage, since it allows to expand the *P* scope and, therefore, to investigate what happens with the materials at higher *Ps*.

According to the 2.2.1 section in the 2nd chapter, the 3 GPa is the upper limit in the OPET's application range, however, it might be worth investigating samples with interesting P - ρ trends beyond that *P*. This does not necessary dictates the exploitation sequence of HP cells. Looking ahead, some materials were measured in PCC and some in DAC only and only a few were measured in both. Another advantage of DAC compared to PCC is that its *P* gauge has no *T* dependence (unlike Manganin) which makes the *T* analyses easier to accomplish.

It was decided that DAC with *P* limit of 10 GPa should sufficiently cover the beyond of interest range (e.g. anything beyond 3 GPa). As it was previously said, the maximum *P* in DAC is highly affected by its design, materials employed and the cullet size of the diamond which in turn dictates the sample dimensions. The selection criteria for the DAC for *R* measurements would, therefore, be the design which allows the sample wire access, as big as possible diamond cullet which allows reaching *Ps* of 10 GPa and the visual and laser access to the reaction chamber for checking contacts during the experiment and probing the *P* using the ruby fluorescence technique.

5.1.2 Diamond

The general rule which relates the maximum achievable *P* and the cullet diameter is as follows [196]:

$$Pmax\ (GPa) = \frac{10}{d(mm)} \tag{5.1}$$

Where *d* is the culet diameter. Which if solved to determine *d* gives:

$$d = \frac{10}{10} = 1\ mm$$

However, to allow some safety margin and, therefore, to routinely exploit the DAC with no fracture risk, it was decided to use the diamond with 0.8 mm in diameter culet which, following equation 5.1 can be pushed up to the 12.5 GPa.

The relatively cheap and well-known supplier of diamonds with good optical properties in the scientific community is the Almax easyLab company [197] that advises using the bevelled culet rather than flat if experiment interest lies upon the electrical measurements. The bevelled profile on the culet not only smoothens the sharp edge which otherwise could cut the probe wires but also reduces the risk of damage during the alignment process which will be further discussed.

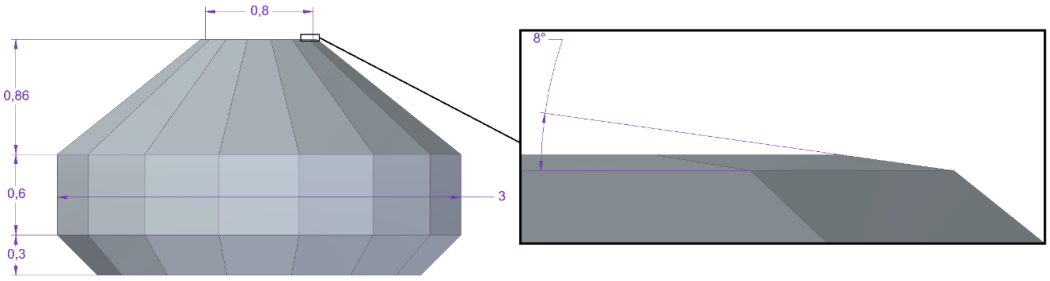

Figure 5.1: Standard type Ia diamond with 0.8 mm cullet and 8° bevel. All dimensions are in mm. Drawn following the guidelines provided by Almax easyLab [197]. Full dimensions can be found in Appendix B.

The diamond in figure 5.1 is the 16-sided diamond which has the overall diameter of 3 mm and is polished parallel to (100) crystallographic diamond plane which is the strongest plane for compression.

5.1.3 Sample dimensions

Unlike in the PCC where CPP's geometry stays uniform, the DAC's CPP lies in between two opposed anvils and experiences a direct physical contact with them under compression. Therefore, the CPP geometry occupies all available space in the gasket's drilled hole in terms of pre-indented thickness and drill diameter. The

typical sample limit which is set by gasket is a 0.1 mm in the vertical direction and about 50% reduction in overall culet diameter [197] which is 0.4 mm in diameter circle for the 0.8 mm diamond cullet. By considering the above said and by applying the MM this led to the following sample geometry and contact wire allocation:

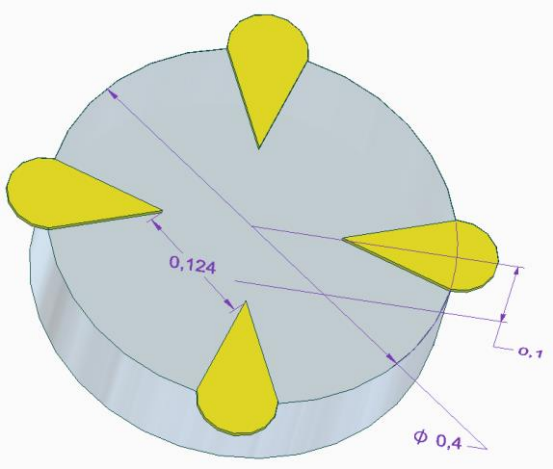

Figure 5.2: Compressed powder pellet example geometry for the DAC. Pellet and contacts are shown in grey and yellow respectively. All dimensions are in mm. Please note that the contact separation can vary in between experiments and must not obligatorily equate to 0.124 mm. This value is only specified as an example.

Unlike in the PCC where the effective pellet thickness (*Z*) for MM's stays constant and can be made to have ideal size for the experiment duration, in DAC the value for *Z* is calculated based on the available dimensions (those which are restricted with gasket hole and indentation thickness) and based on the achieved contact separation which varies in between experiments. With *P* application, the CPP's thickness uncontrollably reduces since diamonds are brought closer. This results in the inability to use the perfect relationship when the actual thickness equals to the *Z* and, therefore, to use equation 4.1. Instead, the value of *Z* is approximated based on what is available. Therefore, using figure 3.5, the value of *Z* would equate to 83.08 μm if the achieved contact separation is 0.124 mm. Please note that value of *Z* also imposes a limit on the maximum attainable *P* in DAC to avoid *Z* being smaller than the actual thickness of CPP which may show inconsistency if DAC data is compared with data collected in PCC where CPP does not undergo physical changes in shape and size during the experiment.

Therefore, the employment of DAC would allow investigating if the MM for *R* into ρ conversion can be applied to the sample geometry in DAC by producing

measurements with the identical sample in both PCC and DAC and checking for consistency.

5.2 Design considerations

5.2.1 In situ pressure measurement (ruby)

To employ the ruby fluorescence technique (See 3.3.2 section in the 3rd chapter) it is required to be able to see the ruby through the diamond. The selected diamond (See figure 5.1) is transparent to visible light and, therefore, the design of DAC should take this into account. It is a common practice to avoid building HP cells from a single unit and, the optical access can be achieved with the help of specially designed diamond seats which are also called backing plates. The diamond seat practically experiences only the compression and the value of stress it withstands can be probed with FEA. Since the optical access is a must, the seat can be made of transparent materials or by the introduction of the hole through it which should be bigger than cullet but also smaller than the diamond base. If the seat is flat, the diamond can be glued to it with the epoxy by covering its height by two thirds. Since PR materials to be measured are of a powder form, they would occupy all the available space in the gasket which means that ruby which also must be loaded into the gasket along with PTM might not be found with a laser. To increase finding chances, it is, therefore, necessary to be able to see the ruby visually which dictates the need to attach it to the surface of the culet. More specifically, to the very centre of it since the *P* varies along the culet with highest being proven to exist in the centre [198]. Therefore, the powder particle size must be smaller than the ruby piece and, since the DAC closes along vertical axis any transparent substance with some level of viscidity can be employed such as the grease to attach the ruby to the required location. It is also a common practice to load several rubies to simplify working and/or to be able to monitor *P* along all of them.

5.2.2 Sample wire access

Since it is required to reach the sample material with probe wires to produce electrical measurements, the design of DAC should allow both the physical working

space with wires and the possibility to allocate them on the cell body (See figure 3.11). The former requirement should also stay true when the DAC is closed to allow visual access from the side. This would allow to check for short circuits in between contacts and cell or gasket as well as to repair junctions and/or leads which may have been damaged during experiment or handling. Since all the reaction volume is to be occupied with the test material, the wires could be fixed to the diamond culet as long as this is not the same culet which is responsible for holding the ruby chip because it can move or damage contacts. The latter requirement was mentioned as to highlight the need of keeping the previously mentioned safety junctions and entire wire assembly on the same unit. This would provide a safe and static work environment.

5.2.3 Materials

Preferably, the DAC should be made of high-strength non-magnetic materials to provide measurement accuracy and safe cyclic exploitation for a wide *T* range (e.g. +/– 100° C). This is especially true for the backing disc which experiences high stress that is translated through the diamond. The disc should be able to stay within the elastic region to avoid yielding and, therefore, most common candidates are hardened BeCu, NiCrAl, maraging steel, Inconel and WC [54, 199, 200]. The last three candidates are more preferred in the ultra-high-pressure region due to their high compressive strength while the first two might be found advantageous for the project preferences since they are having a low magnetic background. The rest of the cell parts can be made of SST if the design of the cell allows this (e.g. if these cell parts would provide enough support for the backing disc).

5.2.4 Clamp design

Given the above, the DAC should have symmetric top and bottom regions. While the top region will be responsible for holding all the wiring for electrical measurements the bottom would be used for holding gasket, it’s lamination, ruby and sample. Such a distribution would result in a possibility to visually access the quality of the wires inside of the culet area from the one side and to easily find the ruby from the other through the optical diamond access when the cell is closed and/or during the experiment duration. This would indeed minimise the wire damage since ruby and

wires will be separated with a layer of sample material. It is, however, worth to note that this may affect the diamond parallelism and, therefore lead to non-axisymmetric gasket deformation under *P* which in turn may result in a diamond fracture. To avoid this, the parallelism can be set as an obligatory constitution for the whole cell rather than only diamonds. It can be achieved by making the paired components (such as cell body and backing plates) as a single unit first with further separation and introduction of the guiding holes and guiding pins for the top and bottom regions.

To simplify the cell exploitation and to allow the *T* analyses the DAC should have the clamped design with the possibility to clamp the given *P* and to study the sample behaviour at it. This can be achieved with the introduction of locking bolts which are circumferentially distributed around and with an equal to the centre (e.g. diamond) distances. These bolts can also be used to generate *P* by tightening them.

In the view of the above considerations and the gained during the literature review study knowledge, an author concludes that the most suitable for all the criteria (e.g sample wire working access, optical ruby access and maximum *P* of 10 GPa) DAC already exists and is called a Merrill Bassett DAC [172]. It is commonly widely employed in the X-ray HP measurements, has simple design and alignment procedure, relatively big working access from the side and when DAC is closed, which makes this cell type suitable for electrical ρ measurements adaptation.

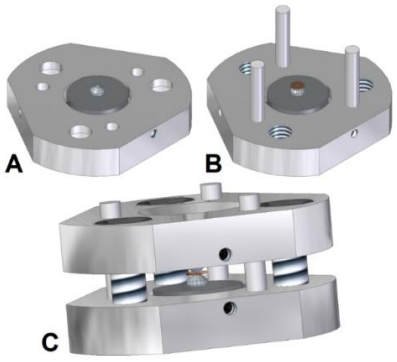

Figure 5.3: The Merrill Bassett DAC. With: A – top region or the upper side of the cell which is responsible for holding all the wiring and junctions. B – bottom region or the bottom side of the cell, which is responsible for holding gasket, it's lamination, ruby, sample and PTM. Please note that gasket is drawn undeformed. In C the assembly of A and B is shown. Dimensions of parts can be found in Appendix B.

P in the cell (See figure 5.3) is generated with 3x M5 bolts which are slowly tightened one after another which means that the appropriate marks should be made

before starting an experiment and during the tightening process to make sure the plates and, therefore, diamonds are kept parallel.

5.3 Gasket

The gasket is one of the most important parts in the DAC (See 3.2.3 section in the 3rd chapter). Gasket confines the sample and provides hydrostatic conditions, minimizes stress on the diamonds and, therefore, allows higher *Ps* to be reached. The selection of the gasket's material is highly affected by experimental preferences. The material must be chemically inert and compatible with samples and PTMs as well as not too hard to allow fast sealing and not too soft to prevent eventual diamonds contact up to the specified maximum *P* [54] which makes metals to be an obvious choice. One such material is BeCu, advantages of which were previously mentioned (See 4.2.1 section in the 4th chapter).

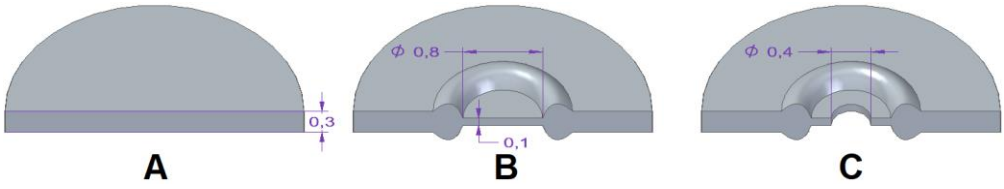

Figure 5.4: General gasket preparation. With: A – the disc formation, B – pre-indentation and C – drilling. All dimensions are in mm.

Gaskets are conventionally made from thin metal sheets which have ≈ 0.3 mm thickness. Once cut into the required shape (usually disc or rectangle) pre-indentation takes place which further decreases the thickness to about 1/3 of the initial value. Once the gasket is pre-indented it is then drilled. It is important to produce a hole (a sample chamber) in the very middle of the indented area. The poorly centred hole might lead to the experiment unsuccess, poor hydrostatic conditions and limited optical access. This happens as a result of culet's edge being reached by the drilled in the gasket hole which with *P* application enlarges asymmetrically.

5.3.1 Gasket indenter

It is a common practice to pre-indent gaskets in DAC; however, this practice is also followed by risks of diamonds fracture (See 3.2.3 section in the 3rd chapter). To avoid those risks the special device was fabricated.

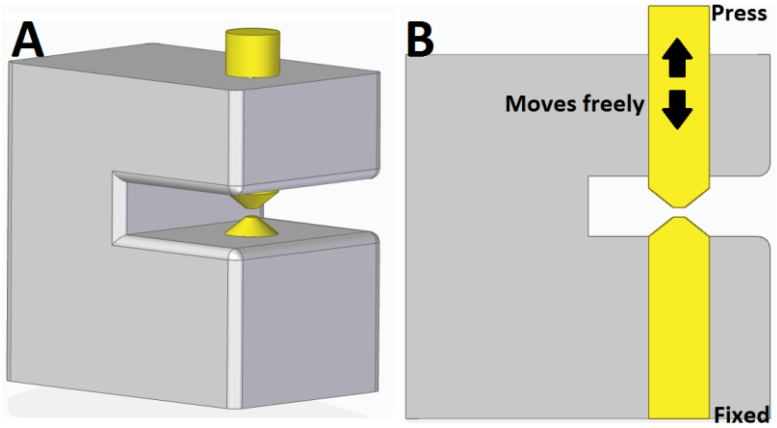

Figure 5.5: Gasket pre-indenter for DAC. The body and indenters are shown in grey and yellow colours respectively. A – isometric representation of the application. B – Section side view with operating principle. This application can be used to pre-indent gaskets to the required thicknesses using a conventional hydraulic press. While the top indenter is allowed to move freely along the vertical axis, the bottom indenter sits securely inside of the body and shares the same level of the surface with it. Dimensions of parts can be found in Appendix B.

The device mimics the procedure which is normally used during gasket pre-indentation. The DAC is replaced by C-type body and diamonds are replaced by WC pistons with DF6 grade number [201] which are equipped with the conical end and a culet at one side and are flat at the other. This allows to pre-indent gaskets of any softer than the selected for the indenters material including BeCu which was used in this thesis. Please note that the conical shape is different from the 16-sided profile of the diamond (See figure 5.1) which results in the same conical indented profile on the gasket. Conical profile was found to be better compared to 16-sided because its placement quality did not depend on the gasket's rotation around the vertical axis. Naturally, the indenters can be redesigned for any type of the diamond by changing the conical angle and/or cullet size, therefore increasing the number of indenter pairs (parts) and expanding the scope of the presented in figure 5.5 device.

5.3.2 Gasket preparation

Once pre-indented, it is required to drill and prepare the gasket for the experiment. To produce the hole in the very centre of the indented area it is first required to centre punch the preferred location and considering the small scale, the sewing needle can be used for it. To produce the 0.4 mm in diameter hole it is a must to first produce the 0.2 mm in diameter hole to increase the success chances as the drill often slips to the side especially during manual drilling.

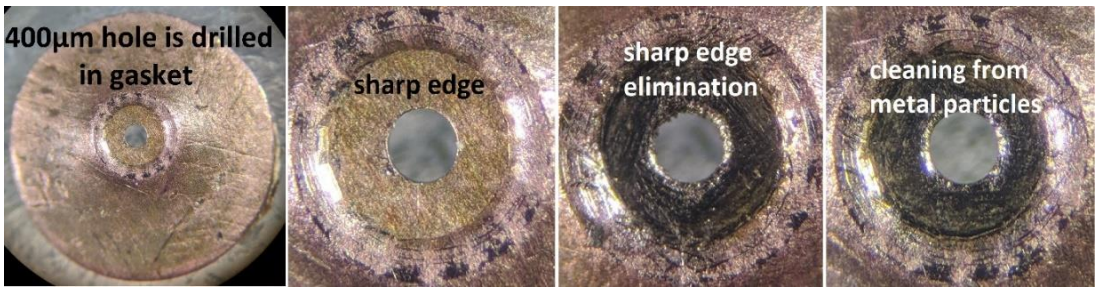

Figure 5.6: Gasket preparation with corresponding comments.

Once the hole is drilled it is important to get rid of the sharp edge at the bore as it can weaken the insulation layer during *P* application and be the main reason of the short circuit. The sharp edge can be eliminated with the sewing needle. Please note the colour change of the indented area in figure 5.6 (between two left and two right images). This is due to the technique used when the sewing needle tip is first leaned against the big diameter of the indented area (e.g. 0.8 mm) and then brought to the hole and then repeated circumferentially until the edge in the drilled hole starts to feel rounded. The ultrasonic bath is then required to get rid of the metal particles and after careful inspection, the gasket can be glued to the diamond.

5.3.3 Lamination of gasket and cell body

Since the contact wires are non-insulated it is required to insulate the parts they adjoin, and the most complicated part is the gasket since it is in a tight contact configuration with probes which are trapped between diamonds. If the gasket is metallic the insulation materials such as MgO, Al_2O_3 or CsI can be employed [54, 202]. Particles of those materials are mixed with the epoxy resin and then are applied on the not fully indented gasket. Once applied the gasket is further indented to the thickness of interest and left clamped until the mixture solidifies. Similar materials could also be used to create standalone non-metallic gasket; however, this process requires a lot of practise and experience not to mention the necessity in the creation of additional instrumentation where such gaskets will be made [203, 204]. Instead, an author invented a new method for metallic gasket lamination which is believed to be less time consuming and easier to be implemented.

The method involves the use of the polyvinyl chloride (PVC) material. Insulation constitutes of few layers (3 – 4) of PVC wrap paper which are first cut into small

square pieces (of the gasket size) and then are placed on top of each other. It is required to make sure that no dust particles would be trapped in between these layers and that the final thickness of the stack would be around 35 μm which was experimentally derived as an optimum numerical value. The stack must then be glued with GE Varnish to the gasket. It is worth to note that no glue should be introduced into the indented area (See figure 5.7). To further improve the working environment, it is advised to gently clamp the gasket with PVC in between two indenters so the PVC stack would repeat the recess geometry of the indented area on the gasket.

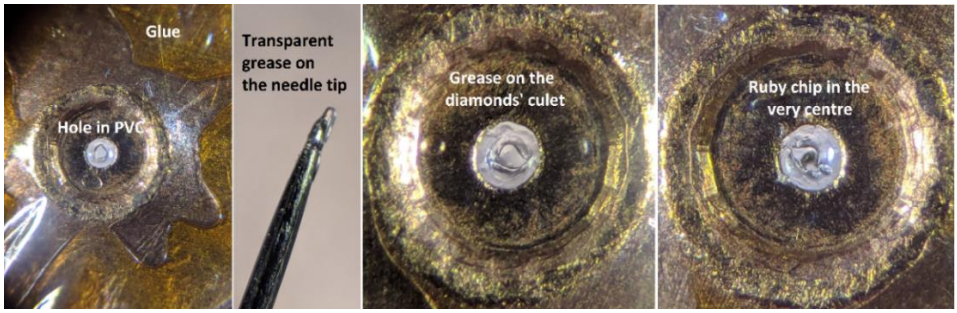

Figure 5.7: Lamination of gasket and implantation of the ruby chip.

When the glue is hard, the hole for the sample must be addressed. The initial hole in PVC can be made with a sharp tool such as the acupuncture needle. To simplify further works that include ruby implantation and sample addition, the initial hole can be widened to a greater size with a wider sharp tool such as the sewing needle. The transparent grease is essential to be applied to the diamond's culet surface to make sure that ruby chip will not shift away from the centre of the hole and/or lose the connection with culet's surface during the sample powder addition process which in turn would entail unwanted consequences that were recently discussed.

If the diamond is glued to the diamond seat with the epoxy as in figure 3.11, there is no need to laminate it since epoxy is non-conductive. Lamination of other cell parts is highly dependent upon the employed in the design materials that conventionally are metals. Those parts, fortunately, can be easily laminated if they are apart from the delicate areas (e.g. small thin wires, gasket and diamond). The furthest from the diamond wire junctions can be separated from the cell body with an insulating material (such as wood). This would allow to increase the mechanical stability of the wire assembly and reduce chances of short-circuiting.

5.4 Analysis of the backing disk

To determine if the presented design (See figure 5.3) can get to the required *P* (e.g. 12.5 GPa) it was required to virtually test it. Just like in the case of PCC, the parts involved in the cell assembly should not go beyond yielding and it is required to access the critical elements of the design from the virtual point of view prior to manufacturing them to dimensions. In the case of PCC, the critical element was the 3D state that occurs in thick walls of the cylinders and, therefore, only cylinders were simulated. In the Merrill Bassett DAC, the critical element of the design is the backing disc since it experiences the highest after the diamond compression load and, using the FEM its material and design can be determined.

As before, to simplify the modelling, only halves of the parts were drawn to save time on computation by producing the axisymmetric 2D analysis which led to the corresponding geometry (See figure 5.8 – A). The diamond was drawn in accordance with Almax easyLab guidelines [197] while the displayed backing disc geometry and dimensions were created for the several reasons among which are the necessity in having good optical access to the sample chamber, fit into the cell plates while allowing the translational alignment of the diamond (See figure 5.12) while also providing enough supporting material as per the "massive support principle".

The idea of the principle is to support the massive loads by the comparatively softer material. Such a principle was used by humankind since antiquity and was first applied to the HP instrumentation by Bridgman who empirically derived that change of shape and size of anvils and their supporting material allows going beyond the yielding of the employed materials. It was established that materials won't yield even if the compressive strength is three times higher than their yield point if the loaded area is much smaller (at least 10 times) then the overall [205 – 207].

As it can be seen in figure 5.8 – B, the load of 6287.5 N was applied to the 0.8 mm (H49*2) cullet face of the diamond which following the equation 3.4 corresponds to 12.5 GPa of *P*. This value corresponds to the normal Y-axis compression if simulated for the model validation purposes and should lead to the concave deformation of the cullet [208]. Since the involved geometries are not of a cylinder type, the translated

to the backing disc stress through the diamond won't follow the same as the cullet *P*/stress rule which is the root cause of employing FEM.

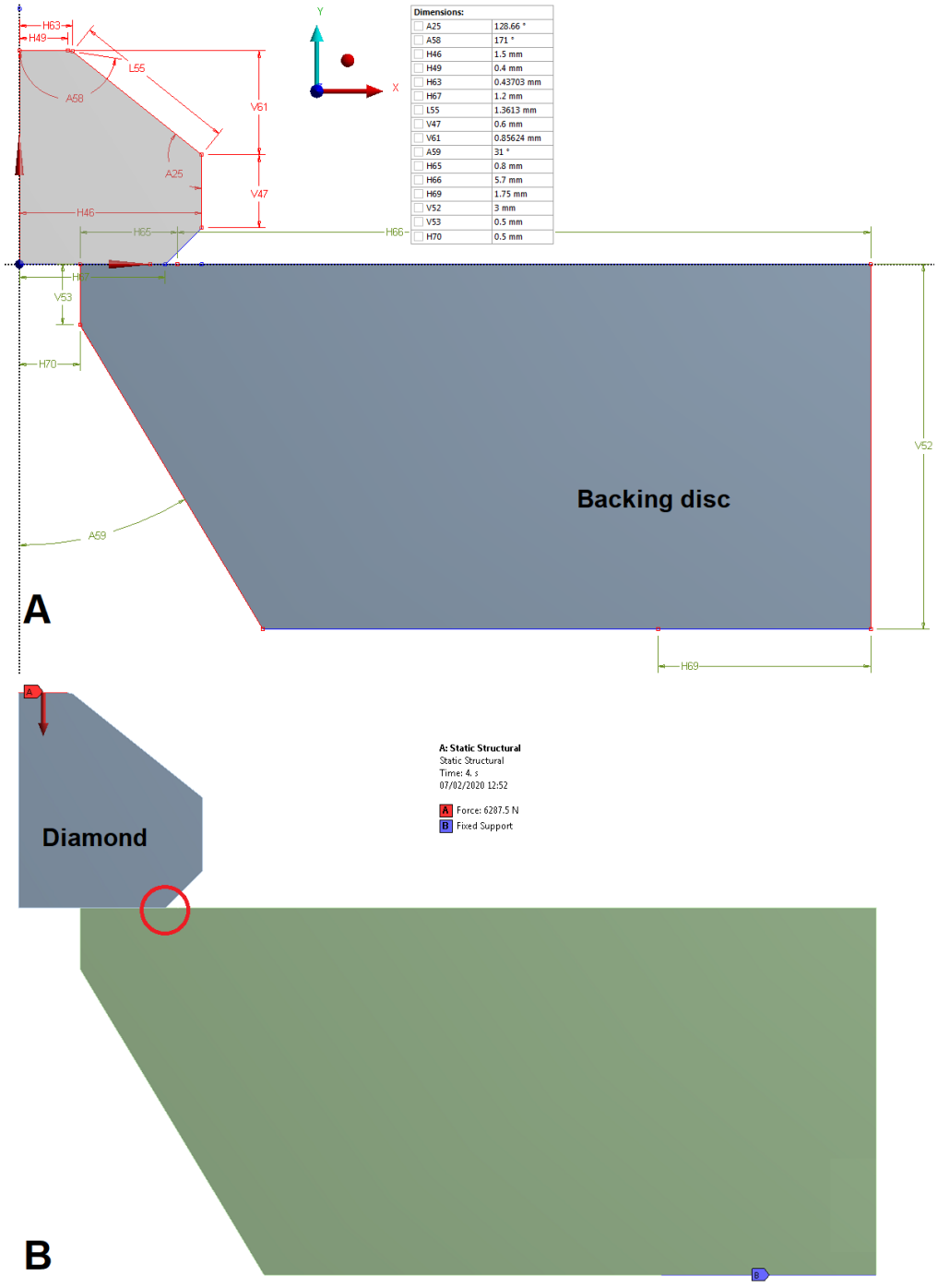

Figure 5.8: 2D geometry of backing disc and diamond. With: A – relevant dimensions and B – structural conditions. The contact type between diamond and the backing disc was chosen to be frictional with a friction coefficient of 0.1 [209]. The fixed support on the backing disc was introduced to prevent rigid body motion of the model. The red circle represents the expected high-stress concentration [209]. The direction of the arrow indicates the direction of the uniformly distributed load with uniform loading which was split into 4 steps. All further results will be demonstrating the final step which corresponds to the 6287.5 N load.

It was previously determined by David M. Adams [209] that the highest stress concentration between diamond and the backing disc occurs at the edge which is marked with a red circle (See figure 5.9) and this can also be used as a sanity check to validate the model. Please note that the contact area of diamond and backing disc is much smaller than the overall area of the backing disc as per "massive support principle". The only support was placed at the base of the backing disc and is represented by the H69 dimension since this is approximately the contact edge of the backing disc and the plate (See figure B.3). The diamond was assumed to have no supports (no side supports such as epoxy) for the simulation purposes and was given the mechanical properties which are outlined in table 5.1.

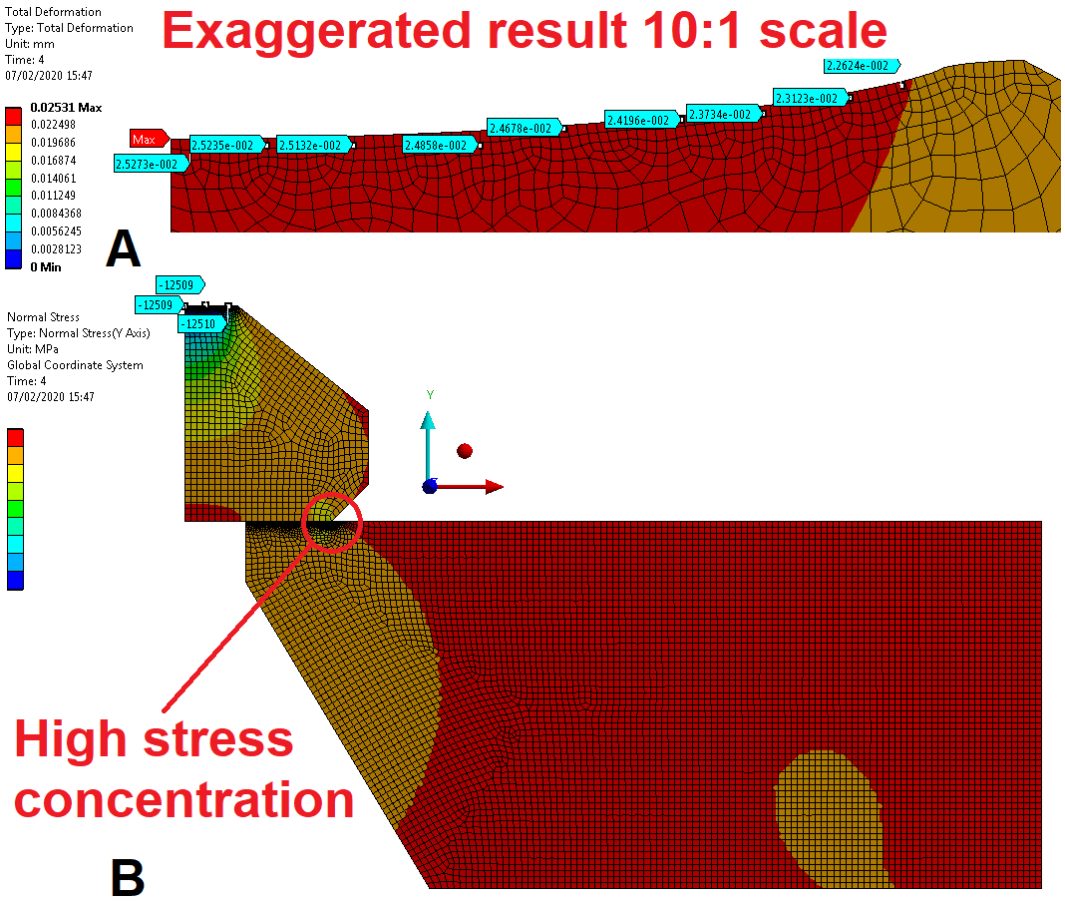

Figure 5.9: Model sanity check. With: A – exaggerated deformation of the cullet using total deformation tool and B – general stress distribution along Y-axis with high concentration region specified. The units are given in MPa. It can be noted that the delicate parts such as the cullet and the H65 edge (See figure 5.8) were being meshed with a high concentration of elements since these are the areas where the high stresses were expected.

Table 5.1: The mechanical properties of the diamond [192].

Mechanical property & units	*Numerical value*
Tensile yield strength – σ_y (MPa)	2900
Poisson's ratio – v	0.11
Young's modulus – E (GPa)	1050

While the coloured ruler still represents the highest and lowest values, the numerical values in B were omitted since these are material dependent while the goal of the figure was to demonstrate the general distribution and the highlighted stress probes (labels with cyan colour). As expected, the cullet deformed inwards with the concave deformation. The maximum deformation occurs at the centre of the cullet which is shown with red label in figure 5.9 – A. Deformation slowly reduces towards the culet's edge which is well supported with deformation probes on the same figure. It is worth to note that the deformation units are mm and that the maximum value which is the 0.02531 mm occurs only under the maximum load (e.g. 6287.5 N) and disappears with *P* release. Also, the applied on the cullet *F* in figure 5.8, as expected, became compression stress of a -12500 MPa magnitude (See figure 5.9 – B). Considering the above said, the model has passed the sanity check and the simulation results are adequate and well supported with the previous findings [208, 209] and, therefore, the further analysis can be performed to choose the right material for the backing plate.

The NiCrAl and the hardened BeCu are the most adequate candidates for the backing disc as they are having non-magnetic character and, therefore, both were simulated to select the most appropriate one for the desired *P* exploitation range of DAC.

Since the general interest lied in the high-stress concentration area (See figure 5.9 – B) it was decided to omit to analyse anything but the magnified view of it. By producing two simulations with different materials for the backing disc it was found that the backing disc which is made of BeCu (See table 4.1) and has the yield strength of 1400 MPa will most likely fail since the observed in the simulation stress probes (See figure 5.10 – A) can be found to be way higher than the 1400 MPa (even considering the massive support principle).

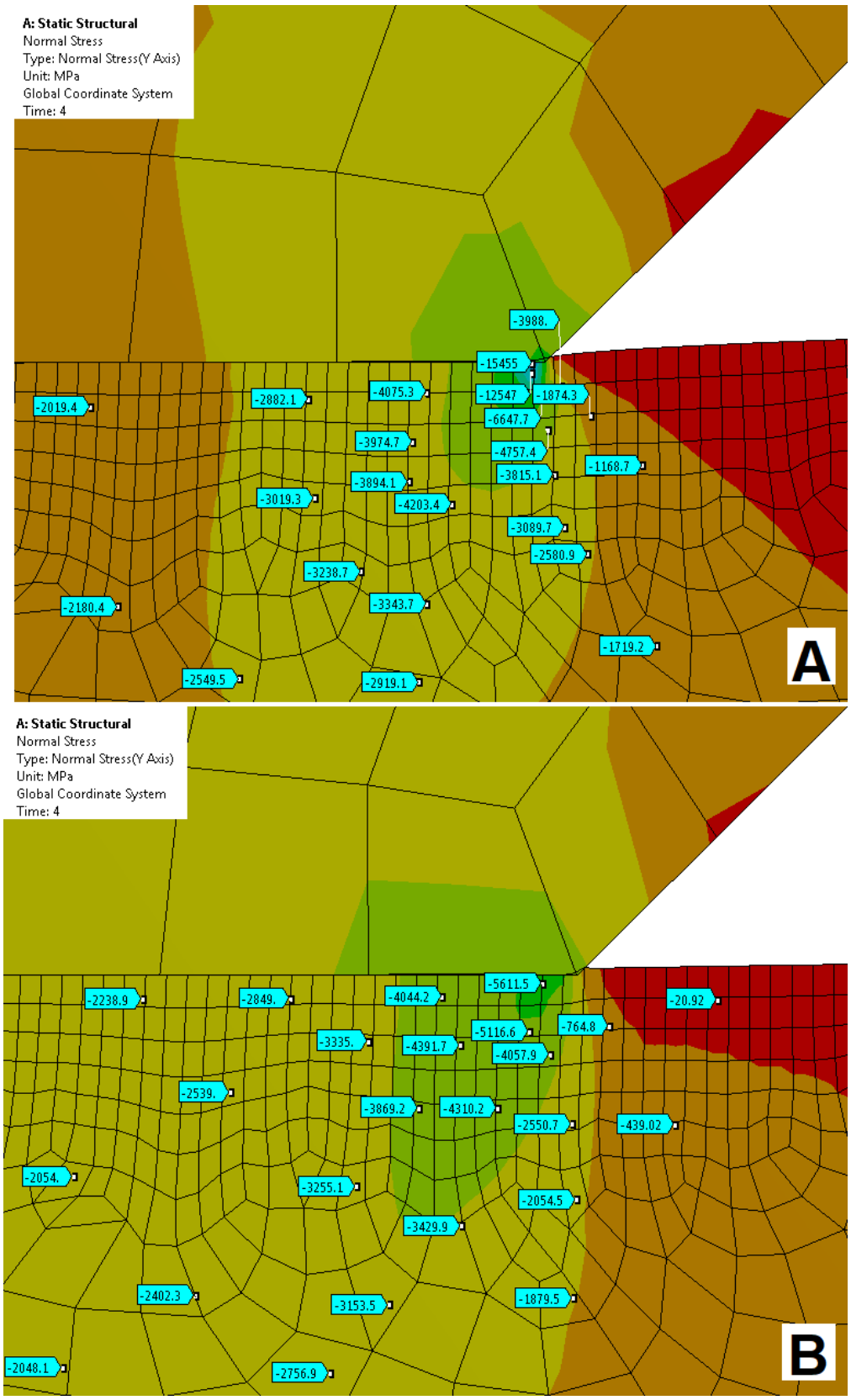

Figure 5.10: Magnified high-stress concentration area. With: A – BeCu and B – NiCrAl as the backing discs. As previously, the red colours are representing high values and blue – low. The highest negative stresses are probed with cyan labels.

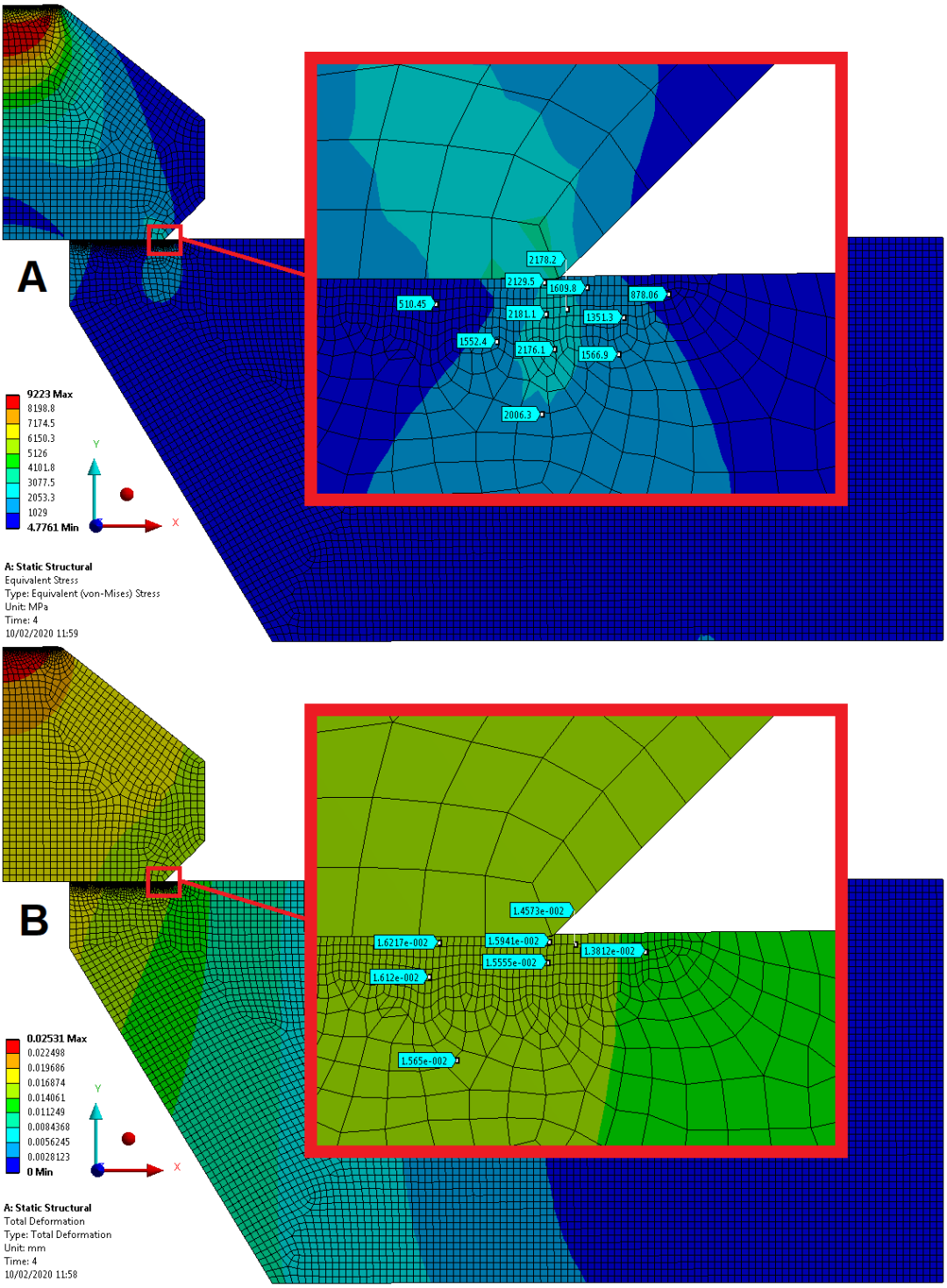

Figure 5.11: Further analysis with NiCrAl. With: A – Von Misses stress and B – Total deformation. Units are MPa and mm for A and B respectively.

The stress magnitudes up to the 15455 MPa can be noted in figure 5.10 – A indicating the high probability of fracture in the BeCu disc and, therefore, this material is not suitable for the desired *P* range in DAC. The simulation of the

backing disc which is made of NiCrAl and has the yield strength of 2000 MPa (See table 4.2) can be found in figure 5.10 – B. It was found that if the 6287.5 N load is applied on the diamond cullet (which corresponds to 12.5 GPa of *P*), the highest stress magnitude would be 5611.5 MPa. By considering the massive support principle, such a magnitude becomes within the elastic region of NiCrAl disc (e.g. 5611.5/3 = 1870.5 MPa). Consequently, the NiCrAl was selected as the material for the backing disc with further analysis being performed to determine Von Misses stress and total deformation which can be found in figure 5.11.

The maximum σ_e in figure 5.11 – A was found to be 2181 MPa which is below the NiCrAl's UTS (See table 4.2) but above it's yielding (e.g. 2000 MPa) and some experimental testing would be required to determine if the backing disc would permanently deform or not. In figure 5.11 – B the maximum deformation does not exceed the 0.018 mm magnitude under the 12.5 GPa of *P* on cullet which is a small change but still worth an investigation.

5.5 Manufacturing process

All parts of the DAC (See figure 5.3) were made using a conventional machining process. To achieve good parallelism the paired components such as backing discs and top and bottom plates were first made as a single unit with further separation. The three guiding pins were then made in accordance with the guiding holes of the top plate to allow tight fitting into them. Pins were then permanently bonded into the bottom plate which allowed to access the quality of the parallel configuration. Plates were assumed to have good parallelism since plates were able to fully close the gap if were brought together via pins. The 0.5 mm difference in the backing disc and its recess in the plate's height (e.g. 3 mm – 2.5 mm) led to the possibility to produce the half-assembled (e.g. without diamonds) check for parallelism which showed no issues.

All parts were hand-finished with a gentle sandpapering process to eliminate the sharpness of the edges and, most importantly, to achieve the good quality surface finish on the backing discs. This is especially important when no diamond recess is made on the backing disc to further improve the parallelism.

5.6 Assembly

5.6.1 Fixing diamond to the disc

It was necessary to fix the diamond (See figure 5.1) to the backing disc in such a way that its cullet would perfectly sit in the middle of the drilled in the backing plates' hole to allow full optical access to the sample chamber. At the initial stage, diamonds were first glued with Araldite® [210] to the backing discs by introducing a very thin layer of this glue around the drilled hole which was also followed by vertical compress on the diamond's cullet to push out all the unwanted glue away. If successfully performed, the cullet can be fully seen under the microscope through the backing disc after the release of the load. To further straighten the diamond's position, which is especially important if no diamond recess was made in backing discs, the Stycast 126 epoxy was applied at the diamond surroundings. This led to the epoxy having fully covered the surface of the backing disc and in submerging the diamond height by approximately two thirds. It is important to note that the whole process (to be successful) must be performed in a clean environment to prevent contamination of the epoxy mixture and, most importantly, the diamond. Last can be held in a supersonic bath while submerged in the alcohol liquid prior to glueing. An author would also like to highlight the necessity to suck out any air bubbles out of the epoxy mixture before its application in case if the DAC is to be used in vacuum environments.

5.6.2 Diamond alignment

The alignment process is a must in the DAC since its quality dictates the maximum *P* apparatus can safely get to and, therefore, the length of exploitation until failure in addition to the previously mentioned advantage: the symmetric gasket deformation. In the proposed Merrill Bassett cell (See figure 5.3) the diamond is fixed to the backing disc and there is no angular alignment mechanism which, on the one hand, simplifies the alignment procedure leaving the experimenter with the need to produce only the translational alignment and, on the other, requires high-quality machining of paired components as well as the diamond glueing delicacy to the backing disc.

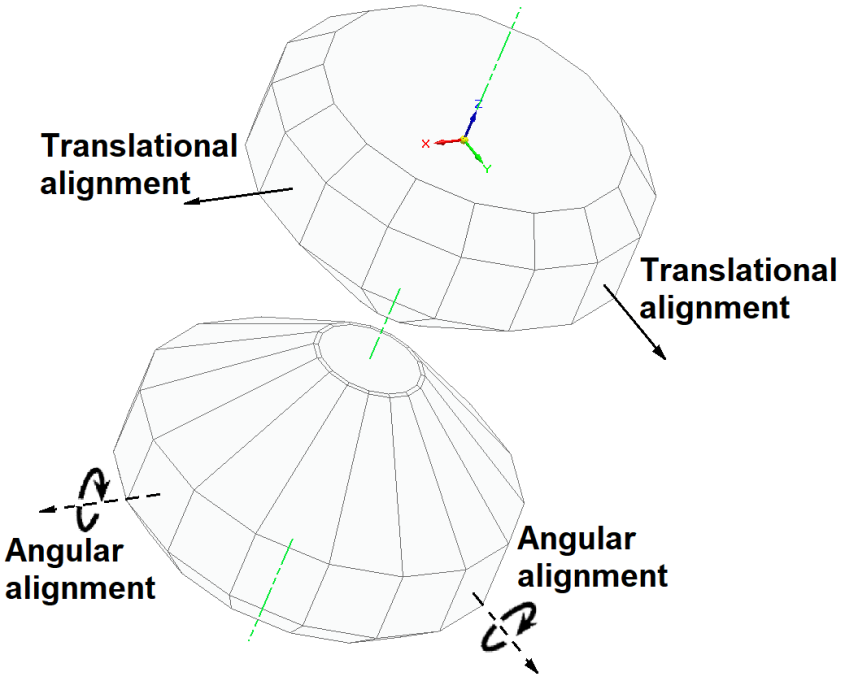

Figure 5.12: Diamond alignment. The green line represents the *P* cell axis. The diamond bases and culets lie on the XY plane while the Z-axis illustrates the axis along which DAC operates.

The parallelism as it may be noted in figure 5.12 relies on the angular alignment only while the lateral alignment is responsible for bringing culets together. Some DACs do have the angular alignment mechanism but in the proposed design (See figure 5.3) the parallelism relies on the thrust mechanism, machining and diamond glueing to the backing disc quality leaving only the need in producing the translational alignment. To produce it, the backing disks with already glued diamonds were fixed to the plates with 3x grub screws. While keeping one of the discs fixed the other one was adjusted under the microscope until the gem culets became aligned and concentric by rotating the disc and by adjusting the grub screws. The machined in the backing discs 62° angle which is normally made to produce diffraction experiments, simplified the alignment procedure since it provided better optical access for light and eyes, not to mention the further need in accessing the sample and contacts quality. Although the translational alignment seemed easy to be done, the main difficulty was associated with glueing the diamond to the backing disc with good parallelism and took several attempts. Another problem was associated with diamond damage risk since alignment requires culet close contact and special care must be taken during this process to avoid any impacts.

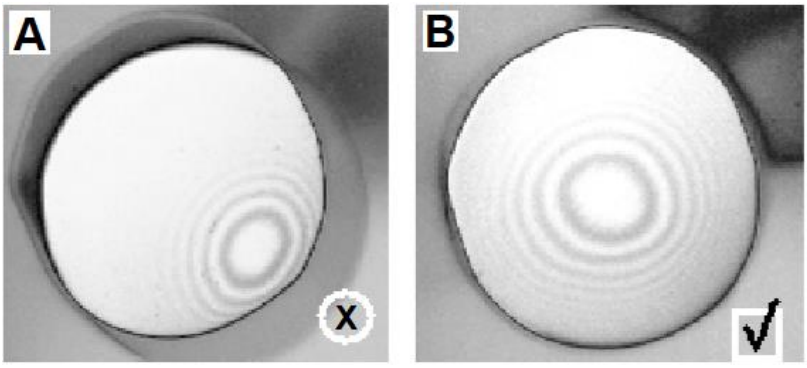

Figure 5.13: Interference fringes. With: A – poor translational alignment and B – an example of good alignment with interference pattern that indicates that the difference in parallelism between culets is less than 0.001 mm [54].

The ideal alignment scenario (See figure 5.13 – B) is hard to achieve with DAC that has no angular alignment mechanism and, therefore, some level of allowance is accepted especially for the DAC that operates below the megabar ranges.

5.6.3 Insulation of other components

The insulations of other components such as the body surfaces of the plates as well as the incorporation of insulating blocks on the cell sides were implemented to avoid short circuiting possibilities as well as to simplify the *R* probing procedure and provide some support for the wiring.

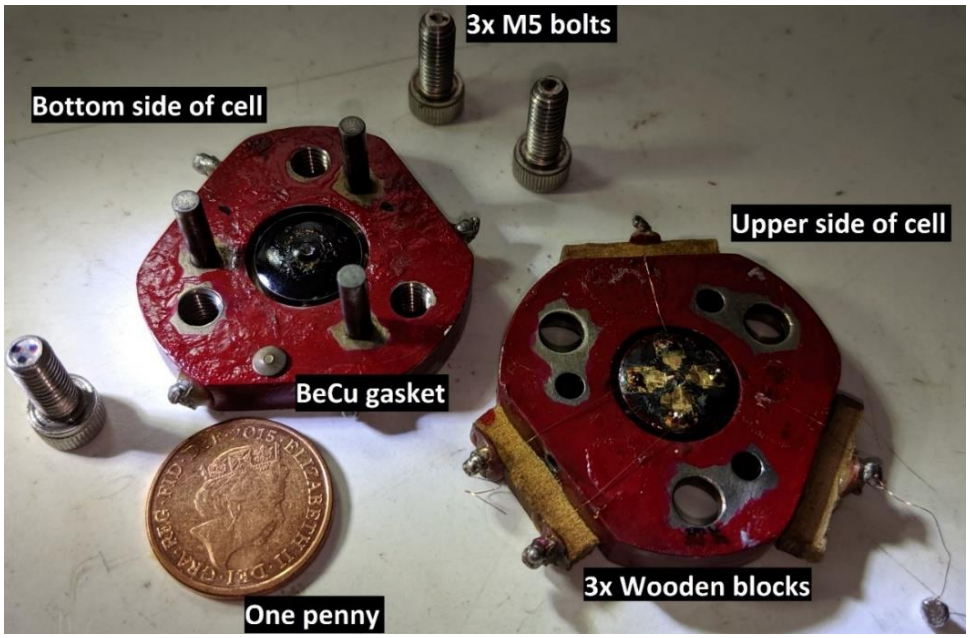

Figure 5.14: Disassembled DAC with insulation. Parts are named and the one penny coin is depicted for a sense of scale.

The cell surfaces were insulated with the help of the nail polish (red colour) and the insulating stations in the form of the wooden blocks were glued to the cell sides. These were used to fix the furthest from the diamond wire junctions from the metallic cell body as it was discussed earlier in the design considerations section of this chapter.

5.7 Experimental testing

The first tests on the DAC were performed to investigate if the NiCrAl backing discs won't plastically deform under 12.5 GPa and, therefore, gasket and cell insulation, as well as the wirings, were not yet implemented. The DAC was cycled up to the previously mentioned HP and showed no degradation in both alignment and material yielding even when tests were combined with *T* changes in the +/– 80° C range. While the alignment check required only the microscope to access its quality, the yielding check demanded epoxy removal since the surface under the diamond was not visually accessible. After careful examination of the backing discs, there were no deformations found which led to the conclusion that DAC can be safely operated, especially up to the 10 GPa if maintained well and regularly checked for the alignment and hardness of the epoxy resin. Last was found to weaken with time due to the use of alcohol-based solutions for diamond cleaning purposes.

It was also required to test if the DAC can be used for electrical measurements. A total of 4 non-insulated Cu wires were glued to the upper side of the DAC (See figure 5.14). Four-wire ends were pulled out to the sides where they are soldered to the metallic surfaces which are separated from the cell body with wooden blocks and another four wire ends were brought as close as possible to the diamond and then soldered to the tiny metallic discs which are glued to the black epoxy. From those stations and up to the anvil (See figure 5.15 – A) the gold contacts were sputtered through a custom-made mask using a sputter coater. The bottom cell part was equipped with insulated gasket with ruby and sample. The 4-iodobenzonitrile in the form of a white colour powder was slowly loaded into the gasket hole until was packed with another cell part. Lastly, the Daphne 7373 oil was added as PTM. The electrical *R* of the sample was measured using a 6517A electrometer using the constant voltage method up to the 7.6 GPa. At just above 5 GPa the expected drop in

sample *R* was observed (See figure 5.16) which was also well accompanied by the darkening of the sample.

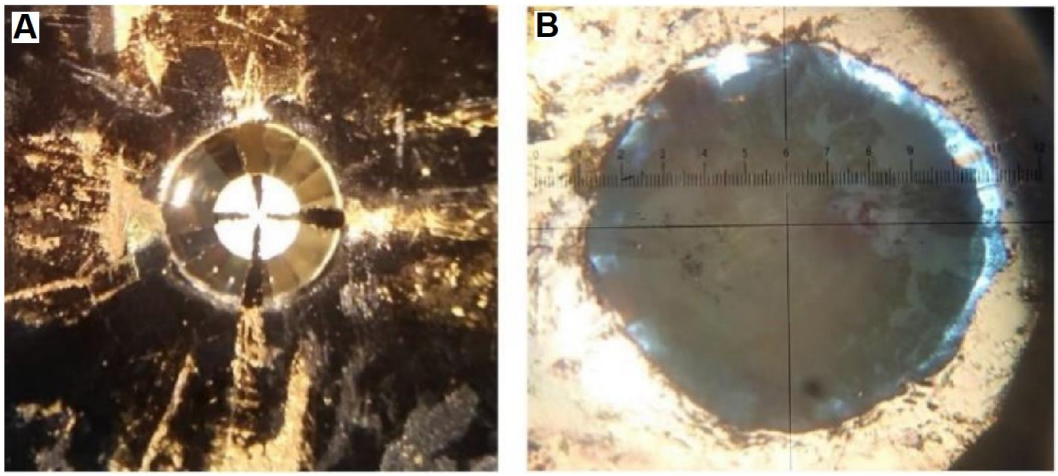

Figure 5.15: Test measurement. With: A – Diamond with gold-sputtered contacts (no sample) and B – sample within a gasket hole at 5 GPa. The PVC layer is seen in the transparent light blue areas between the inner gasket hole and sample. Please refer to the 7th chapter for more details regarding the gold contact sputtering.

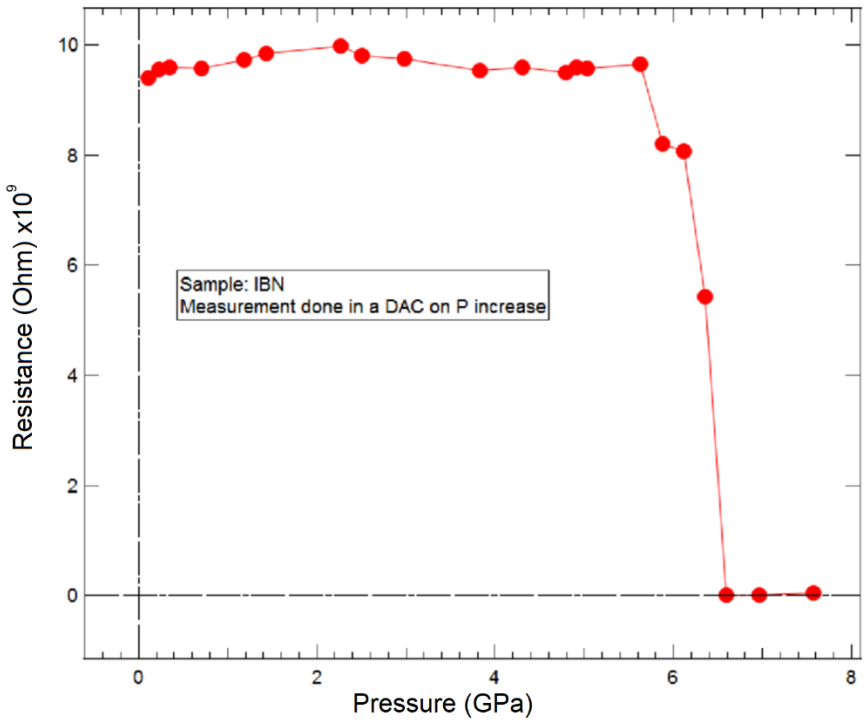

Figure 5.16: The *R* of polycrystalline 4-iodobenzonitrile as a function of *P*. A drop from 10^{10} to 8×10^{9} Ω occurs at the phase transition. The precipitous drop beyond 6 GPa comes from interference from the gasket.

More details about the test sample material and its conducting mechanism can be found in [211]. These are not provided here since the main goal of this thesis was to

work with materials which are listed in the 2nd chapter of this thesis and are having low *P* changes in electronic behaviour.

Although the DAC did not reach the 10 GPa, considering the above it was decided that DAC was ready for the experiments with *R* measurement on the PR materials since it already expanded the *P* scope above 3 GPa.

Chapter 6

Development of UHPC

This chapter is dedicated to the development of UHPC for *R* measurements and starts with the requirements and reasoning. Further, the design considerations are outlined along with the device operation principle based on which the final design was developed. The UHPC was designed to produce both static and dynamic *P* applications depending on the employed components. At the end of this chapter, the manufacturing, assembly and experimental testing of the UHPC are provided.

6.1 Requirements and reasoning

6.1.1 Pressure limit

The uniaxial high-pressure cell (UHPC) compresses the sample along the single axis (usually the vertical). It is employed when non-hydrostatic conditions are required (See figure 3.7) to study the sample material in a certain direction. In this case, the direction of interest is vertical as per the OPET device concept (See figure 1.3) which also played an important role in the choice of PR materials, more precisely, their conducting mechanism to allow the piezoresistive applications. As a result, materials were PVDed to grow their conducting needles in a specific direction. For more information please refer to the 2nd and 3rd chapters.

Since the UHPC should mimic the final device operation (See figure 1.3) it must be able to reach at least 3 GPa of *P* – the upper limit of *P* within the suitable OPET application range (See 2.2.1 section in the 2nd chapter). Since the *P* is not of a hydrostatic character there would be no PTM employed which simplifies working. It is, however, worth to note that the UHPC must be designed in such a way that it would be able to produce both static and dynamic experiments. Static ones to probe the initial thin film sample behaviours and dynamic ones to examine how cycling affects thin films and if the high-speed *R* response follows the actuation and relaxation of the indenter. Since the thin film sample thickness is so small a special device is required to produce the dynamic experiments – the high-performance PE actuator which was previously mentioned in the 1st chapter of this thesis (one of the key components in the OPET device concept).

6.1.2 Sample dimensions

Considering the above said the materials which are to be tested in the UHPC are all the thin film type. To allow probing their electronics behaviour the contact configuration should be as in the concept shown in figure 3.6. The goal is to measure the change in *R* between *Pamb* and *Pelevated* through the film so it can be converted into ρ using equation 3.2. Therefore, it is hard to say anything specific regarding the sample dimensions except for some general thoughts. For example, the thin films

should have enough surface area to produce several experiments with an indenter being placed at different locations since the PVD takes a lot of time to produce a thin film. A rough estimate for the sample dimensions can be at least 10 mm in diameter but not exceed 15 mm to allow its fitting into the PVD system (See figure 2.6).

The height of the thin film is not a criterion here since it can be adjusted by the thickness choice of the substrate material to fit into the final system. Generally, the quality of the thin film is more important than its size since it should provide the homogeneous thickness of sample across the surface area, good sample adhesion to the gold and good gold adhesion to the substrate. Although the slip problems are not expected as the *P* is applied along the vertical axis resulting in uniaxial compression, the adhesion should be good enough to allow attaching the side contact to the gold layer with silver paint.

6.2 Design considerations

6.2.1 Pressure application

Since the main goal of the UHPC is to allow both static and dynamic experiments to be employed, its design and mechanism must take this into account. While the static *P* mechanism is relatively flexible in terms of implementation, the ability to produce dynamic experiments becomes the key driving parameter of the design. Therefore, the clamp designs and locking mechanisms that involve threaded components are not desired and the upper part of the UHPC should allow the piston/indenter to move/slide freely in the vertical direction.

To mimic the device concept (See figure 1.3) it was decided to employ the high-performance PE actuator of a larger scale which would have enough pushing force to produce the required *P* on the thin film. Therefore, the cell body and other components should be built around the dimensional specifications of the employed PE actuator – P-840.4 [212].

The idea of the operation is as follows: the static part of the actuator is fixed into the cell body while the dynamic head which can be coupled with the indenter produces compression on the thin film. Please note that the actuator is twisted upside down

(See figure 6.1) which simplifies the thin film positioning as well as allows to couple actuator with the conventional hydraulic press by fixing actuator on top. This would also allow producing additional *P* on the thin film if needed. The proposed operation concept implies the fact that the cell body needs to have vertical throughout hole with open ends.

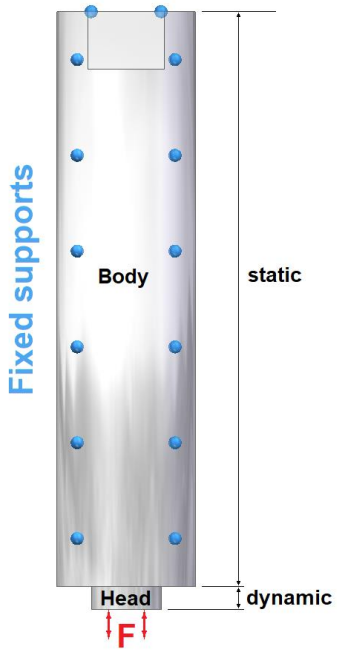

Figure 6.1: PE Actuator operation principle. With static body which is fixed and dynamic head which actuates pushing force. Please note that red arrows are pointing in both downward and upward directions to illustrate that the head can move in both.

For the static experiments, the PE actuator can be replaced with the solid steel component of the similar with actuator dimensions. This would allow building single UHPC body which can be coupled with both components depending on the experiment preferences (e.g. static or dynamic) and in case of the static experiments apply *P* on the thin film directly with the hydraulic press.

6.2.2 Pressure measurement

Since the desired *P* in UHPC is not of a hydrostatic character, the easiest way to determine it would be to equip the UHPC with the load cell which has good response speed to the static and dynamic compression loads and must be located under the thin film. The load cell would allow to precisely convert the load from the PE actuator or the hydraulic press into the measurable electric current. Prior to experimental

exploitation, the load cell needs to be calibrated. This would allow to precisely determine which output parameters (e.g. mV) corresponds to which force. Knowing force and the cross-sectional area of the indenter, the *P* can be easily calculated with equation 3.4. There are various types of load cells for various load ranges however the key factor is the output sensitivity since it would allow collecting more mV and, therefore, *P* points to construct them against the observable *Rs*/*ρs*. It is worth to note that the weight of the PE actuator or its dimensional imitator for the static experiments along with the weight of the indenters would already produce small *P* on the sample and it will be possible to measure only the close to the *Pamb R* of the thin film. However, for the relatively large cross-sectional areas of the indenter, this weigh can be negligible.

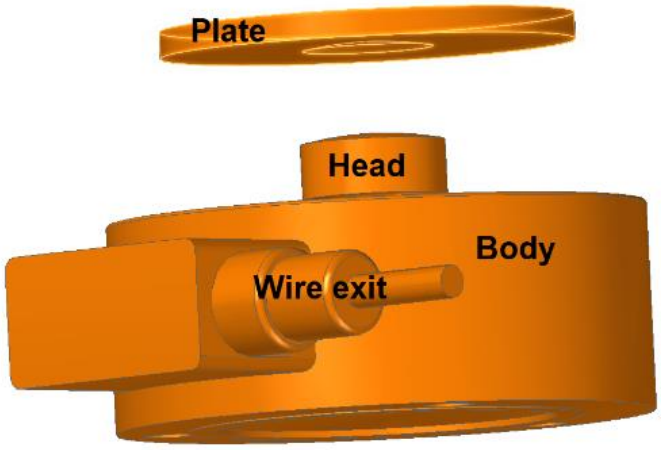

Figure 6.2: Load cell model. Conventional load cells with cambered head and concave plate to sit on it. Please note that the head, body and wire exit components cannot be disassembled.

In case if the sample will be very sensitive to the *P*, the hydraulic press and the load cell device can be omitted and replaced with a set of weights with manual loading procedure. This is especially important if the load cell sensitivity is too small to monitor initial R / ρ changes in response to the applied load.

6.2.3 Insulation

The general idea to probe the *R* of the thin films was well explained in figure 3.6 where the top contact is the indenter and the bottom contact is the Cu wire which is interconnected with a thin layer of gold. The recently discussed sample dimension requirements (which are relatively big) allow employing insulated Cu contacts to

connect the thin film with *R* probing devices. To further minimize the short-circuiting risks the plate of the load cell (See figure 6.2) which is conventionally made of steel needs to be separated with a thin insulating material from the thin film's substrate because last was found to pick up particles of gold during the sputtering process. Rest of the UHPC parts require no insulation since they all can be used as a probing point of the top contact.

6.2.4 Parallelism and indenter

Due to the very small size of the thickness of the deposited-on the gold material, it is important to properly align its surface with the surface of the indenter. The use of the WC ball was previously employed as an indenter to produce thin film ρ studies on the PR material [30]. Although the use of the ball geometry greatly minimises the shirt circuiting chances through the sample layer into gold since the ball has no sharp edges, it implies the high difficulties in controlling the cross-sectional area (See figure 6.3) to make the *P* scalar in accordance with equation 3.4.

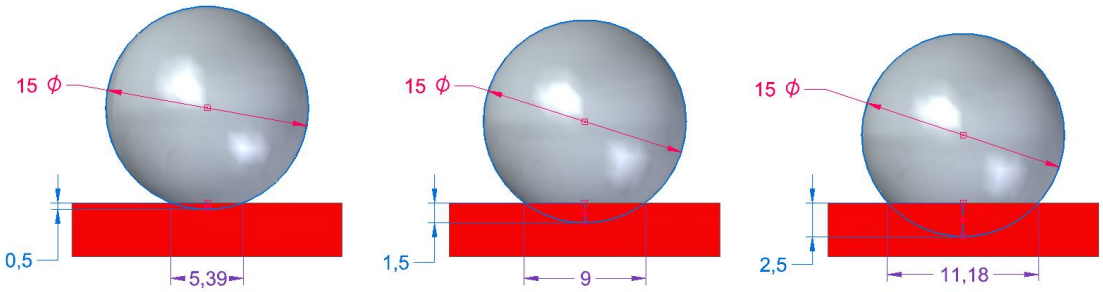

Figure 6.3: WC ball penetration. With grey WC ball and red sample. Dimensions are not to scale but for the demonstration purposes. From left to right: the WC ball of the same diameter (e.g. 15) penetrates the sample as a result of applied uniaxial force by 0.5, 1.5 and 2.5 which implies the change in the cross-sectional diameter which becomes 5.39, 9 and 11.18 respectively.

Since it is hard to predict which force would lead to which indentation value in the thin film (especially for the small thicknesses), the diameter and, therefore, the area of the cross-section becomes an unknown parameter which is hard to control.

Therefore, to precisely evaluate the *P* it is required to have the fixed value of the cross-sectional area which implies the existence of the sharp edges and, therefore, a necessity in the proper alignment of indenter with respect to the sample surface to avoid short-circuiting problems.

To accomplish both goals the indenter of the ball shape with the polished to the fixed value cross-section area can be employed with the ball bearing-alike indenter holder. The holder would allow rotation and, therefore, self-assembly of the ball's cross-sectional area with the sample surface (See figure 6.4).

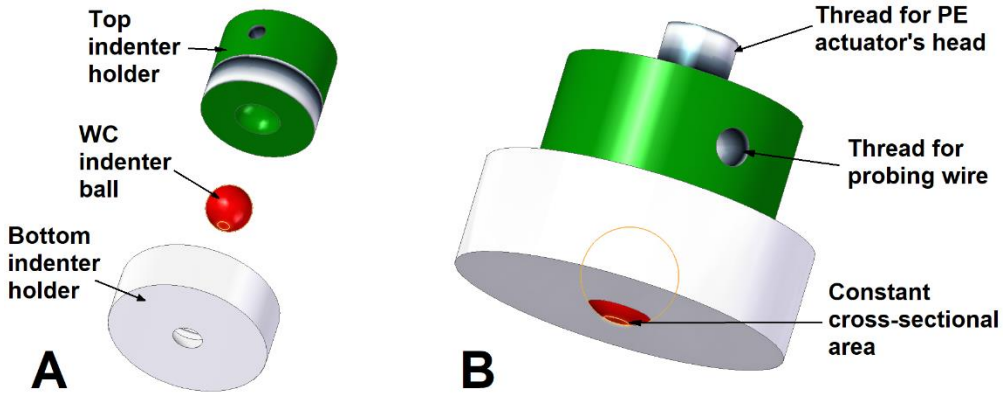

Figure 6.4: Indenter and its holder. With: A – exploded view with the corresponding part names and B – assembled version with key element details.

The top and bottom holders would be responsible for keeping the indenter ball within the circular recesses which are allowing twisting of the ball (See figure 6.4). Indenter holders should also be able to easily engage with each other with the help of a threaded connection and, also, the top indenter should have the ability to be interconnected with PE actuator's head. To further improve the concept the small thread for probing Cu wire can be introduced to simplify the *R* probing necessity. This would allow to securely/mechanically connect one of the non-insulated Cu wire ends into the shown in the figure threaded hole while the other Cu wire end being interconnected with the suitable *R* monitoring apparatus.

6.2.5 Materials

Since the *P* has the uniaxial character, the involved in the design materials should be able to cope with the compression extremes only. The cell body can be made of any soft metal such as aluminium (Al) since it barely participates in the experiment while the indenter holders and the bulged bolt can be made of SST since these parts are participating in force translation to the WC ball. The WC was chosen for the indenter since it is a conductive ceramic with high compressive strength which would allow having a safety margin in further cross-sectional area decreases which might be

needed to increase *P* the thin film is subjected to. For the thin insulating layer that is separating substrate and the load cell's plate, any conventional high-density plastic such as Polyetheline (HDPE) can be employed since the translated to its surface stress would be small due to the relatively big area of the substrate.

6.2.6 Other considerations

It is required to keep all the above-mentioned parts within UHPC by the means of a cell body. It was previously mentioned that the cell body needs to have vertical throughout hole for the PE actuator's vertical movement. To further improve the design, the cell body can be coupled with the load cell, so it becomes immobile. This can be achieved by clamping the load cell circumferentially or by screwing it into the base of the cell body (given that the employed load cell was made to have such a capability by the manufacturer). Another important advantage of keeping the load cell attached to the cell body is the lack of need in the translational alignment of the load cell with respect to the indenter. Also, by keeping all the parts within the UHPC's cell body, the whole system becomes a single unit which is simple in handling and transportation.

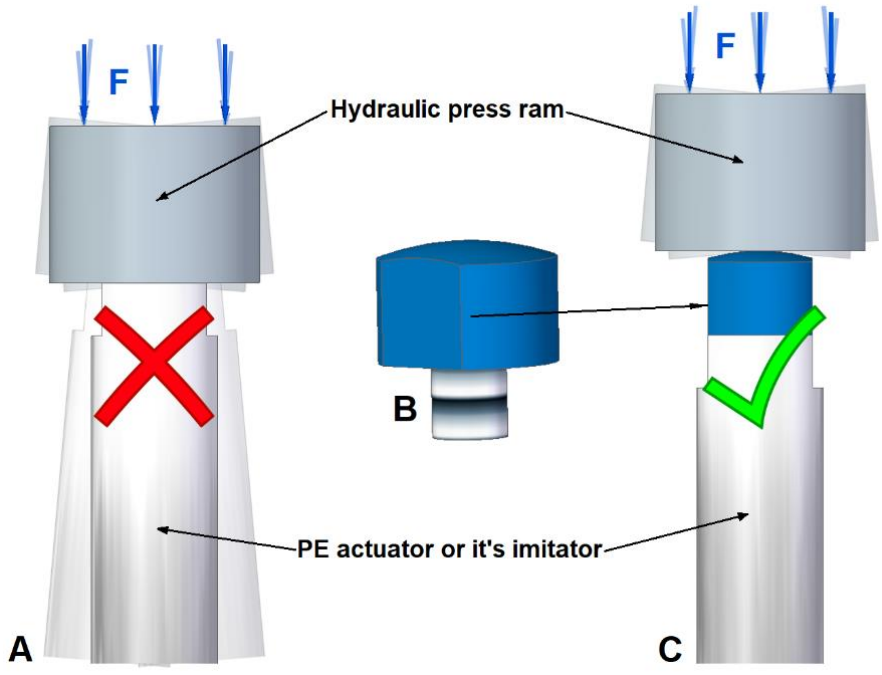

Figure 6.5: Alignment of the actuator. With: A – flat connection, B – bulged bolt and C – bulged connection. Red cross and green tick are illustrating the bad and good scenarios respectively. Please note how much y-axis deviation exists in the case of a bad scenario.

To make sure that the PE actuator or its imitator is sliding within the cell body's bore vertically only, the bore needs to be greased. This would highly minimise the friction between surfaces of the named parts. To further minimise the risks which are associated with the potential bore damage as a result of the applied load with the hydraulic press, the PE actuator and its imitator must be equipped with an additional component which will separate them from the hydraulic press ram and would eliminate the flat connection and, therefore, the possible y-axis deviations providing only the ideal vertical movement along the axis of interest. Such a component must be fixed into the PE actuator or its imitator and be equipped with the circular bulge (See figure 6.5 – B) to provide self-alignment of the sliding elements in the bore with respect to the hydraulic press ram.

Since it will be hard to predict how parallel will be the key components of the overall design within the hydraulic press system, the introduced into the design bulged bolt would significantly improve the quality of the overall uniaxial *P* concept and eliminate any possible damage to the cell body's bore.

In view of the foregoing the overall height of the UHPC would include the heights of PE actuator (See figure 6.1), load cell (See figure 6.2), indenter and it's holder (See figure 6.4), thin insulating layer (to separate load cell's plate from the substrate), thin film sample, cell body base (to attach load cell into it) and the bulged bolt (See figure 6.5 – B). It is therefore required to make sure that the overall height of the assembled UHPC would not go above the working height of the available hydraulic press.

6.3 Final design

For static *P* experiments, especially those which are not involving the hydraulic press, it was found that the addition of the small weights on top of the PE actuator's imitator is producing unwanted rotation of the moving element and, therefore, the indenter around the z-axis (See figure 6.6). Even the small rotation was found to cause damage to the thin film in the form of scratches through the PVDed layer into gold layer/substrate which was well supported by the inconsistency between experiments in terms of observable trends not to mention the later inspections of thin films under the microscope.

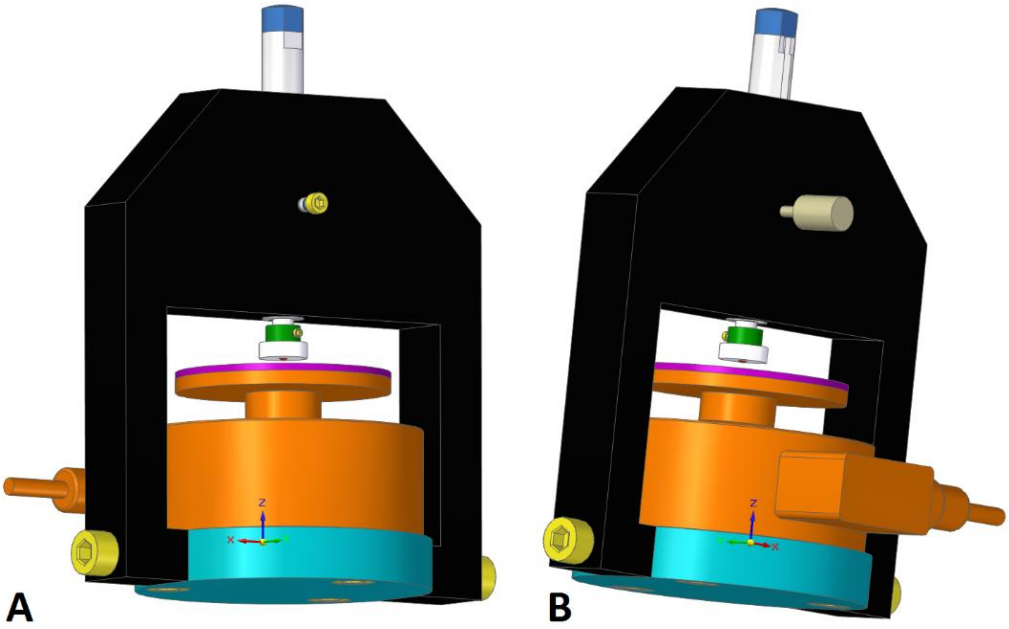

Figure 6.6: The UHPC. With A & B showing cell from different angles which can be noted by observing the included coordinate systems. Parts are coloured: black cell body, cyan base, orange load cell & load cell's plate, purple insulation plate, blue bulged bolt, khaki guiding pin, yellow bolts, grey PE actuator or its imitator, green top indenter holder, white bottom indenter holder and red WC indenter. The more detailed drawing of indenter's assembly can be found in figure 6.4. Dimensions of parts can be found in Appendix C.

The problem was overcome with modification of the PE actuator's imitator which was equipped with the hollow channel along the vertical axis and the introduction of the guiding pin (See figure 6.6 – B) which goes through the cell body into that hollow channel preventing the moving element to rotate and guiding it along the vertical axis during the *P* applications.

Another small addition was the introduction of the clamping bolt which can be noted in figure 6.6 – A. It is responsible for clamping the moving element to the cell body which was found to be an advantage during experiment preparations since it allowed to align the desired indentation location on the thin film with the indenter without the necessity in holding the whole moving element. The precise positioning allowed to employ the same thin film for several experiments which saved both time and money on the creation of new thin films.

6.4 Manufacturing

All parts of the UHPC (See figure 6.6) were made using a conventional machining process except for the WC balls which were ordered from Dejay Distribution

Limited [213] and the load cell from the AEP transducers [214]. It was decided to order several WC balls to be able to produce several cross-sectional areas and employ the most relevant (e.g. big or small) depending on how the sample behaves. WC balls were grinded and hand polished to a total of three (for now) cross-sections: 7.16, 0.53 and 0.337 mm^2. The largest cross-section cannot be combined with the bottom indenter holder (See figure 6.4) since its working height does not allow this, however, it is lighter (due to reduced amounts of material) and, if pushed into the top indenter holder, it won't fall out.

Figure 6.7: WC ball polishing. With: A – big fossa in the centre after grinding, B – smaller fossa and C – final shining cross-section. The WC ball sits in the recess in the metal plate which allows applying more force on the ball during the hand polishing process. The excessive WC material particles can be seen in A and B.

The WC balls were machined using the grinding wheel however this led to the fossa in the middle of the cross-sectional area (See figure 6.7) which must be flat to succeed in the experiment. It was decided to try to get rid of the fossa using the hand polishing and the silicon carbide paper which was employed in the following paper order: P800, P1000, P1200, P2000 and P4000 with last being the finest available. It was later determined that even this technique did not light up the expectations by inspecting the indentations on the thin films which were subjected to high and low *P*. The low *P* indentations were found to have fossa and it was decided to order the custom cut WC balls.

The thread for probing wire in the top indenter holder (See figure 6.4 – B) was found as a non-ideal interconnection with Cu wire since it used to tear off the wire during the bolt tightening process. Instead, the Cu wire was soldered into the threaded hole directly.

6.5 Assembly

An assembly of the UHPC (See figure 6.6) was found to be a relatively easy process. The further provided assembly order is given as a general guideline because it is only related to the static experiments that require a hydraulic press and a load cell:

1) The load cell was screwed with 3x M8 bolts to the base and base was screwed with the 2x M8 bolts to the cell body.

2) Load cell's plate was put on the load cell along with the insulation plate.

3) The bulged bolt was screwed into the PE actuator's imitator which was then inserted into the cell body's bore until it touched the insulation plate.

4) The thread for probing wire in the top indenter holder was fulfilled with liquid solder and Cu wire with the non-insulated end was inserted into it.

5) The PE actuator's imitator was lifted within the bore to screw it into the top indenter holder. Since the holder is equipped with the Cu wire it was reasonable to rotate imitator rather than holder to avoid wire twisting.

6) Using the M4 bolt the PE actuator's imitator along with all which was already interconnected to it was lifted in the bore and clamped to the cell body.

7) The WC ball was inserted into the top indenter holder with cross-section being facing downwards.

8) If cross-section allowed, the bottom indenter holder was screwed onto the top indenter holder. The sliding element was unclamped from the cell body using an M4 bolt.

9) The hollow channel of the PE actuator's imitator was aligned with the hole for guiding pin by the means of rotation of whole sliding element and guiding pin was inserted into the corresponding hole.

10) The sliding element was clamped again to the bore with the M4 bolt at the required height to allow the thin film positioning.

11) The UHPC was placed on to the worktable plate of the hydraulic press with bulged bolt facing the hydraulic ram.

12) Lastly, the load cell was interconnected with the voltage source to supply DC voltage to the input leads and multimeter to monitor the signal between the output leads.

Depending on the experiment preferences, as it was previously said, some parts of the device such as a bulged bolt, load cell and a guiding pin can be omitted. Also, the imitator might be replaced with the actual PE actuator for dynamic experiments.

6.6 Experimental testing

Before the cell assembly, it was first required to test if the WC ball rotates within the top and bottom indenter holders (See figure 6.4) to find out if the cross-section of the WC ball would self align with the surface of the thin film. By producing a set of tests it was found that ball can easily rotate within the holders (as long as no dust or other particles are trapped between the colliding surfaces indicating the necessity in regular cleaning) and is capable of self-alignment against any flat surface if it already, to some extend, is facing it with a cross-section. Cross-section, therefore, requires to be positioned in such a way that it is already facing the flat surface (even at an angle) to further become ideally parallel at an impact with it.

Once the UHPC was assembled it was decided to avoid impacting the thin film surface with the sharp edges of the WC balls to avoid any scratch probabilities. Instead, it was decided to first align the cross-section with any flat material such as sheet glass. The experimentally derived load of 30 MPa on the glass was sufficient enough to achieve the final parallelism of WC ball’s cross-section with the surface of the further employed thin films.

During experiments with the thin films, it was found that WC ball sometimes picks up deposited material (See figure 6.8) which indicates the necessity in cross-section cleaning before accessing the new indentation areas on the thin film to avoid increases in the overall testing thickness of the material.

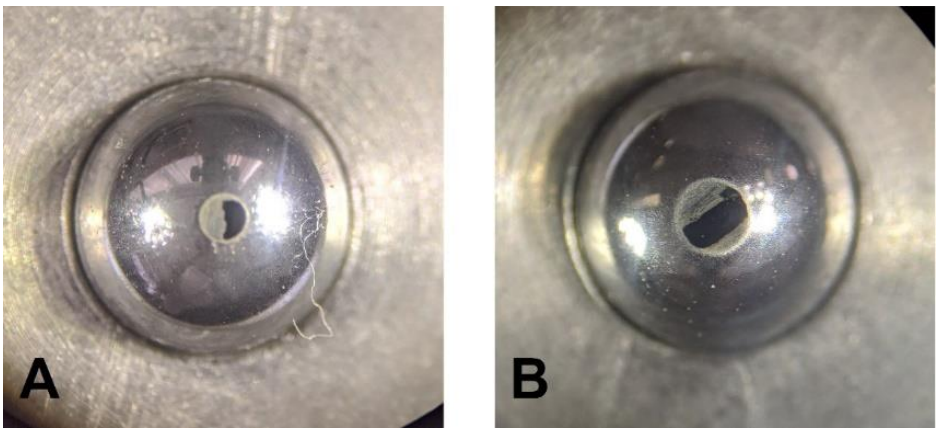

Figure 6.8: WC ball with the material on a cross-section. With A & B demonstrating 0.337 & 0.53 mm^2 cross-sections respectively. Black colour on top of the cross-section is the picked up from the thin film material.

However, these were the self-cut WC balls which also implied the probability of uneven surface compression. It was later found that this was indeed the case and, to some extend, was also associated with the material adhesion to the gold layer of the substrate issues.

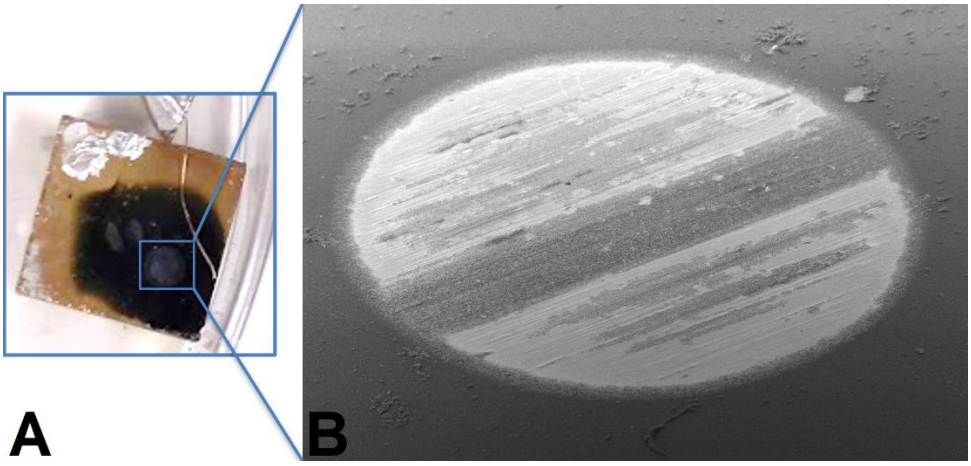

Figure 6.9: Thin film impact site. With: A – a thin film with indentation area of 7.16 mm^2 and B – its 37x magnification.

As it can be noted in figure 6.9, the impact site shows signs of uneven compression which means that the collected *R* data has no scientific value. This, however, was found to be the best achievable result with the self-cut WC balls (across all cross-sections) which only at *Pelevated* was providing the shown in figure 6.9 – B circular indentation shape. At lower *P* the impact shape looked like a ring with fossa (untouched material) in the middle of it.

Chapter 7

HP measurements

This chapter provides full experimental details and techniques which were used to produce the HP *R* and *T* measurements in PCC and DAC, HP *R* measurements in UHPC and modified gasket pre-indenter as well as the *Pamb R* and *T* measurements on CPPs along with the employed instrumentation.

7.1 Gold sputter coating

The gold sputter coating was employed to produce a thin gold layer on the thin film substrates as well as on the diamond's cullet to create a single and multiple *R* probing contacts respectively using SC7620 Mini Sputter Coater [215] which allows controlling the thickness of the gold layer.

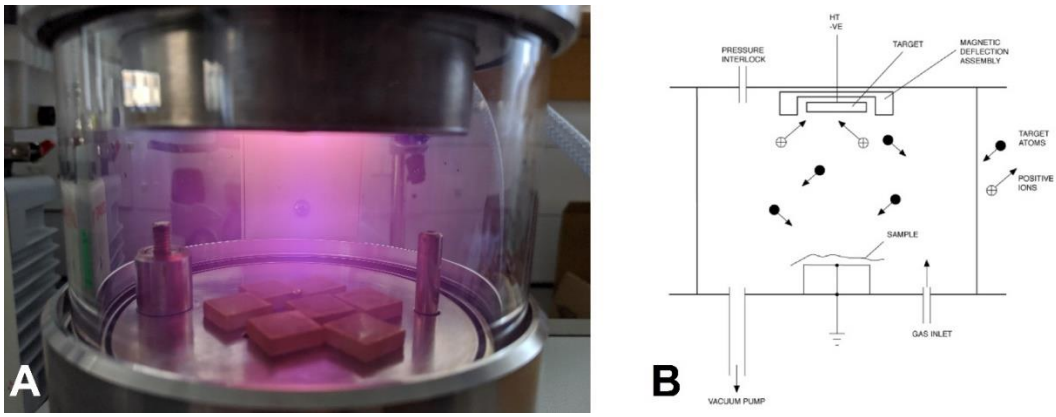

Figure 7.1: Gold sputtering on the substrates. With: A – seven 10x10 mm square substrates being covered with 45 nm of gold layer and B – employed sputter coater operation principle [215].

The vacuum pump creates the negative *P* inside of the chamber (value of which is dependent upon the employed target material). The high voltage is then applied between the base (anode) – on which the source is resting and the target (cathode). The target in the form of a thin disc sits inside of the magnetic deflection assembly which utilizes the magnet to confine the plasma within the target area. The gas inlet allows introducing the argon gas into the chamber which is required to provide a medium for ionization. Once the required plasma current is selected the sputtering process starts during which the target electrons (which are highly concentrated nearby the target due to existence of the magnetic field) are colliding with argon molecules and, as a result, form positive ions. These positively charged ions are becoming attracted by the cathode and bombard the target which causes its erosion. The target atoms are then falling towards the sample material in multiple directions since they are colliding with the ionized argon molecules on their path resulting in the homogeneous sample coating on all the exposed areas. The high voltage power supply for safety reasons cannot be activated until the negative *P* in the chamber has reached the specified in the device manual value due to the existence of the *P*

interlock. The lilac glow (See figure 7.1 – A) appears as a result of argon gas being discharged.

7.2 Resistance measurements

The *R* measurements were monitored using the most appropriate for the given observable value monitoring instrument in accordance with guidelines which were outlined in the 3rd chapter of this thesis with further conversion to ρ as per MM.

7.2.1 In the PCC

R measurements in the PCC were produced on PR samples which were made into the CPP of the appropriate dimension (See figure 4.1) with the help of the custom-made press (See figure 4.2) and the surgery blade (if necessary) to reduce CPP's thickness to 0.43 mm as per MM. The thickness reduction process took place under the microscope to make sure that the final thickness is homogeneous. Prior to producing the thickness reduction, the CPP was attached with non-conductive GE Varnish glue to the PEEK table (See figure 4.18 & 4.19) to restrict its motion. During the thickness reduction process, the thickness was checked/measured with the conventional callipers.

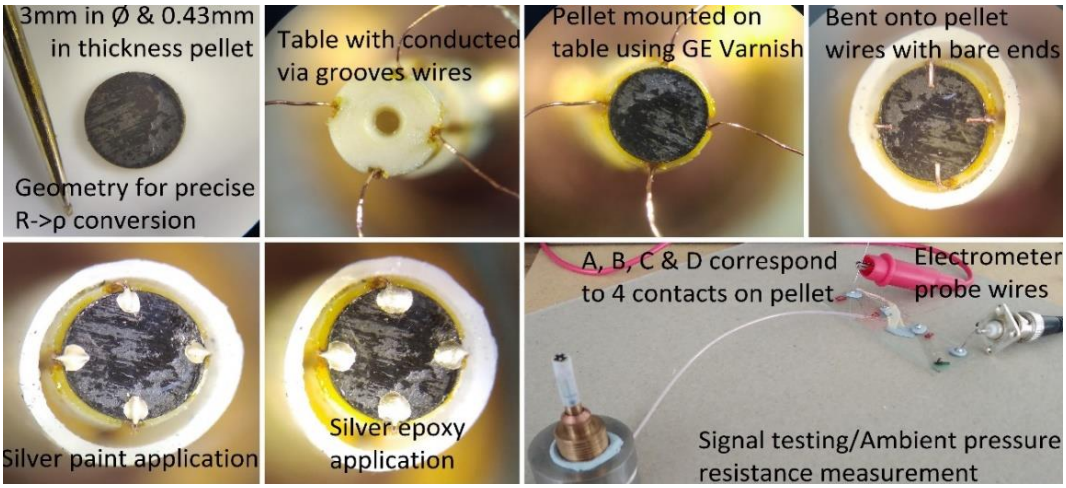

Figure 7.2: CPP mounting for PCC. Left to right, top to bottom stages with the corresponding comments.

The Cu wire preparation and management process in figure 7.2 are well explained with the help of the corresponding comments, however, it is worth to note that the

special care was taken during the wire end insulation removal as well as the wire bending onto the pellet processes since they posed a wire tearing and CPP cracking threats. Also, the non-insulated wire lengths which are bent onto CPP were made to not exceed the 0.4 mm to make sure that the contact distance to the tablet thickness relationship adheres. Both silver paints were employed to prevent contacts detachment from CPP's with silver paint being given ordinal preferences since it was empirically found to have higher penetrability and, therefore, better fastening as well as the smaller *R* compared to silver epoxy. It was important to let the employed silver paint fully cure prior to the silver epoxy application since it was found that the latter cures faster and former might not solidify underneath it. The main reason for silver epoxy employment was the necessity of having an additional layer of contact protection against PTM and PTFE tube as they greatly increased the chances of wires staying on the CPP during the experiment. The signal testing at *Pamb* was also followed with CPP insertion into liquid Parrafin, which solidifies at *Troom* and provides an extra level of contact protection against the above-mentioned threats.

7.2.2 In the DAC

Sample addition into the gasket hole

Sample powder addition into the gasket hole (See figure 5.7) is a process during which the well-grinded powder particles (See figure 7.3 – 2) are introduced into the upcoming HP environment through the hole in the PVC. Unlike in the PCC where the external device is used to make a CPP, in DAC the powder becomes compressed during the cell closure.

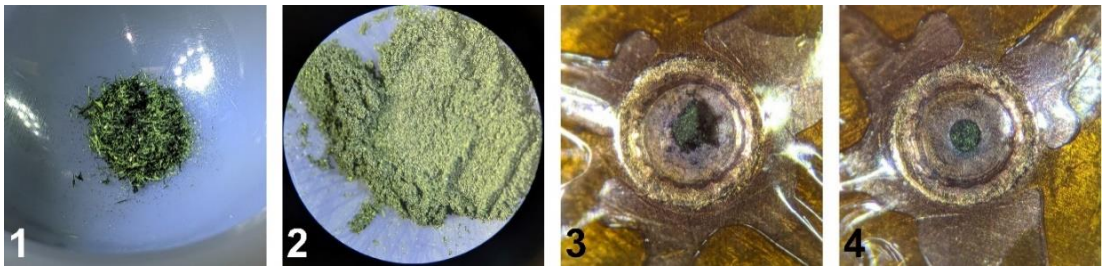

Figure 7.3: Sample addition. With: 1 – sample needles, 2 – well-grinded powder, 3 – sample loading with the excessive amount and 4 – final loaded sample.

The sample powder was introduced into the drilled hole with the help of a conventional needle and since it is required to introduce as much powder as possible, several powder addition cycles were required. Each cycle implies the sample addition which is followed by DAC closure without any force application and then reopening which allows pushing the powder into the reaction chamber with the help of the opposed diamond. Due to the small-scale (during powder loading) some excessive amount of powder used to stay around the hole on top of the PVC at the indented area (See figure 7.3 – 3) which is a problem since powder particles could become imprinted into the PVC and, therefore, may lead to insulation layer's damage. This was overcome by cleaning that area during each cycle before the cell closure with the help of the tiny amount of Blu Tack® [216] adhesive which was attached to the tip of the sewing needle. Stickiness and flexibility of the Blu Tack® were found to be good enough in picking up the material particles without damaging the PVC all around the hole (See figure 7.3 – 4). However, it is important to note that regardless of powder addition cycle quantity this process will not lead to the CPP product since greater *P* is required for it (at around 1 – 2 kbar). The necessity in having as much powder as possible being pushed into the reaction chamber is still a must to achieve some low-level of substance rigidity to avoid powder being washed away during PTM addition.

Gold sputtering on the diamond

The experimentally derived optimum thickness of gold contact on the diamond which belongs to the upper side of the cell (See figure 5.14) was found to be in the 35 – 45 nm range for the 35 μm thick PVC insulation layer.

Gold sputtering was found to be a complicated procedure (See figure 7.4) which requires patience and precision. First, the diamond was cleaned (1) with ethanol and the Blu Tack® was used to picking up small unwanted dust particles. After cleaning, the GE Varnish glue was applied to the diamond (2) and the surrounding epoxy area. It is important to make sure that glue has a low viscosity level (this can be altered with an addition/reduction of ethanol) to produce a thin layer on the diamond. The thinner the better since more gold will get onto the diamond's surface. During solidification of glue, 4x extrusions (3 & 4) were introduced in the glue with the help

of the WC thin needle to create a pattern for the probe wires. This process, however, leads to the formation of unwanted glue particles and other leftover materials in the extruded canals that must be cleaned preparatory to the sputtering process. The cleaning of these elements was performed with the Blu Tack® and the set of the custom-made tools. It was also required to cover the unwanted for the sputtering areas (5 & 6) to make sure that gold patterns do not overlap and are extended to the metallic discs which act as a junction between the sputtered gold and the non-insulated Cu wires which are connected to stations with solder. The upper cell body was then placed in the sputter coater (7) and covered with custom-made plastic cover (8) with a hole for sputtering access. Once the optimum thickness of gold was achieved (9) the paper layer of the mask was removed (10) and followed by removal of glue layer (11) to achieve four contact probes with no overlaps (12). Distances between the contacts were then measured and adapted for the pellet geometry to allow R into the ρ conversion.

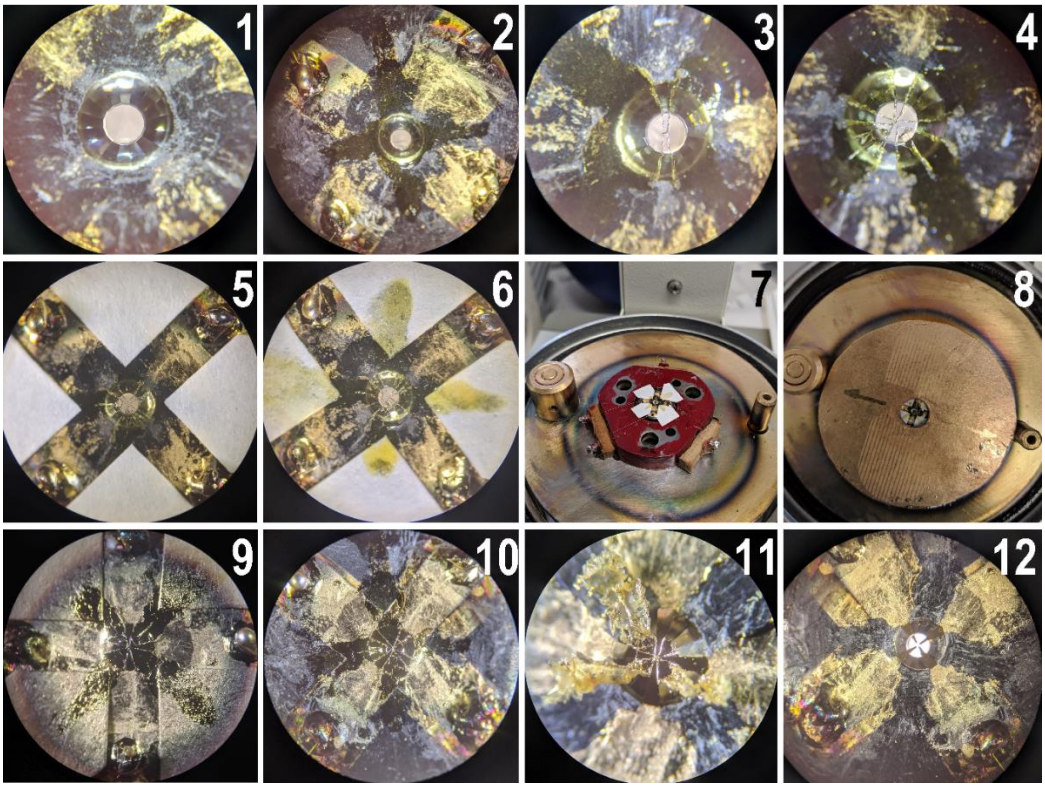

Figure 7.4: Gold sputtering procedure. Numbers 1 to 12 are representing execution order.

Figure 7.5 demonstrated how the deposited gold contacts are touching the sample material in the closed DAC configuration. Since contacts are deposited to the

diamond it is essential to have loaded enough material into the gasket hole to produce the *R* measurement on it.

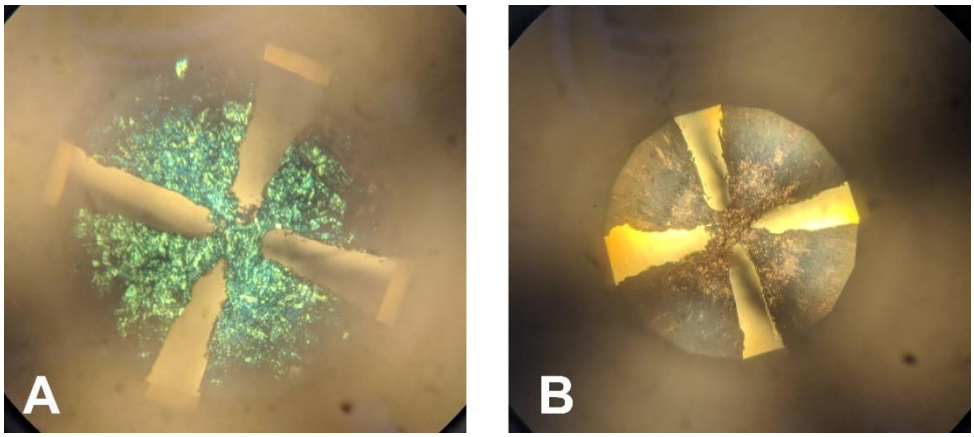

Figure 7.5: DAC gold contacts on the sample. With: A – at 2 kbar and B – at 20 kbar. Please note the sample colour change.

7.2.3 In the UHPC

R in the UHPC was measured through the thin layer of the sample using the 2-probe method with top contact being the WC indenter and the bottom contact being the deposited on the substrate gold layer.

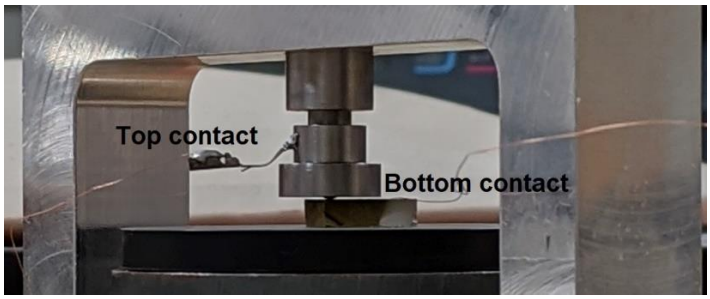

Figure 7.6: Top and bottom contacts in UHPC. Please note the gap in between thin film and the WC ball's holder.

Only two Cu wires were required to produce a measurement (See figure 7.6). The top contact was soldered to the metallic pad which is soldered to the WC ball's holder. This connection was found to be advantageous compared to the screw contact since screw thread used to tear off the Cu wire. The bottom contact was attached to the deposited on the substrate gold layer (See figure 7.1 – A) with the help of silver paste. The surface area of the gold was, for this only purpose, masked during the sample PVD process. The height of the silver paste is limited with the available gap

in between thin film and WC ball's holder. If the applied amount is in excess, the thin film must be positioned carefully to prevent direct contact (e.g. short-circuiting).

7.2.4 In the gasket pre-indenter

The gasket pre-indenter was modified to produce *R* measurements on the thin films (See figure 7.7) since the self-cut WC balls which were employed in the UHPC were found to have the uneven surface of the cross-sectional area after grinding and polishing in the form of the fossa and the pre-cut balls with a perfectly flat cross-sectional area for indentation were not available for delivery due to COVID-19 interruption.

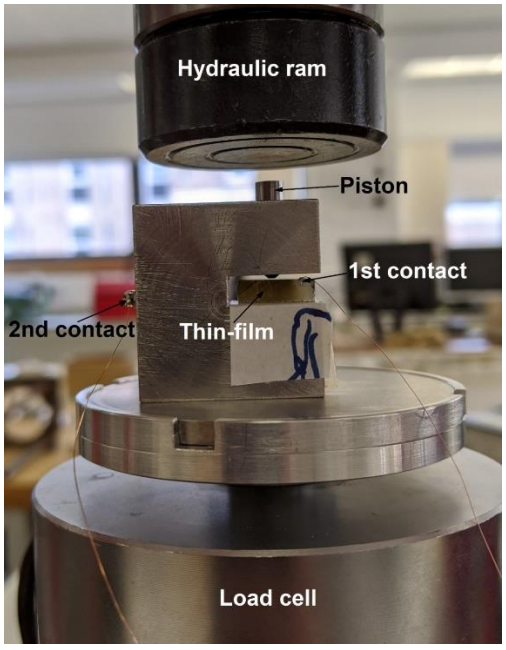

Figure 7.7: The modified gasket pre-indenter setup.

To produce the *R* measurements in the gasket pre-indenter the bottom piston was omitted since it was required to place the thin film on a flat surface inside of the pre-indentor's body. Prior to the placement, the thin layer of BeCu was compressed with the top piston to access the quality of the indentation. It was determined that the employed in the experiment piston with 0.28 mm^2 indenter head produces equal indentation in terms of thickness across the cross-sectional area. The metallic surface where thin film sits was covered with the layer of insulating paper to eliminate the shirt-circuit probabilities. The *R* was measured through the thin layer of PVDed

material of the thin film with a 2-probe method. The 1st contact point was attached to the sputtered gold layer on the substrate using silver paste and the 2nd contact point was attached to the cell body using the solder. Please note that the resistance reading between the WC piston and SST body is ≈ 2 Ω. The piston is in the tight configuration with the cell body and, therefore, some level of friction exists. This is a double-sided coin in terms of experiment quality. On the one side tight configuration provides a parallel arrangement of indenter's cross-sectional area with the surface of the thin film and, on the other, affects the precision of the collected data if the experimental load is not sufficient enough to overcome the friction. That was the case when the hydraulic press was omitted due to the poor cell's sensitivity for the employed in the experiment material (this sensitive material required more data points between *Pamb* and 110 MPa – the very first reading voltage on the load cell that can be quantified). Instead, the *P* application was performed with a set of small weights with known masses by stacking them on top of the piston. This must be considered when studying the *R* - *P* charts.

7.2.5 *Pamb* on CPP

The *Pamb R* measurements were produced prior to any cell exploitation since these were mainly produced to yield some initial information/general idea regarding the sample material. These were often combined with the *T* analyses to determine the *T* dependence on electronic properties (See figure 2.5). *Pamb R* measurements were performed on the CPPs with identical geometries as if these would be further employed in HP studies in the PCC to save time. Compared to the *R* measurement procedure for PCC, CPP for *Pamb R* measurements were glued to the glass slides with Cu contacts being attached to the CPP with silver paint only. The other Cu contact ends were extended to sides where they were interconnected with a blob of solder which was attached to the glass with Blu Tack® to simplify the probing procedure as well as to still be able to apply the MM for *R* into ρ conversion as it is shown in figure 7.8.

It was important to produce a total of four *Pamb R* measurements on a single CPP: R_{AB}, R_{BC}, R_{CD} and R_{DA} to determine if values converge and if the CPP is of good quality for further measurements in HP devices. Since, in most cases, the CPPs were

having *Rs* above the GΩ range it was assumed that the quality is acceptable if the observable values between those four *Rs* had identical first digit and same degree.

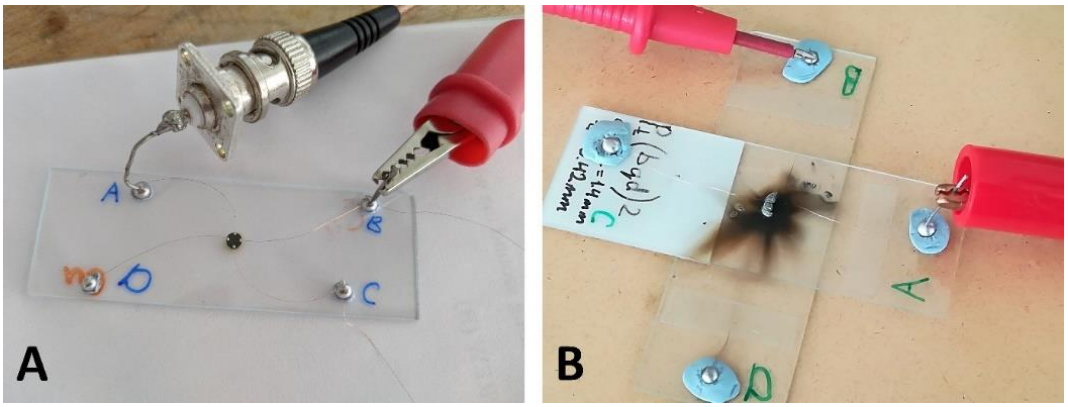

Figure 7.8: *Pamb R* measurement. With: A – measurement configuration and B – the burned CPP during the high voltage tests on the electrometer.

For example, if *R* readings were found to be as follows:

$$R_{AB} = 5.2456*10^9$$

$$R_{BC} = 5.8854*10^9$$

$$R_{CD} = 5.6564*10^9$$

$$R_{DA} = 5.7885*10^9$$

then, the CPP quality was assumed to be acceptable for further exploitation. However, since the Electrometer is capable of producing only two-probe measurements, it was decided to calculate the mean value of the *R* and to use the *R* of the contact pair which has the closest to it value for any further work with CPP.

Mean $= (5.2456*10^9 + 5.8854*10^9 + 5.6564*10^9 + 5.7885*10^9)/4 = 5.643975*10^9$ which is closer to the *R* in between contacts C and D and, therefore, R_{CD} is the reference *R* which will be further used in all upcoming experiments.

7.3 Cryogenic and low-temperature measurements

7.3.1 Closed cycle refrigerator

The Closed cycle refrigerator (CCR) system which is located in CSEC was made by SHI Cryogenics Group [217] and is capable of reaching 15° K at the specified by the

user cooling rate while measuring *Rs* of up to 3 samples simultaneously on the same *R* measurement device such as DMM by switching the channels. The measurement process is fully automated, and program-controlled through the LabView software which allows producing measurements while the experimenter is not around by logging the *R* and *T* data into the text file. The big chamber volume of CCR was found to be able to fit both PCC and DAC at the cost of the limiting the number of samples that can be tested to 1, however, such an instrumentation combination has not been produced. Instead, the *Pamb* measurement on a CPP was undertaken both on cooling and the heat up.

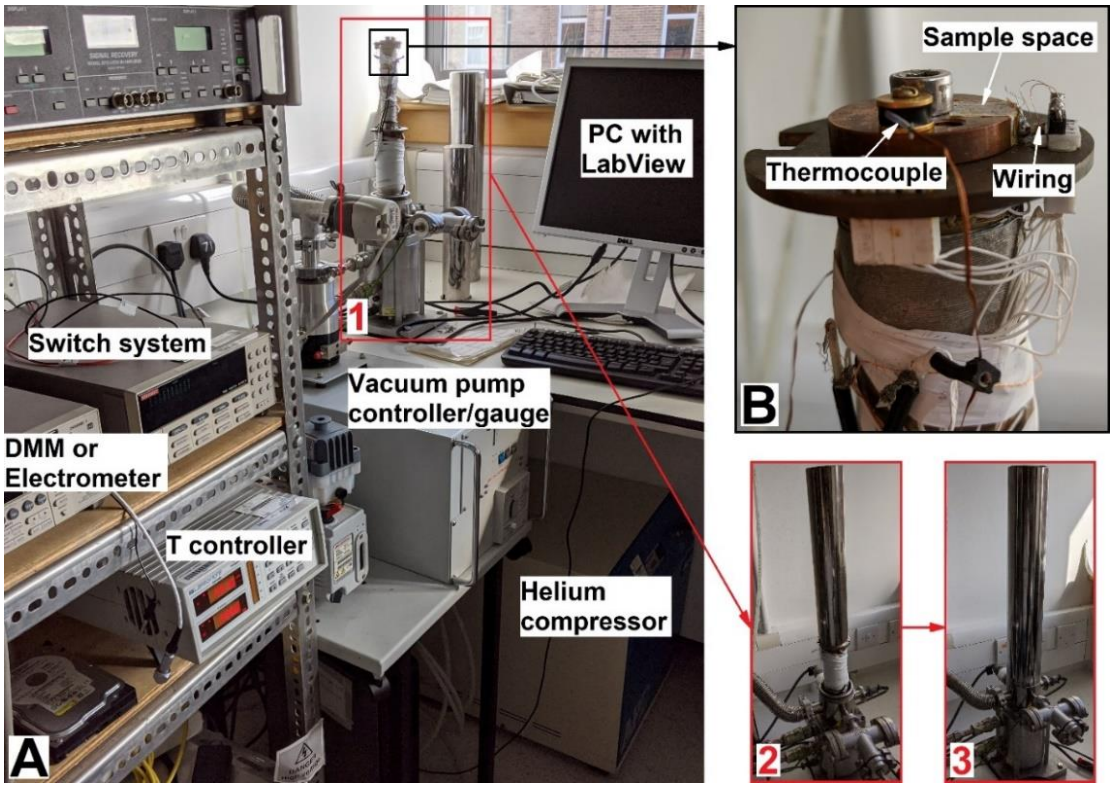

Figure 7.9: The CCR. With: A – Whole station with essential instrumentation and B – the magnified view of the cold head which has the probing station. Numbers from one to three show the sequence of closing the system with two vacuum cans.

In essence, the CCR operates by cycling Helium (He) gas around the system, cooling it with the help of the compressor. When operated, the cold head (B) and everything which is inside of the cylinder (2) is cooled by the constant He gas flow. The cold head is also equipped with the built-in heater which allows maintaining intermediate *T* with the help of the *T* controller. The system is equipped with two pumps: conventional and turbo. The latter allows for maintaining a high vacuum.

7.3.2 Physical property measurement system

The physical property measurement system (PPMS) which is made by Quantum Design [218] is capable of producing magnetic AC and DC susceptibility, specific heat and electrical transport properties measurements with two and four-probe configurations on the sample materials down to 2° K. Compared to the CCR which is controlled through the LabView, the PPMS has the built-in software that allows creating a particular experiment sequence which is especially handy if the user is producing the magnetic properties measurements and wants to alter the magnetic field at the specific *T* range. An author of this thesis had an interest in producing the low-*T R* measurements and the available in the CSEC PPMS was capable of producing them up to the 38.9 MΩ (nominal maximum measurable *R*) which was found to be not enough, not to mention the measurement error which was claimed to increase drastically above 4 MΩ [219]. The issue was resolved by interconnecting the PPMS with the external *R* measurement device – electrometer which extended the measurable *R* range but also resulted in measurement process becoming semi-automated; with the *T* being controlled through the sequence file and the *R* readings being collected manually.

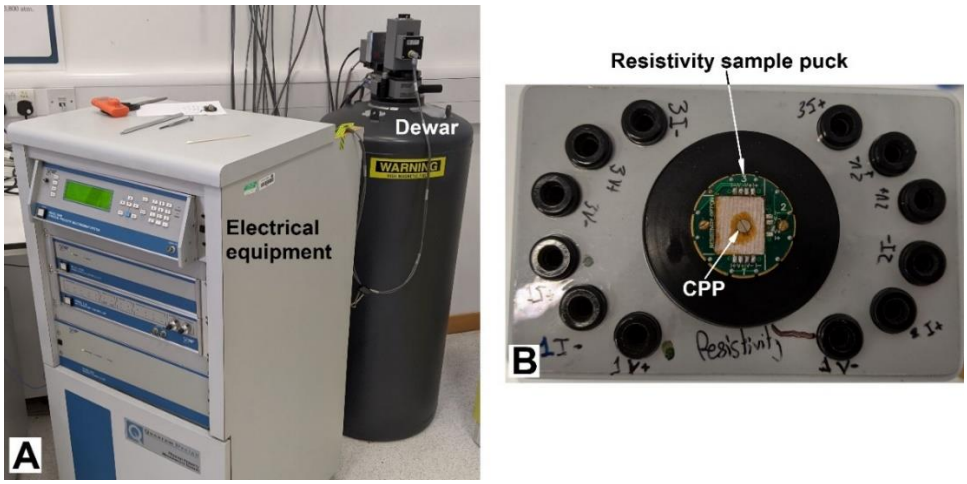

Figure 7.10: The PPMS for *R* measurements. With: A – the PPMS and B – signal testing station for *ρ* sample puck.

The base of the PPMS's dewar (See figure 7.10 – A) is equipped with a cryostat to which the *ρ* sample pack is introduced through the vertical sample chamber. The bottom part of the puck has the signal channels which, prior to insertion into dewar,

are tested on the tasting station (See figure 7.10 – B). The illustrated in the figure CPP was found to be a super insulator and, therefore, its surface was split into two areas which were fully covered with silver paste with a thin channel of sample material in between them to produce low-*T* two-probe *R* measurement.

7.3.3 Cold box

The cold box is the conventional plastic box which was filled with refrigerant gel (ice packs). The ice packs prior to the employment were submerged into the liquid nitrogen until cooled to the same *T* (e.g. 77° K). The small shape of packs was found to be an advantage since it allowed to produce rapid cooling of small instrumentation such as DAC down to 170° K. However, it also meant that anything bigger would not reach the same low *T* unless the economically disadvantageous quantity of ice packs were increased as well as the amounts of the required liquid nitrogen to cool them, and, therefore, utilization of PCC in the cold box was omitted. Instead, the DAC at different *P* points was utilized with the set up as shown in figure 7.11.

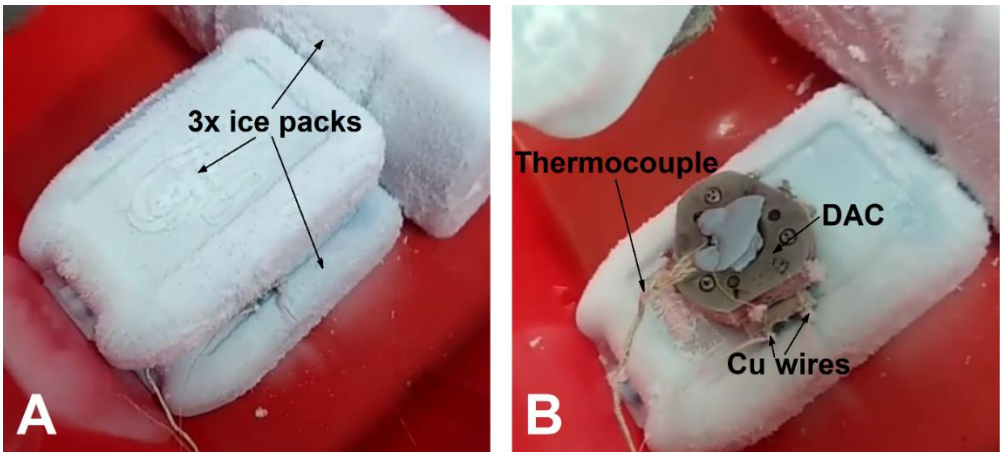

Figure 7.11: The cold box. With: A – sandwiched in between ice packs DAC and B – DAC at 170° K. Please note the Blu Tack® which holds the K-type thermocouple wire's tip to make sure that it is touching the diamond and, therefore, probing the sample *T*. The copper wires are hard to see since they became covered with ice crystals.

To produce the *R* measurement the length of the Cu probing wires was extended from the probing stations to allow better interconnection with the Electrometer/DMM. It was required to act fast when DAC was sandwiched in between the ice packs since the readings had to be taken manually unlike in the CCR and initially the *T* was falling fast with a gradual speed decrease approaching the

170° K. Lower *Ts* were not reached since there was no external cooler employed during the measurement and, therefore, nothing kept the cold. This method allowed to measure *R* during the cool down and slow warm-up.

7.4 High-temperature equipment

7.4.1 Resistive heaters

The resistive heaters of the polyimide type were used to produce *Televated* studies in PCC (See figure 7.12) because they are flexible and thin which allowed to cover the cylindrical surface of the BeCu outer cylinder (See figure 4.12) and still fit it into the protective cylinder (See figure 4.21 – B). Polyimide heating elements produce heat by passing an electric current through the etched metal foil which acts as a resistive element and impedes current causing it to give off the heat. The metal foil is etched to form the *R* pattern which is sandwiched in between two layers of polyimide providing even heat distribution while staying flexible and able to withstand *Ts* up to 533° K [220].

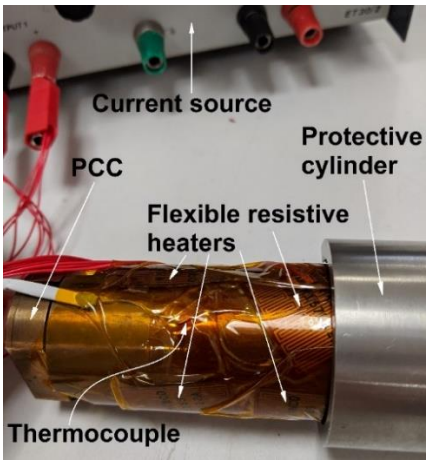

Figure 7.12: Resistive heaters on PCC. Tip of the thermocouple is probing the surface *T* of the BeCu cylinder and is attached to the same level of sample height.

The sample *T* was assumed to be the same as the *T* of the surface of PCC and was measured using K-type thermocouple. Both, resistive heaters and thermocouple were attached to the BeCu cylinder with a thermally conductive Kapton tape. All wiring just like in the case of Cu probing wires from the feedthrough plug was introduced through the notch in the protective cylinder to be interconnected with suitable instrumentation. In the case of the thermocouple, it was the OMEGA® thermometer

[221] and the *T* in the resistive heaters was controlled using an E30/2T [222] current source.

Due to the non-linear behaviour of *R* to *P* in Manganin coil (HP gauge in PCC) at *Televated* [152], the calibration of the *R* - *P* scale which requires *Ro* value at *Pamb* (See equation 3.6), resulted in the inability to alter *Ts* during *P* application. Even with the proper seasoning (See 3.3.1 section in the 3rd chapter), the value of *R* in the Manganin coil was found to undergo small change and to eliminate experiment error it was decided to omit the constant *P* varying *T* method. Instead, the constant *T* varying *P* method was employed in the PCC resulting in the necessity in producing several full *P* cycles (e.g. from *Pamb* to *Pelevated*) for single test material at different *T* points which was found to be a time-consuming procedure. The main complication was associated with the inability to reach *Pamb* during the *P* release due to the stuck in WC piston in the NiCrAl inner cylinder dictating the need in full PCC disassembly prior to producing next *P* cycle at a constant *T*. Which in turn was often accompanied with CPP integrity damages and the necessity in producing new CPP which yielded some experiment inconsistency not to mention the time-consuming CPP mounting on the table process (See figure 7.2). Summarizing the above said, the *T* analyses in PCC were found to be inefficient in terms of the allocated to them time and were limited in working with only one PR material candidate.

7.4.2 Hot plate

The conventional hot plate was used in *Televated* experiments at *Pelevated* for DAC and *Pamb* for CPP on the glass substrate. Although the hot plate was able to reach 523° K, the produced measurements did not go above 353° K since that was not necessary and the collected data already allowed to construct precise *R* - *T* curves and based on them to judge upon the material's electronic behaviour.

The similar setup was used for *Televated* experiment for DAC with thermocouple tip attached to the diamond with Blu Tack® and pointing towards the sample chamber. The DAC was placed on to the hot plate's surface with the bottom side of the cell for safety reasons since the top side had wooden blocks surrounding it (See figure 5.14).

Just like it is shown in figure 7.13 where *R* between contacts B and C is measured on the extended Cu wires, the probe wires in DAC were also elongated to avoid direct contact of probe wires with the hot plate. The thick sheet of steel in between the hot plate and the CPP on the glass substrate was mainly employed to evenly distribute the heat on the substrate since the surface of the hot plate turned out to be rough, possibly as a result of previously conducted experiments on it. This method allowed to measure *R* during warm-up and slow cool down within the above-mentioned *T* range.

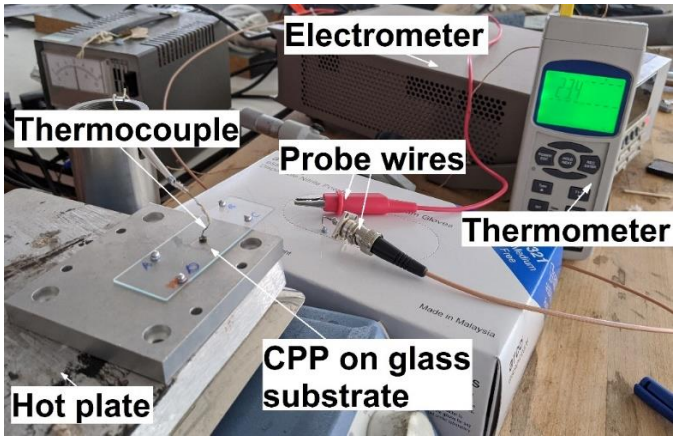

Figure 7.13: The hot plate for *Televated* analyses. With key components being named on the figure.

Unlike the PCC, DAC was suitable for the variable *T* constant *P* method which allowed to produce comprehensive *T* studies during single sample loading and single *P* application. In other words, the experimenter was able to stop at any given *P* point, produce the *T* analysis and continue his way up in terms of *P* without cell opening. This method was therefore employed more often.

7.4.3 Heat gun

The conventional heat gun was used in the *Televated* experiments for CPP on the glass substrate. It is the less accurate method if compared to a hot plate or resistive heaters since the created heat was also accompanied by the directional airflow. The setup used was similar to the one shown in figure 7.7 – A with extensions of Cu contacts to avoid heating of probe wires. Although the airflow was found to be strong

the contact junctions were able to survive it and all the necessary readings were collected.

The experiment itself required at least two people to be successful: one person to hold down the heat gun pointing with hot airflow towards the CPP while slowly shortening the distance in between heat gun's nozzle and CPP to increase the *T* CPP is subjected to and the other person to monitor and collect the *R* and *T* readings from electrometer and thermometer respectively.

Since the experiment was relying on the human factor in terms of the speed and accuracy with which the nozzle was moving towards the CPP, the error bars were introduced for *T* values in the range of +/– 2° C.

Chapter 8

Discussion

This chapter provides the experimentally derived data on the PR materials from the 2nd chapter in the form of the *R* - *T*, BG - *P* and ρ - *P* charts using the techniques which are outlined in the 7th chapter and using the apparatuses from the 4th – 6th chapters. Each chart is accompanied by the experimental details and data analysis, as well as the author's thoughts regarding the suitability of the PR samples for the use in the OPET device. Numerical data is available in Appendix D.

8.1 The $Pt(bqd)_2$ complex

A set of *P* and *T* experiments were conducted in both: PCC and DAC to refurnish the previously reported literature of this known intrinsic organic semiconductor [59, 82, 83, 84], expand it by producing measurement on a CPP as well as to determine if *R* into ρ conversion using MM [119] can be applied to the sample geometry in DAC. All measurements were undertaken on a CPP.

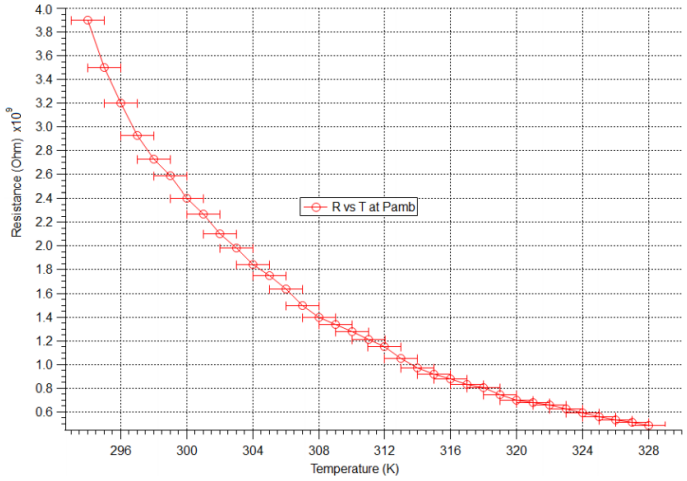

Figure 8.1: *R* vs *T* at *Pamb* for $Pt(bqd)_2$.

The *R* - *T* at *Pamb* was initially performed on a CPP using a hot plate to determine if sample *R* is measurable and probe its electronic behaviour which was found to have the semiconductor character. The +/– 1° K error bars were introduced since the numerical readings were collected manually and may lack the *T* to *R* allocation precision which also applies to the subsequent *R* vs *T* charts.

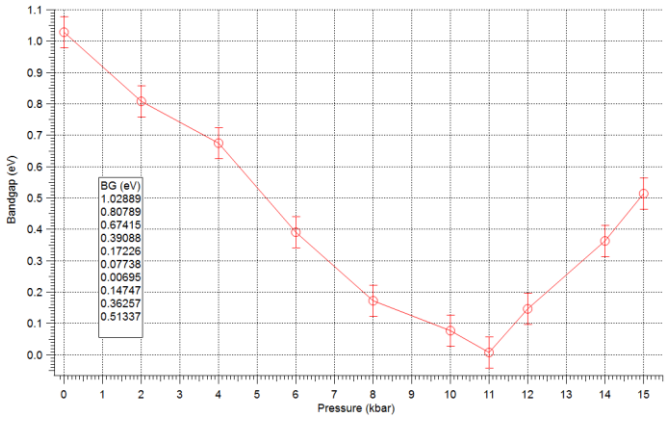

Figure 8.2: BGs vs *P* in PCC for $Pt(bqd)_2$. BG numerical values are provided in the textbox with the top value corresponding to the 0 kbars and last to the 15 kbar.

A total of four *T* points were used to construct BG vs *P* in figure 8.2: *Troom*, T_{31}, T_{40} &T_{51} in ° C, which means that a total of four *P* applications were performed on a CPP using constant *T* varying *P* method with the help of the resistive heaters. Resistivity values at the corresponding *P* points were derived from the original *P* - *ρ* data charts using interpolation. The error bars for the BG values were introduced due to the involvement of several CPPs being employed between experiments, which, even having the same production method and the value of the contact separations, led to some inconsistencies.

According to figure 8.2, under *P* application the experimentally derived BG of $Pt(bqd)_2$ decreased from 1.029 eV at *Pamb* to 0.007 eV at 11 kbar indicating the metallic state. Further *P* application showed increases in the BG value. This sample behaviour is consistent with the previously reported trend with insulator-to-metal-to-semiconductor transitions with the metallic state being reached in between 8 & 14 kbars [82, 83, 84].

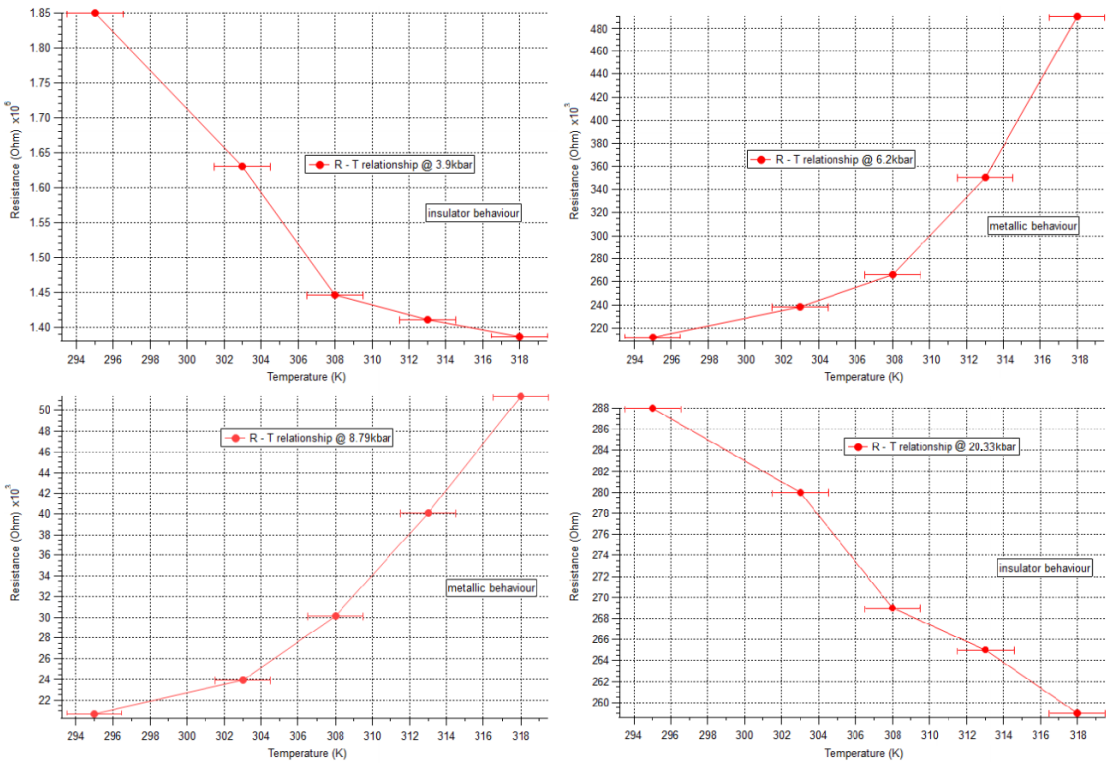

Figure 8.3: *R* vs *T* analysis in DAC for $Pt(bqd)_2$.

The *R* - *T* analysis in DAC was performed on a hot plate on a total of four *P* points to illustrate the electronic behaviour of the sample at the transition-wise important *P*s.

The collected data (See figure 8.3) agrees with the previously reported insulator-to-metal-to-semiconductor behaviour of the sample with metallic behaviour at 6.2 and 8.79 kbars & insulator and semiconductor behaviours at 3.9 and 20.33 kbars respectively.

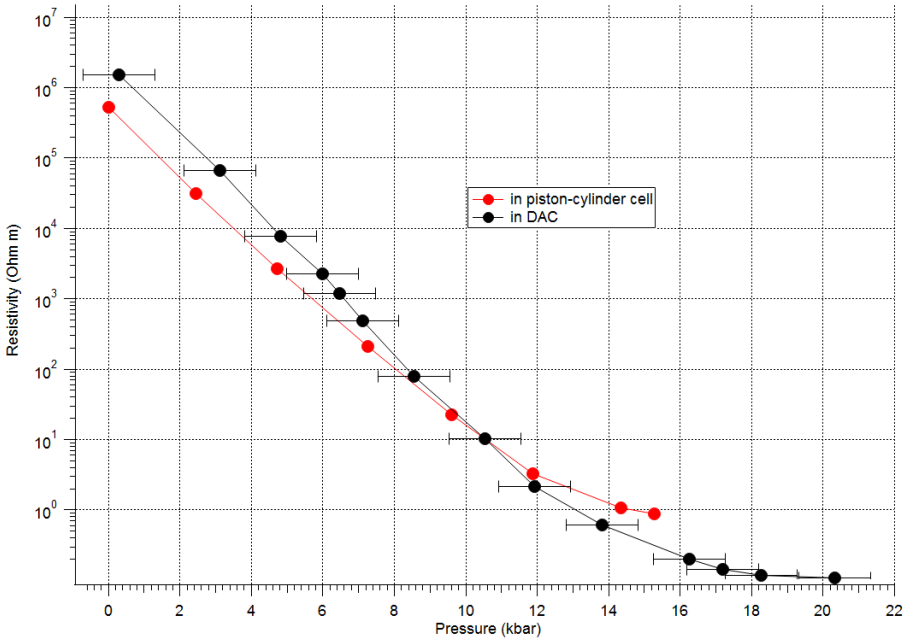

Figure 8.4: ρ vs P comparison in between DAC and PCC for $Pt(bqd)_2$.

The CPP ρ of the $Pt(bqd)_2$ sample in both apparatuses drastically decreases in between *Pamb* and 11 kbars which is followed with further moderate decrease up to the 15.28 kbar for PCC and 20.33 kbar for DAC. As a result, the sample undergoes 7 orders of magnitude change in ρ [59].

There were no further P increases to avoid any damage to the feedthrough plug in case of the PCC and gasket thinning beyond the optimal thickness for the pellet geometry in case of DAC. Moreover, inspected P range stays within the high hydrostaticity of PTM [164] as well as covers the previously reported in the literature transition-wise important P points [82, 83, 84].

Please note that the x-axis (e.g. P) error bars are not visible on figure 8.4 for the PCC since they are smaller in size than the diameter of the dot markers. In the case of the DAC, they are presented and are illustrating the uncertainty in measuring P with ruby as a P sensor. The probability of +/– 1 kbar error can be accounted for factors such as ruby orientation, ruby geometry and P distribution in the gasket hole [54].

The above-mentioned error range can be assumed to be reasonable since the used in the experiment ruby chip was not spherical and that it was not perfectly centred in the middle of the sample chamber which was determined during *P* probing. The small shift can occur whether due to the *P* application whether during sample loading procedure (See figure 7.3). This statement also explains the existence or lack of error bars on all subsequent ρ vs *P* charts.

By comparing resistivities in both cells it can be concluded that the MM is well suited for converting *R* into ρ in DAC. Although the CPP thickness was not controlled during the experiment because of the gasket's flow, the observed ρ tendency in DAC agrees with one in PCC where CPP of a different geometry had no physical contacts with cell parts. Therefore, it can be concluded that, if the contact separation to the CPP thickness relationship is adhered (See figure 4.1 & 5.2), the *R* into ρ conversion is accurate.

The $Pt(bqd)_2$ sample was also deposited using the PVD method into thin film form and it's *R* was measured in the modified gasket pre-indenter.

As it can be noted in figure 8.5, the very first 13 out of 14 points were collected with the help of the small weights which were previously mentioned as a replacement for hydraulic press and a load cell for the very sensitive samples in terms of *R* response to the applied *P*. It was, unfortunately, impossible to reach anything beyond 25 MPa with these weights due to poor stability of the weights stack on top of the piston. The very last point (number 14) was collected using a hydraulic press and the load cell. Unfortunately, this 110 MPa *P* corresponds to the very first reading voltage of the load cell (e.g. 0.1 mV) – the value which can be quantified. Any further *P* increases were omitted since the readable *R* was already very low (e.g. 35 Ω).

Combination of those two *P* application methods showed that the *R* - *P* response trend of the sample remains and that the thin film undergoes 4 orders of magnitude change in *R*.

Both charts in figure 8.5 are having visible error bars for the y-axis while the x-axis error bars are smaller than the dot markers. Compared to DAC and PCC this experiment has higher *P* control than the *R* because there were no external *P* probing

methods involved and *P* was directly calculated from equation 3.4. Quality of the collected *R* however showed some signs of uncertainty due to rapid changes in terms of the applied load and big sample sensitivity. It was decided to allocate +/– 20% of the base value error for the collected *Rs* since approximately this kind of variation in the numerical data was noted during the experiment conduction. Also, it was previously noted that at low loads there might be issues with friction between the cell body and piston (See 7.2.4 section in the 7th chapter) and this can be accounted for the first 4 – 5 points up to 10 Mpa.

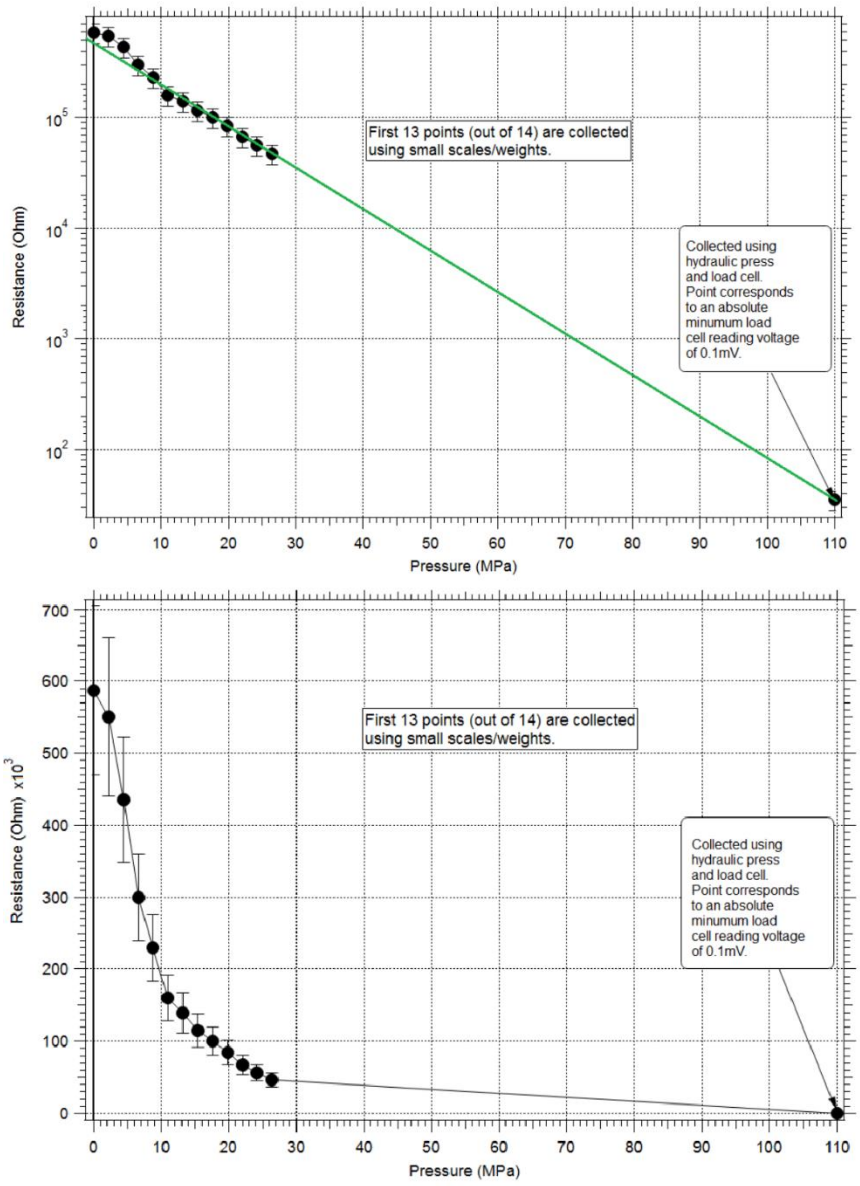

Figure 8.5: *R* vs *P* for thin film Pt(bqd)$_2$. The top chart is log-linear and the bottom is linear-linear. The green line on the top chart was drawn to show that the *R* - *P* tendency remains between the combined *P* application methods.

The surface area of the thin film allowed to produce another indentation to determine if the collected in figure 8.5 data indeed represents the sample behaviour.

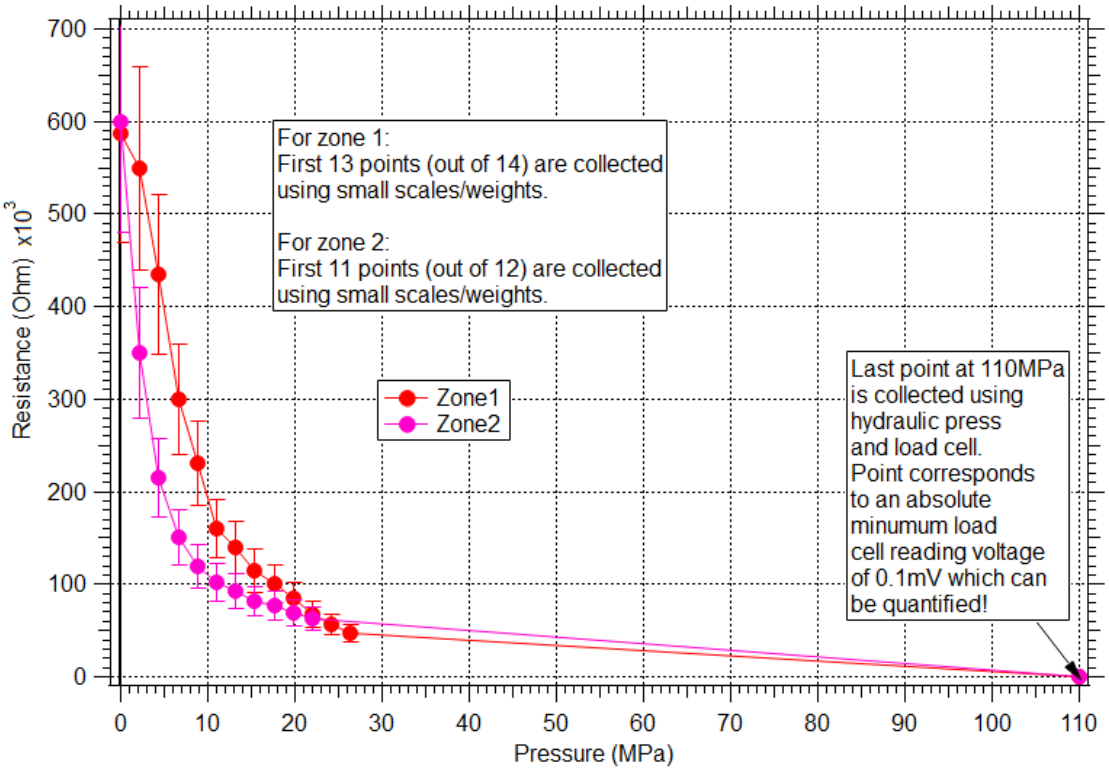

Figure 8.6: *R* vs *P* for thin film Pt(bqd)$_2$. The liner-linear chart with two indentation zones. Zone 1 is the same indentation as in figure 8.5 and zone 2 data represents new indentation.

As it can be noted in figure 8.6 the 2nd zone had fewer weights being applied since the stack started to feel wobbly. Although the overall *R* - *P* response was the same, the 2nd zone was found to have smaller *Rs* compared to the 1st zone. This can be explained by the positioning of indenter on the thin film. The thickness of the deposited material layer was found to vary with a thicker layer at the substrate edges and thinner towards the masked gold layer for the *R* probing which can be noted by examining figure 6.9. The 1st zone is closer to the edge compared to the 2nd zone and, therefore, initially has higher *R* values. After ≈ 20 Mpa the 1st and 2nd zone's readings consent. This is probably where the indentation area in both zones starts to have a similar level of densification.

It was also decided to cycle the thin film between *Pamb* and *Pelevated* to determine if the *R* response would follow the observed in figure 8.6 trend.

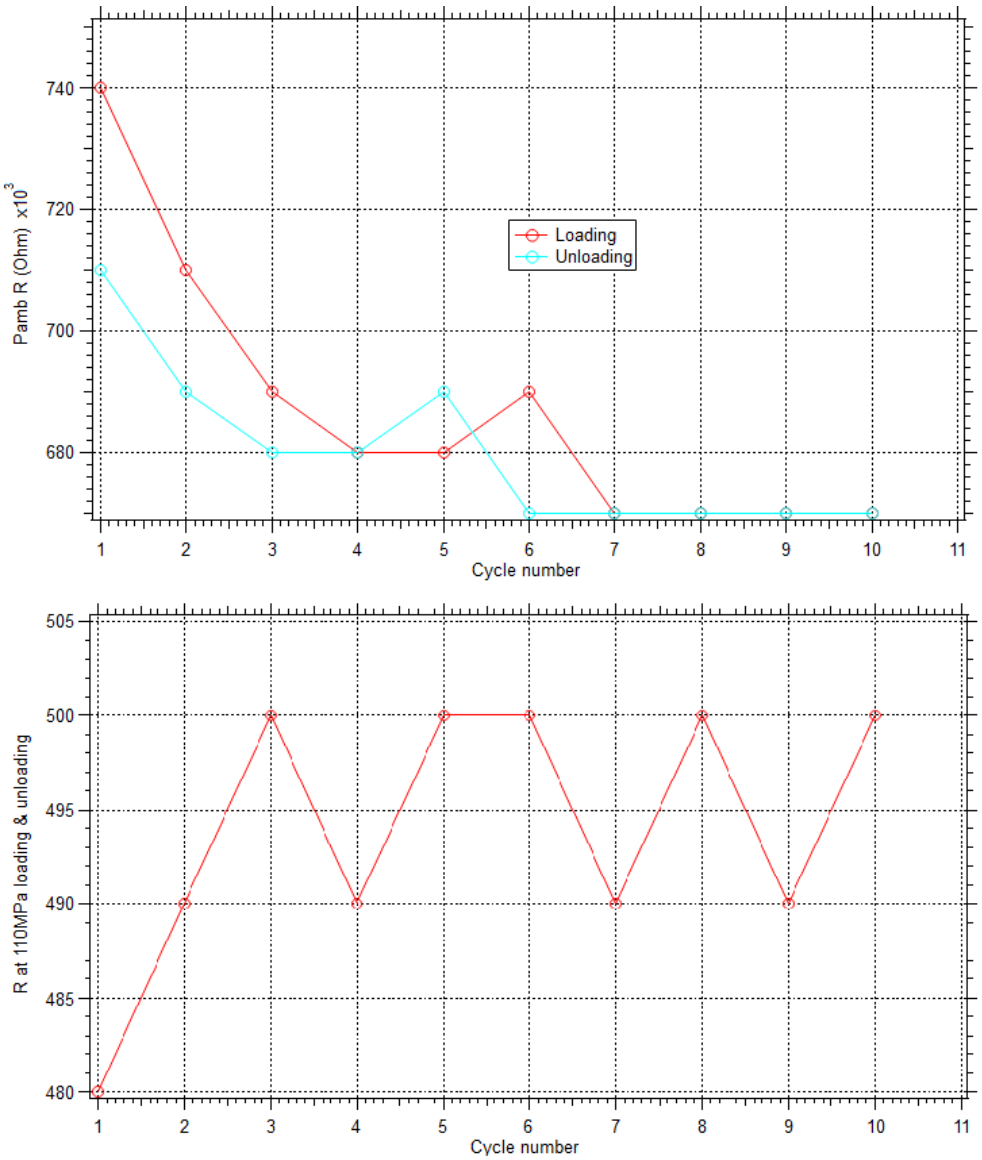

Figure 8.7: *R* vs cycle number for thin film Pt(bqd)$_2$. The top chart is *Pamb R* vs cycle number and the bottom is R at 110 MPa.

The illustrated in figure 8.7 data was collected by cycling 2nd indentation zone between *Pamb* and 110 Mpa using a hydraulic press and a load cell. Please note that the previously mentioned friction between the piston and the cell body influenced the *R Pamb* values in the top chart. This time, however, it was the other way round – and, therefore, the *R* is believed to be higher than it is shown (anywhere but 1st cycle) since the friction was preventing piston from pushing out (e.g. it was still applying pressure on the thin film where the *P* is shown as *Pamb*).

It can be noted that a total of 10 cycles were performed and that the *R* at 110 Mpa was found to be higher than before (e.g. ≈ 495 Ω vs 35 Ω). Since this is a molecular

sample this cannot be explained by any chemical change and, therefore, it is believed that this difference in *R* readings at 110 MPa can only be accounted for densification of thin layer of the deposited material. It is believed that some vertically oriented needles break/fall during the first compression and, therefore, the R increases. Nonetheless, based on figure 8.7 it can be concluded that the sample *R* in response to the applied *P* is indeed reproducible during cycling operations and densifies after 3rd cycle (by taking into account the very first cycle which is demonstrated in figure 8.6 for 2nd zone).

8.2 The Pt(F-bqd)$_2$ complex

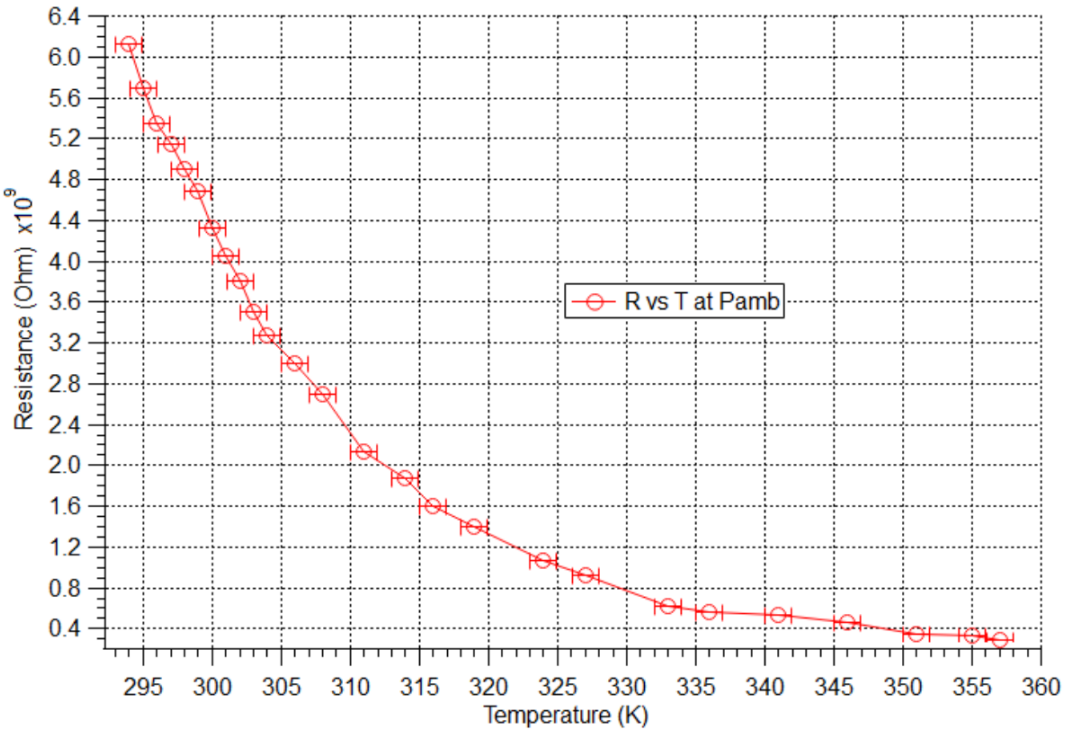

Figure 8.8: *R* vs *T* at *Pamb* for Pt(F-bqd)$_2$.

The *R* - *T* analysis at *Pamb* for Pt(F-bqd)$_2$ sample was performed using a heat gun. The illustrated trend shows the semiconductor behaviour of the sample material at *Pamb*. The *Troom R* was found to be a bit higher than that of a Pt(bqd)$_2$ sample but with the same degree of power and, which was found to be promising, the smaller *Pamb* BG value which was calculated to be 0.8937 eV using the figure 8.8.

The sample was also exposed to low *T* analysis in CCR to determine what will be the lowest *T* that can still read the *R* with the Electrometer.

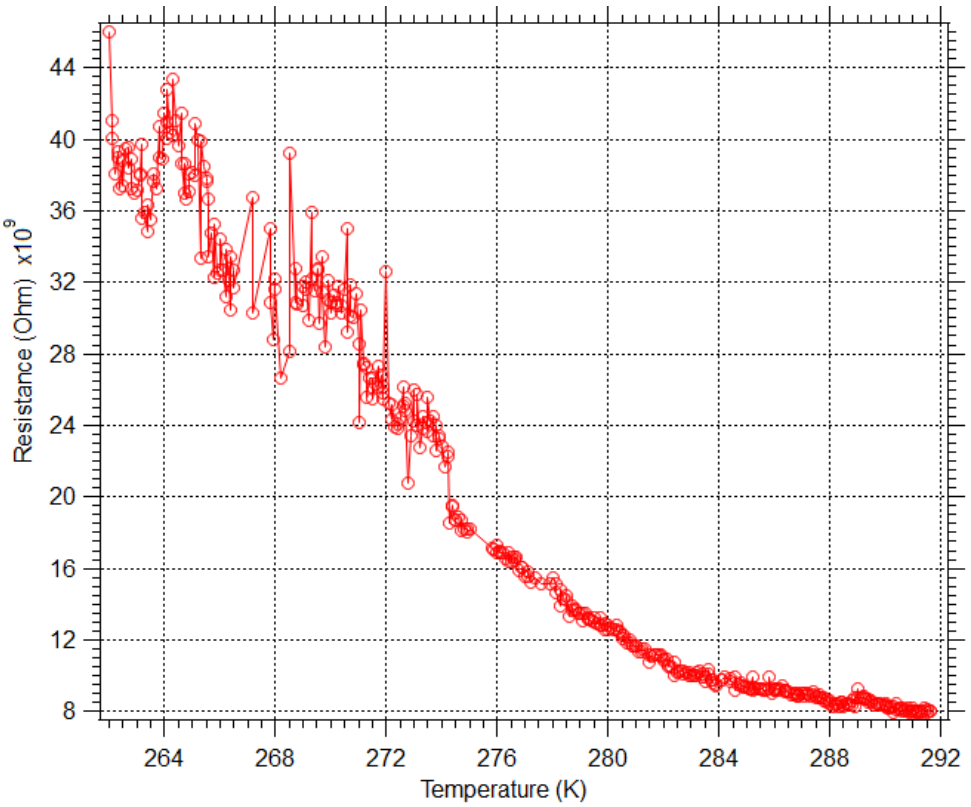

Figure 8.9: *R* vs *T* at *Pamb* for Pt(F-bqd)$_2$ in CCR.

Although the CCR allowed getting to 15° K, the *R* values below 262° K were omitted in figure 8.9 because of the unrealistic noise profile. The reading noise was observed to start occurring below 274° K but was still having the right *R* - *T* trend up until the 262° K and for the same reason was left for the illustration purposes in figure 8.9. It is believed that the possible reason/reasons which caused such a noise is a compatibility issue between Electrometer and the switch system (See figure 7.9) and/or the fast logging speed with which readings were taken by the LabView. Another possible explanation of the high noise profile is the poor shielding. It was therefore concluded that the CCR is not an ideal device for probing high resistances with Electrometer and due to the limited time scales the problem which caused such a reading noise was not unequivocally determined.

The elevated *P* analysis was required to determine if the fluorinated version of the Pt(bqd)$_2$ sample would have similar ρ - *P* response. The sample was first exposed to *P* extremes in the PCC and then it was decided to measure it in DAC since PCC was found to have a time-consuming *T* analysis which required constant *T* varying *P* method to be employed (See 7.4.1 section in the 7th chapter).

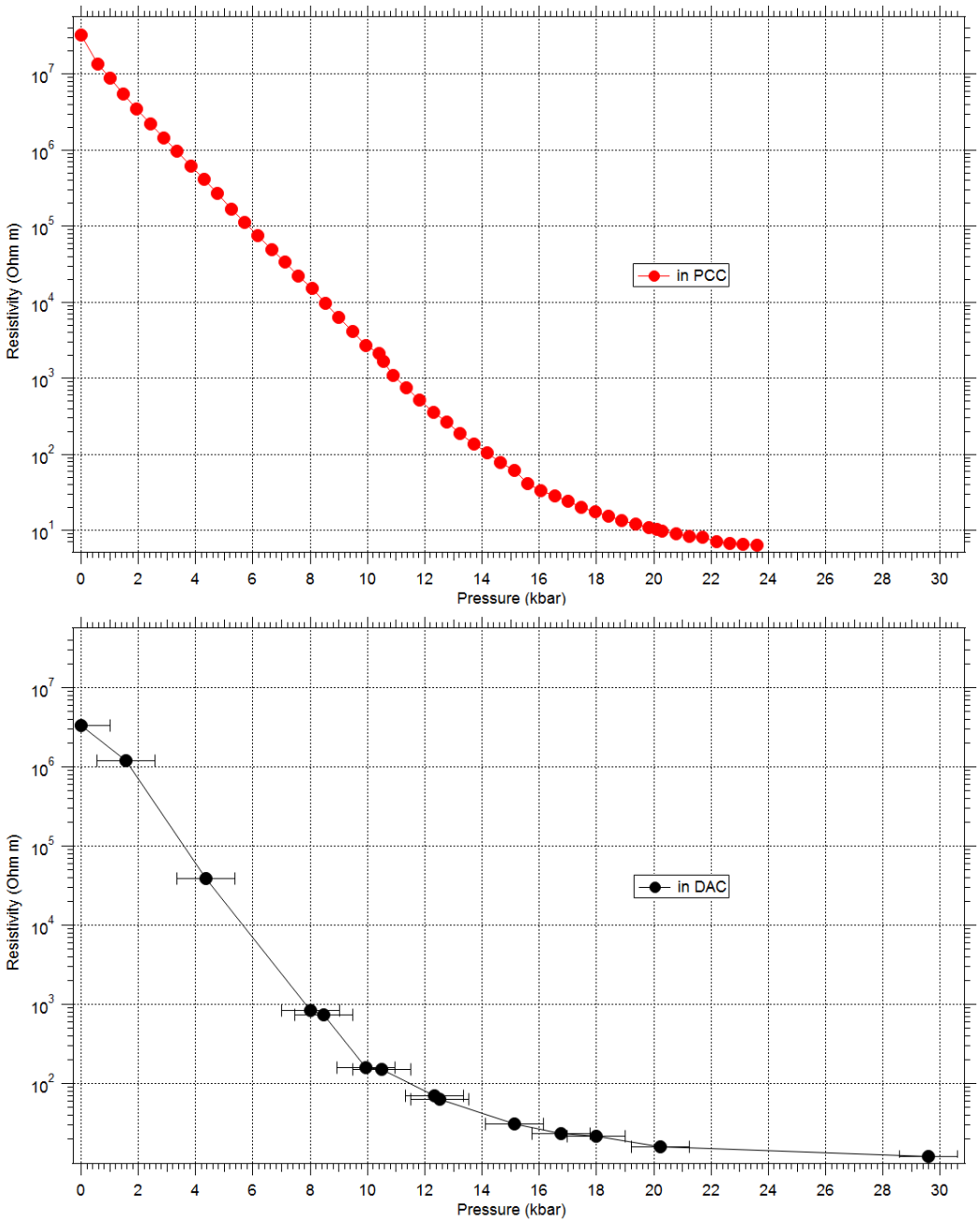

Figure 8.10: ρ vs P for Pt(F-bqd)$_2$. With PCC at the top and DAC at the bottom.

The ρ in both apparatuses drastically decreases in between *Pamb* and 11 kbar. In the case of the DAC, it can be seen how moderate the effect is yielded on the ρ with further P increases since it has a wider P range. According to the PCC, which is believed to be more precise than DAC, the sample undergoes 7 orders of magnitude change in ρ just like in the case of Pt(bqd)$_2$ however the fluorinated version is less conductive than it's parent compound which can be noted by comparing numerical values at the corresponding pressures between two (See Appendix D).

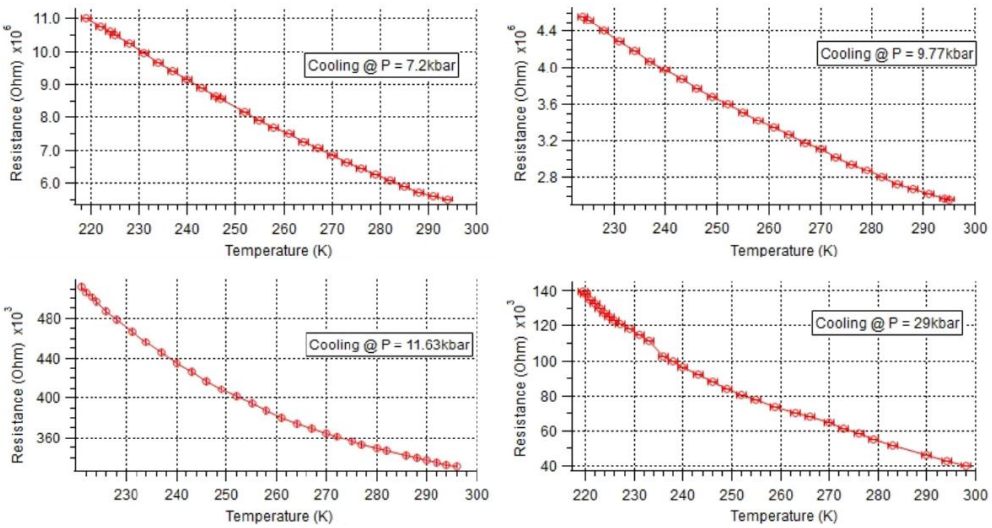

Figure 8.11: *R* vs *T* analysis in DAC for Pt(F-bqd)$_2$.

It was decided to produce the low-*T* analysis rather than high-*T* because of the previous failure with CCR as well as to widen the skills of the experimenter. The employed *P* points were selected based on the observed DAC ρ - *P* trend (See figure 8.10) to probe the sample's electronic behaviour before the line bending and after. In all four *P* points (See figure 8.11) the sample was found to act as a semiconductor with no metallic state being reached with the lowest BG to be found at 11.63 kbar which corresponds to the 0.064662 eV.

8.3 The PTC1 complex

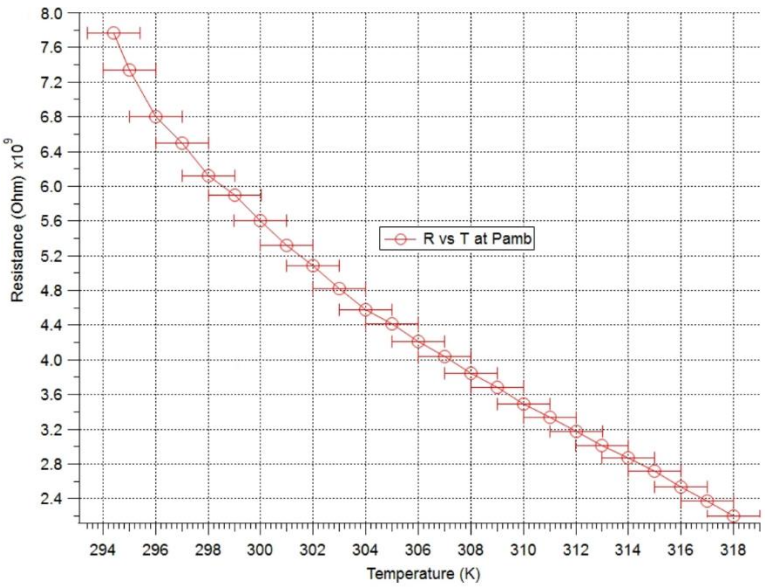

Figure 8.12: *R* vs *T* at *Pamb* for PTC1.

The *R* - *T* analysis at *Pamb* for PTC1 sample was performed on a CPP on the hot plate. At *Pamb* sample behaves as a semiconductor with the *Troom R* being higher than in the fluorinated Pt complex but still within the same degree of power. Using the data from figure 8.12, the *Pamb* BG was calculated to be 0.8025 eV which is a promising number and, therefore, it was worth producing the *R* - *P* analysis on this complex.

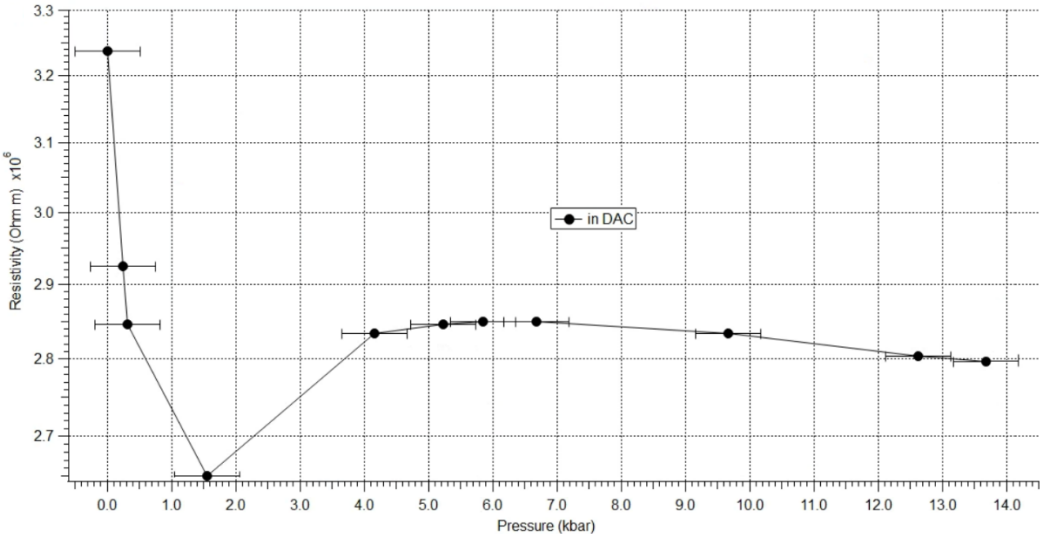

Figure 8.13: ρ vs *P* for PTC1.

The PTC1 was measured in DAC only with the illustrated in figure 8.13 ρ response to the applied *P*. Initially, the ρ used to fall rapidly until it hit the value at ≈ 1.5 kbar where it started to grow and stabilized in between the 2.87 – 2.77 $*10^6$ Ωm range. It was decided not to go further in terms of *P* since the observed between 4 and 14 kbars trend showed no prerequisites for rapid change. The initial ρ drop can be accounted for not yet compressed powder within the sample chamber of DAC which, in this case, stabilized after 4 kbars. Assuming reversible nature of the material, such an explanation is reasonable since the sample ρ stayed in the 2.87 – 2.77 $*10^6$ Ωm range during the *P* release, never coming back to the initially observed trend which is illustrated in the figure 8.13.

Since the PTC1 complex showed no desirable ρ - *P* change, it was not further studied, and no *R* - *T* analyses were performed at elevated *Ps* because the investigated *P* range does not portend any close future changes in the semiconductor nature of the complex material.

8.4 The $Pt(NH_3)_4PtCl_4$ complex

The $Pt(NH_3)_4PtCl_4$ complex was previously reported in the literature back in 1971 [97] and it was decided to refurbish the previously reported data on powder material to investigate the differences and/or similarities. Since the reported *P* range was way beyond the PCC capabilities, the sample *R* was measured in DAC and converted into ρ using MM. It is believed that DAC data is more precise than the belt-type HP device.

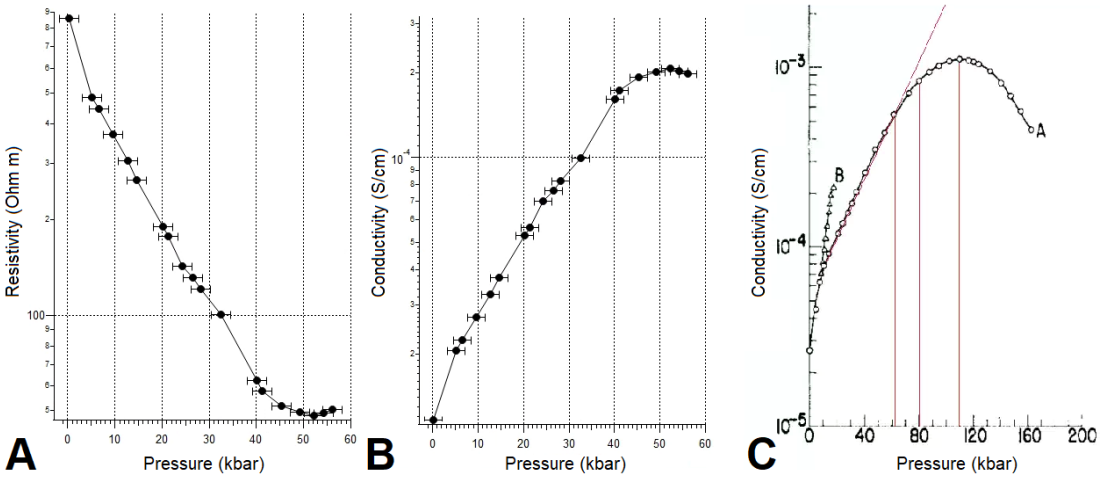

Figure 8.14: HP data for $Pt(NH_3)_4PtCl_4$. With: A – ρ vs *P* (DAC), B – γ vs *P* (DAC) and C – previously reported data [97].

The complex has identical to the reported tendency where it initially almost linearly drops in ρ as a result of the applied *P* which shortens the metal-metal distances up until the 52 kbar in DAC or the 100 kbar in belt-type apparatus as a powder, where it starts to increase. By comparing B and C charts in figure 8.14 it can be noted that the γ was reported to be much higher to the one an author observed during his experiments. It is believed that such a difference may arise due to the different *R* into ρ conversion method being employed. The demonstrated in this work method as well as the precision in probe contact allocation is believed to be more precise to the techniques from 1971 which means that the complex is not that conductive as it was thought however twice as low *P* is required to achieve the conductive peak of the material in the powder form.

A total of two *T* analyses were then performed on the complex: at HP and low *P* which corresponds to the 56.1 and 2.1 kbars respectively. Those analyses showed

than the complex behaves as a semiconductor in both scenarios (See figure 8.15). The *T* analyses were performed in the DAC using the hot plate method and allowed to calculate BGs to be 0.7837 and 0.5037 eV at 2.1 and 56.1 kbars respectively. Further work with this complex was omitted since the acquired results were not sufficiently good in terms of the acquired *ρs* and the employed *Ps*.

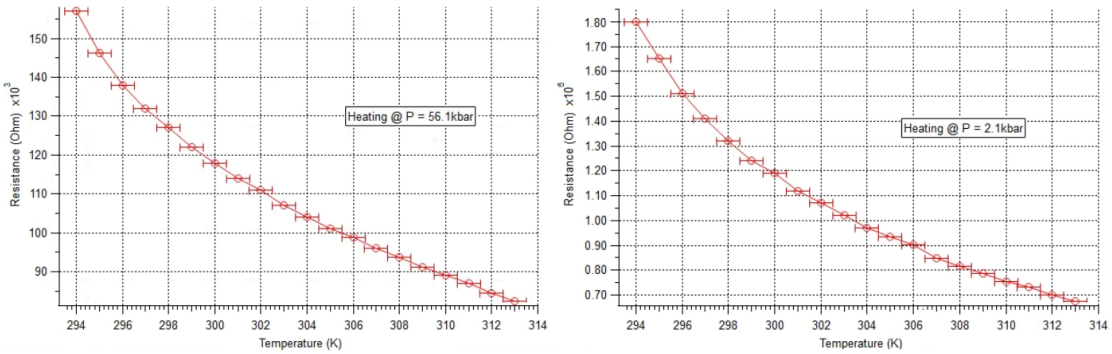

Figure 8.15: *R* vs *T* for $Pt(NH_3)_4PtCl_4$.

8.5 The $Pt(CH_3NH_2)_4PtCl_4$ complex

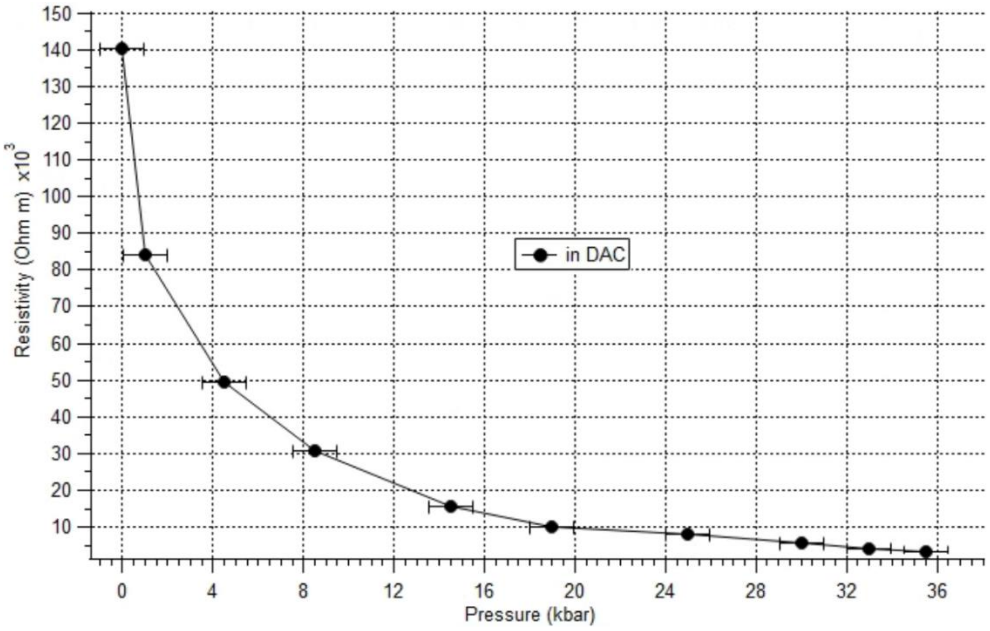

Figure 8.16: *ρ* vs *P* for $Pt(CH_3NH_2)_4PtCl_4$.

The $Pt(CH_3NH_2)_4PtCl_4$ complex was exposed to HP in the DAC up to the 35.5 kbars. Any further *P* increases were omitted since the observed *ρ* - *P* trend in figure 8.16 did not promise anything extraordinary. Please note that the *ρ* stays within the same degree of power (e.g. 10^3) and that the *P* application did not lead to any big changes.

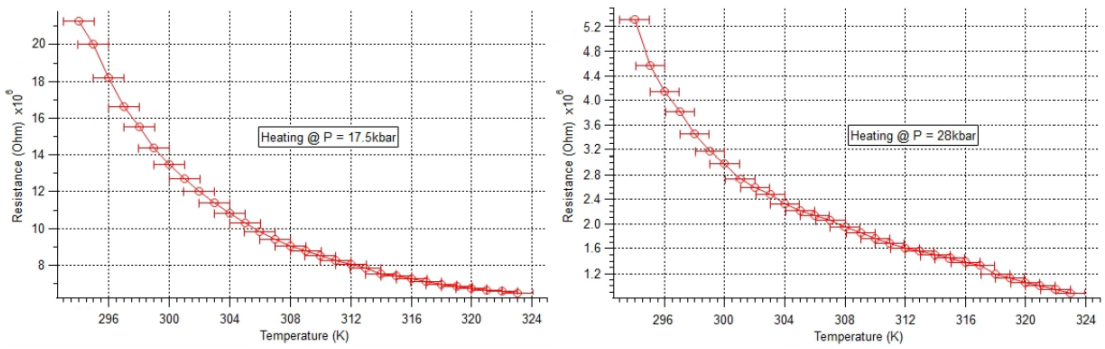

Figure 8.17: *R* vs *T* for $Pt(CH_3NH_2)_4PtCl_4$.

Since the sample was previously reported to act as a semiconductor at *Pamb*, it was decided to produce two *T* analyses (See figure 8.17) to find out what happens with electronic behaviour at different *Ps*. Since the ρ - *P* trend (See figure 8.16) showed no prerequisites for the desired *P* points for *T* analyses it was decided to produce *T* analyses at HP and somewhere mid-through which corresponds to the 28 and 17.5 kbars respectively. The hot plate method was employed and it showed that sample stays to act as a semiconductor over the tested *P* range. The *T* analyses at 17.5 and 28 kbar allowed to calculate the BGs to be 0.6509 & 0.9009 eV respectively which if combined with the reported *Pamb* BG value of 0.35 eV [96] indicates that *P* increases only widen the BG in this complex and it is, therefore, not suitable for PR applications (not to mention how big its ρ stays to be even beyond the *P* range of the OPET concept).

8.6 The $Ir(CO)_2(bta)$ complex

The iridium complex with bta ligand was exposed to HP in the DAC since it was hard to predict the ρ - *P* trend and DAC has wider *P* range for the experiment.

The very first point at *P* = 0 kbars (See figure 8.18) can be omitted since the powder was not compressed yet. The other points are following the trend which shows that the sample stays within the $3 - 3.5*10^6$ Ωm ρ range up to the 50 kbars where the sample ρ starts to rapidly fall. Assuming the same tendency in ρ to *P* response, the $Ir(CO)_2(bta)$ would reach the ρ = 0.0108 Ωm roughly at 155 kbar. The ρ = 0.0108 Ωm value was taken for the comparison reasons which from the $Pt(bqd)_2$ data corresponds to ρ at 20.33 kbar (See figure D.2). Although this is an interesting prediction to investigate, the estimated low ρ appears far beyond the operation *P*

range of the OPET device and, therefore, any further analyses on the $Ir(CO)_2$(bta) complex were omitted.

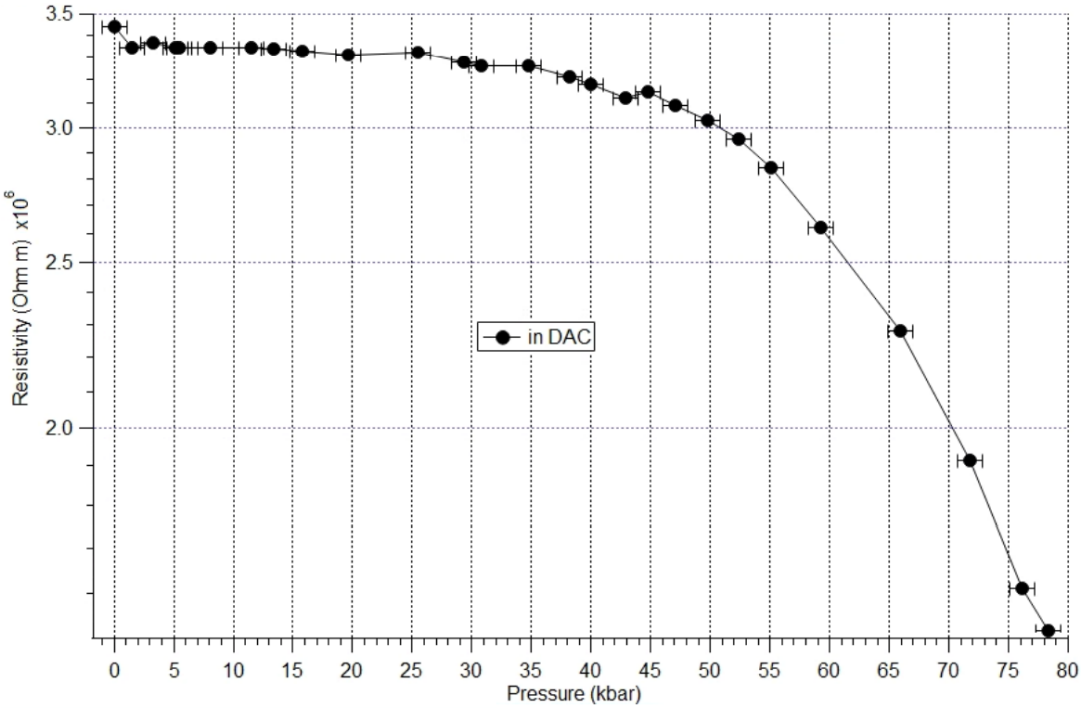

Figure 8.18: ρ vs P for $Ir(CO)_2$(bta).

The sample was not employed in the precise T analyses which can be presented in here in the form of the R - T charts since no low or hight T techniques which are outlined in the 7th chapter were applied to this material. Instead, an author has produced sanity checks at all P points by visually observing/checking whether R grows or falls due to the translated to the DAC and, therefore, to the sample heat from the hand finger. Although this method is not scientifically valuable, yields no concrete values and, therefore, no BG information, it is a fast and reliable method to probe sample's electronic behaviour which as expected had a semiconductor character across all 27 P points.

8.7 The $Ir(CO)_2$(tfp) complex

Just like in the case of iridium complex with bta ligand, the tfp ligand complex was exposed to HP in the DAC since it has wider P range for the experiment if compared to PCC.

By observing the black curve (See figure 8.19) which corresponds to the *P* application it can be noted that the sample ρ slowly decreases up to the 26 kbars where the ρ drop increases with the applied *P*. If in between 0 and 26 kbars sample ρ decreases approximately by a factor of two (e.g. from $3.86*10^6$ to $1.95*10^6$ Ωm), in between 26 and 40 kbars the ρ decreased by a factor of forty (e.g. from $1.95*10^6$ to $4.92*10^4$ Ωm). Further *P* increases, however, were leading to increases in the ρ which can be noted by observing the trend in between 40 and 49 kbars. Since such a sample behaviour was not desired/expected it was decided to slowly release the *P* and see if the ρ deepening would occur again. By observing the green curve which corresponds to the *P* release, the deepening indeed occurred in between the previously noted *P* range with a slight shift towards lower *P* which can be explained by the fact that CPP is more compact now within the sample chamber which led to lower ρ readings being collected in between 33 and 8 kbars. Since the observed during the *P* application ρ vs *P* trend was repeated during the *P* release and came back to the original ρ at *Pamb*, it can be assumed that the experiment is not an artefact.

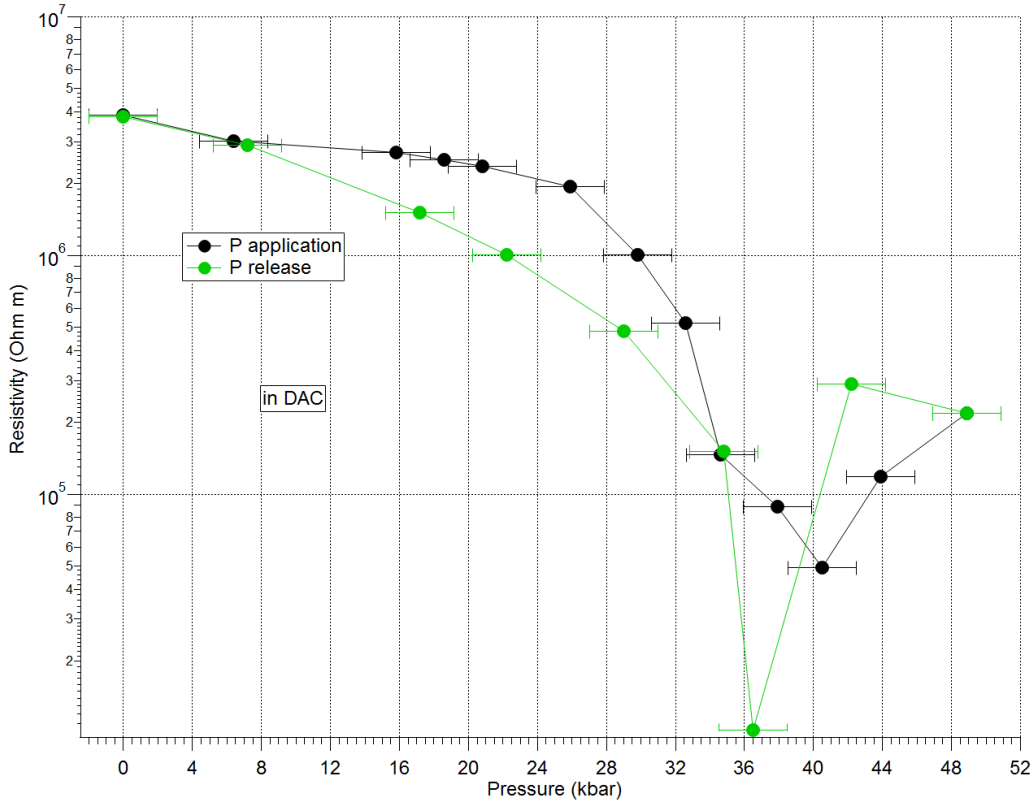

Figure 8.19: ρ vs *P* for $Ir(CO)_2(tfp)$.

Before, during and after the deepening sample used to behave as a semiconductor which was determined using the same method as in the case of the iridium sample with bta ligand. Since no desired ρ change occurred in between *Pamb* and 30 kbars, the sample was omitted for any further analyses.

8.8 The GDC1 complex

The GDC1 complex was found to have polymorph modifications when the in-house made single crystals of this complex were tested in the diffractometer which showed that the sample had not crystallised in the expected space group although the same crystallisation method (electrochemical oxidation) as was reported in [103] was utilized. Due to this, the polymorph 1 (e.g. the reported in the literature material) was not achieved and, therefore, no HP studies nor *R* - *T* analyses were performed on it. Instead, only polymorph 2 was studied.

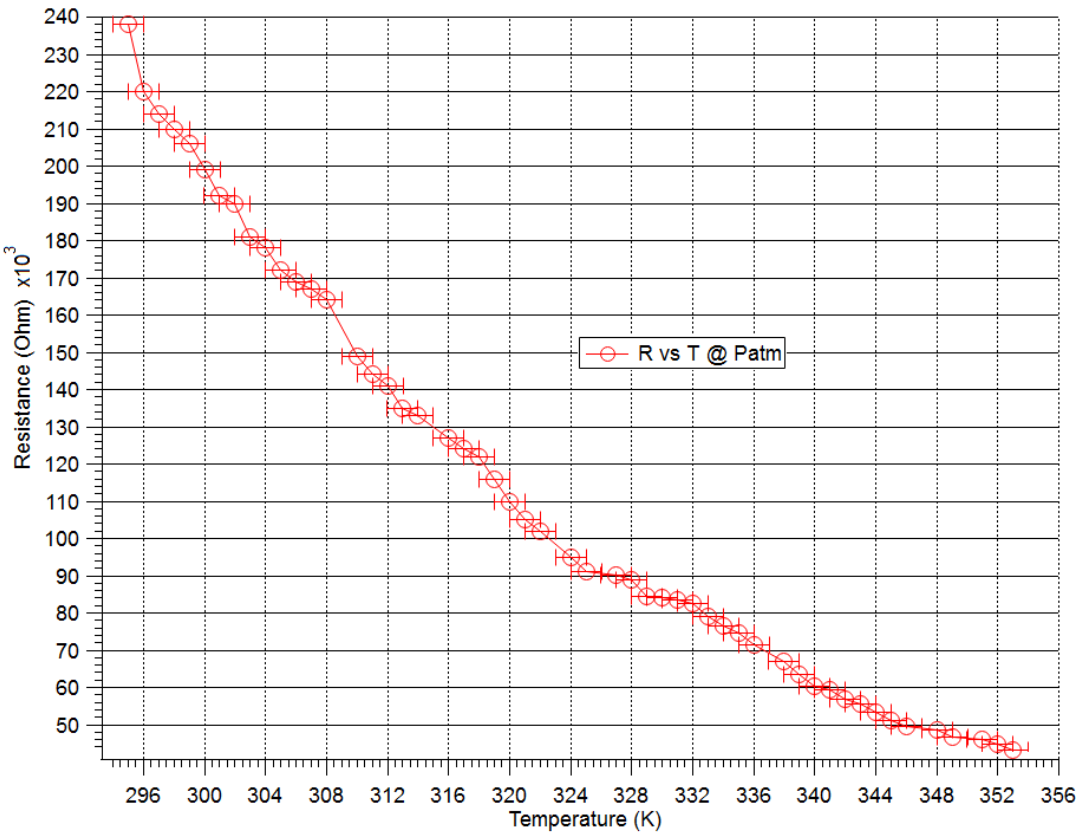

Figure 8.20: *R* vs *T* for GDC1 polymorph 2.

The hot plate method was employed in the *R* - *T* analysis for the GDC1 polymorph 2 complex which yielded the shown in figure 8.20 trend. Please note how low the

Pamb Troom R is if compared with previous complexes in this thesis which marks this complex as a promising candidate. The *R* response to the applied *T* indicates that the sample behaves as a semiconductor with *Pamb* BG value being calculated to be 0.5252 eV which is five times bigger than the BG of the polymorph 1.

Although the acquired *R* - *T* data on the GDC1 polymorph 2 indicated the necessity in producing the elevated *P* analyses to determine if the *R* and, therefore, ρ would drop with the applied *P*, this has not been done since the produced sample material quantity was not sufficient. It is, however, the material which clearly needs more attention and will be mentioned in the 9th chapter of this thesis.

8.9 The GDC2 complex

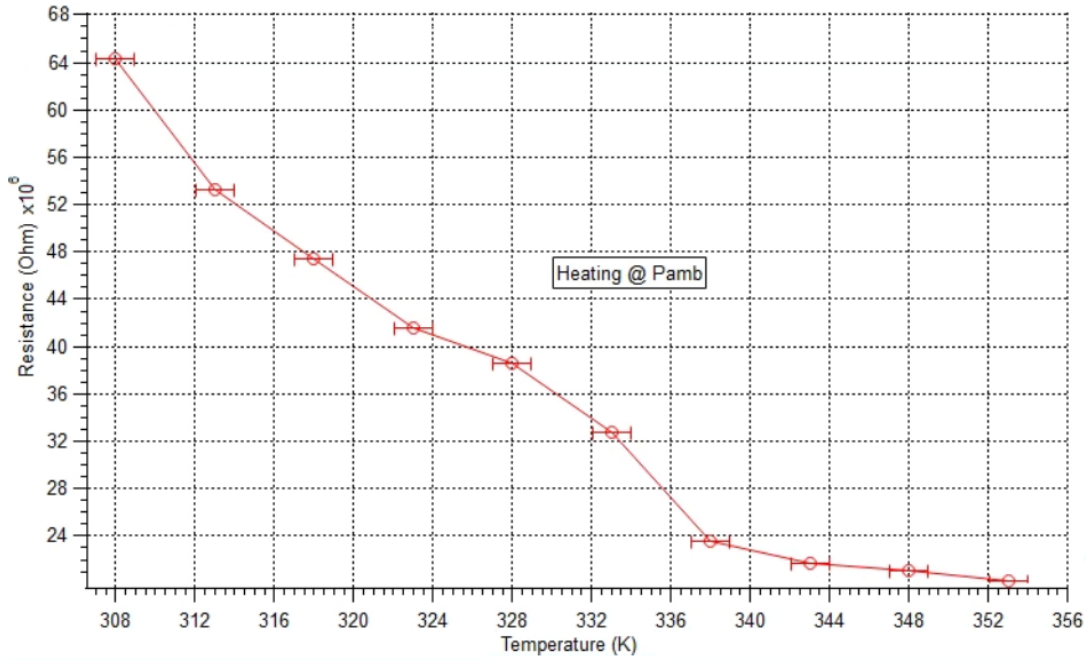

Figure 8.21: *R* vs *T* at *Pamb* for GDC2 heating.

The *R* - *T* analysis at *Pamb* for GDC2 complex was performed on a CPP using a heat gun resulting in the trend shown in figure 8.21. Generally, the semiconductor character was there with some uncertainty in 4th, 5th and 6th *R* points which are corresponding to 318, 323 and 328° K respectively and were found to be higher than expected. The possible explanation was the lack of quality during the monitoring procedure with the employed technique and it was decided to repeat the *R* - *T* analysis using the cooling technique in PPMS.

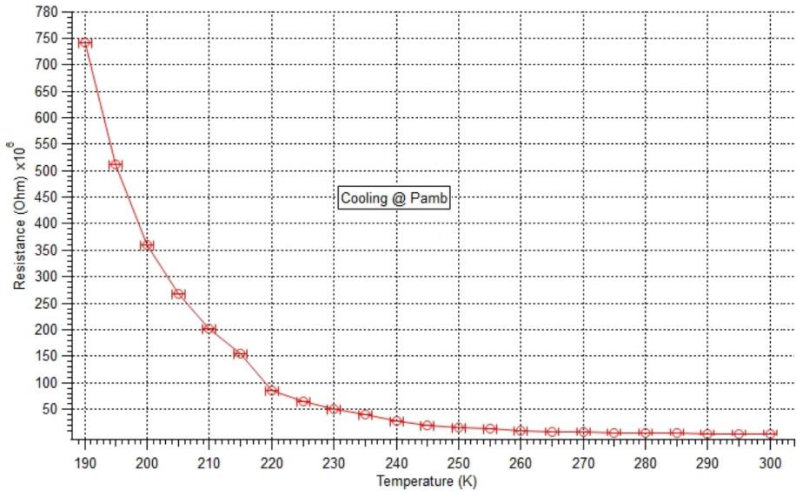

Figure 8.22: *R* vs *T* at *Pamb* for GDC2 cooling [223].

The PPMS which allowed more *T* control allowed to produce *R* - *T* analysis at *Pamb* for the GDC2 complex by subsequently cooling it from 300 to 190° K in 5° K/min steps with equilibration for 10 s at each 5° K interval to collect the stabilized *R* readings. The observed sample behaviour (See figure 8.22) indicated the semiconductor character of the complex material. Using the data from figure 8.21 & 8.22 the *Pamb* BGs were calculated to be 0.5161 and 0.5073 eV respectively, indicating both: the consistency in between employed techniques (although the trend was not precise enough in figure 8.21) and the necessity in producing elevated ρ - *P* analysis on this complex. Due to the low BG value, it was decided to employ the PCC.

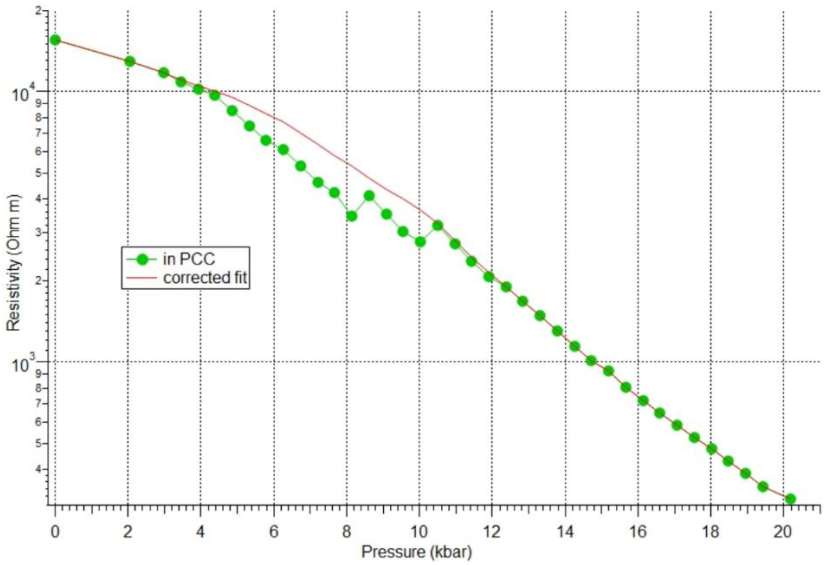

Figure 8.23: ρ vs *P* for GDC2.

According to figure 8.23, the ρ of the GDC2 complex was found to undergo 3 orders of magnitude change between *Pamb* and 20 kbars. The green curve represents the raw data which was collected during the experiment duration and the red line represents the corrected fit. The uncertainty in ρ between 8 and 10.5 kbars was associated with the PTM leakage issues due to the not sealed until the 10.5 kbars sample chamber from the piston side. This is a common issue when the copper sealing ring which is located in between PTFE capsule and piston (See figure 4.12) has not deformed yet due to low *P* being exerted on it and, therefore, small PTM leaks are present. The fact that there were no ρ jumps after 10.5 kbar (*P* at which copper ring sealed the system) only supports this statement. It was decided to introduce the corrected fit in between 4 and 10.5 kbars to illustrate the more realistic sample behaviour. Further *P* increases were omitted to avoid the damage to the feedthrough plug since it was not worth risking it for the observed ρ - *P* trend, the rough extrapolation of which predicts the conductor character approximately at 57 kbars (e.g. way above the suitable OPET operation range in terms of *P*) if we take the fact that the slope of the line, which is observed between 11 and 20 kbar, will be the same.

8.10 Other complexes

The $Pt(OBu)_2$, $Pt(Bu\text{-}bqd)_2$, PTC2, PTC3, $Ir(CO)_2(dbm)$, Cu and Co complexes were found to have *Pamb Rs* being higher than those Electrometer can measure (e.g. > 200 TΩ) even when combined with elevated *T* studies up to the 353° K (which in theory should have lowered their *Rs* in accordance with figure 2.5) indicating the inability and, therefore, the inexpediency in producing the elevated *P* studies on these materials.

Chapter 9

Conclusions and future directions

This chapter summarises the completed work, highlights the achievements of this PhD research through the conclusions and outlines future potential directions of the project.

9.1 Conclusions

The original direction of this research was the instrumentation development to realize the OPET which implied the creation of the new or adaptation of the existing HP devices to study the selected in the 2nd chapter materials at *Pelevated* and variable *Ts* for their electric γ.

An author has successfully developed and tested two HP devices: PCC and UHPC. The former device is capable of producing static *P* experiments and reaching 3 GPa of hydrostatic *P* while allowing to *in situ* monitor the *R* of the test specimen as well as the *P* it is exposed to with high precision. The *Pelevated* - ρ studies in PCC can also be combined with the *T* analyses using constant *T* varying *P* method. The latter device was designed to produce both: static and dynamic uniaxial *Ps* and was built to mimic the OPET device concept to measure the electric γ of a thin film material through its thickness.

An author has also adapted the existing HP device – the Merrill Bassett DAC for the electric γ measurements. The DAC was equipped with NiCrAl seats to safely achieve the static hydrostatic or quasi hydrostatic pressures up to the 10 GPa using 0.8 mm in diameter diamond cullets. To allow producing the electric γ measurements in the DAC an author developed special techniques and procedures which he outlined in the 7th chapter to achieve the experimental success.

An author has also successfully applied the relevant for the anisotropic nature of the selected PR materials method for *R* into ρ conversion [119]. Both: PCC and DAC are capable of employing this method which requires high precision in the probe contact allocation on the specimen resulting in the ability to produce 4-probe *R* measurements with the consistency in the interpreted data between both HP devices (See figure 8.4).

An author has also developed the necessary set of skills and knowledge for the exploitation of the required, to produce the measurements of interest, instrumentation which include DMM, Electrometer, CCR, PPMS and PVD systems.

Among various successfully tested PR materials, the most promising candidate in terms of a ρ change within the OPET *P* operation range which was mentioned to be 0

– 3 GPa was found to be $Pt(bqd)_2$ complex. The complex was successfully deposited on top of the deposited gold layer on a substrate with preferred needle orientation and measured in the modified version of the gasket indenter (See figure 7.7) since the pre-cut WC balls with a perfectly flat cross-sectional area (for the UHPC device) were not available for delivery due to COVID-19 interruption.

9.2 Future directions

In terms of future directions, the other promising PR candidate needs to be tested – the GDC1 polymorph 2 which was found to have low *Pamb* ρ and requires HP investigation on electronic properties to determine if sample turns into conductor within the suitable OPET operation *P* range with potential study in how to deposit this material into the thin film form with the required molecular orientation.

It is also required to acquire the above-mentioned pre-cut WC balls to allow exploitation of the UHPC for the measurements on the thin film samples.

Another important future direction is the acquisition of the previously mentioned PE actuator [212] which would allow producing dynamic *P* analysis to investigate if the promising candidates are having the high On/Off ratios (e.g. if the *R* changes fast with time). This will significantly expand the project scope and, if successful, will certainly attract attention and funding. Unfortunately, such an acquisition was delayed during the COVID-19 interruption.

Appendix A

Drawings related to the 4th chapter

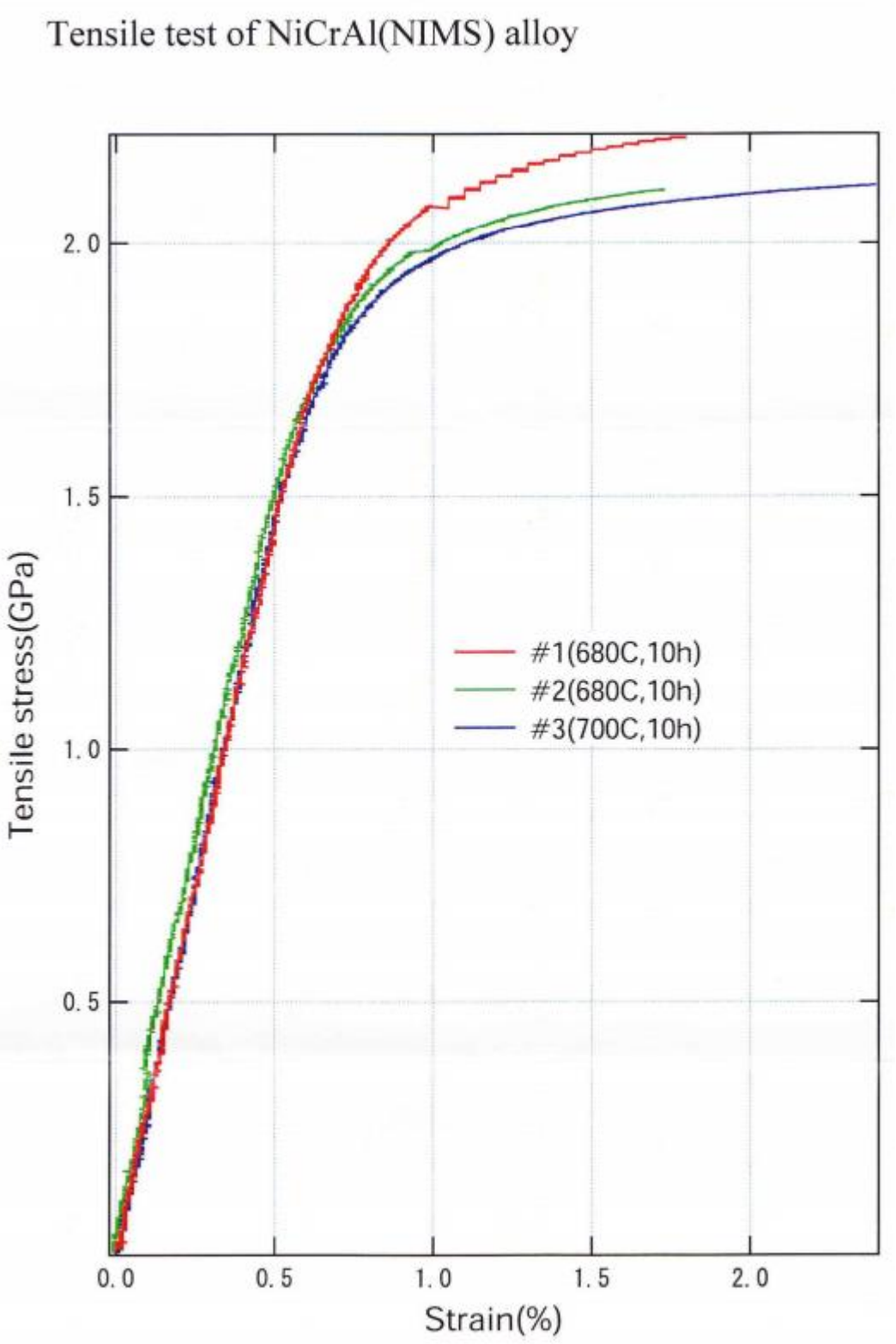

Figure A.1: The NiCrAl datasheets from supplier part one. The stress-strain curves for three specimens with different ageing procedures.

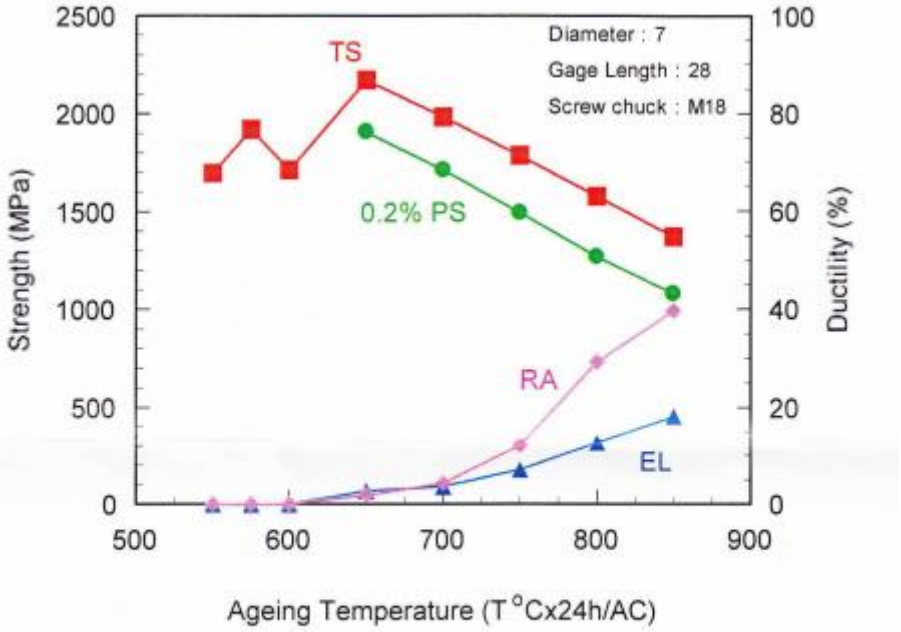

Fig. Influence of ageing temperature on tensile properties

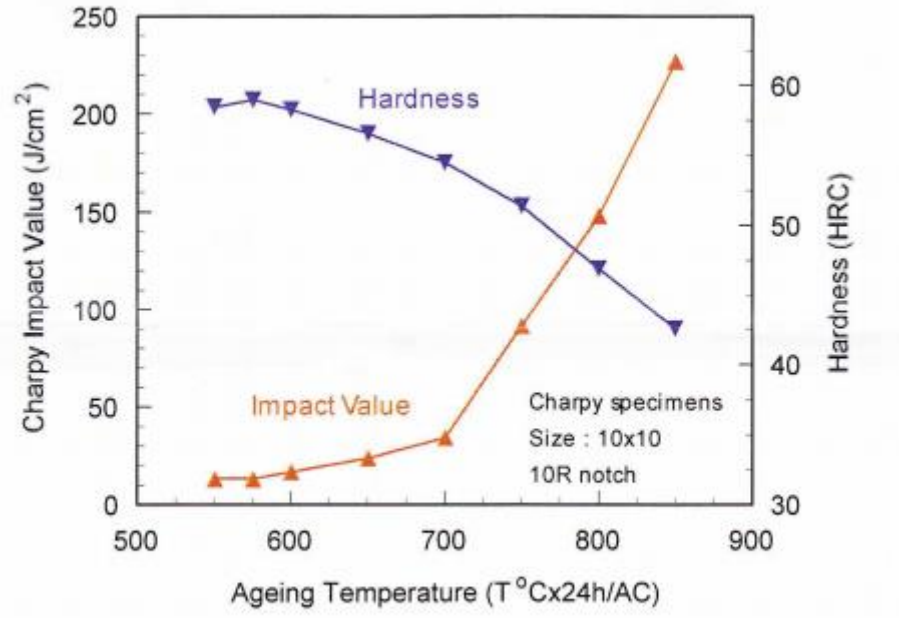

Fig. Influence of ageing temperature on charpy impact value

Figure A.2: The NiCrAl datasheets from supplier part two. Ageing procedure guidelines with two figures with names as specified underneath of each graph.

		Under 3000MPa of pressure			Under no pressure	
		Von Misses	Radial	Tangential	Radial	Tangential
	Length [mm]	Value [MPa]	Value [MPa]	Value [MPa]	Value [MPa]	Value [MPa]
1	0.	2200.	-2907.3	-376.81	-6.9998	-1140.7
2	0.31771	2199.9	-2653.6	-126.25	-132.67	-1015.1
3	0.63542	2181.2	-2379.3	123.58	-223.44	-924.33
4	0.95313	2148.1	-2118.2	344.56	-289.77	-858.
5	1.2708	2104.6	-1884.9	527.32	-339.43	-808.32
6	1.5885	2055.5	-1675.7	680.82	-377.31	-770.36
7	1.9063	1939.7	-1509.8	713.67	-405.17	-742.39
8	2.224	1718.6	-1355.8	610.68	-427.23	-720.19
9	2.5417	1469.3	-1210.3	465.32	-446.82	-700.46
10	2.8594	1305.6	-1114.5	369.38	-460.98	-686.13
11	3.1771	1160.1	-1029.	283.77	-473.55	-673.34
12	3.4948	1039.7	-957.88	212.58	-483.92	-662.71
13	3.8125	941.31	-899.53	154.12	-492.37	-654.02
14	4.1302	852.26	-846.37	100.86	-500.02	-646.11
15	4.4479	781.95	-804.03	58.635	-505.89	-639.8
16	4.7656	718.21	-765.43	19.918	-511.37	-634.1
17	5.0833	663.61	-732.22	-13.754	-516.29	-629.23
18	5.401	615.94	-702.48	-42.373	-519.46	-624.84
19	5.7188	571.77	-674.64	-68.999	-522.25	-620.74
20	6.0365	542.03	-657.41	-92.305	-529.37	-618.41
21	6.3542	1395.5	-608.5	1001.1	-501.73	811.47
22	6.6719	1294.7	-550.18	942.86	-453.69	763.78
23	6.9896	1209.8	-500.91	893.84	-413.07	723.6
24	7.3073	1130.1	-454.73	847.85	-374.98	685.91
25	7.625	1057.9	-412.9	806.14	-340.47	651.72
26	7.9427	994.23	-375.99	769.3	-309.99	621.53
27	8.2604	934.28	-341.26	734.61	-281.3	593.1
28	8.5781	880.95	-310.39	703.73	-255.78	567.78
29	8.8958	832.	-282.05	675.35	-232.36	544.52
30	9.2135	785.85	-255.34	648.58	-210.27	522.57
31	9.5313	745.29	-231.89	625.03	-190.86	503.26
32	9.849	707.	-209.76	602.78	-172.54	485.02
33	10.167	671.5	-189.24	582.13	-155.56	468.09
34	10.484	638.84	-170.38	563.11	-139.95	452.5
35	10.802	608.88	-153.09	545.65	-125.63	438.19
36	11.12	580.8	-136.89	529.27	-112.23	424.77
37	11.438	554.49	-121.72	513.91	-99.671	412.18
38	11.755	530.07	-107.64	499.63	-88.027	400.48
39	12.073	507.64	-94.71	486.51	-77.35	389.74
40	12.391	486.24	-82.373	473.98	-67.168	379.48
41	12.708	466.26	-70.855	462.28	-57.675	369.9
42	13.026	447.77	-60.192	451.43	-48.907	361.03
43	13.344	430.06	-49.972	441.04	-40.516	352.53
44	13.661	413.61	-40.468	431.38	-32.737	344.64
45	13.979	398.14	-31.515	422.29	-25.435	337.22
46	14.297	383.29	-22.91	413.56	-18.434	330.09
47	14.615	369.56	-14.929	405.48	-11.981	323.51
48	14.932	356.47	-7.2921	397.77	-5.8364	317.23
49	15.25	343.88	7.3918e-002	390.35	6.6738e-002	311.2

Figure A.3: Tabular stresses in the compound cylinder.

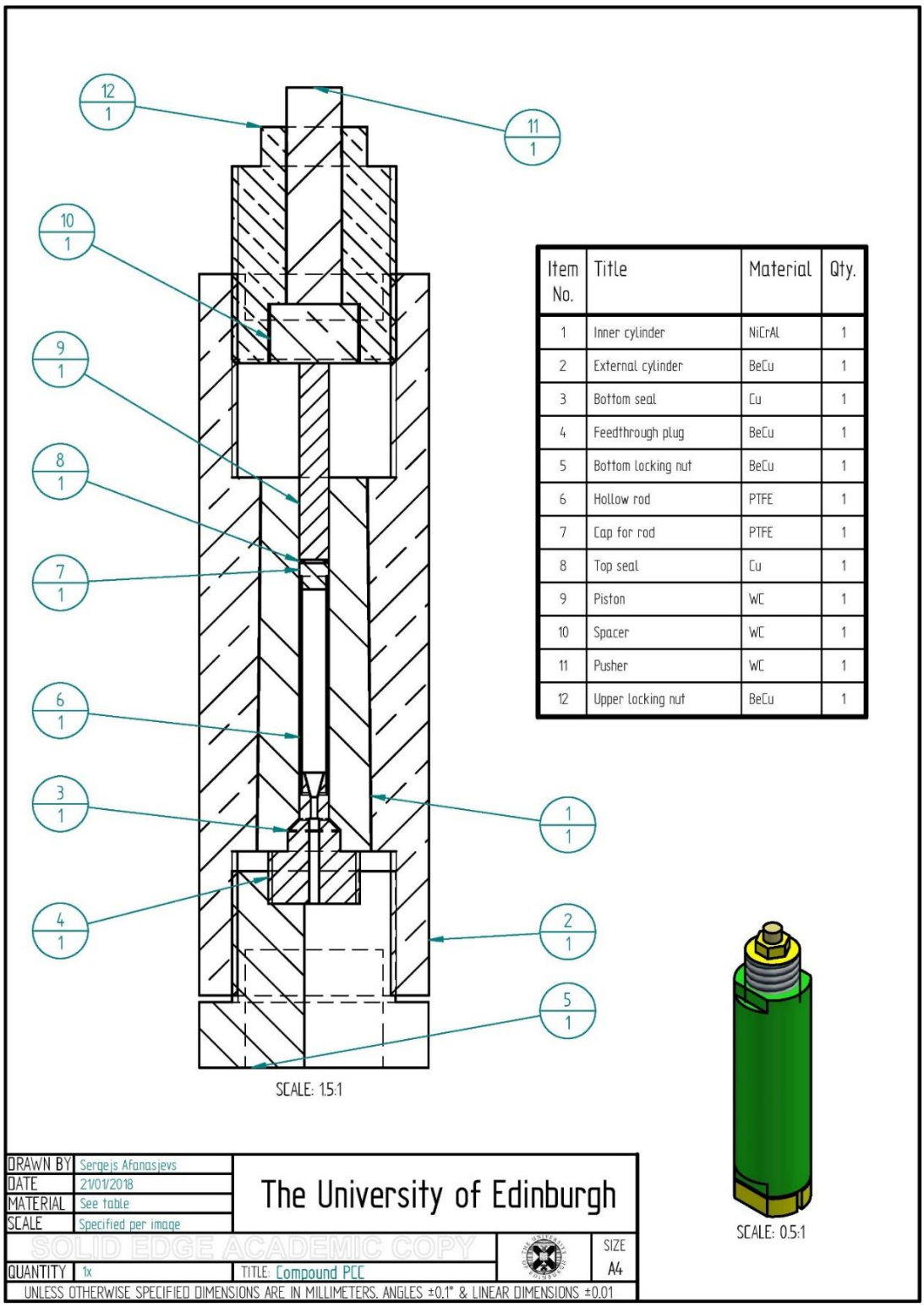

Figure A.4: Compound PCC with parts table.

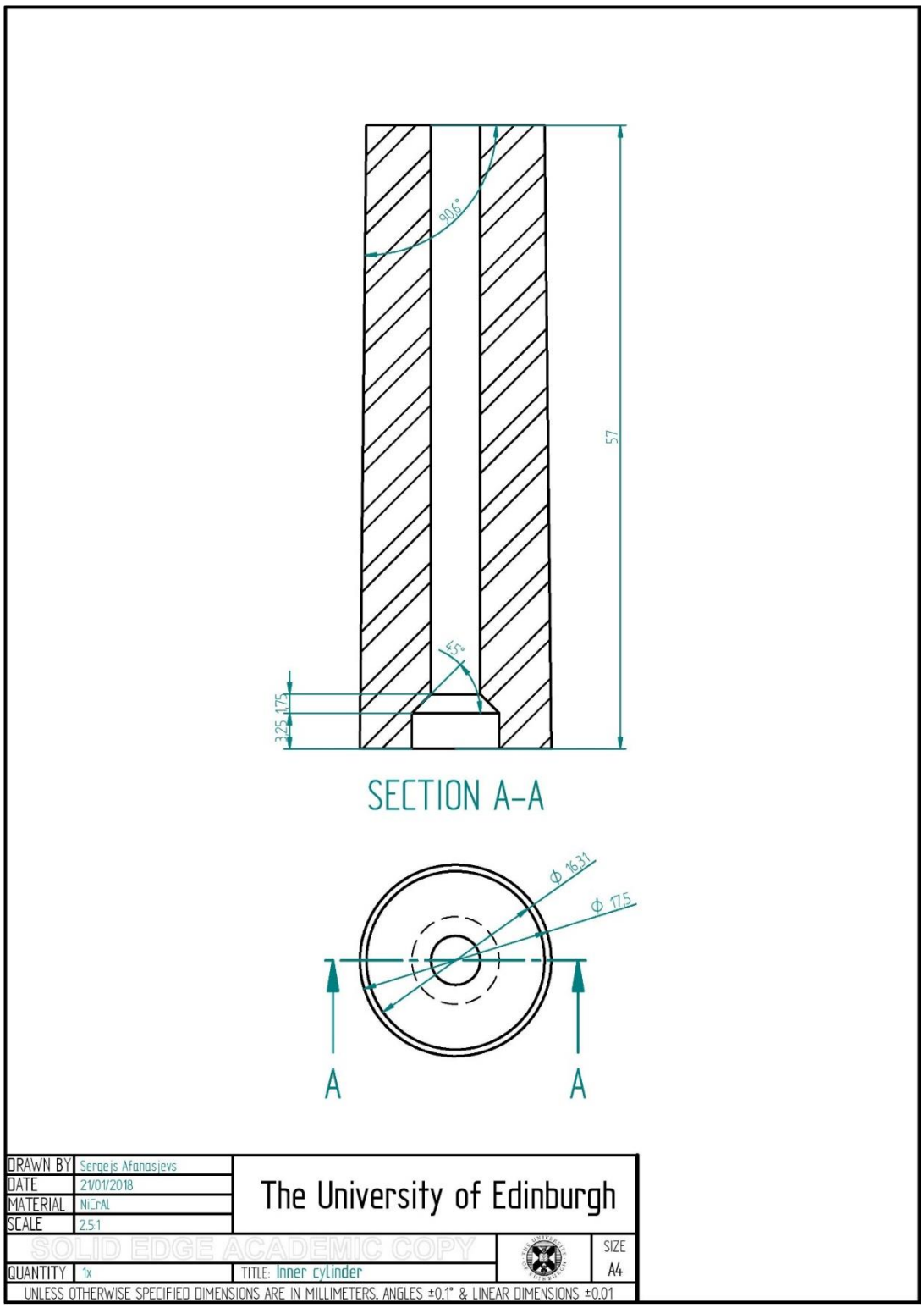

Figure A.5: Inner cylinder.

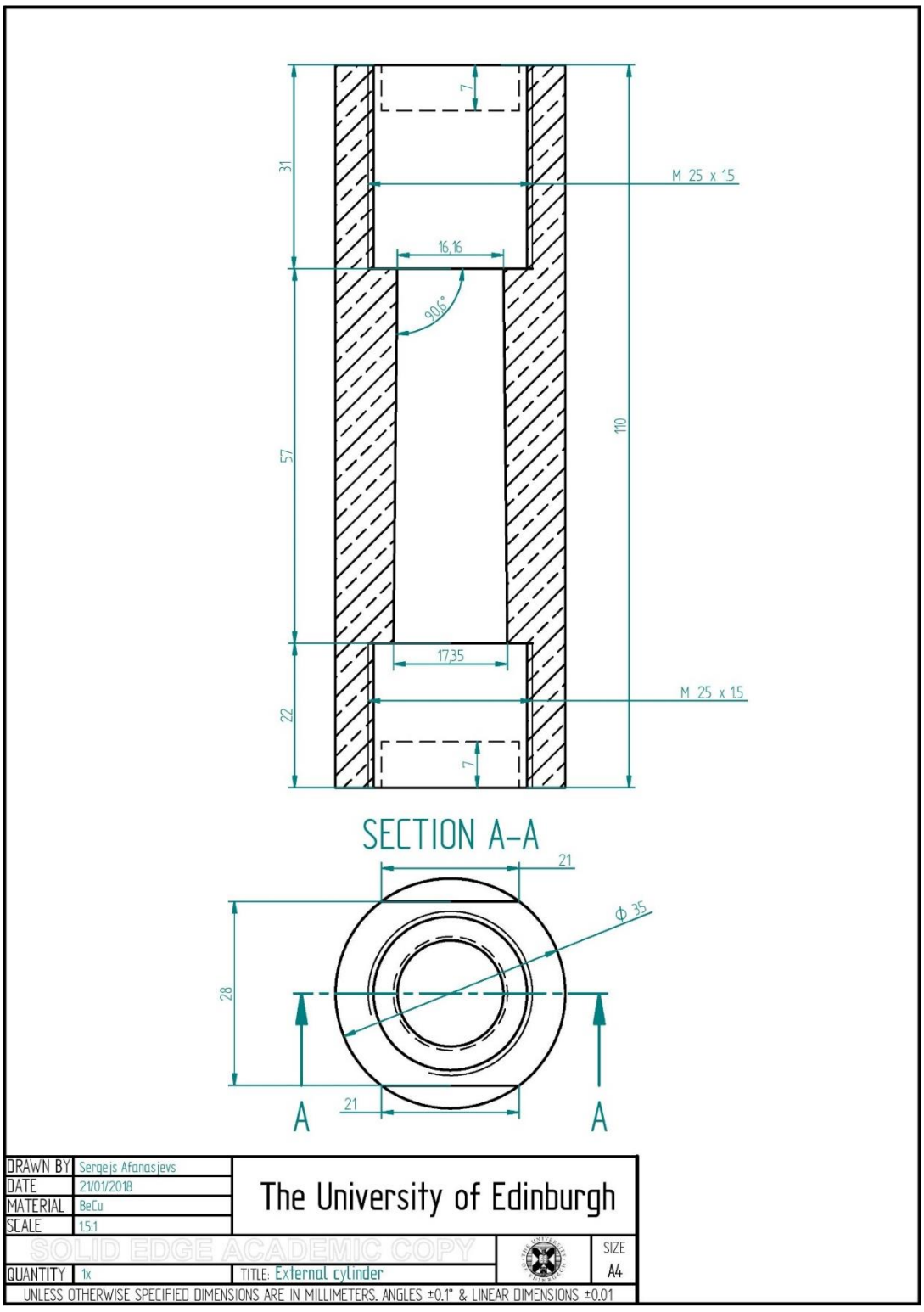

Figure A.6: External cylinder.

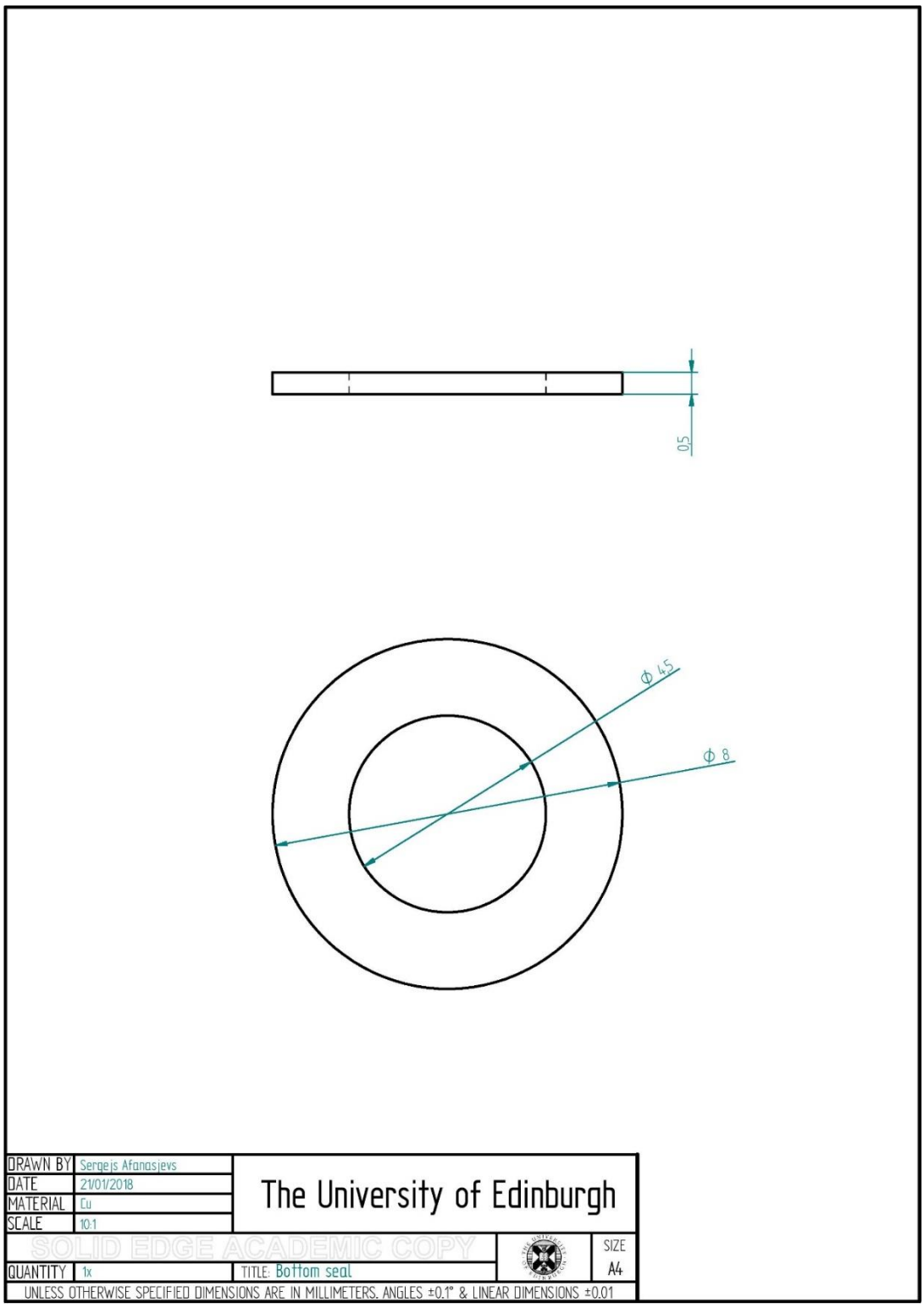

Figure A.7: Bottom seal.

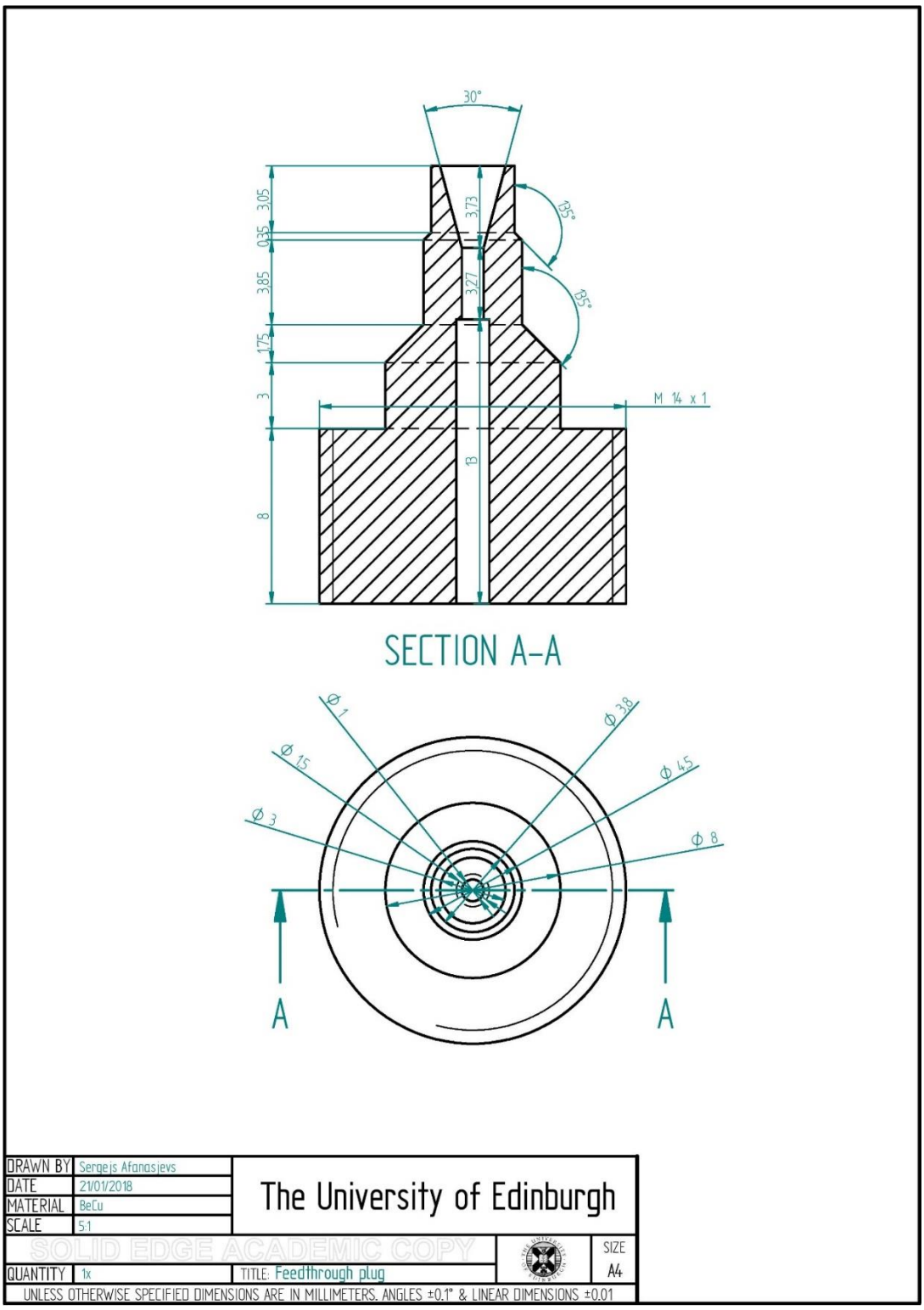

Figure A.8: Feedthrough plug.

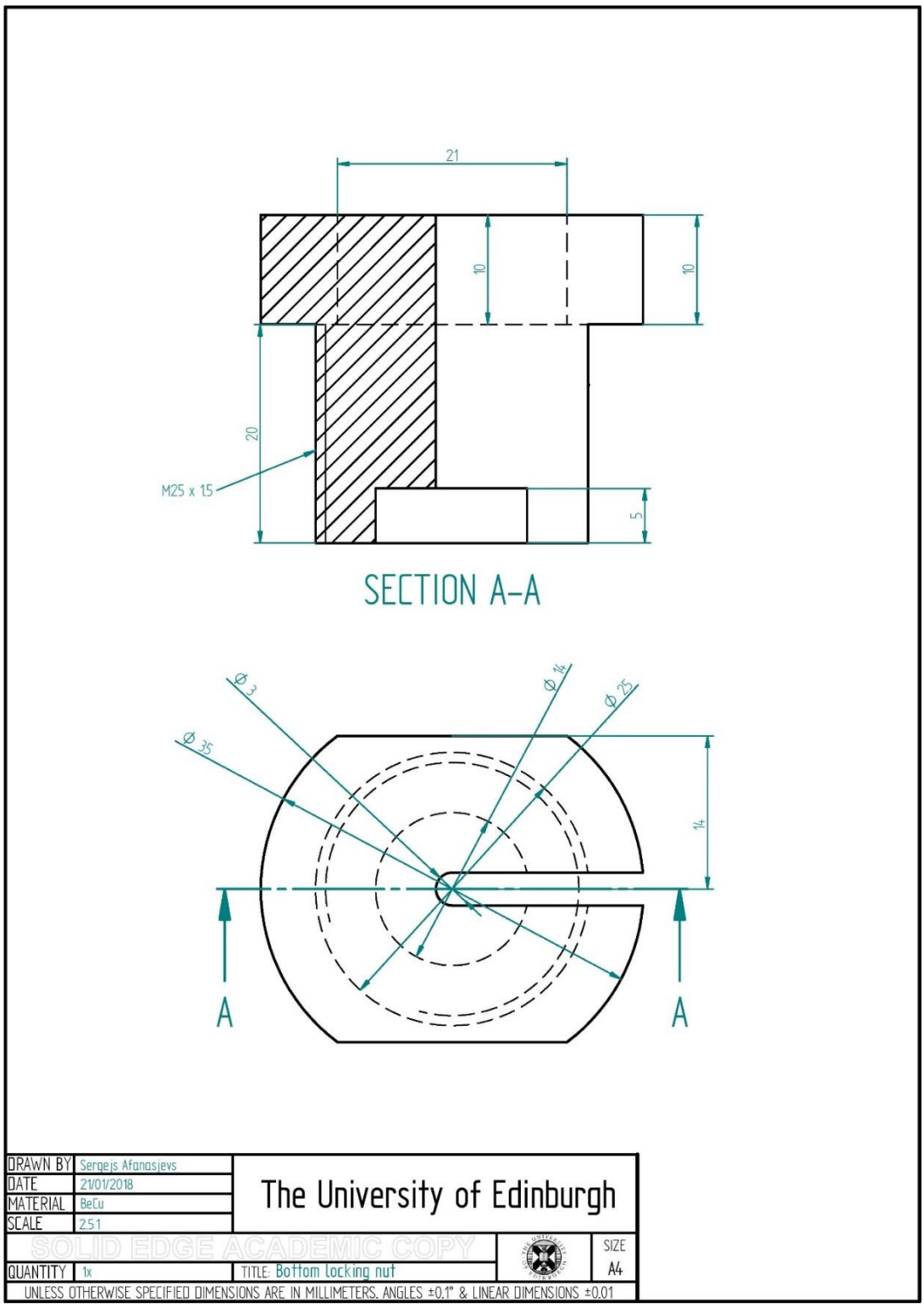

Figure A.9: Bottom locking nut.

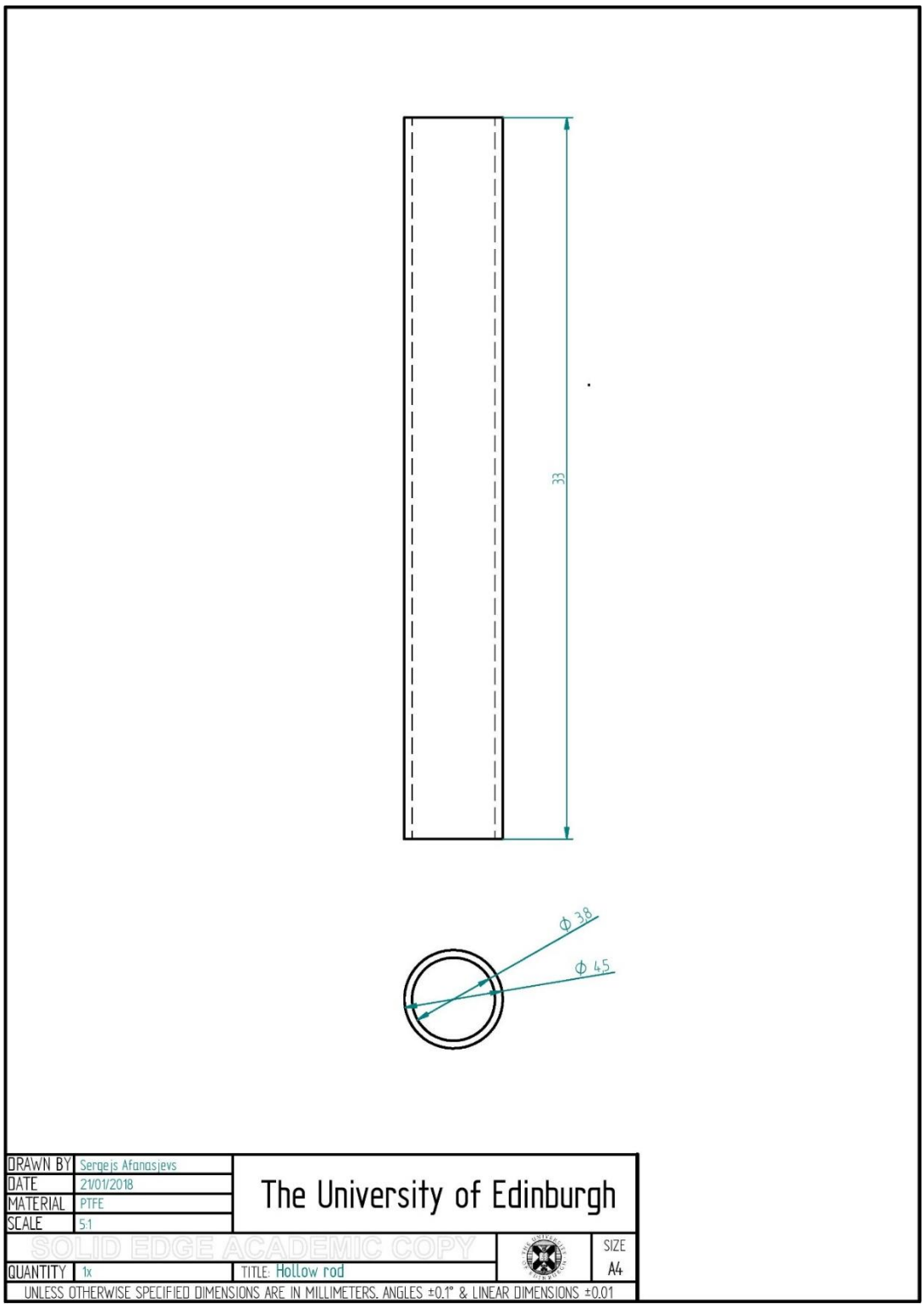

Figure A.10: Hollow rod.

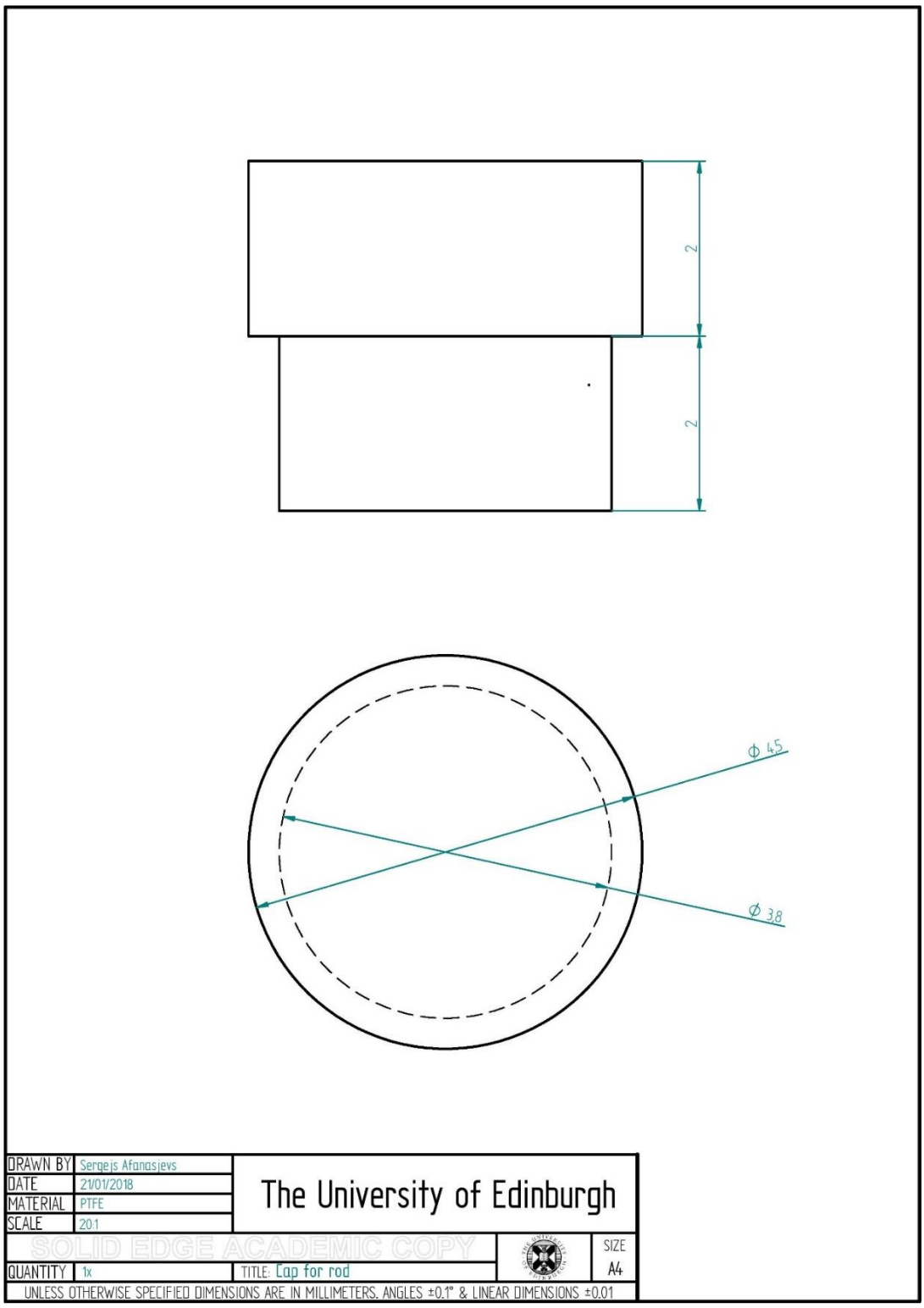

Figure A.11: Cap for the rod.

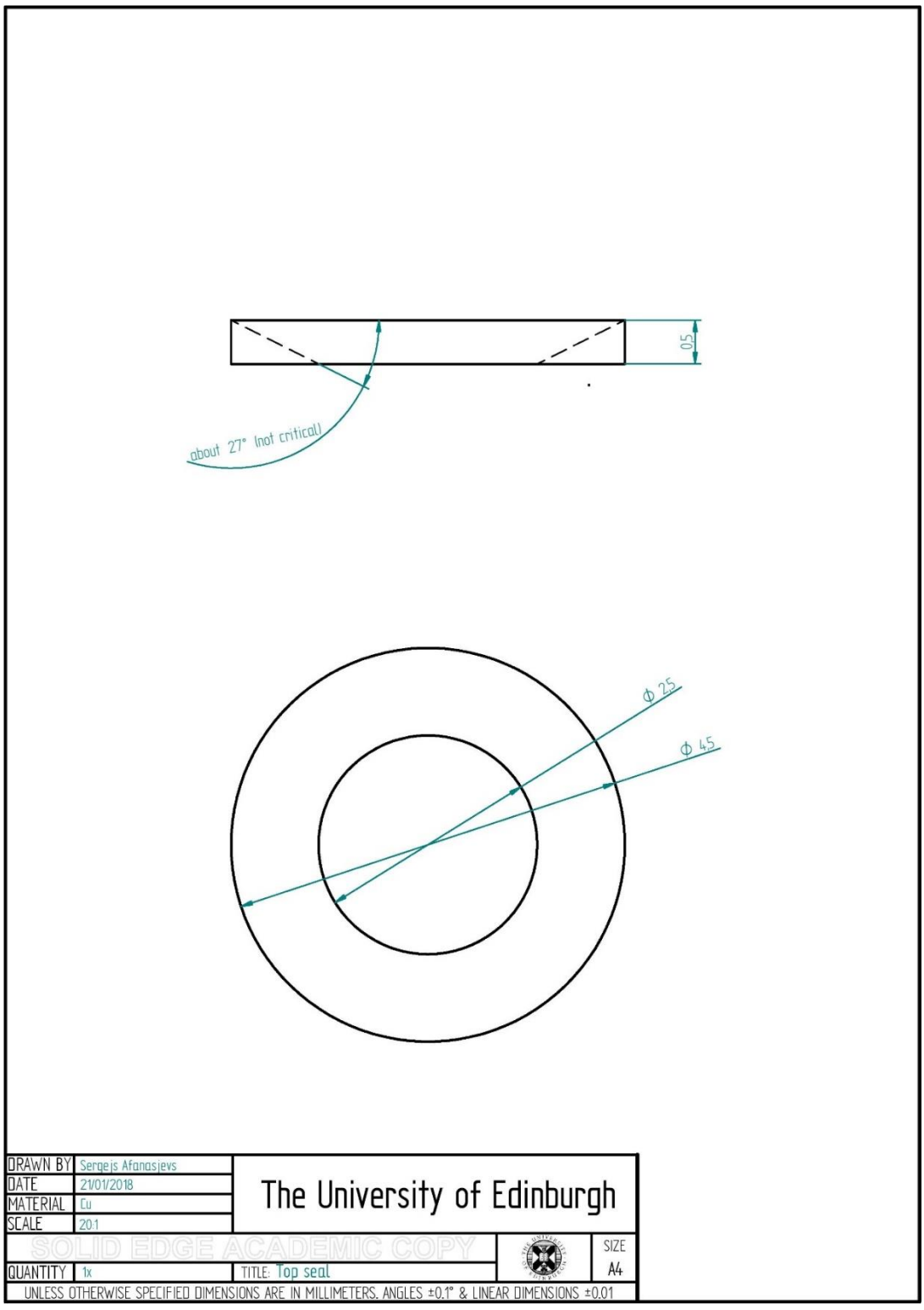

Figure A.12: Top seal.

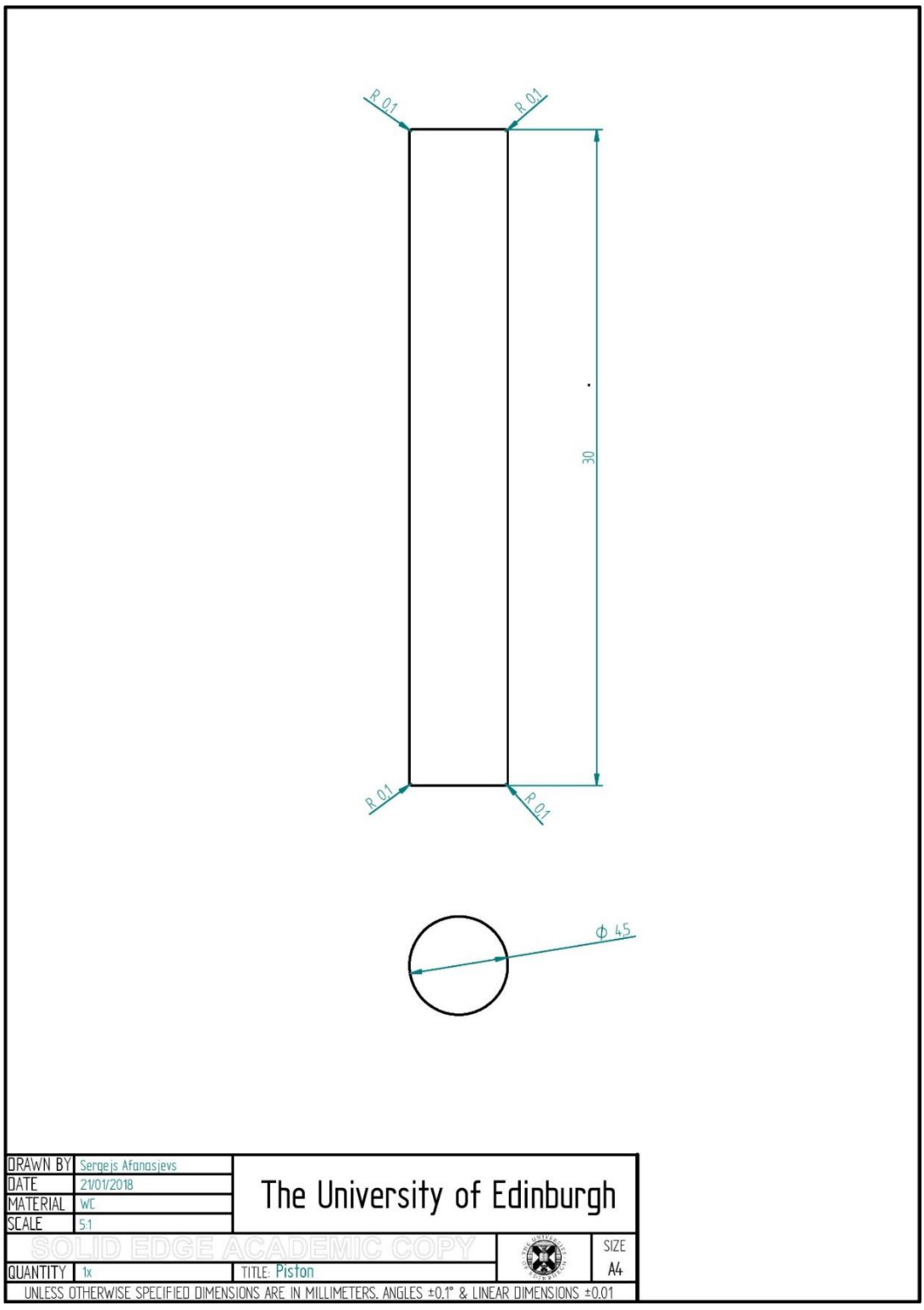

Figure A.13: Piston.

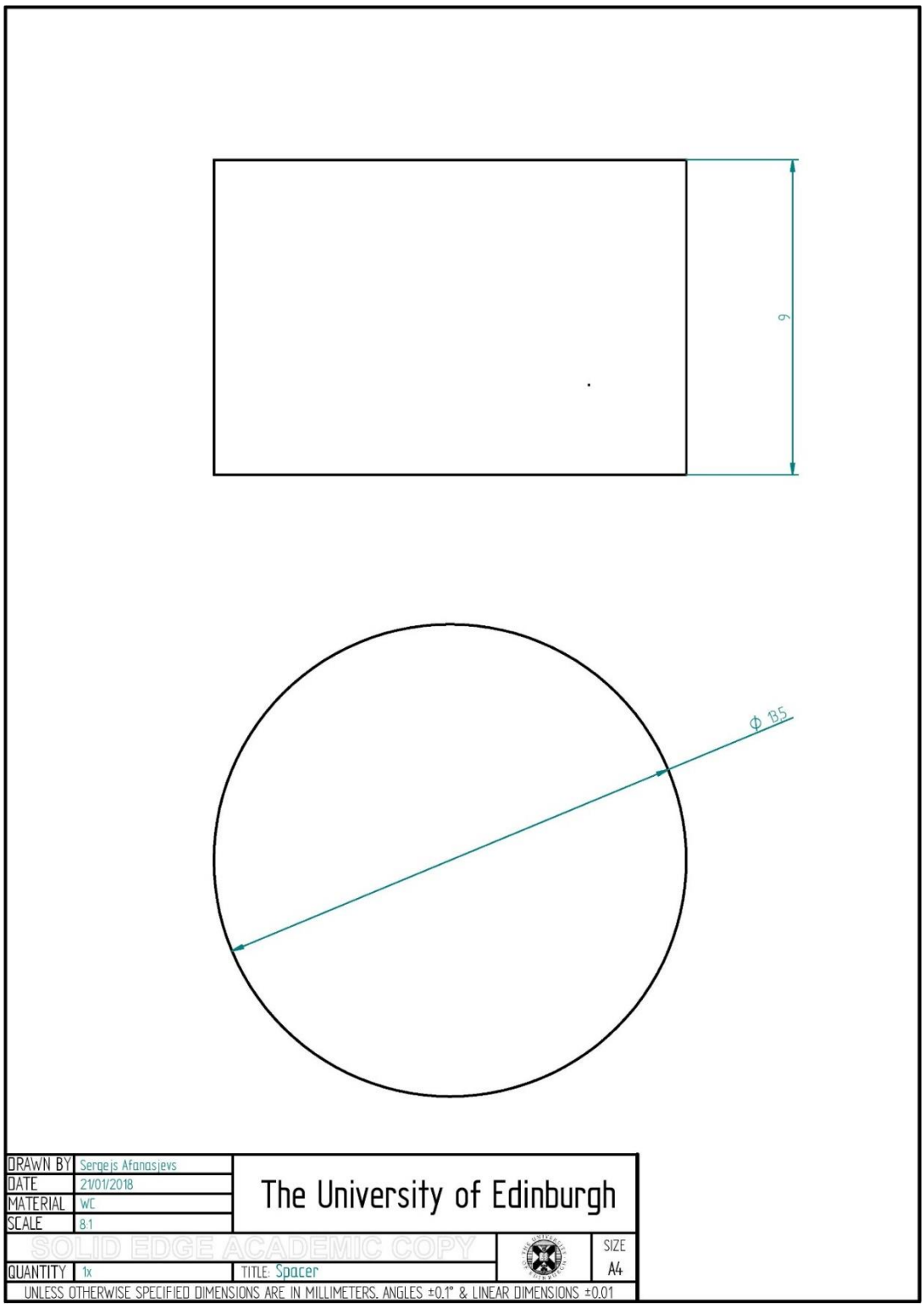

Figure A.14: Spacer.

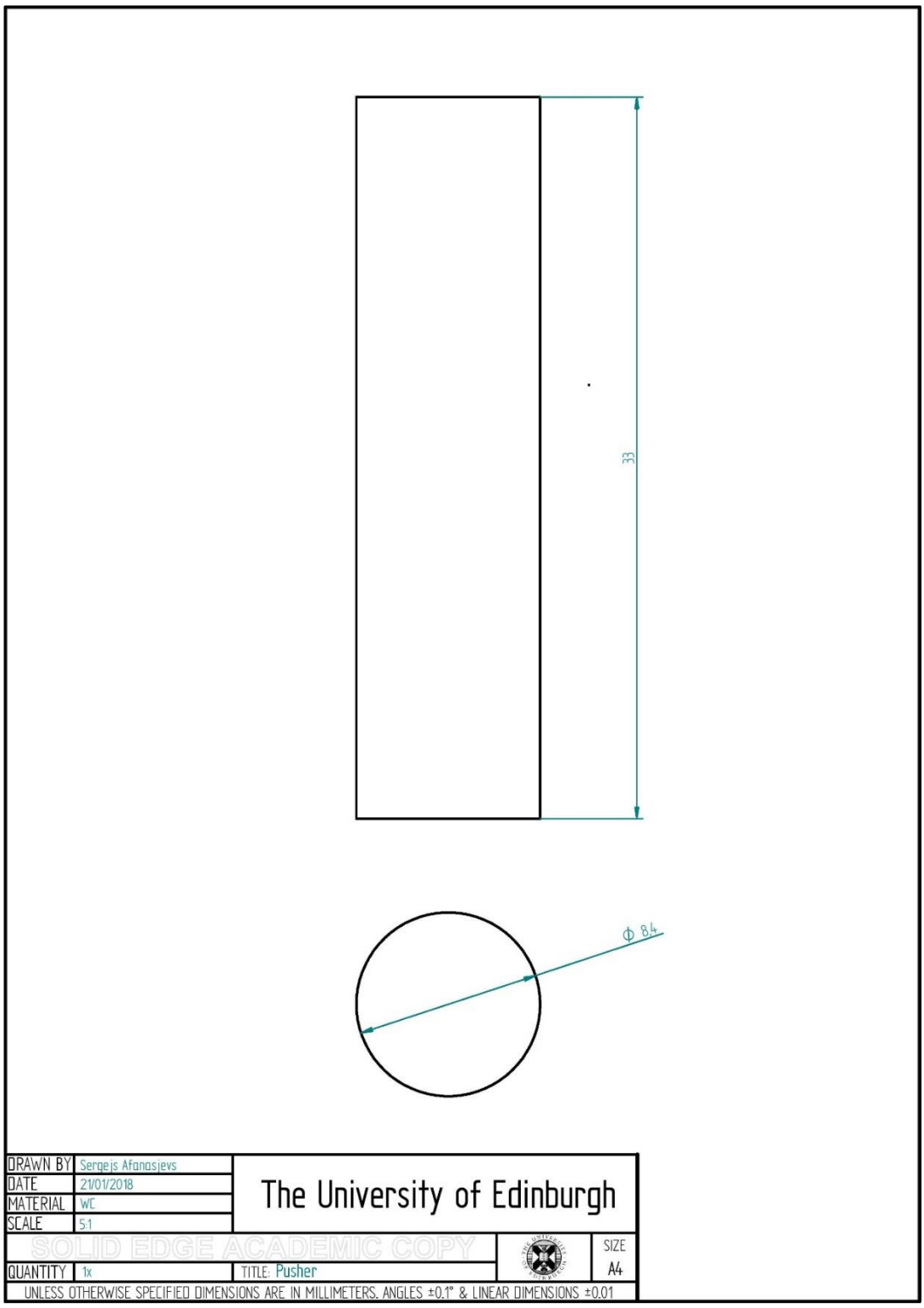

Figure A.15: Pusher.

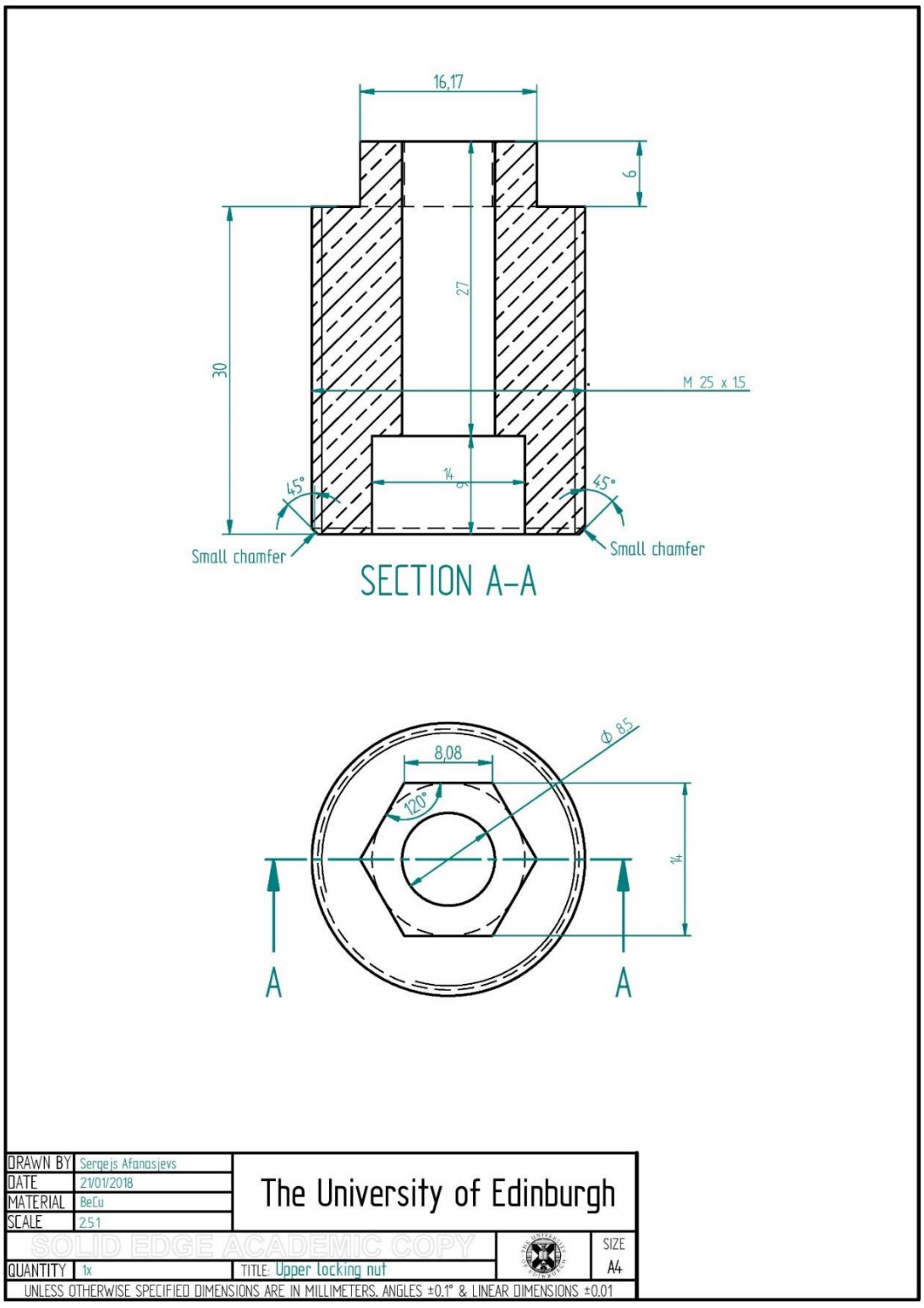

Figure A.16: Upper locking nut.

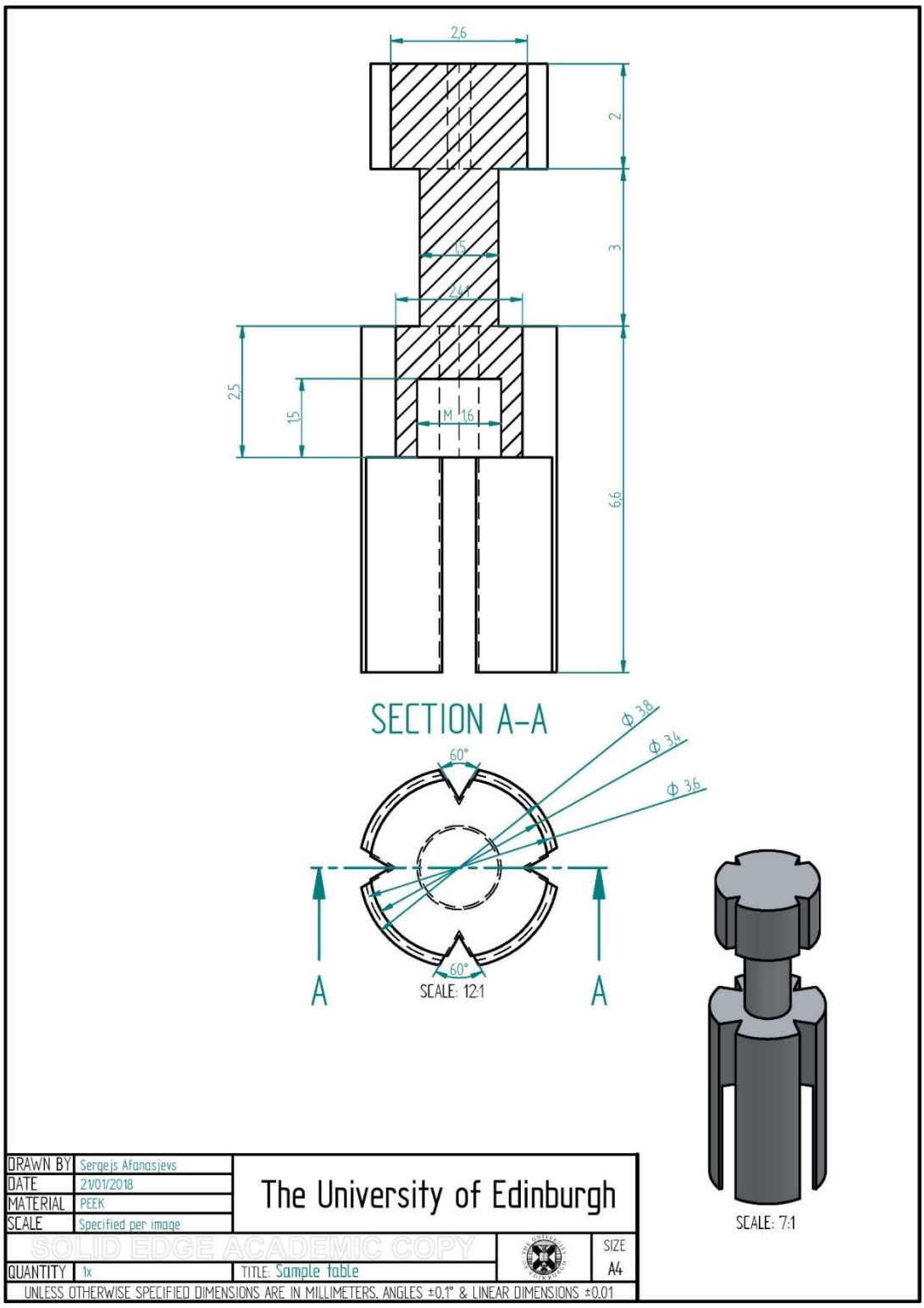

Figure A.17: Sample table.

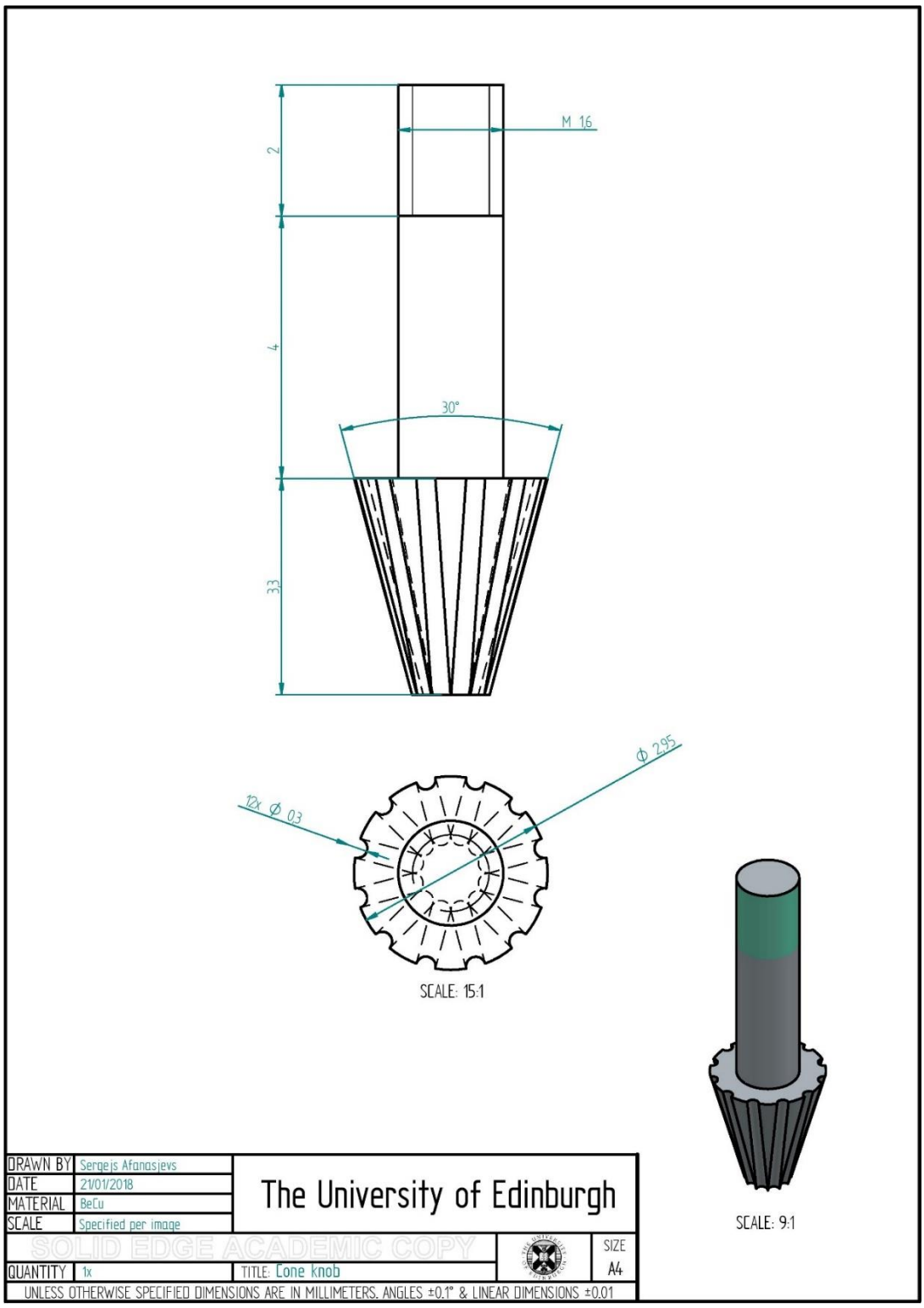

Figure A.18: Cone knob.

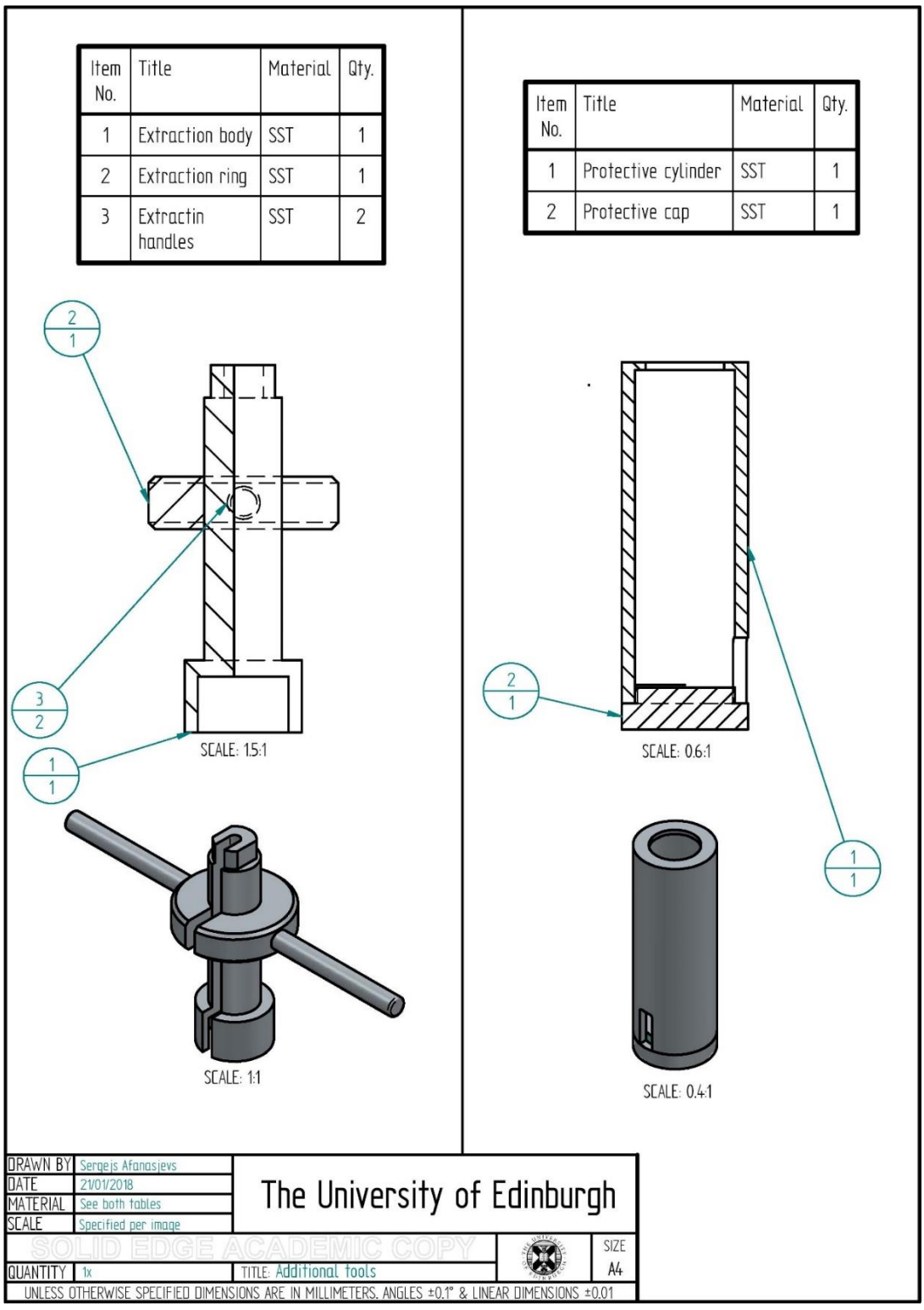

Figure A.19: Additional tools.

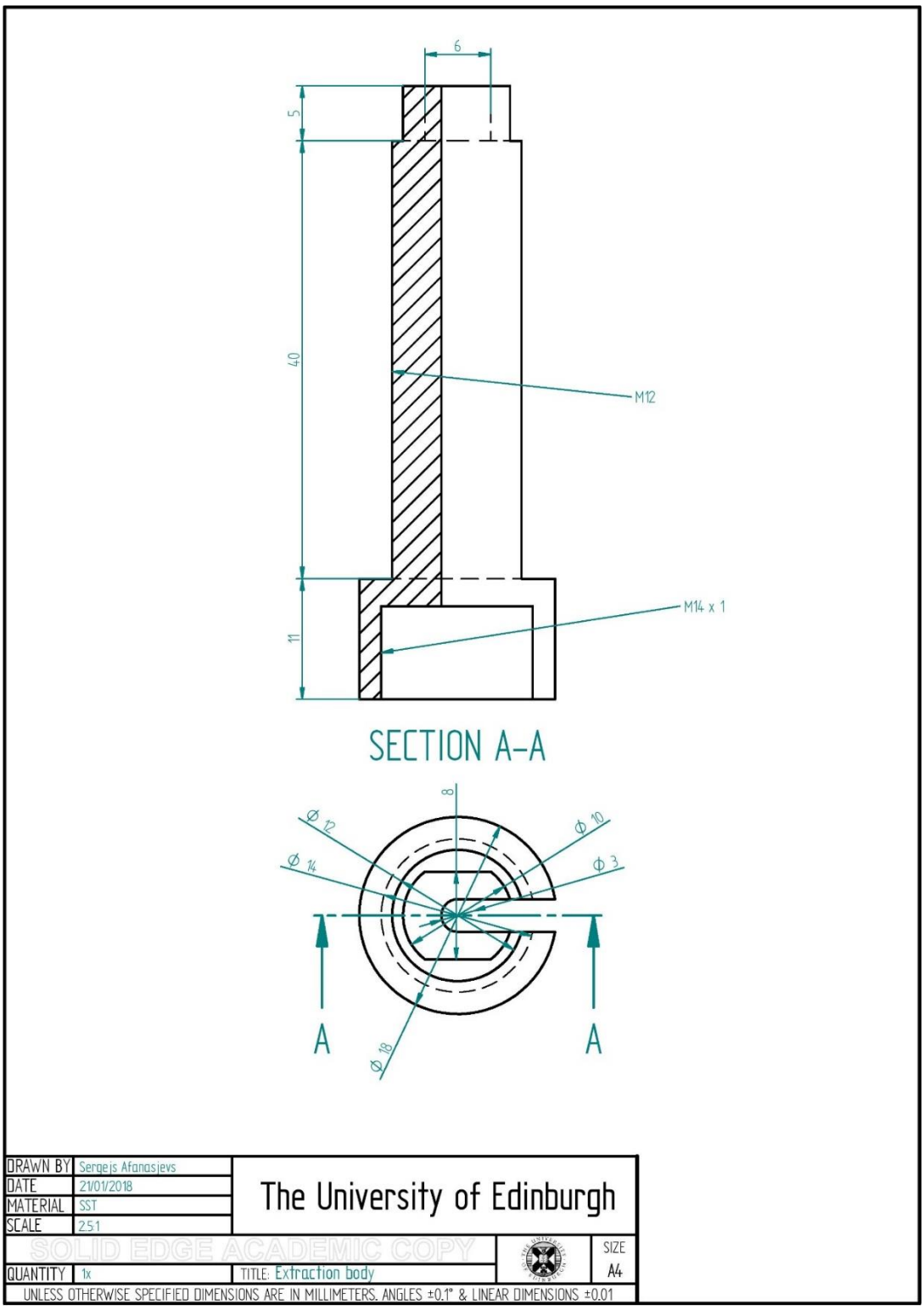

Figure A.20: Extraction body.

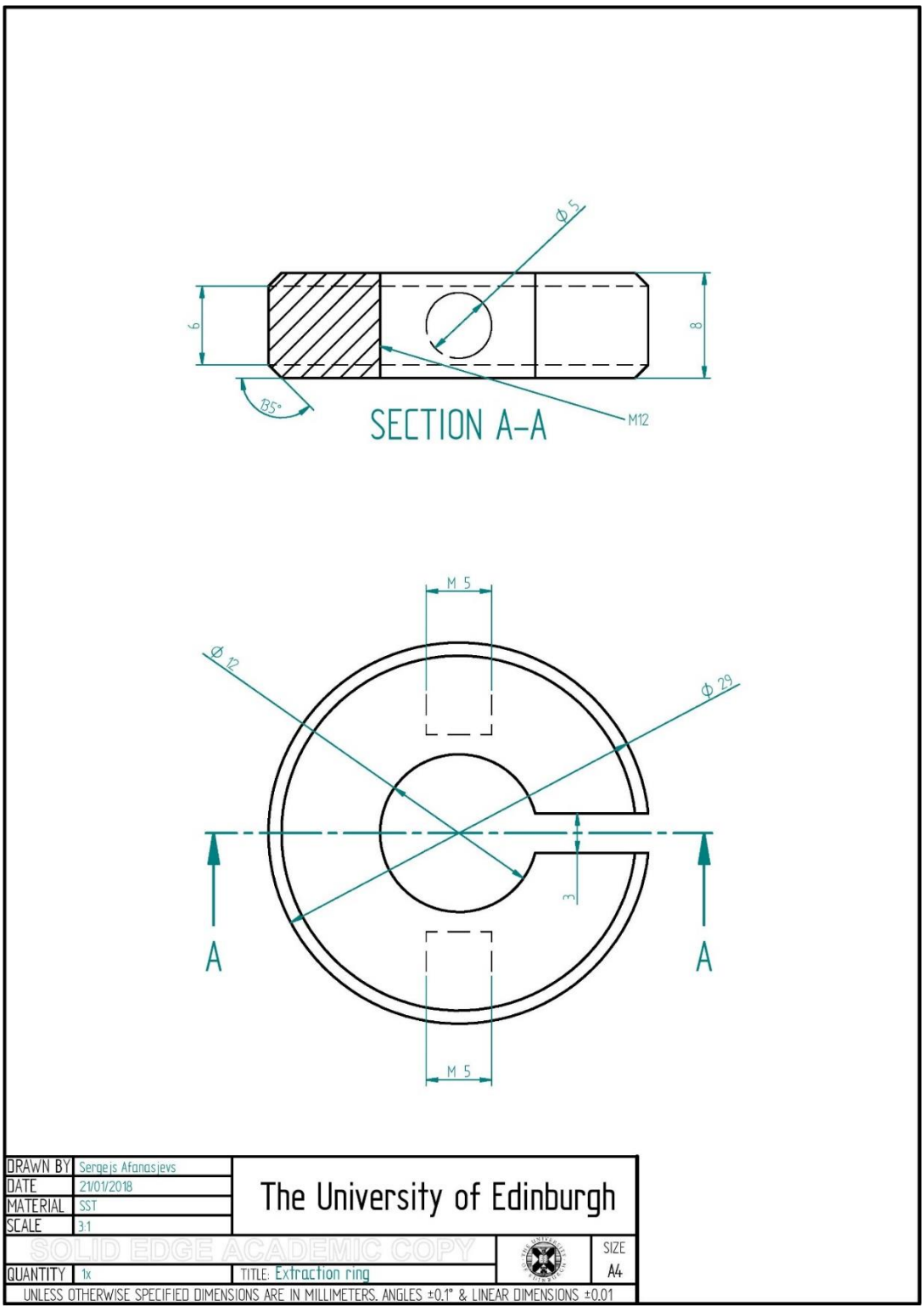

Figure A.21: Extraction ring.

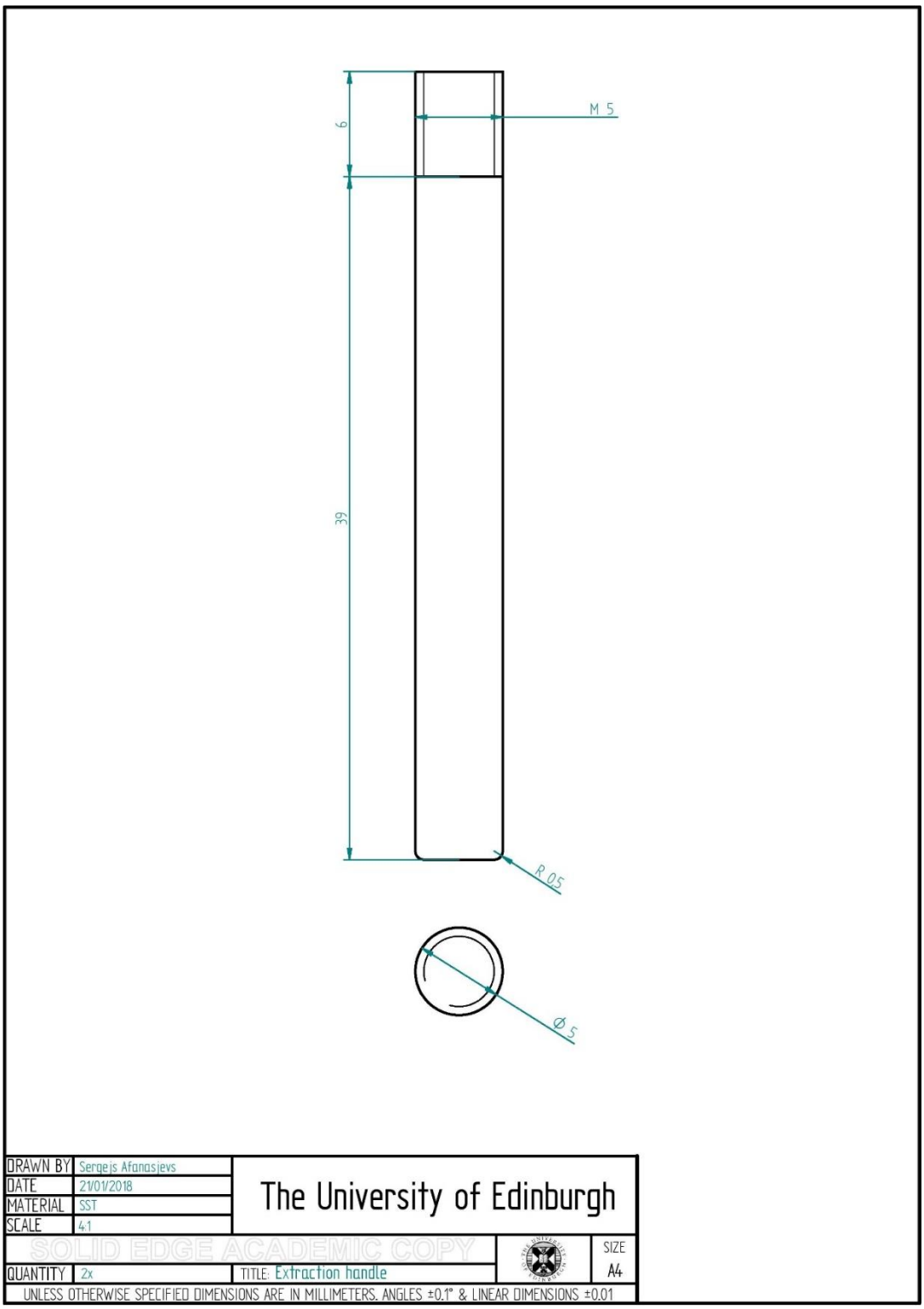

Figure A.22: Extraction handle.

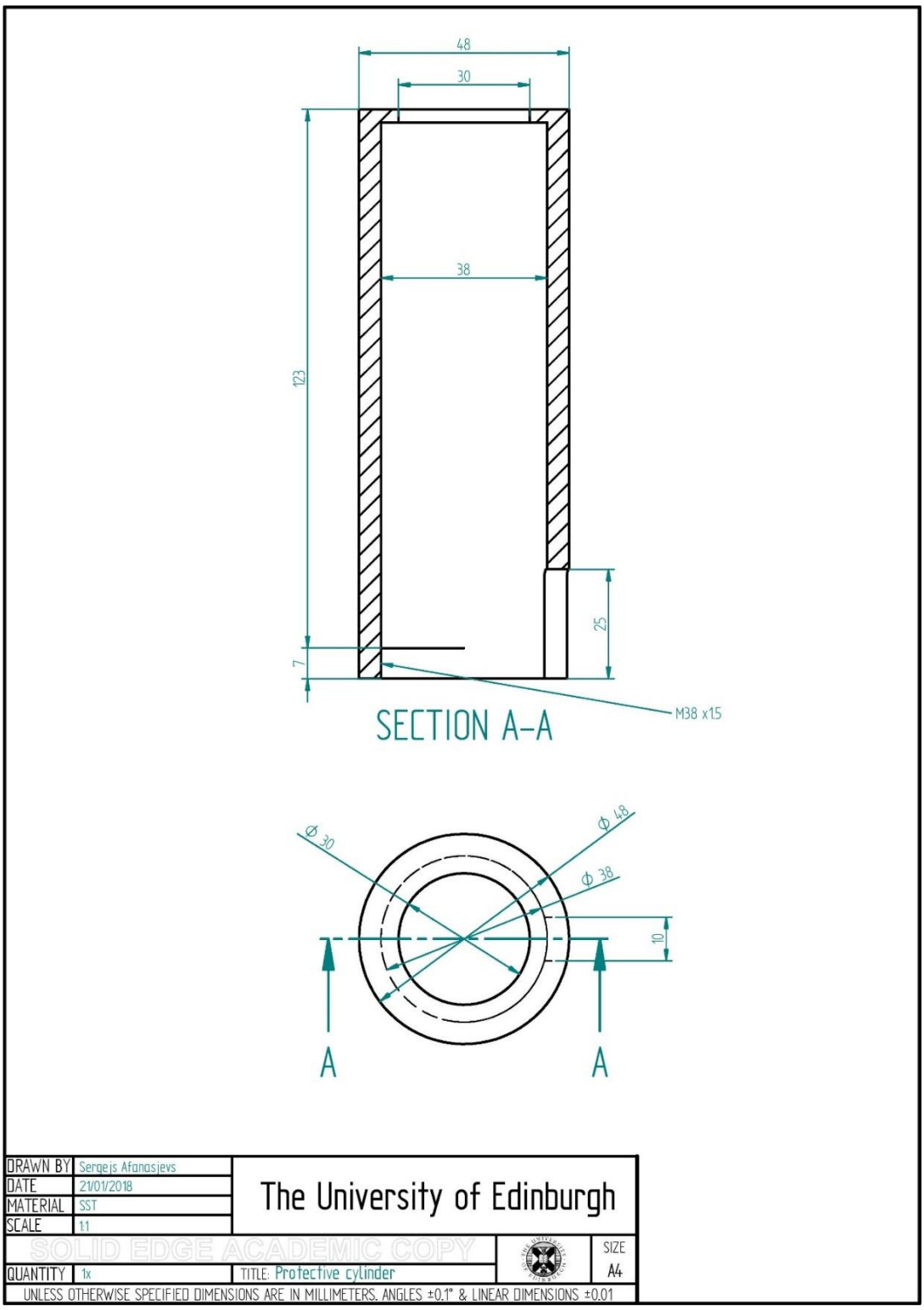

Figure A.23: Protective cylinder.

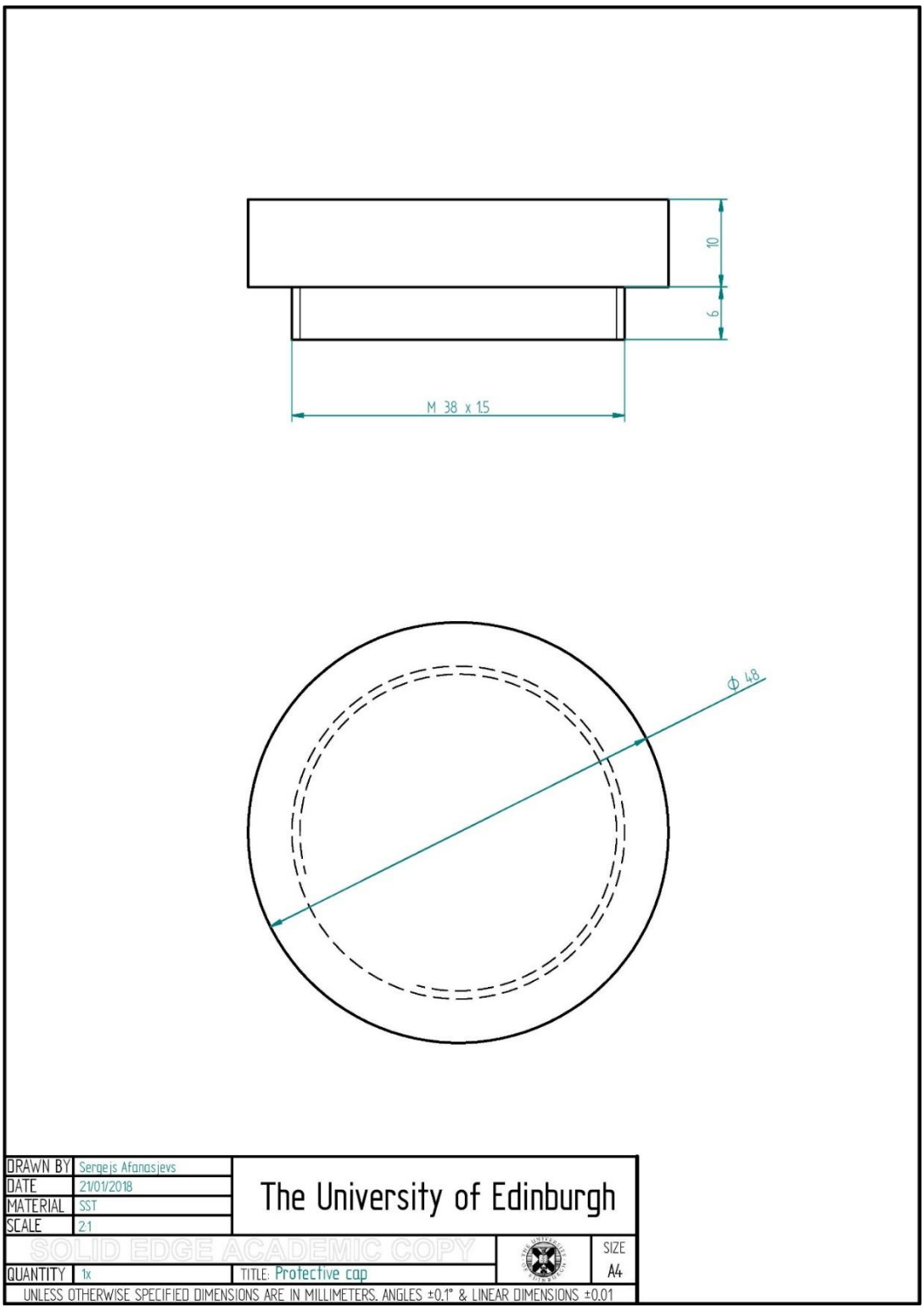

Figure A.24: Protective cap.

Appendix B

Drawings related to the 5th chapter

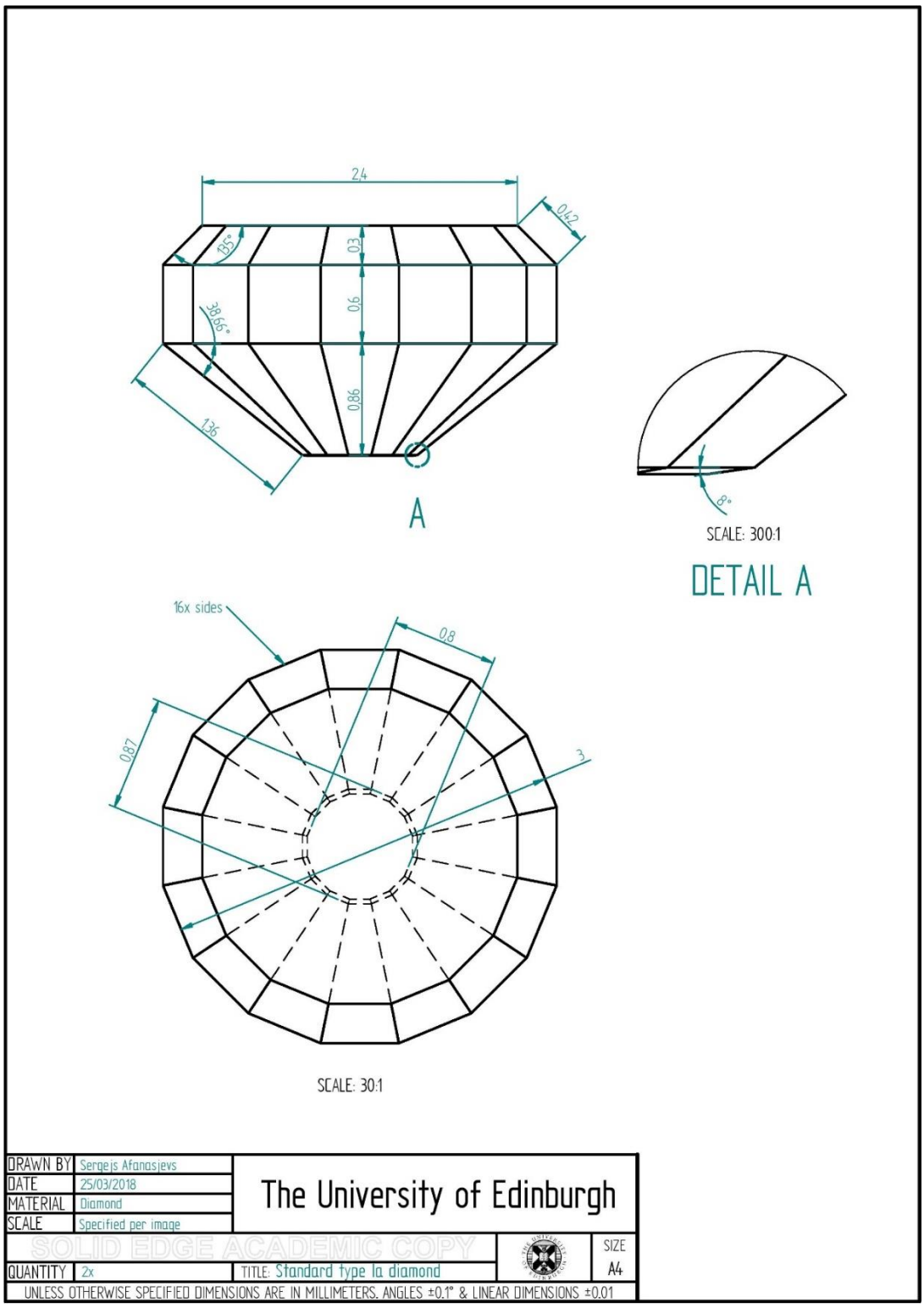

Figure B.1: Standard type Ia diamond

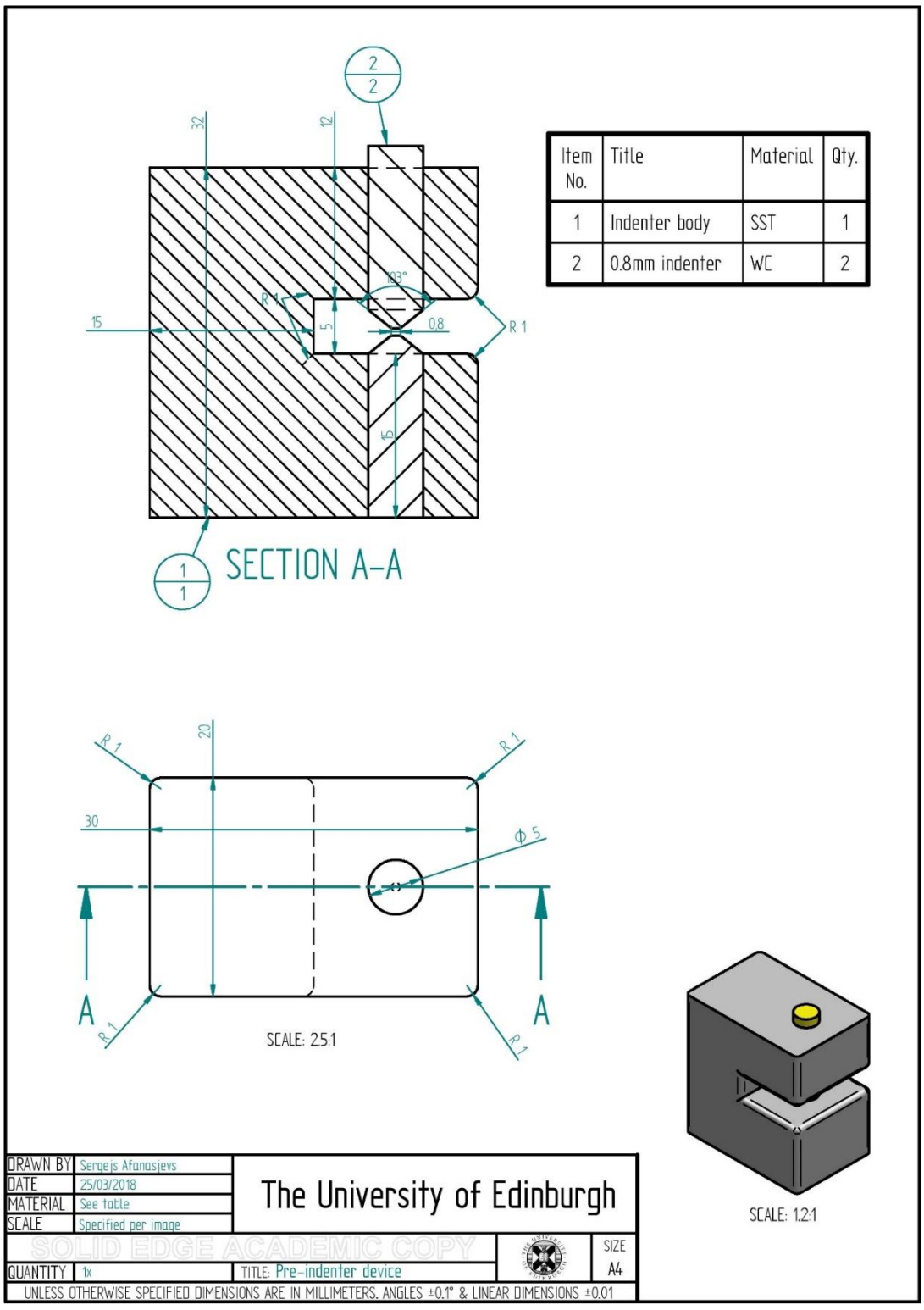

Figure B.2: Gasket pre-indenter device.

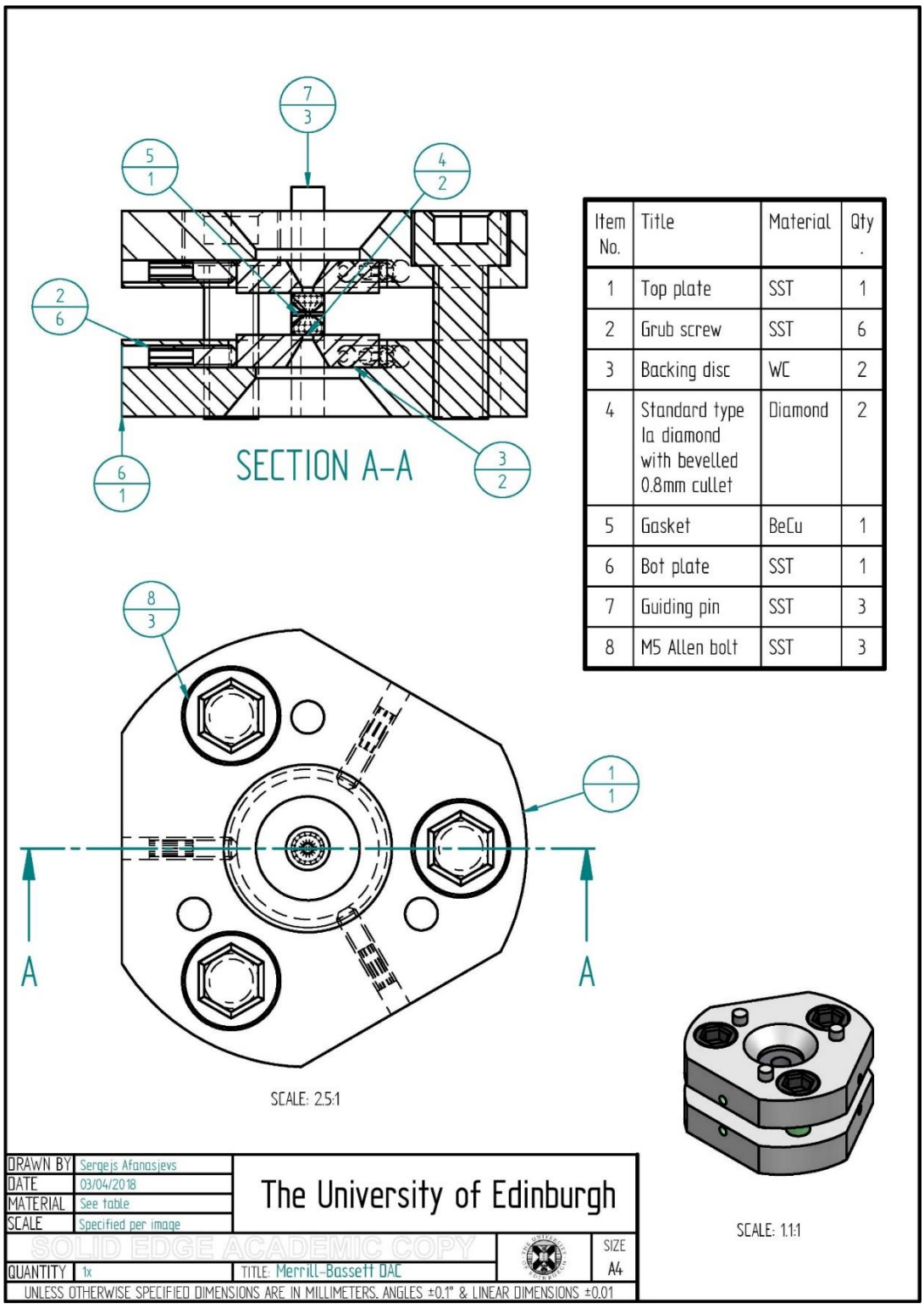

Item No.	Title	Material	Qty.
1	Top plate	SST	1
2	Grub screw	SST	6
3	Backing disc	WC	2
4	Standard type Ia diamond with bevelled 0.8mm cullet	Diamond	2
5	Gasket	BeCu	1
6	Bot plate	SST	1
7	Guiding pin	SST	3
8	M5 Allen bolt	SST	3

Figure B.3: The Merrill Bassett DAC.

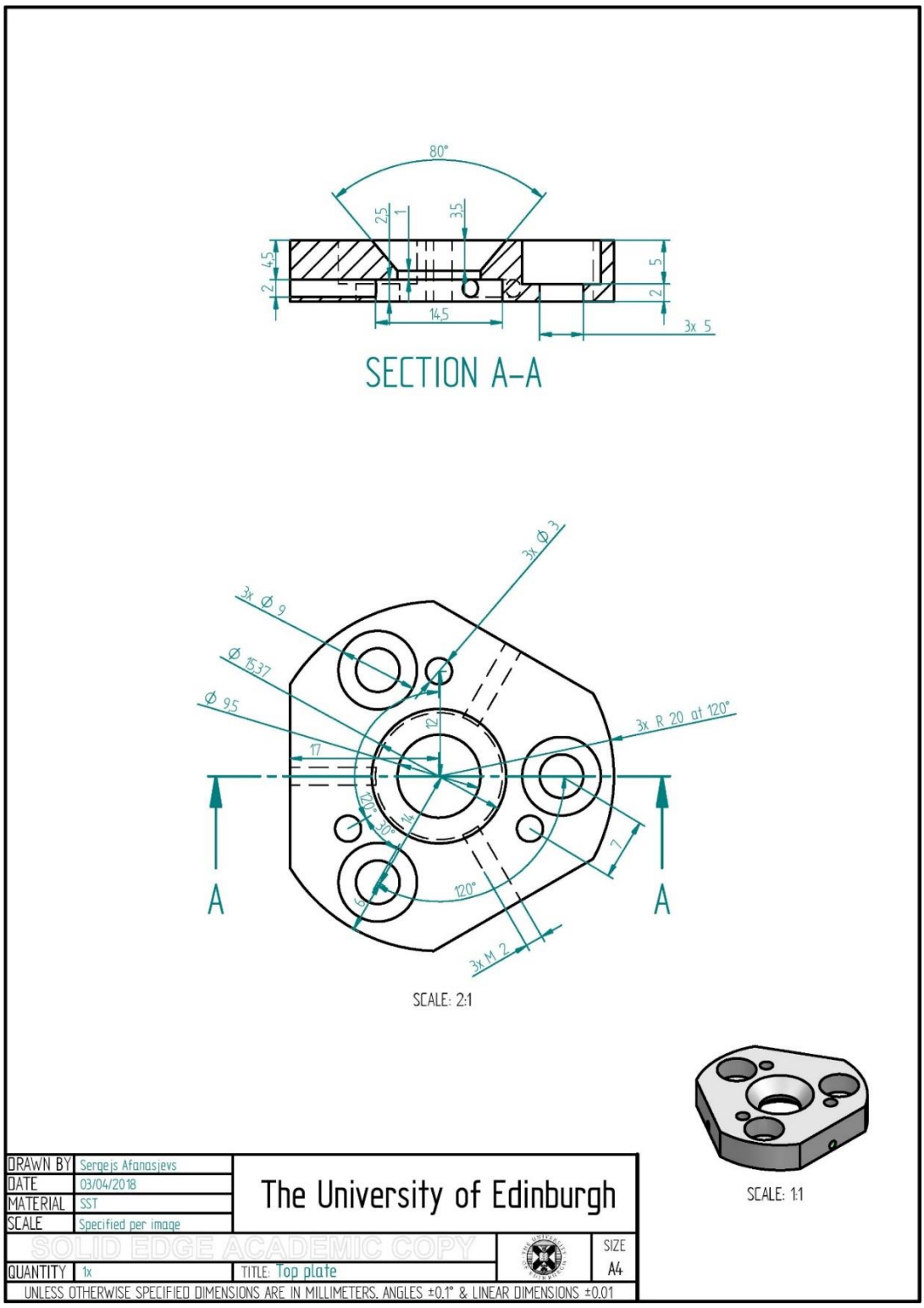

Figure B.4: Top plate.

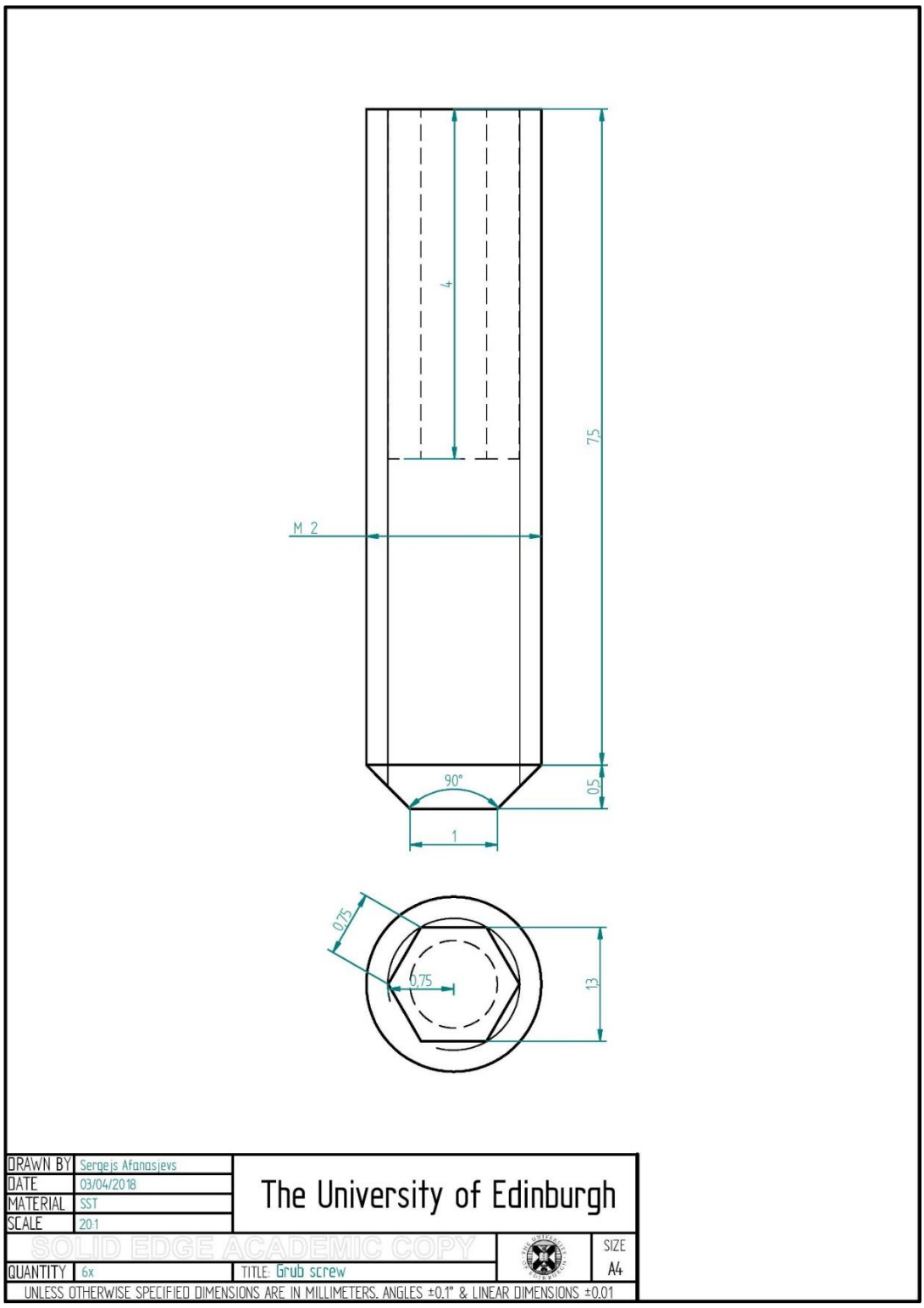

Figure B.5: Grub screw.

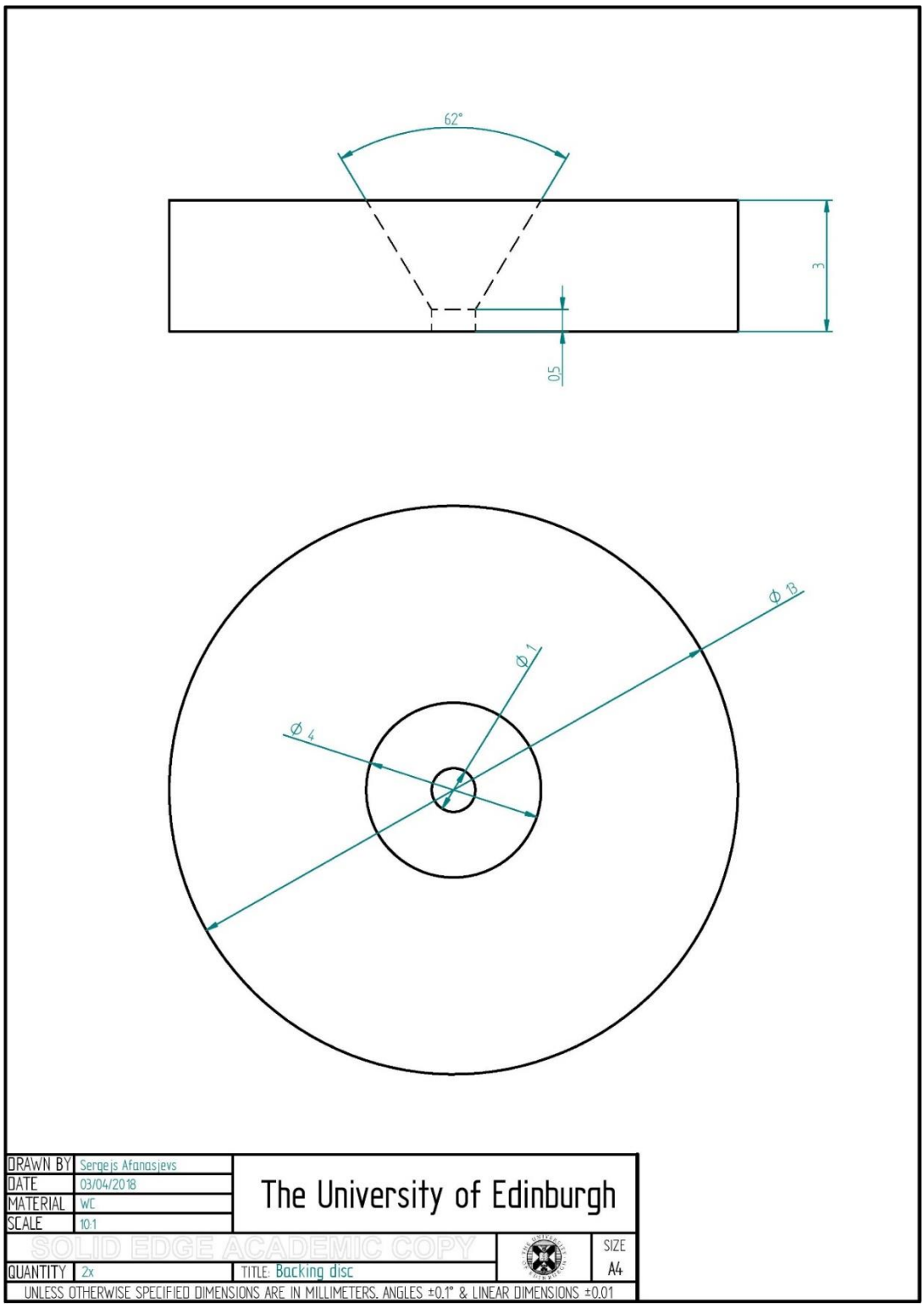

Figure B.6: Backing disc.

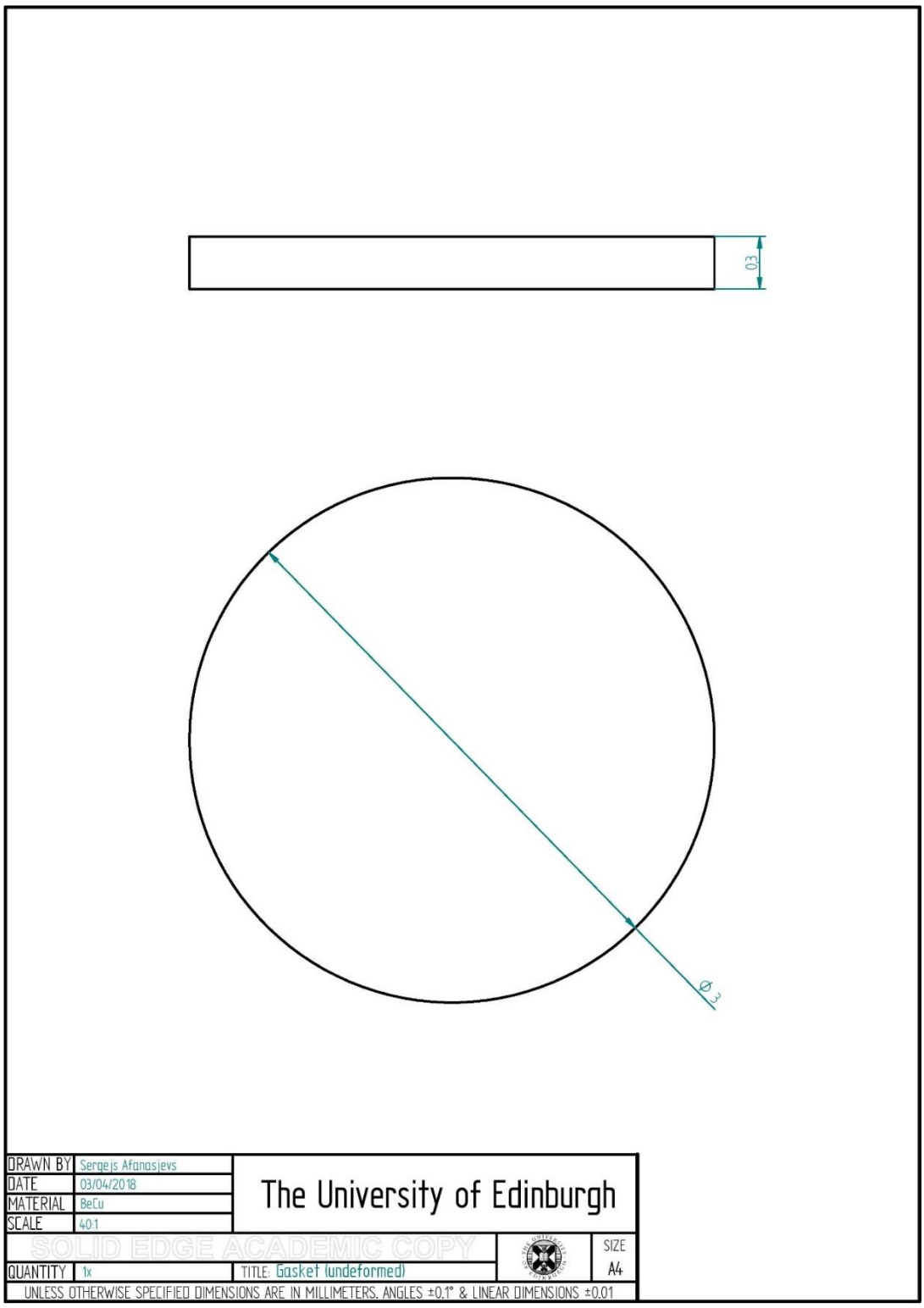

Figure B.7: Gasket.

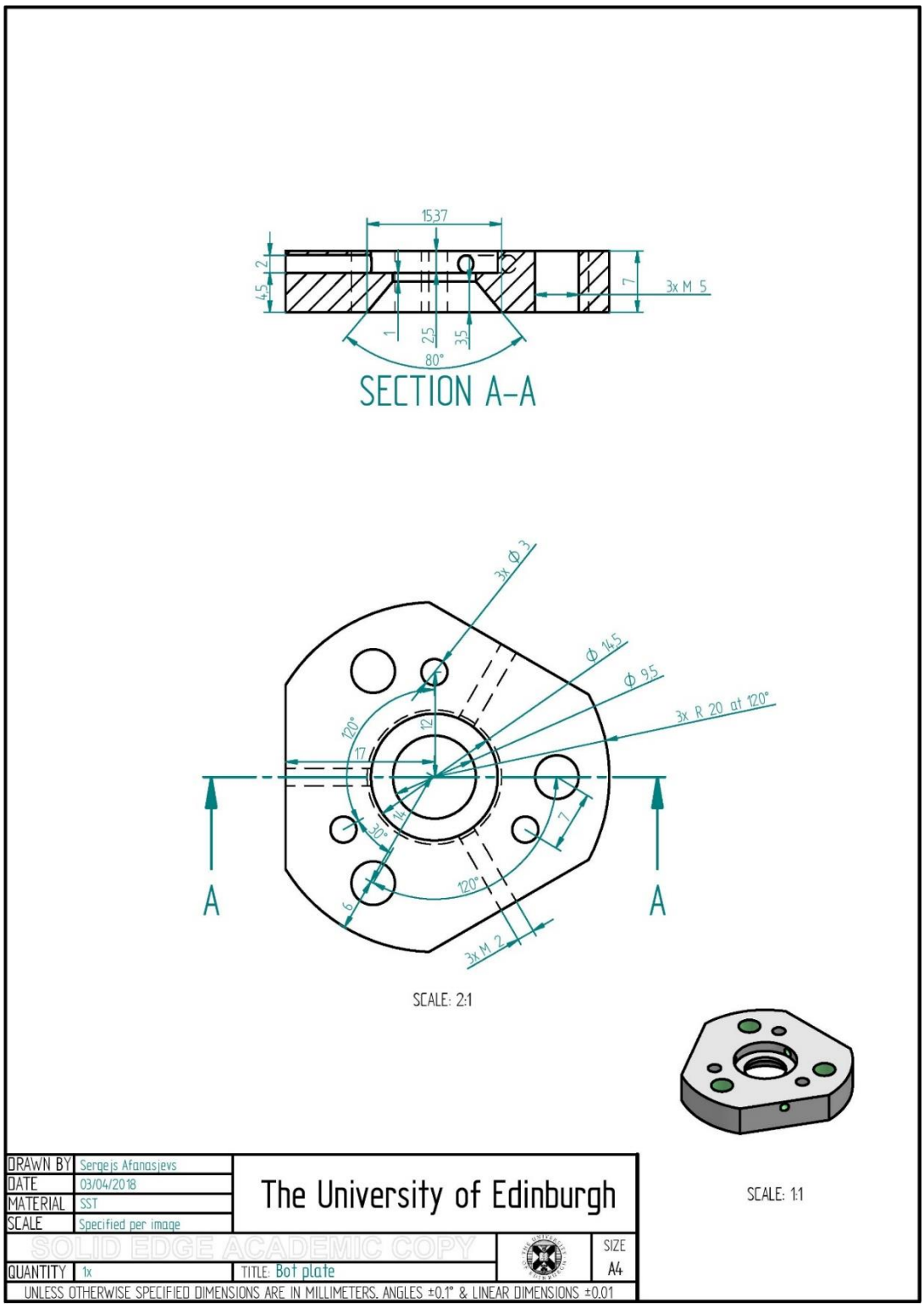

Figure B.8: Bot plate.

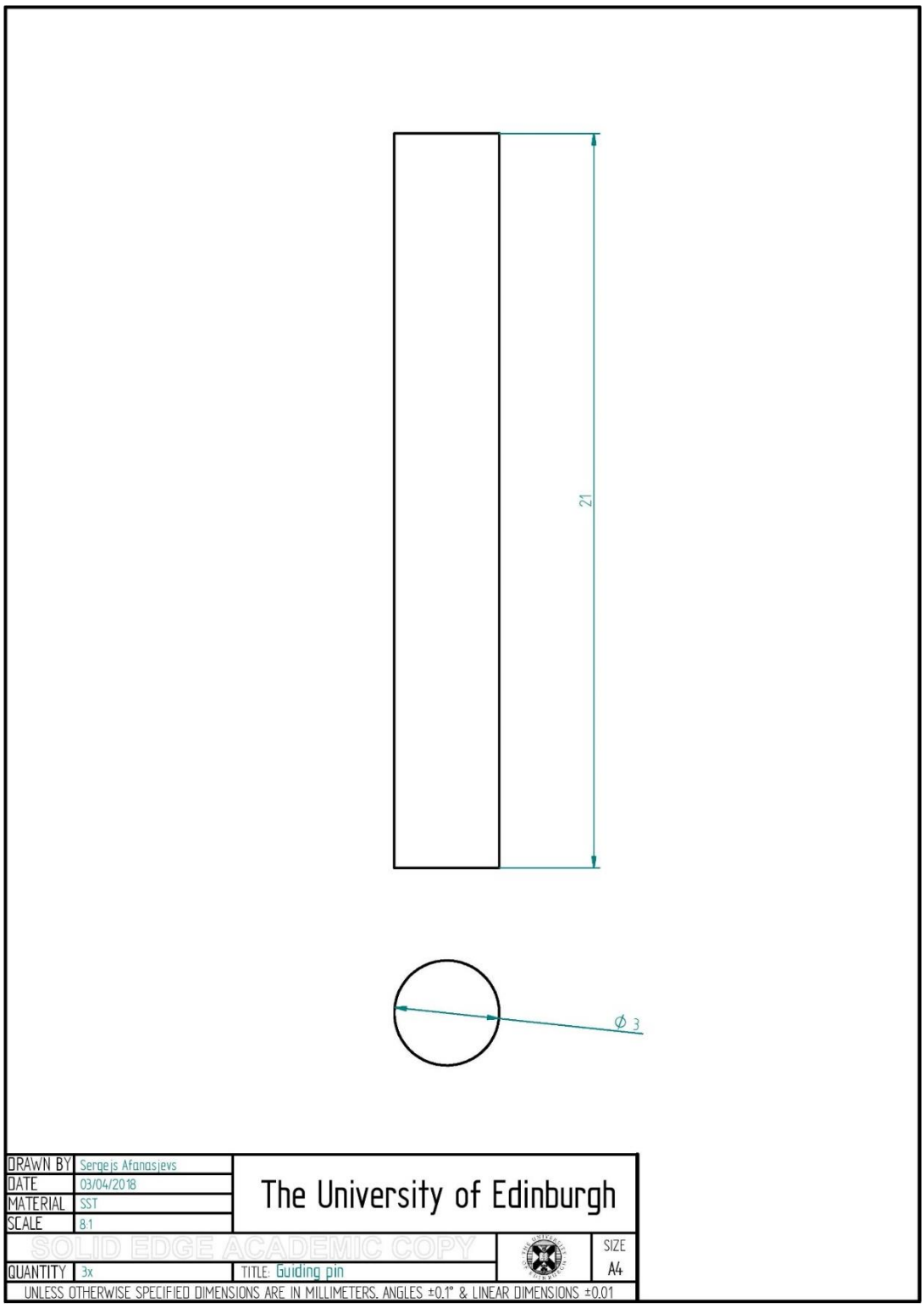

Figure B.9: Guiding pin.

Appendix C

Drawings related to the 6th chapter

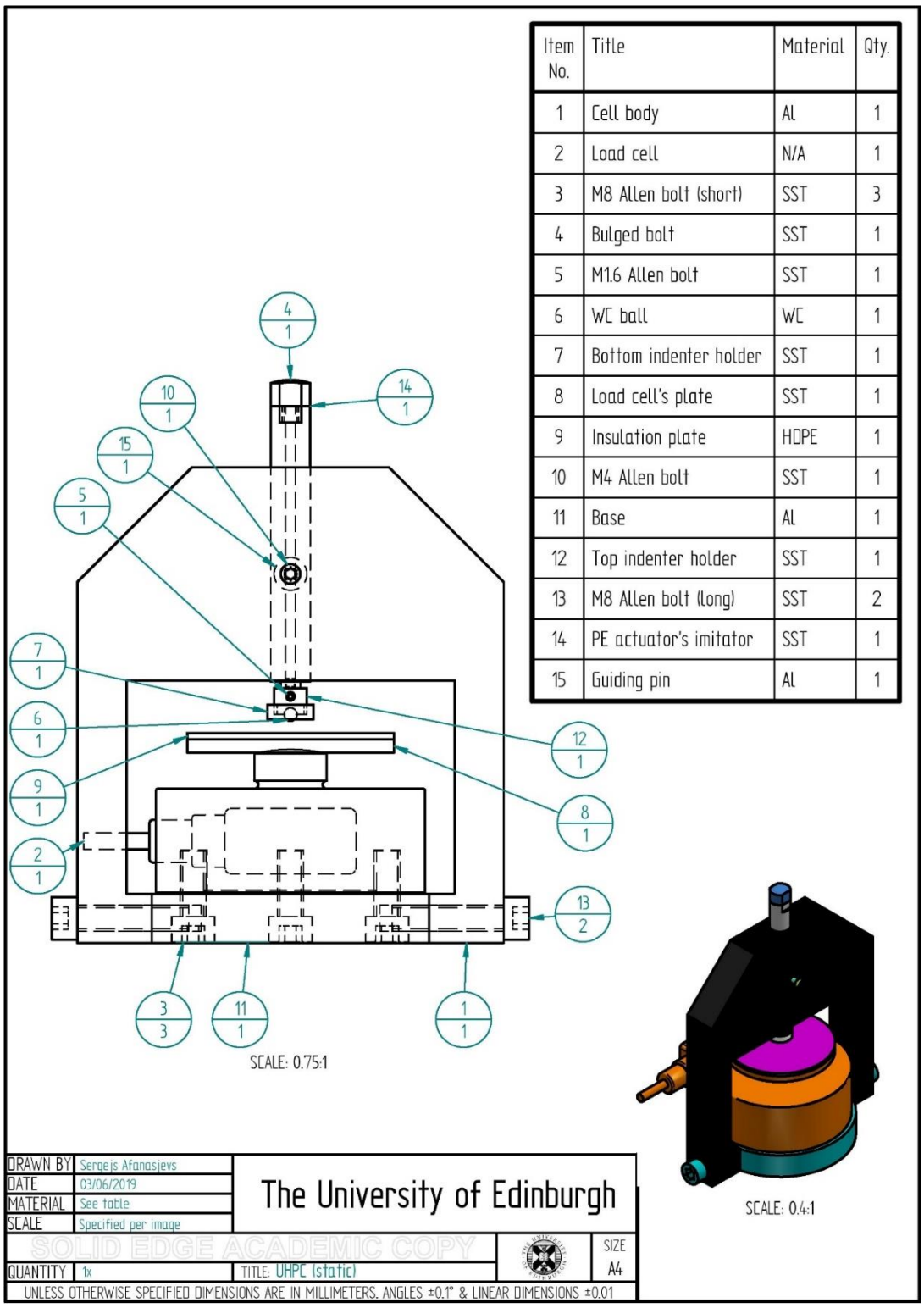

Figure C.1: The uniaxial high-pressure cell (static).

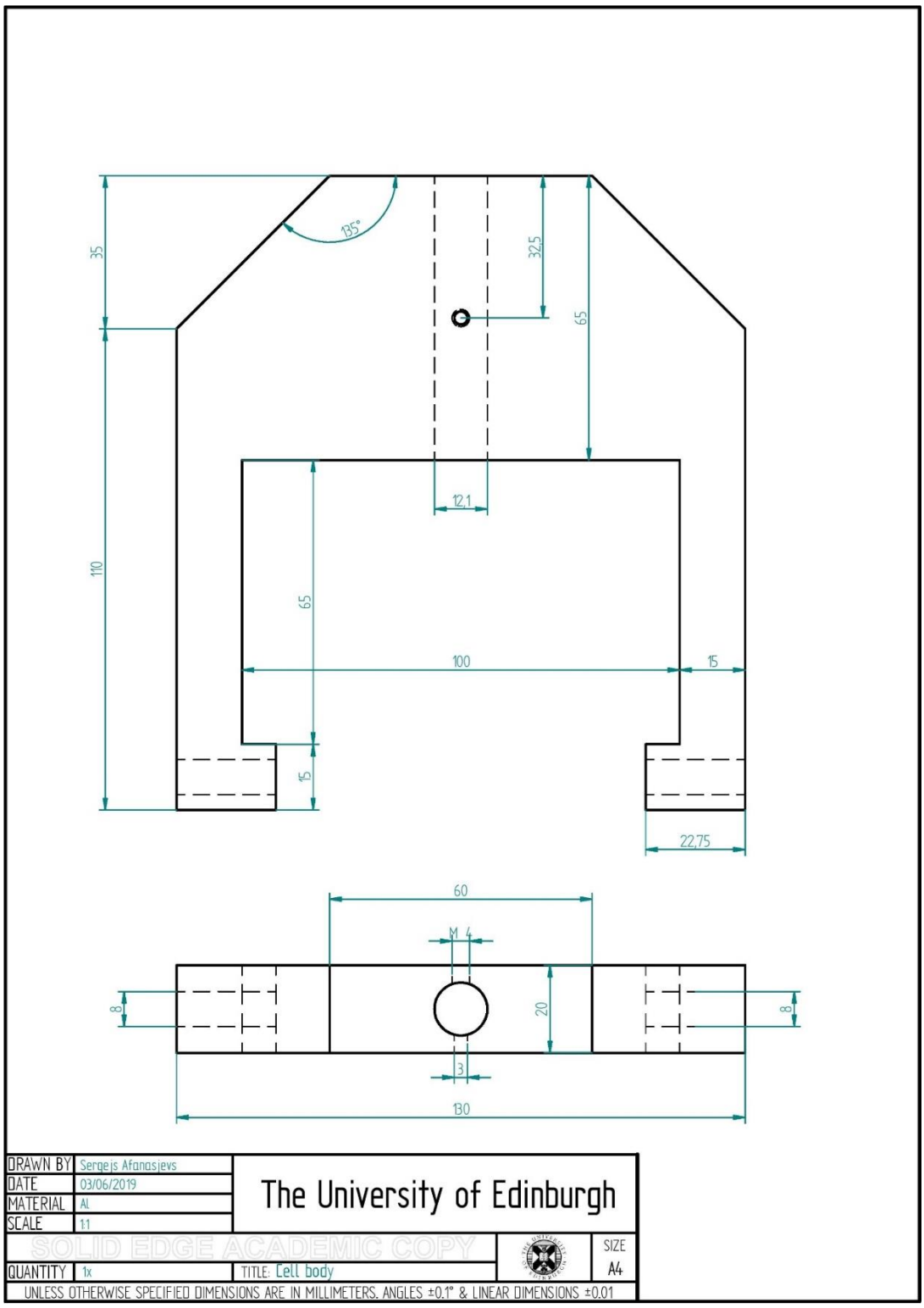

Figure C.2: The cell body.

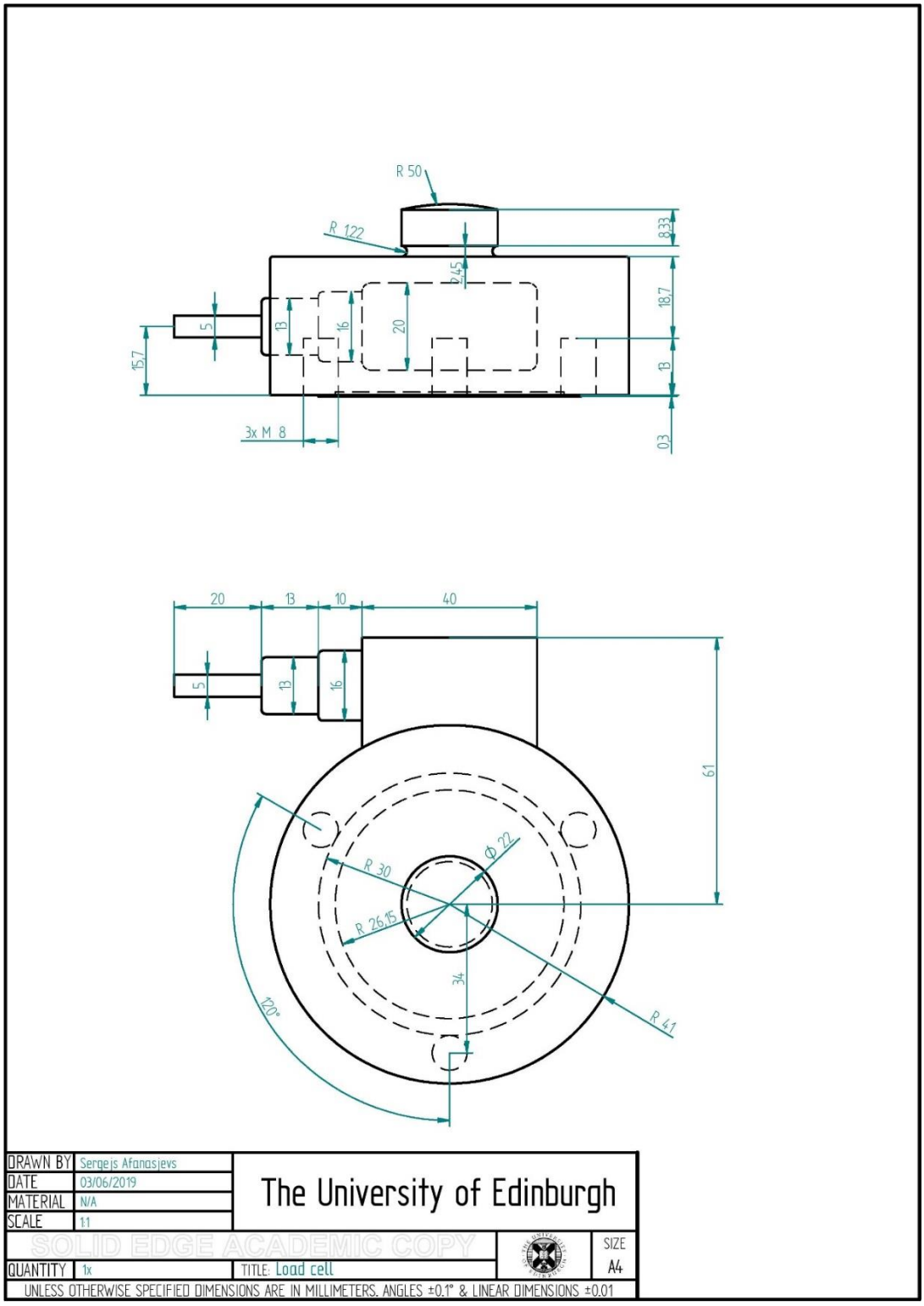

Figure C.3: The load cell. Built to dimensions [214].

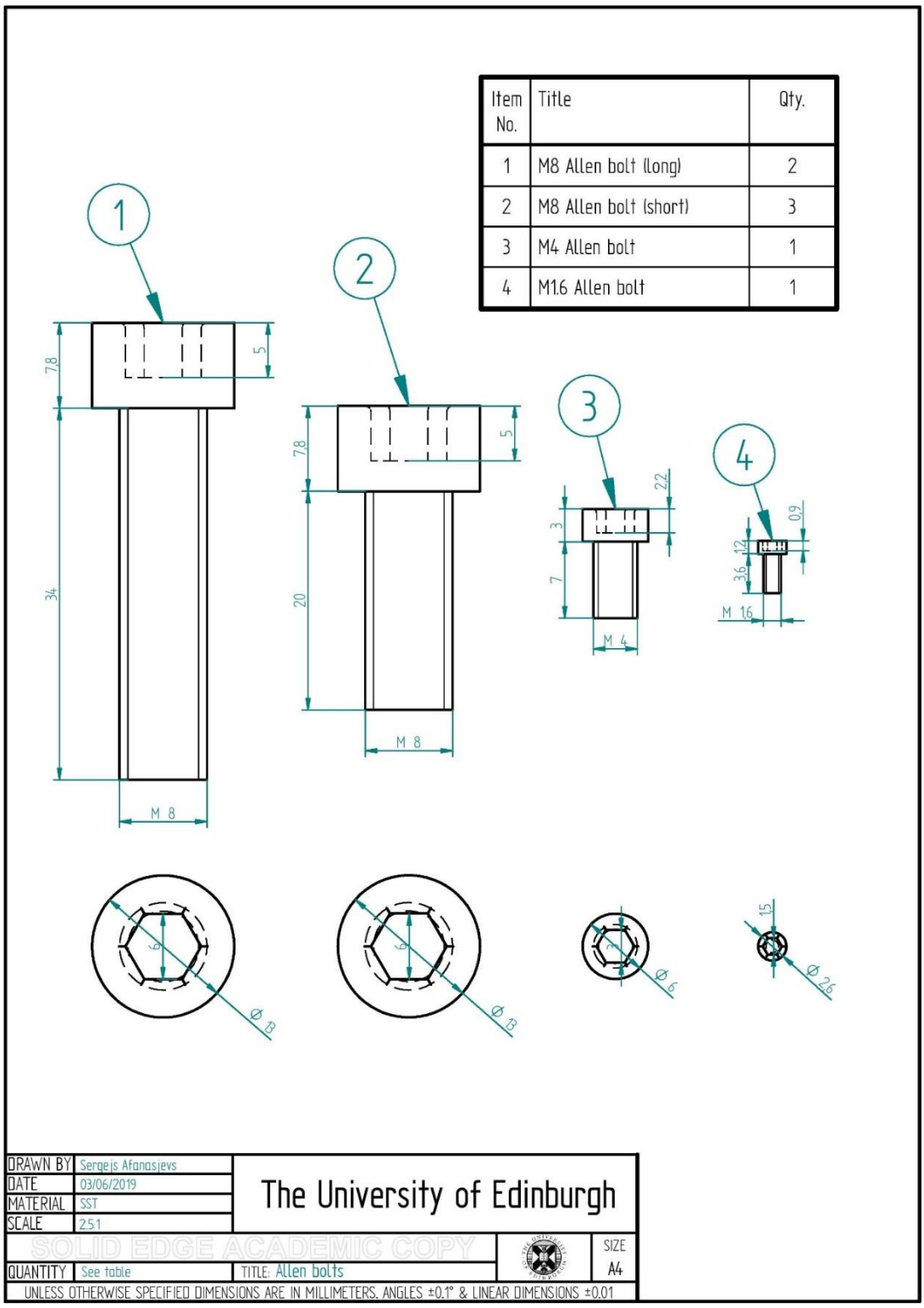

Figure C.4: All Allen bolts.

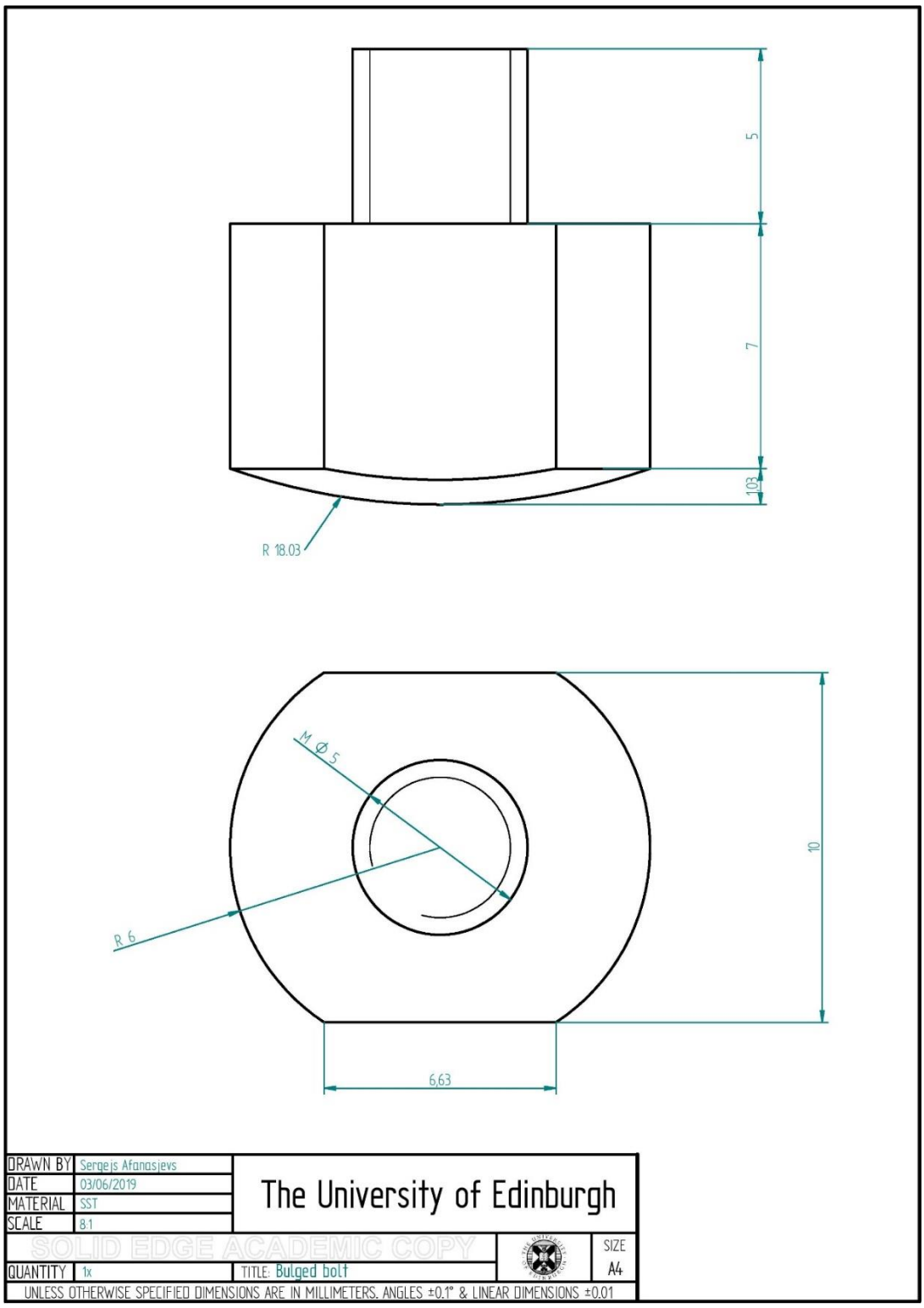

Figure C.5: Bulged bolt.

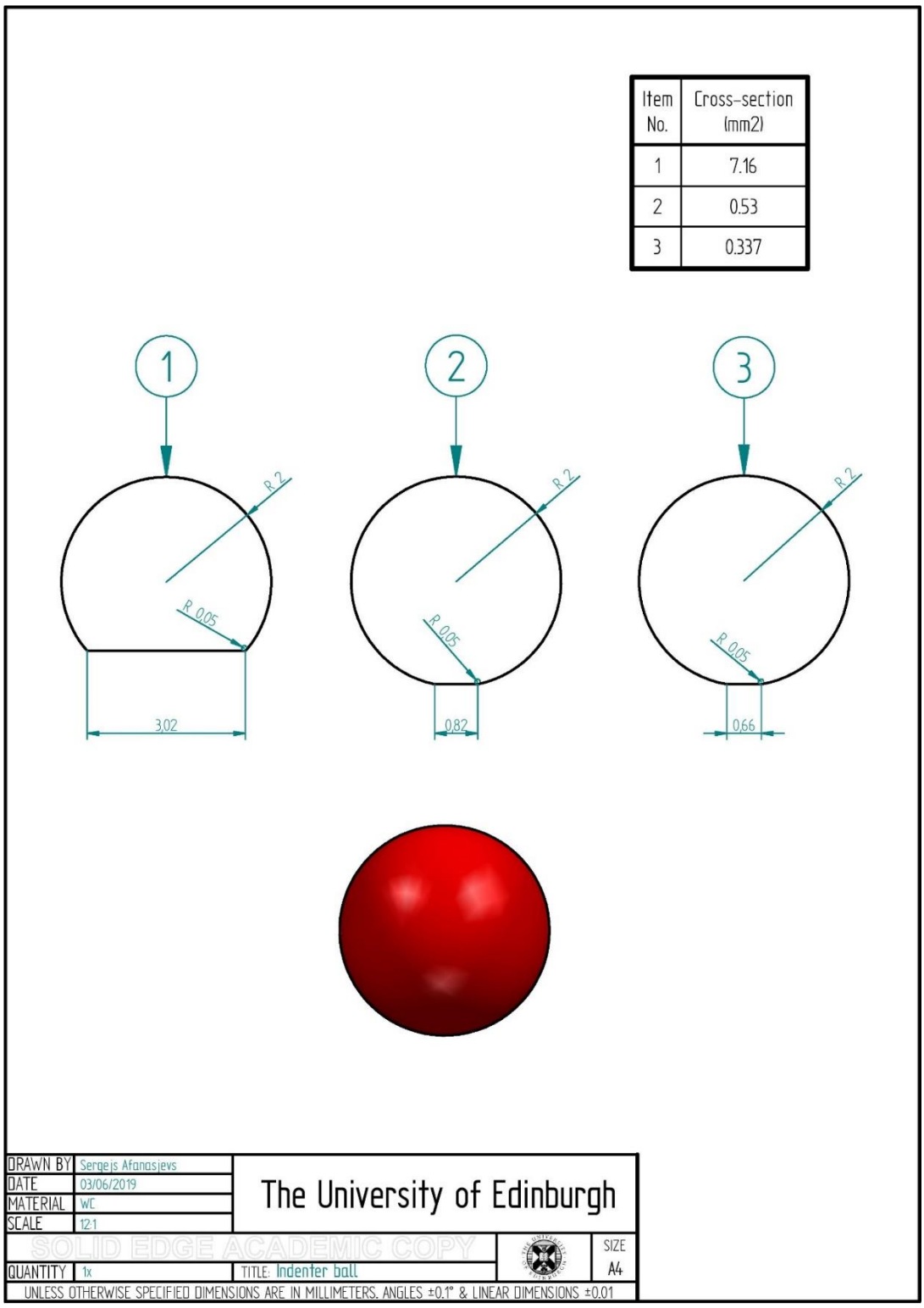

Figure C.6: Indenter balls.

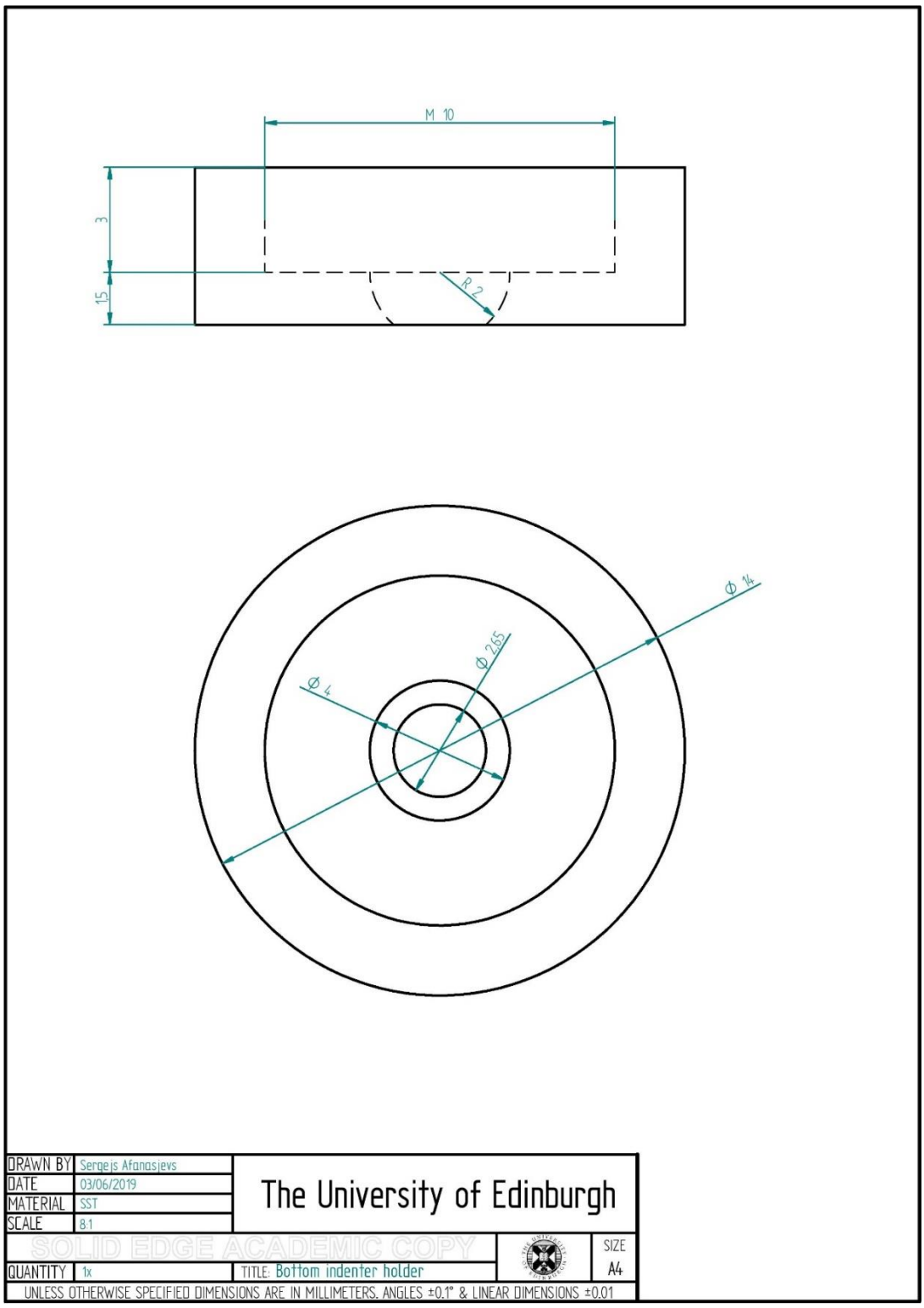

Figure C.7: Bottom indenter holder.

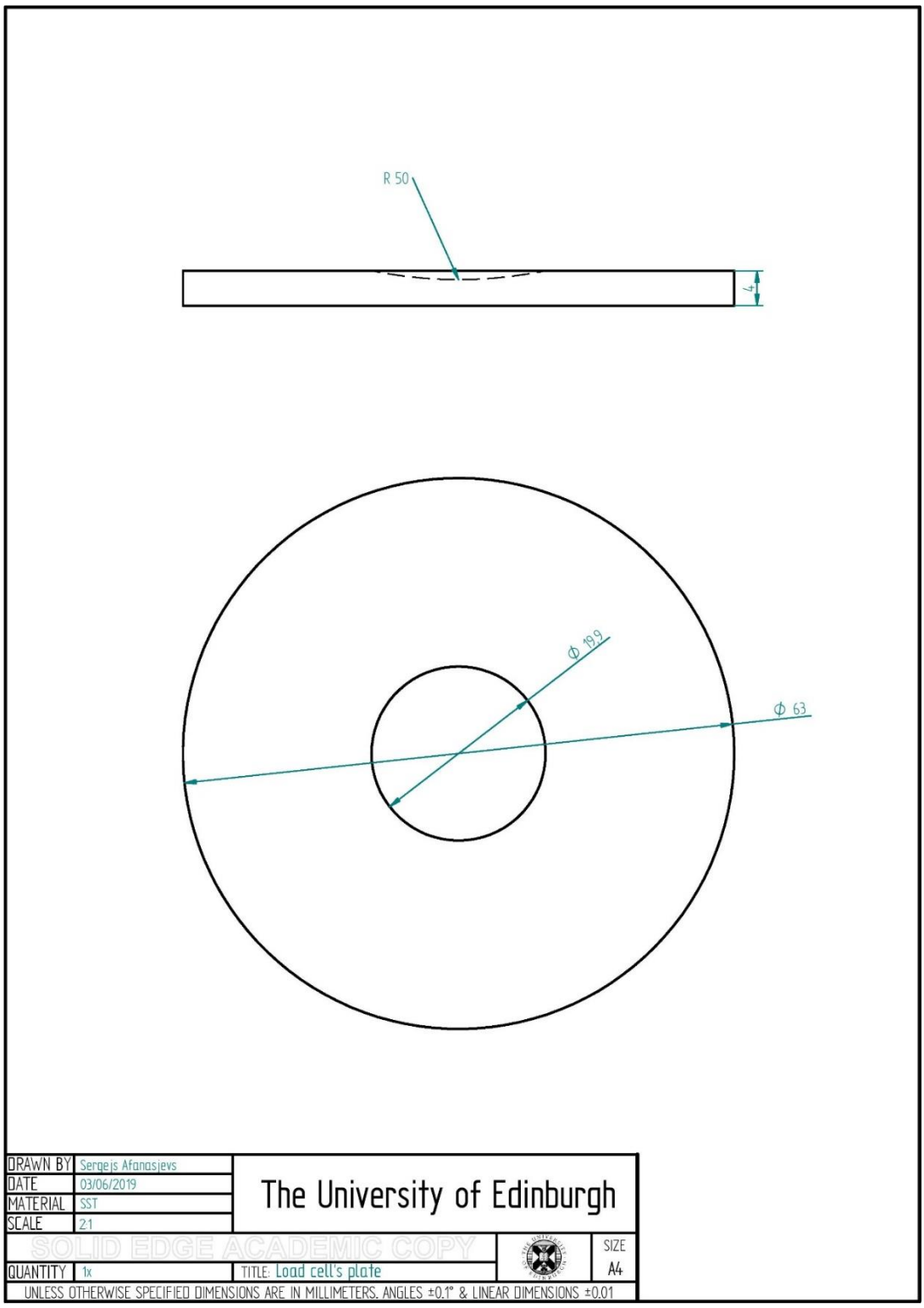

Figure C.8: Load cell's plate.

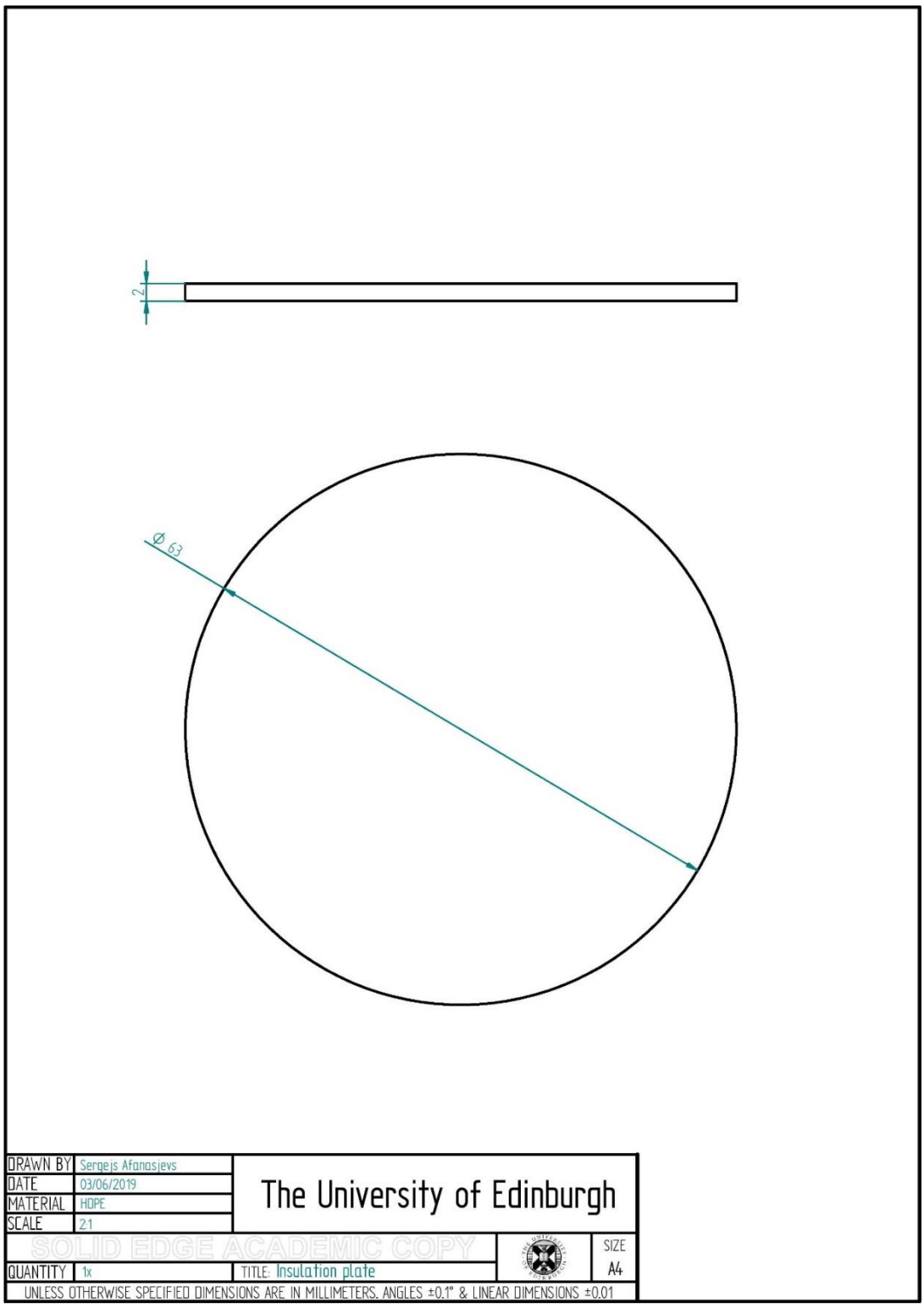

Figure C.9: Insulation plate.

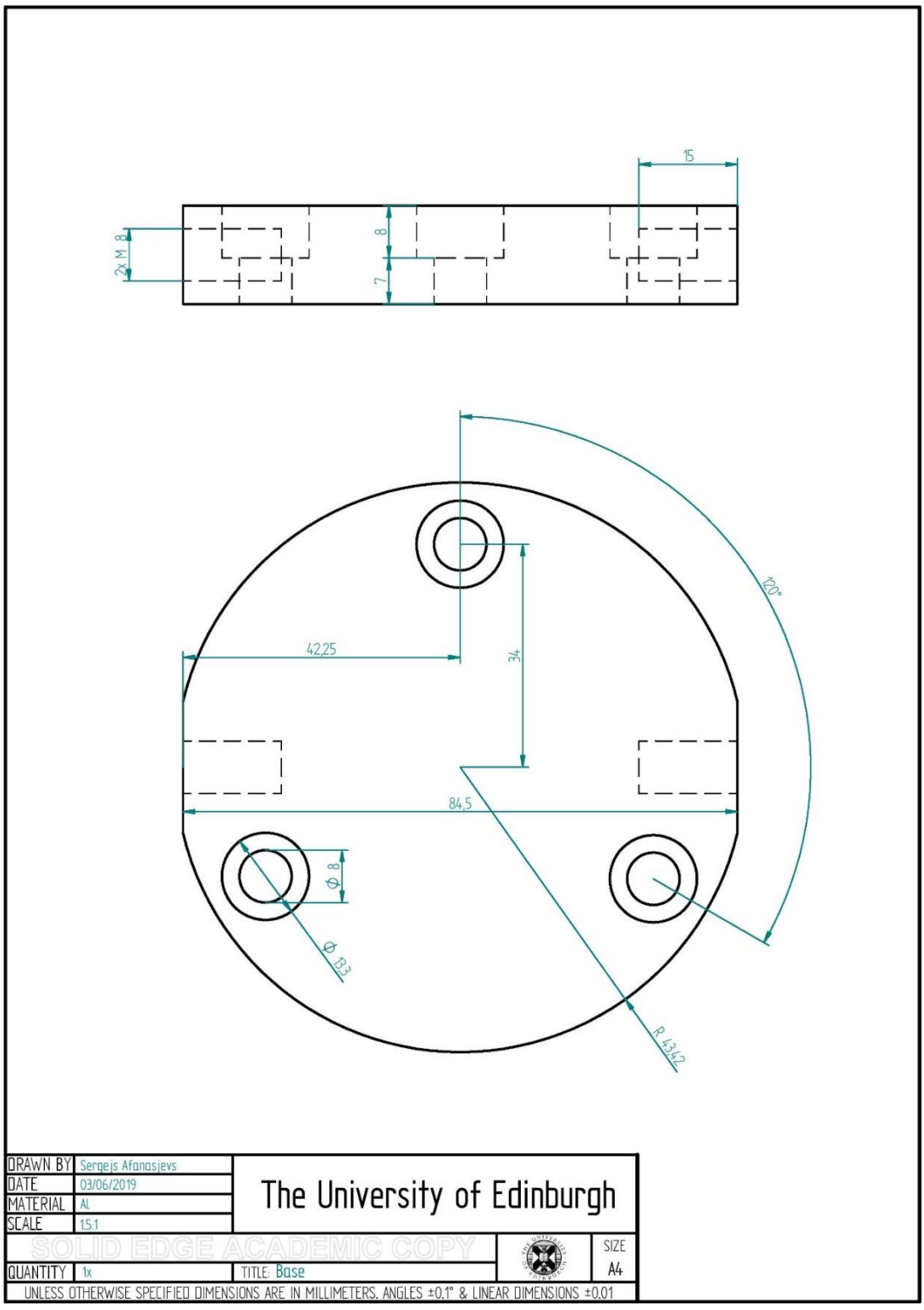

Figure C.10: Base.

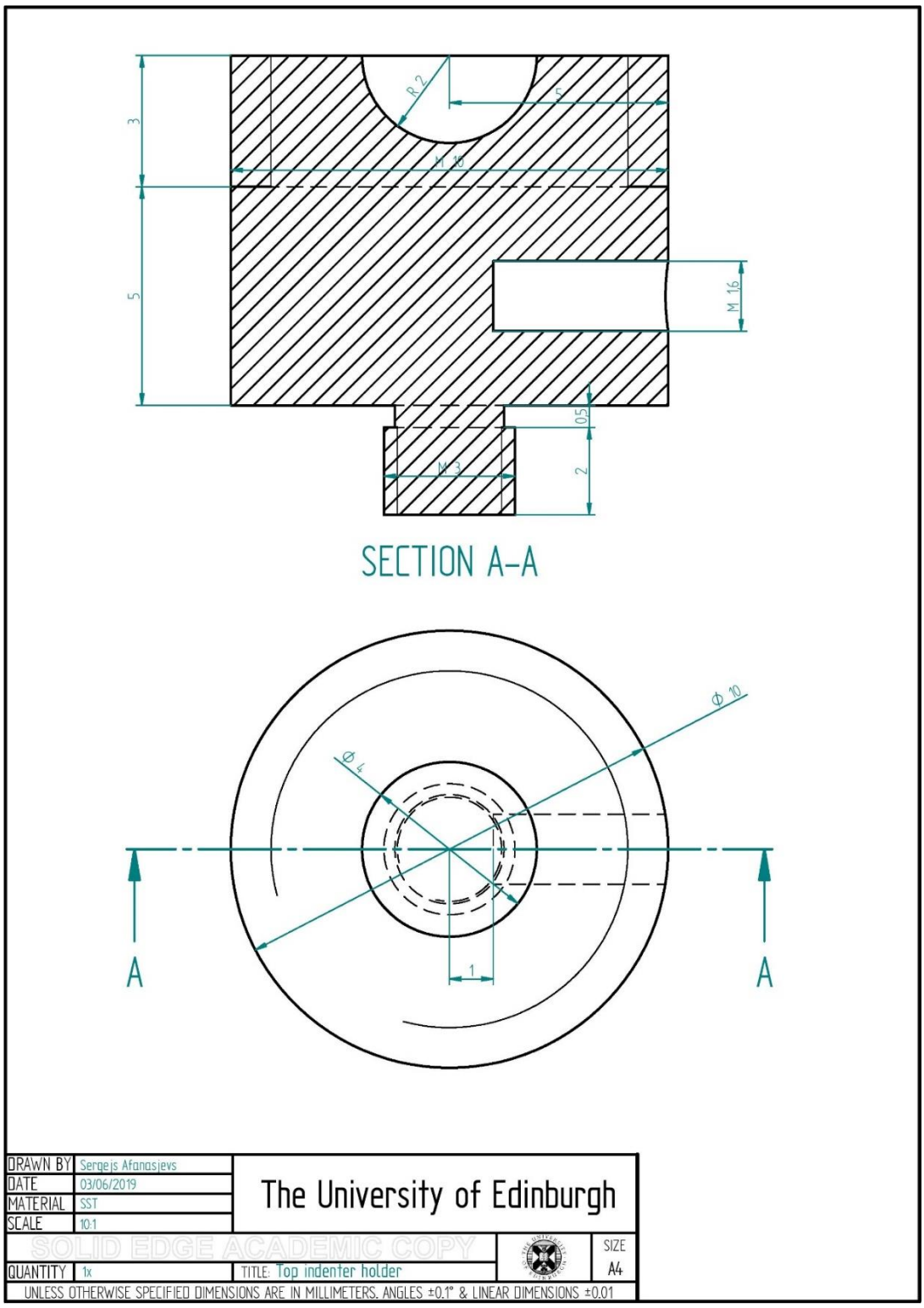

Figure C.11: Top indenter holder.

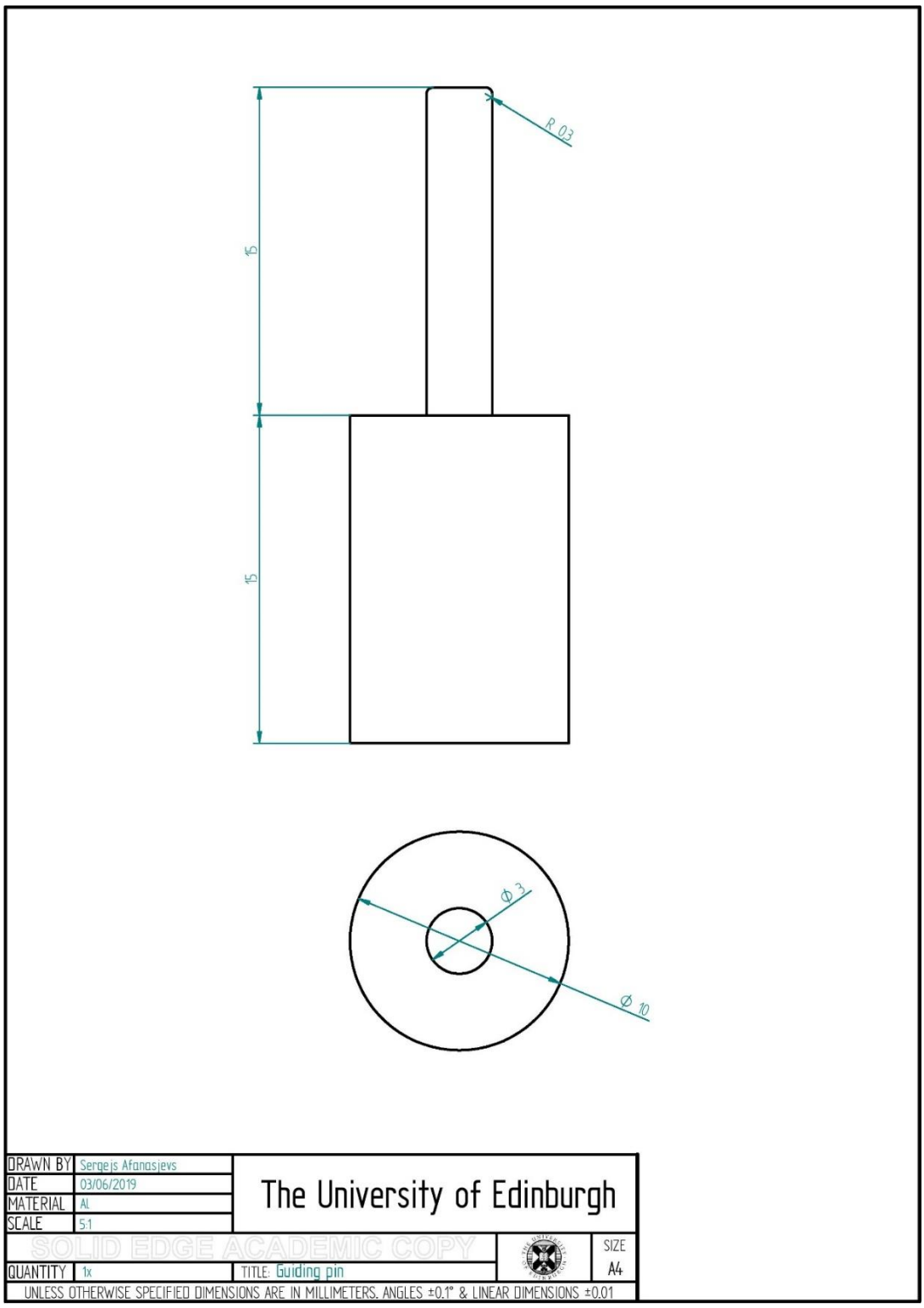

Figure C.12: Guiding pin.

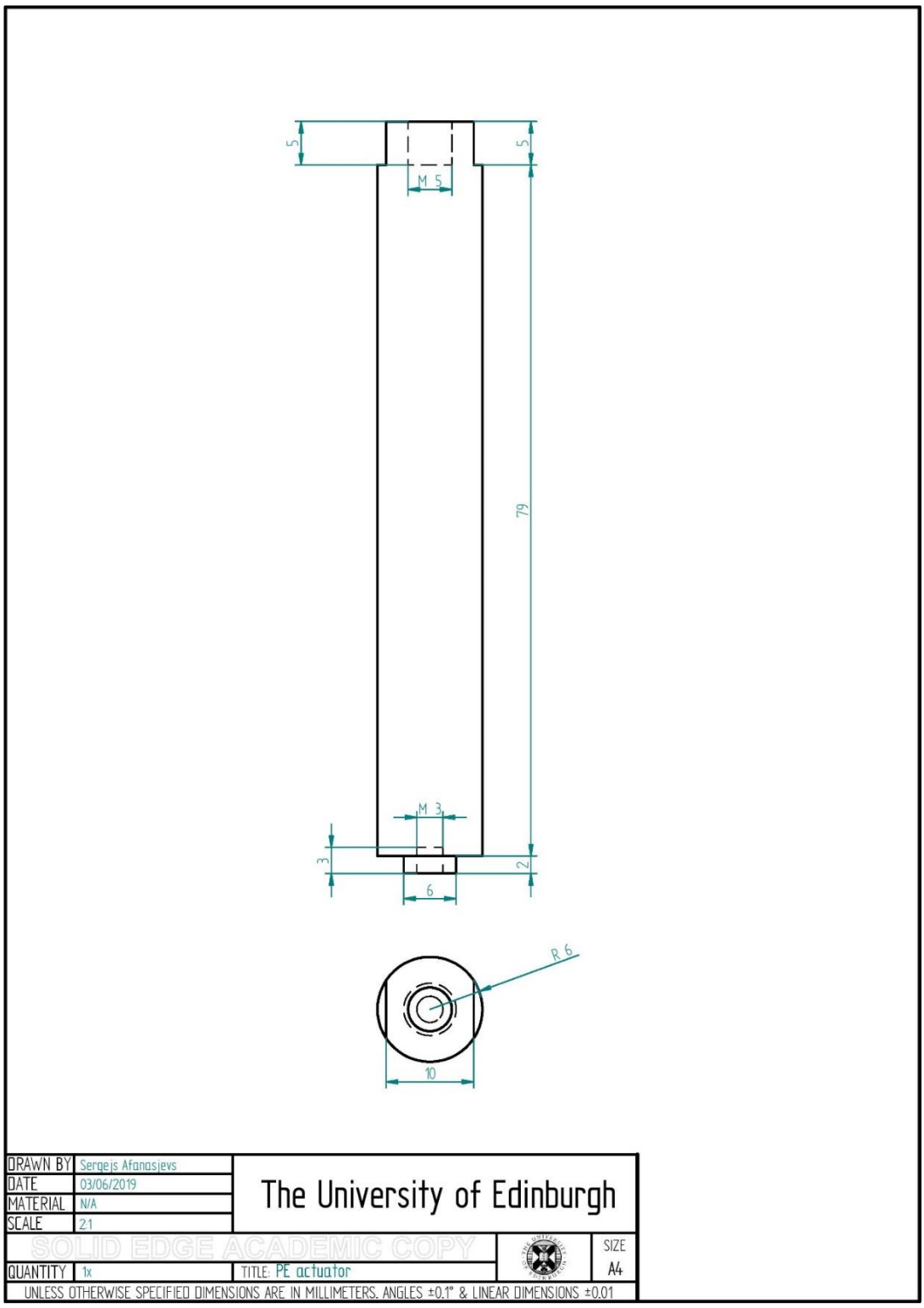

Figure C.13: PE actuator. Built to dimension [212].

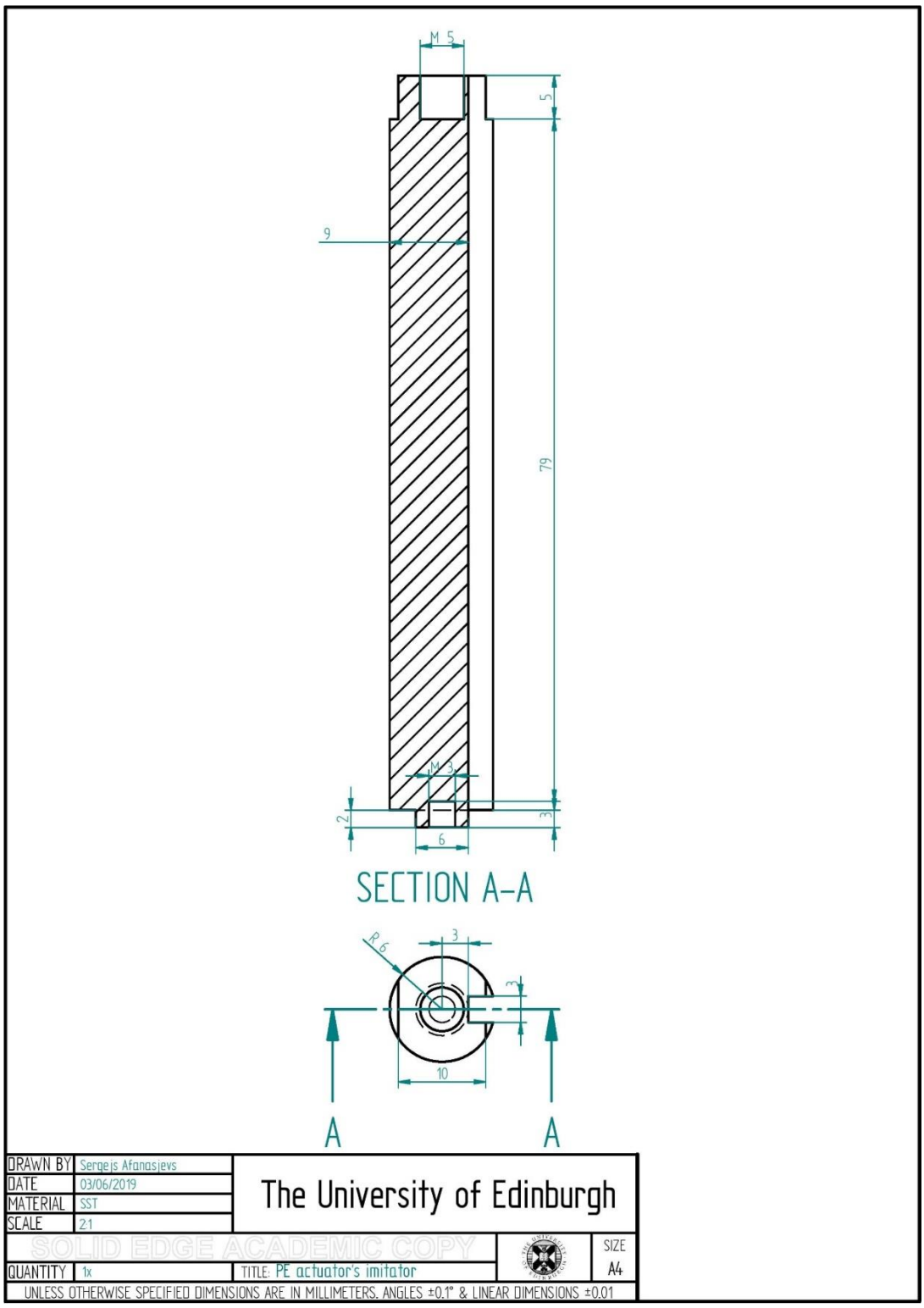

Figure C.14: PE actuator's imitator.

Appendix D

Numerical data for charts from the 8th chapter

The $Pt(bqd)_2$ complex

Pamb hot plate	
R (Ohm)	T (K)
3.9E+09	294
3.5E+09	295
3.2E+09	296
2.93E+09	297
2.73E+09	298
2.59E+09	299
2.4E+09	300
2.27E+09	301
2.1E+09	302
1.98E+09	303
1.84E+09	304
1.75E+09	305
1.64E+09	306
1.5E+09	307
1.4E+09	308
1.34E+09	309
1.28E+09	310
1.21E+09	311
1.15E+09	312
1.05E+09	313
9.7E+08	314
9.2E+08	315
8.8E+08	316
8.34E+08	317
8.03E+08	318
7.45E+08	319
7.01E+08	320
6.8E+08	321
6.56E+08	322
6.28E+08	323
5.9E+08	324
5.61E+08	325
5.3E+08	326
5.11E+08	327
4.85E+08	328

At P = amb			
1/T	Log conductivity	Energy Gap	Band Gap
0.0034	-17.78570013	0.514446	1.028891
0.0033	-17.12154048		
0.0032	-16.2574355		
0.0031	-16.14071123		
At P = 2kbar			
1/T	Log conductivity	Energy Gap	
0.0034	-15.13609571	0.403945	0.80789
0.0033	-14.7363615		
0.0032	-14.0580421		
0.0031	-13.85266691		
At P = 4kbar			
1/T	Log conductivity	Energy Gap	
0.0034	-12.83420227	0.337074	0.674149
0.0033	-12.83350767		
0.0032	-12.08283381		
0.0031	-11.8417035		
At P = 6kbar			
1/T	Log conductivity	Energy Gap	
0.0034	-10.55778064	0.195438	0.390877
0.0033	-10.88817197		
0.0032	-10.12828818		
0.0031	-10.10297881		
At P = 8kbar			
1/T	Log conductivity	Energy Gap	
0.0034	-8.650724742	0.08613	0.17226
0.0033	-8.961524306		
0.0032	-8.48464147		
0.0031	-8.504462965		
At P = 10kbar			
1/T	Log conductivity	Energy Gap	
0.0034	-7.015658421	0.038691	0.077383
0.0033	-6.969158139		
0.0032	-6.693102868		
0.0031	-6.955997976		
At P = 11kbar			
1/T	Log conductivity	Energy Gap	
0.0034	-6.19848998	0.003473	0.006945
0.0033	-6.160769563		
0.0032	-5.817433943		
0.0031	-6.287182898		
At P = 12kbar			
1/T	Log conductivity	Energy Gap	
0.0034	-5.69317703	0.073734	0.147468
0.0033	-4.961575055		
0.0032	-4.966612541		
0.0031	-5.375162982		
At P = 14kbar			
1/T	Log conductivity	Energy Gap	
0.0034	-4.764664267	0.181287	0.362574
0.0033	-3.574215301		
0.0032	-3.586488957		
0.0031	-4.024167098		
At P = 15kbar			
1/T	Log conductivity	Energy Gap	
0.0034	-4.526351565	0.256686	0.513372
0.0033	-3.102675518		
0.0032	-3.040945003		
0.0031	-3.519602474		

Figure D.1: Numerical data for figure 8.1 (on the left) & 8.2 (on the right).

At P=3.9kbar		At P=6.2kbar	
R (Ohm)	T (K)	R (Ohm)	T (K)
1850000	295	212000	295
1630000	303	238000	303
1446000	308	266000	308
1410000	313	350000	313
1386000	318	490000	318
At P=8.79kbar		At P=20.33kbar	
R (Ohm)	T (K)	R (Ohm)	T (K)
20670	295	288	295
23890	303	280	303
30100	308	269	308
40100	313	265	313
51400	318	259	318

PCC			DAC		
P (kbar)	R (Ohm)	ρ (Ohm*m)	P (kbar)	R (Ohm)	ρ (Ohm*m)
0	272000000	529945.76	0.29	4010000000	1509506.3
2.44	16000000	31173.28	3.13	178000000	67005.515
4.73	1370000	2669.2121	4.81	20300000	7641.6402
7.25	108000	210.41964	6	6060000	2281.199
9.61	11400	22.210962	6.48	3120000	1174.4787
11.88	1690	3.2926777	7.12	1300000	489.36612
14.34	545	1.06183985	8.55	213000	80.180757
15.28	450	0.8767485	10.53	27100	10.201402
			11.92	5710	2.1494466
			13.82	1620	0.6098255
			16.26	530	0.1995108
			17.18	378	0.1422926
			18.27	312	0.1174479
			20.33	288	0.1084134

Figure D.2: Numerical data for figure 8.3 (on the left) & 8.4 (on the right).

R (Ohm)	P (Mpa)
587000	0
550000	2.2
435000	4.4
300000	6.6
230000	8.8
160000	11
140000	13.2
115000	15.4
100000	17.6
84000	19.8
67000	22
56000	24.2
47000	26.4
35	110

Zone 1		Zone 2	
R (Ohm)	P (Mpa)	R (Ohm)	P (Mpa)
587000	0	600000	0
550000	2.2	350000	2.2
435000	4.4	215000	4.4
300000	6.6	150000	6.6
230000	8.8	120000	8.8
160000	11	102000	11
140000	13.2	92000	13.2
115000	15.4	82000	15.4
100000	17.6	77000	17.6
84000	19.8	69000	19.8
67000	22	63000	22
56000	24.2	20	110
47000	26.4		
35	110		

Figure D.3: Numerical data for figure 8.5 (on the left) & 8.6 (on the right).

R at Pamb (loading)	R at Pamb (unloading)	R at 110 Mpa	Cycle number
740000	710000	480	1
710000	690000	490	2
690000	680000	500	3
680000	680000	490	4
680000	690000	500	5
690000	670000	500	6
670000	670000	490	7
670000	670000	500	8
670000	670000	490	9
670000	670000	500	10

Figure D.4: Numerical data for figure 8.7.

The Pt(F-bqd)$_2$ complex

Pamb heat gun	
R (Ohm)	T (K)
6.12E+09	294
5.7E+09	295
5.35E+09	296
5.15E+09	297
4.9E+09	298
4.68E+09	299
4.32E+09	300
4.05E+09	301
3.8E+09	302
3.5E+09	303
3.28E+09	304
3E+09	306
2.7E+09	308
2.14E+09	311
1.88E+09	314
1.6E+09	316
1.4E+09	319
1.07E+09	324
9.3E+08	327
6.27E+08	333
5.6E+08	336
5.35E+08	341
4.7E+08	346
3.47E+08	351
3.28E+08	355
2.9E+08	357

Pamb CCR								Pamb CCR								Pamb CCR					
R (Ohm)	T (K)	R (Ohm)	T (K)	R (Ohm)	T (K)	R (Ohm)	T (K)	R (Ohm)	T (K)	R (Ohm)	T (K)	R (Ohm)	T (K)	R (Ohm)	T (K)	R (Ohm)	T (K)	R (Ohm)	T (K)	R (Ohm)	T (K)
7.99E+09	291.6	8.36E+09	289.6	9.07E+09	287.4	9.37E+09	285	1.05E+10	282.3	1.33E+10	279.7	1.67E+10	276.5	2.57E+10	273.1	3.5E+10	270.6	3.27E+10	266.5	3.89E+10	263.9
8.01E+09	291.6	8.51E+09	289.5	8.87E+09	287.3	9.34E+09	284.9	1.06E+10	282.2	1.29E+10	279.6	1.64E+10	276.4	2.4E+10	273.1	3.16E+10	270.5	3.34E+10	266.4	3.9E+10	263.8
8.13E+09	291.5	8.58E+09	289.5	8.93E+09	287.2	9.39E+09	284.9	1.06E+10	282.2	1.3E+10	279.5	1.69E+10	276.4	2.43E+10	273	3.07E+10	270.4	3.05E+10	266.4	4.07E+10	263.8
7.94E+09	291.5	8.52E+09	289.4	9.04E+09	287.2	9.47E+09	284.8	1.09E+10	282.1	1.32E+10	279.5	1.66E+10	276.3	2.59E+10	273	3.03E+10	270.4	3.21E+10	266.3	3.73E+10	263.7
7.99E+09	291.4	8.72E+09	289.4	8.87E+09	287.1	9.64E+09	284.8	1.08E+10	282	1.31E+10	279.4	1.69E+10	276.2	2.34E+10	272.9	3.18E+10	270.3	3.39E+10	266.2	3.76E+10	263.6
8.16E+09	291.4	8.69E+09	289.3	9.04E+09	287.1	9.5E+09	284.7	1.09E+10	282	1.32E+10	279.3	1.68E+10	276.1	2.07E+10	272.8	3.08E+10	270.2	3.12E+10	266.2	3.81E+10	263.6
7.96E+09	291.3	8.67E+09	289.3	9.02E+09	287	9.2E+09	284.6	1.11E+10	281.9	1.32E+10	279.3	1.7E+10	276.1	2.53E+10	272.7	3.07E+10	270.2	3.27E+10	266.1	3.55E+10	263.5
8.02E+09	291.3	8.86E+09	289.2	8.82E+09	286.9	9.91E+09	284.6	1.12E+10	281.9	1.32E+10	279.3	1.69E+10	276	2.49E+10	272.7	3.13E+10	270.1	3.44E+10	266	3.63E+10	263.4
8.06E+09	291.2	8.8E+09	289.2	8.94E+09	286.9	9.85E+09	284.4	1.12E+10	281.8	1.35E+10	279.2	1.73E+10	276	2.51E+10	272.6	3.08E+10	270	3.26E+10	266	3.48E+10	263.4
7.97E+09	291.2	8.77E+09	289.1	9E+09	286.8	9.71E+09	284.4	1.12E+10	281.7	1.31E+10	279.1	1.7E+10	275.9	2.62E+10	272.6	3.03E+10	270	3.25E+10	265.9	3.59E+10	263.3
7.98E+09	291.1	8.76E+09	289	8.83E+09	286.8	9.92E+09	284.2	1.11E+10	281.7	1.35E+10	279.1	1.71E+10	275.8	2.44E+10	272.5	3.21E+10	269.9	3.53E+10	265.8	3.56E+10	263.2
8.07E+09	291.1	9.24E+09	289	8.96E+09	286.7	9.77E+09	284.1	1.11E+10	281.6	1.35E+10	279	1.82E+10	275	2.38E+10	272.4	3.1E+10	269.9	3.22E+10	265.8	3.97E+10	263.2
8E+09	291	8.3E+09	288.9	9E+09	286.7	9.73E+09	284.1	1.11E+10	281.5	1.35E+10	278.9	1.81E+10	274.9	2.41E+10	272.4	2.84E+10	269.8	3.47E+10	265.7	3.81E+10	263.1
8.04E+09	291	8.75E+09	288.9	8.93E+09	286.6	9.42E+09	283.9	1.07E+10	281.5	1.36E+10	278.8	1.82E+10	274.9	2.39E+10	272.3	3.14E+10	269.7	3.34E+10	265.6	3.8E+10	263.1
8.16E+09	291	8.37E+09	288.8	9.07E+09	286.5	9.5E+09	283.9	1.15E+10	281.3	1.37E+10	278.8	1.82E+10	274.8	2.51E+10	272.2	3.35E+10	269.7	3.66E+10	265.6	3.72E+10	263
7.95E+09	290.9	8.64E+09	288.8	9.2E+09	286.4	9.6E+09	283.8	1.13E+10	281.2	1.36E+10	278.7	1.87E+10	274.7	2.44E+10	272.2	2.97E+10	269.6	3.77E+10	265.5	3.69E+10	262.9
8.07E+09	290.9	8.44E+09	288.7	9.2E+09	286.4	9.75E+09	283.8	1.15E+10	281.2	1.39E+10	278.7	1.81E+10	274.7	2.52E+10	272.1	3.27E+10	269.5	3.78E+10	265.5	3.73E+10	262.8
8.16E+09	290.8	8.32E+09	288.7	9.13E+09	286.4	9.73E+09	283.7	1.14E+10	281.1	1.33E+10	278.6	1.88E+10	274.6	3.26E+10	272	3.28E+10	269.5	3.84E+10	265.4	3.89E+10	262.8
8.03E+09	290.7	8.46E+09	288.6	9.46E+09	286.3	1.04E+10	283.6	1.16E+10	281	1.45E+10	278.5	1.87E+10	274.5	2.62E+10	271.9	3.15E+10	269.4	3.99E+10	265.3	3.84E+10	262.7
8.11E+09	290.7	8.4E+09	288.5	9.2E+09	286.2	1.01E+10	283.6	1.16E+10	281	1.42E+10	278.5	1.87E+10	274.5	2.58E+10	271.9	3.22E+10	269.3	3.33E+10	265.3	3.95E+10	262.7
8.2E+09	290.6	8.25E+09	288.5	9.28E+09	286.2	9.72E+09	283.5	1.16E+10	280.9	1.43E+10	278.4	1.94E+10	274.4	2.55E+10	271.9	3.59E+10	269.3	4E+10	265.2	3.95E+10	262.6
8.07E+09	290.6	8.55E+09	288.4	9.28E+09	286.1	9.95E+09	283.5	1.17E+10	280.9	1.48E+10	278.3	1.95E+10	274.4	2.68E+10	271.8	2.98E+10	269.2	4.08E+10	265.1	3.74E+10	262.5
8.13E+09	290.5	8.49E+09	288.4	9.21E+09	286	1.01E+10	283.4	1.2E+10	280.8	1.39E+10	278.3	1.85E+10	274.3	2.62E+10	271.7	3.2E+10	269.1	3.8E+10	265.1	3.88E+10	262.5
8.15E+09	290.5	8.3E+09	288.3	9.28E+09	286	9.95E+09	283.4	1.18E+10	280.8	1.47E+10	278.1	2.25E+10	274.2	2.73E+10	271.7	3.16E+10	269.1	3.81E+10	265	3.73E+10	262.4
8.1E+09	290.4	8.48E+09	288.3	9.22E+09	286	1.03E+10	283.3	1.18E+10	280.7	1.51E+10	278.1	2.23E+10	274.2	2.63E+10	271.6	3.18E+10	269	3.81E+10	264.9	3.9E+10	262.3
8.45E+09	290.4	8.47E+09	288.2	8.98E+09	285.9	1.02E+10	283.2	1.22E+10	280.6	1.55E+10	278	2.17E+10	274.1	2.55E+10	271.5	3.07E+10	269	3.71E+10	264.9	3.93E+10	262.3
7.97E+09	290.3	8.37E+09	288.2	9.92E+09	285.8	1E+10	283.2	1.21E+10	280.5	1.51E+10	277.9	2.29E+10	274	2.67E+10	271.5	3.08E+10	268.8	3.66E+10	264.8	3.8E+10	262.2
8.29E+09	290.3	8.26E+09	288.1	9.25E+09	285.8	1E+10	283.1	1.22E+10	280.5	1.51E+10	277.6	2.34E+10	273.9	2.66E+10	271.4	3.28E+10	268.7	3.86E+10	264.7	4E+10	262.1
8.18E+09	290.2	8.61E+09	288	9.21E+09	285.7	1E+10	283.1	1.25E+10	280.4	1.55E+10	277.4	2.32E+10	273.9	2.56E+10	271.3	3.09E+10	268.7	3.7E+10	264.7	4.1E+10	262.1
8.3E+09	290.2	8.43E+09	288	9.19E+09	285.6	1E+10	283	1.24E+10	280.4	1.52E+10	277.2	2.25E+10	273.8	2.72E+10	271.3	3.92E+10	268.5	3.87E+10	264.6	4.6E+10	262
8.19E+09	290.1	8.53E+09	287.9	9.24E+09	285.6	1E+10	282.9	1.25E+10	280.3	1.58E+10	277.1	2.4E+10	273.8	2.75E+10	271.2	2.81E+10	268.5	4.15E+10	264.6		
8.33E+09	290	8.71E+09	287.9	9.27E+09	285.5	1.01E+10	282.9	1.28E+10	280.3	1.56E+10	277.1	2.34E+10	273.7	2.74E+10	271.2	2.66E+10	268.2	3.97E+10	264.5		
8.44E+09	290	8.57E+09	287.8	9.31E+09	285.5	1.02E+10	282.8	1.26E+10	280.2	1.55E+10	277	2.45E+10	273.7	3.04E+10	271.1	3.16E+10	268	4.11E+10	264.4		
8.3E+09	290	8.78E+09	287.8	9.24E+09	285.4	1.01E+10	282.7	1.27E+10	280.1	1.6E+10	276.9	2.42E+10	273.6	2.42E+10	271	3.22E+10	268	4.34E+10	264.3		
8.33E+09	289.9	8.81E+09	287.7	9.38E+09	285.3	1.03E+10	282.7	1.28E+10	280	1.6E+10	276.9	2.56E+10	273.5	2.85E+10	271	2.88E+10	267.9	4.02E+10	264.3		
8.48E+09	289.8	8.79E+09	287.6	9.27E+09	285.3	1.02E+10	282.6	1.26E+10	280	1.59E+10	276.8	2.37E+10	273.5	3.14E+10	270.9	3.09E+10	267.8	4.04E+10	264.2		
8.35E+09	289.8	8.92E+09	287.6	9.19E+09	285.2	1.02E+10	282.5	1.26E+10	279.9	1.66E+10	276.7	2.41E+10	273.4	3.01E+10	270.8	3.5E+10	267.8	4.28E+10	264.1		
8.41E+09	289.7	8.89E+09	287.5	9.93E+09	285.2	1.02E+10	282.5	1.29E+10	279.9	1.64E+10	276.6	2.45E+10	273.3	3.01E+10	270.7	3.03E+10	267.2	4E+10	264.1		
8.44E+09	289.7	8.78E+09	287.5	9.28E+09	285.1	1E+10	282.4	1.29E+10	279.8	1.66E+10	276.6	2.38E+10	273.3	3.19E+10	270.7	3.68E+10	267.2	4.1E+10	264.1		
8.38E+09	289.6	8.93E+09	287.4	9.3E+09	285.1	1.08E+10	282.4	1.28E+10	279.7	1.64E+10	276.5	2.28E+10	273.2	2.92E+10	270.6	3.17E+10	266.5	4.14E+10	264		

Figure D.5: Numerical data for figure 8.8 (on the left) & 8.9 (on the right).

PCC			PCC			DAC		
P (kbar)	R (Ohm)	ρ (Ohm*m)	P (kbar)	R (Ohm)	ρ (Ohm*m)	P (kbar)	R (Ohm)	ρ (Ohm*m)
0	1.66E+10	32342278	12.295	185000	360.4411	0	8779999999	3305104
0.5978	6.9E+09	13443477	12.7657	136000	264.9729	1.58	3150000000	1185772
0.99791	4.57E+09	8903868	13.2364	95400	185.8707	4.36	103500000	38961.07
1.46862	2.84E+09	5533257	13.7071	70300	136.9676	8	2250000	846.9798
1.93934	1.77E+09	3448544	14.1779	53300	103.846	8.47	1940000	730.2848
2.41005	1.15E+09	2240580	14.6486	40300	78.5177	9.95	426700	160.625
2.88076	7.5E+08	1461248	15.1193	31500	61.3724	10.5	401000	150.9506
3.35147	5.04E+08	981958.3	15.59	21000	40.91493	12.35	188000	70.76987
3.82219	3.2E+08	623465.6	16.0607	17000	33.12161	12.51	170000	63.99403
4.2929	2.13E+08	414994.3	16.5314	14600	28.44562	15.14	82000	30.86771
4.76361	1.4E+08	272766.2	17.0021	12500	24.35413	16.75	62240	23.42934
5.23432	85700000	166971.9	17.4728	10300	20.0678	18	57620	21.69021
5.70504	58300000	113587.6	17.9436	8990	17.51549	20.23	42125	15.85734
6.17575	38500000	75010.71	18.4143	7820	15.23594	29.58	32012	12.05045
6.64646	25300000	49292.75	18.885	6960	13.56038			
7.11717	17600000	34290.61	19.3557	6200	12.07965			
7.58788	11300000	22016.13	19.8264	5560	10.83271			
8.0586	7820000	15235.94	20.1041	5300	10.32615			
8.52931	5000000	9741.65	20.2971	5050	9.839066			
9.00002	3280000	6390.522	20.7678	4670	9.098701			
9.47073	2140000	4169.426	21.2385	4300	8.377819			
9.94145	1380000	2688.695	21.7093	4180	8.144019			
10.4122	1080000	2104.196	22.18	3630	7.072438			
10.5534	862000	1679.46	22.6507	3450	6.721739			
10.8829	560000	1091.065	23.1214	3350	6.526906			
11.3536	381000	742.3137	23.5921	3270	6.371039			
11.8243	266000	518.2558						

Figure D.6: Numerical data for figure 8.10.

At P=7.2kbar		At P=9.77kbar		At P=11.63kbar		At P=29kbar	
R (Ohm)	T (K)	R (Ohm)	T (K)	R (Ohm)	T (K)	R (Ohm)	T (K)
5500000	294	2560000	295	331400	296	40000	298
5620000	291	2575000	294	332900	294	43000	294
5724000	288	2624000	291	335400	292	46000	290
5900000	285	2671000	288	337300	290	51500	283
6074000	282	2727000	285	339700	288	55300	279
6258000	279	2802000	282	341700	286	58500	276
6452000	276	2880000	279	346500	282	61400	273
6647000	273	2953000	276	348900	280	64800	270
6849000	270	3028000	273	353100	277	67800	266
7051000	267	3108000	270	356400	275	70100	263
7253000	264	3181000	267	360800	272	73800	259
7489000	261	3265000	264	364100	270	77500	255
7701000	258	3343000	261	369200	267	80600	252
7912000	255	3426000	258	374600	264	84120	249
8167000	252	3515000	255	380600	261	87920	246
8571000	247	3598000	252	387300	258	91900	243
8641000	246	3686000	249	394000	255	96100	240
8910000	243	3778000	246	401400	252	99400	238
9155000	240	3877000	243	409100	249	102400	236
9417000	237	3975000	240	417300	246	111100	233
9669000	234	4074000	237	425900	243	114800	231
9948000	231	4184000	234	435200	240	118540	229
10230000	228	4288000	231	444900	237	120670	227
10500000	225	4398000	228	455600	234	122800	226
10590000	224	4521000	225	466300	231	125040	225
10752000	222	4562000	224	478300	228	127300	224
11026000	219			487400	226	129900	223
				496400	224	132400	222
				500600	223	134900	221
				505900	222	138300	220
				511300	221	139700	219.5

Figure D.7: Numerical data for figure 8.11.

At P=7.2kbar		in DAC					
T (K)	1/T	R (Ohm)	p (Ohm*c	S (S/cm)	Log conduct	Energy Ga	Band Gap
294	0.003401	5500000	207039.5	4.83E-06	-12.240665	0.05411	0.1082209
291	0.003436	5620000	211556.7	4.7269E-06	-12.262249		
288	0.003472	5724000	215471.7	4.641E-06	-12.280585		
285	0.003509	5900000	222096.9	4.5025E-06	-12.310869		
282	0.003546	6074000	228646.9	4.3736E-06	-12.339934		
279	0.003584	6258000	235573.3	4.245E-06	-12.369777		
276	0.003623	6452000	242876.2	4.1173E-06	-12.400307		
273	0.003663	6647000	250216.7	3.9965E-06	-12.430082		
270	0.003704	6849000	257820.7	3.8787E-06	-12.46002		
267	0.003745	7051000	265424.7	3.7675E-06	-12.489086		
264	0.003788	7253000	273028.7	3.6626E-06	-12.517332		
261	0.003831	7489000	281912.5	3.5472E-06	-12.549352		
258	0.003876	7701000	289893	3.4495E-06	-12.577267		
255	0.003922	7912000	297835.8	3.3576E-06	-12.604297		
252	0.003968	8167000	307434.9	3.2527E-06	-12.636018		
247	0.004049	8571000	322642.8	3.0994E-06	-12.684301		
246	0.004065	8641000	325277.9	3.0743E-06	-12.692435		
243	0.004115	8910000	335404	2.9815E-06	-12.723091		
240	0.004167	9155000	344626.7	2.9017E-06	-12.750217		
237	0.004219	9417000	354489.3	2.821E-06	-12.778433		
234	0.004274	9669000	363975.5	2.7474E-06	-12.804842		
231	0.004329	9948000	374478	2.6704E-06	-12.833288		
228	0.004386	10230000	385093.5	2.5968E-06	-12.861241		
225	0.004444	10500000	395257.3	2.53E-06	-12.887292		
224	0.004464	10590000	398645.2	2.5085E-06	-12.895827		

At P=9.77kbar		in DAC					
T (K)	1/T	R (Ohm)	p (Ohm*c	S (S/cm)	Log conduct	Energy Ga	Band Gap
294	0.003401	2575000	96932.14	1.0316E-05	-11.481766	0.046695	0.0933905
291	0.003436	2624000	98776.67	1.0124E-05	-11.500617		
288	0.003472	2671000	100545.9	9.9457E-06	-11.51837		
285	0.003509	2727000	102654	9.7415E-06	-11.539119		
282	0.003546	2802000	105477.2	9.4807E-06	-11.56625		
279	0.003584	2880000	108413.4	9.224E-06	-11.593707		
276	0.003623	2953000	111161.4	8.9959E-06	-11.618738		
273	0.003663	3028000	113984.7	8.7731E-06	-11.643819		
270	0.003704	3108000	116996.1	8.5473E-06	-11.669896		
267	0.003745	3181000	119744.1	8.3511E-06	-11.693112		
264	0.003788	3265000	122906.2	8.1363E-06	-11.719177		
261	0.003831	3343000	125842.4	7.9464E-06	-11.742785		
258	0.003876	3426000	128966.8	7.7539E-06	-11.76731		
255	0.003922	3515000	132317.1	7.5576E-06	-11.792956		
252	0.003968	3598000	135441.5	7.3833E-06	-11.816295		
249	0.004016	3686000	138754.1	7.207E-06	-11.840459		
246	0.004065	3778000	142217.3	7.0315E-06	-11.865112		
243	0.004115	3877000	145944	6.8519E-06	-11.890979		
240	0.004167	3975000	149633.1	6.683E-06	-11.915942		
237	0.004219	4074000	153359.8	6.5206E-06	-11.940542		
234	0.004274	4184000	157500.6	6.3492E-06	-11.967185		
231	0.004329	4288000	161415.5	6.1952E-06	-11.991737		
228	0.004386	4398000	165556.3	6.0402E-06	-12.017067		
225	0.004444	4521000	170186.5	5.8759E-06	-12.04465		
224	0.004464	4562000	171729.9	5.8231E-06	-12.053678		

At P=11.63kbar		in DAC					
T (K)	1/T	R (Ohm)	p (Ohm*c	S (S/cm)	Log conduct	Energy Ga	Band Gap
294	0.003401	332900	12531.54	7.9799E-05	-9.4360037	0.032331	0.0646621
292	0.003425	335400	12625.65	7.9204E-05	-9.4434854		
290	0.003448	337300	12697.17	7.8758E-05	-9.4491343		
288	0.003472	339700	12787.51	7.8201E-05	-9.4562244		
286	0.003497	341700	12862.8	7.7744E-05	-9.4620947		
282	0.003546	346500	13043.49	7.6667E-05	-9.4760444		
280	0.003571	348900	13133.83	7.6139E-05	-9.4829469		
277	0.00361	353100	13291.94	7.5234E-05	-9.4949129		
275	0.003636	356400	13416.16	7.4537E-05	-9.5042153		
272	0.003676	360800	13581.79	7.3628E-05	-9.5164854		
270	0.003704	364100	13706.02	7.2961E-05	-9.5255901		
267	0.003745	369200	13898	7.1953E-05	-9.5395001		
264	0.003788	374600	14101.27	7.0916E-05	-9.5540204		
261	0.003831	380600	14327.13	6.9798E-05	-9.5699105		
258	0.003876	387300	14579.35	6.859E-05	-9.5873612		
255	0.003922	394000	14831.56	6.7424E-05	-9.6045125		
252	0.003968	401400	15110.12	6.6181E-05	-9.62312		
249	0.004016	409100	15399.98	6.4935E-05	-9.6421212		
246	0.004065	417300	15708.65	6.3659E-05	-9.661967		
243	0.004115	425900	16032.39	6.2374E-05	-9.6823661		
240	0.004167	435200	16382.47	6.1041E-05	-9.7039673		
237	0.004219	444900	16747.61	5.971E-05	-9.7260111		
234	0.004274	455600	17150.4	5.8308E-05	-9.7497768		
231	0.004329	466300	17553.19	5.697E-05	-9.7729908		
228	0.004386	478300	18004.91	5.554E-05	-9.7983997		
226	0.004425	487400	18347.47	5.4503E-05	-9.8172467		
224	0.004464	496400	18686.26	5.3515E-05	-9.8355436		

At P=0kbar		on CPP					
T (K)	1/T	R (Ohm)	p (Ohm*c	S (S/cm)	Log conduct	Energy Ga	Band Gap
294	0.003401	6120000000	1.19E+09	8.3866E-10	-20.899215	0.446851	0.8937024
295	0.00339	5700000000	1.11E+09	9.0046E-10	-20.82812		
296	0.003378	5350000000	1.04E+09	9.5936E-10	-20.76475		
297	0.003367	5150000000	1E+09	9.9662E-10	-20.72665		
298	0.003356	4900000000	9.55E+08	1.0475E-09	-20.676889		
299	0.003344	4680000000	9.12E+08	1.0967E-09	-20.630951		
300	0.003333	4320000000	8.42E+08	1.1881E-09	-20.550909		
301	0.003322	4050000000	7.89E+08	1.2673E-09	-20.48637		
302	0.003311	3800000000	7.4E+08	1.3507E-09	-20.422654		
303	0.0033	3500000000	6.82E+08	1.4665E-09	-20.340416		
304	0.003289	3280000000	6.39E+08	1.5648E-09	-20.275497		
306	0.003268	3000000000	5.84E+08	1.7109E-09	-20.186266		
308	0.003247	2700000000	5.26E+08	1.901E-09	-20.080905		
311	0.003215	2140000000	4.17E+08	2.3984E-09	-19.848459		
314	0.003185	1880000000	3.66E+08	2.7301E-09	-19.718925		
316	0.003165	1600000000	3.12E+08	3.2079E-09	-19.557657		
319	0.003135	1400000000	2.73E+08	3.6661E-09	-19.424126		
324	0.003086	1070000000	2.08E+08	4.7968E-09	-19.155312		
327	0.003058	930000000	1.81E+08	5.5189E-09	-19.015083		
333	0.003003	627000000	1.22E+08	8.186E-09	-18.620845		
336	0.002976	560000000	1.09E+08	9.1654E-09	-18.507835		
341	0.002933	535000000	1.04E+08	9.5936E-09	-18.462165		
346	0.00289	470000000	91571510	1.092E-08	-18.332631		
351	0.002849	347000000	67607051	1.4791E-08	-18.029223		
355	0.002817	328000000	63905224	1.5648E-08	-17.972912		
357	0.002801	290000000	56501570	1.7699E-08	-17.849779		

Figure D.8: BGs at *Pelevated* in DAC & *Pamb* on CPP for the Pt(F-bqd)$_2$ complex.

The PTC1 complex

Pamb heat gun	
R (Ohm)	T (K)
7.77E+09	294.4
7.34E+09	295
6.8E+09	296
6.5E+09	297
6.12E+09	298
5.9E+09	299
5.6E+09	300
5.32E+09	301
5.08E+09	302
4.82E+09	303
4.58E+09	304
4.41E+09	305
4.21E+09	306
4.04E+09	307
3.85E+09	308
3.68E+09	309
3.49E+09	310
3.34E+09	311
3.18E+09	312
3.01E+09	313
2.87E+09	314
2.72E+09	315
2.54E+09	316
2.37E+09	317
2.2E+09	318

DAC		
P (kbar)	R (Ohm)	ρ (Ohm*m)
0	8600000000	3237345.1
0.24	7770000000	2924903.7
0.32	7560000000	2845852.2
1.55	7040000000	2650105.8
4.16	7530000000	2834559.2
5.23	7560000000	2845852.2
5.85	7570000000	2849616.6
6.68	7570000000	2849616.6
9.67	7530000000	2834559.2
12.62	7450000000	2804444.3
13.69	7430000000	2796915.6

At P=0kbar		on CPP					
T (K)	1/T	R (Ohm)	ρ (Ohm*c	S (S/cm)	Log conduct	Energy Ga	Band Gap
294.4	0.003397	7770000000	2.92E+08	3.4189E-09	-19.493942	0.401241	0.8024829
295	0.00339	7340000000	2.76E+08	3.6192E-09	-19.437011		
296	0.003378	6800000000	2.56E+08	3.9066E-09	-19.360595		
297	0.003367	6500000000	2.45E+08	4.0869E-09	-19.315474		
298	0.003356	6120000000	2.3E+08	4.3407E-09	-19.255234		
299	0.003344	5900000000	2.22E+08	4.5025E-09	-19.218624		
300	0.003333	5600000000	2.11E+08	4.7437E-09	-19.166439		
301	0.003322	5320000000	2E+08	4.9934E-09	-19.115145		
302	0.003311	5080000000	1.91E+08	5.2293E-09	-19.068983		
303	0.0033	4820000000	1.81E+08	5.5114E-09	-19.016446		
304	0.003289	4580000000	1.72E+08	5.8002E-09	-18.965371		
305	0.003279	4410000000	1.66E+08	6.0238E-09	-18.927547		
306	0.003268	4210000000	1.58E+08	6.31E-09	-18.881135		
307	0.003257	4040000000	1.52E+08	6.5755E-09	-18.839917		
308	0.003247	3850000000	1.45E+08	6.9E-09	-18.791745		
309	0.003236	3680000000	1.39E+08	7.2187E-09	-18.746585		
310	0.003226	3490000000	1.31E+08	7.6117E-09	-18.693574		
311	0.003215	3340000000	1.26E+08	7.9536E-09	-18.649643		
312	0.003205	3180000000	1.2E+08	8.3538E-09	-18.600553		
313	0.003195	3010000000	1.13E+08	8.8256E-09	-18.545612		
314	0.003185	2870000000	1.08E+08	9.2561E-09	-18.497984		
315	0.003175	2720000000	1.02E+08	9.7665E-09	-18.444304		
316	0.003165	2540000000	95614612	1.0459E-08	-18.375836		
317	0.003155	2370000000	89215209	1.1209E-08	-18.306562		
318	0.003145	2200000000	82815806	1.2075E-08	-18.232129		

Figure D.9: Numerical data for figure 8.12 (on the left), 8.13 (in the middle) and BG calculations for the PTC1 complex (on the right).

The $Pt(NH_3)_4PtCl_4$ complex

DAC			
P (kbar)	R (Ohm)	ρ (Ohm*m)	Conductivity (S/cm)
0.26	2670000	858.94167	1.16422E-05
5.2	1510000	485.76851	2.05859E-05
6.6	1387000	446.19929	2.24115E-05
9.64	1153000	370.92125	2.69599E-05
12.74	952000	306.25935	3.26521E-05
14.71	830600	267.20485	3.74245E-05
20.2	590000	189.80359	5.2686E-05
21.39	552000	177.57895	5.6313E-05
24.27	444000	142.83524	7.00107E-05
26.54	408000	131.25401	7.61881E-05
28.18	376000	120.95958	8.26722E-05
32.57	312000	100.37071	9.96307E-05
40.05	193200	62.152633	0.000160894
41.14	179000	57.584479	0.000173658
45.4	161000	51.793861	0.000193073
49.16	154000	49.541954	0.000201849
52.2	150000	48.25515	0.000207232
54.27	153000	49.220253	0.000203168
56.1	157000	50.507057	0.000197992

At P=2.1kbar		At P=56.1kbar	
R (Ohm)	T (K)	R (Ohm)	T (K)
1800000	294	157000	294
1650000	295	146300	295
1510000	296	138000	296
1410000	297	132000	297
1320000	298	127000	298
1240000	299	122000	299
1190000	300	118000	300
1120000	301	114000	301
1070000	302	111000	302
1020000	303	107000	303
969000	304	104000	304
936000	305	101000	305
901000	306	98800	306
848000	307	96100	307
814000	308	93600	308
786000	309	91100	309
754000	310	89000	310
733000	311	86900	311
700000	312	84500	312
675000	313	82400	313

Figure D.10: Numerical data for figure 8.14 (on the left) & 8.15 (on the right).

At P=2.1kbar		in DAC					
T (K)	1/T	R (Ohm)	ρ (Ohm*cm)	S (S/cm)	Log conduct	Energy Ga	Band Gap
294	0.003401	1800000	57906.18	1.7269E-05	-10.966579	0.391869	0.7837377
295	0.00339	1650000	53080.665	1.8839E-05	-10.879568		
296	0.003378	1510000	48576.851	2.0586E-05	-10.790902		
297	0.003367	1410000	45359.841	2.2046E-05	-10.722382		
298	0.003356	1320000	42464.532	2.3549E-05	-10.656424		
299	0.003344	1240000	39890.924	2.5068E-05	-10.593904		
300	0.003333	1190000	38282.419	2.6122E-05	-10.552746		
301	0.003322	1120000	36030.512	2.7754E-05	-10.492121		
302	0.003311	1070000	34422.007	2.9051E-05	-10.446451		
303	0.0033	1020000	32813.502	3.0475E-05	-10.398595		
304	0.003289	969000	31172.8269	3.2079E-05	-10.347302		
305	0.003279	936000	30111.2136	3.321E-05	-10.312653		
306	0.003268	901000	28985.2601	3.45E-05	-10.274543		
307	0.003257	848000	27280.2448	3.6657E-05	-10.213918		
308	0.003247	814000	26186.4614	3.8188E-05	-10.172998		
309	0.003236	786000	25285.6986	3.9548E-05	-10.137994		
310	0.003226	754000	24256.2554	4.1226E-05	-10.09643		
311	0.003215	733000	23580.6833	4.2408E-05	-10.068183		
312	0.003205	700000	22519.07	4.4407E-05	-10.022118		
313	0.003195	675000	21714.8175	4.6052E-05	-9.9857501		

At P=56.1kbar		in DAC					
T (K)	1/T	R (Ohm)	ρ (Ohm*cm)	S (S/cm)	Log conduct	Energy Ga	Band Gap
294	0.003401	157000	5050.7057	0.00019799	-8.5272833	0.251827	0.5036544
295	0.00339	146300	4706.48563	0.00021247	-8.4566968		
296	0.003378	138000	4439.4738	0.00022525	-8.3982911		
297	0.003367	132000	4246.4532	0.00023549	-8.3538394		
298	0.003356	127000	4085.6027	0.00024476	-8.3152245		
299	0.003344	122000	3924.7522	0.00025479	-8.2750585		
300	0.003333	118000	3796.0718	0.00026343	-8.2417221		
301	0.003322	114000	3667.3914	0.00027267	-8.2072359		
302	0.003311	111000	3570.8811	0.00028004	-8.1805677		
303	0.0033	107000	3442.2007	0.00029051	-8.1438663		
304	0.003289	104000	3345.6904	0.00029889	-8.1154283		
305	0.003279	101000	3249.1801	0.00030777	-8.086158		
306	0.003268	98800	3178.40588	0.00031462	-8.0641351		
307	0.003257	96100	3091.54661	0.00032346	-8.0364268		
308	0.003247	93600	3011.12136	0.0003321	-8.0100678		
309	0.003236	91100	2930.69611	0.00034122	-7.9829953		
310	0.003226	89000	2863.1389	0.00034927	-7.9596738		
311	0.003215	86900	2795.58169	0.00035771	-7.9357955		
312	0.003205	84500	2718.37345	0.00036787	-7.907789		
313	0.003195	82400	2650.81624	0.00037724	-7.8826229		

Figure D.11: BGs at *Pelevated* in DAC for the $Pt(NH_3)_4PtCl_4$ complex.

The $Pt(CH_3NH_2)_4PtCl_4$ complex

DAC		
P (kbar)	R (Ohm)	ρ (Ohm*m)
0	436000000	140261.64
1	262000000	84285.662
4.5	154000000	49541.954
8.5	96000000	30883.296
14.5	48200000	15505.988
19	31300000	10069.241
25	24900000	8010.3549
30	17200000	5533.2572
33	13100000	4214.2831
35.5	10100000	3249.1801

At P=17.5kbar		At P=28kbar	
R (Ohm)	T (K)	R (Ohm)	T (K)
21300000	294	5310000	294
20000000	295	4570000	295
18200000	296	4150000	296
16600000	297	3820000	297
15500000	298	3460000	298
14400000	299	3180000	299
13500000	300	2980000	300
12700000	301	2730000	301
12000000	302	2590000	302
11400000	303	2490000	303
10800000	304	2330000	304
10300000	305	2220000	305
9820000	306	2140000	306
9390000	307	2060000	307
9050000	308	1950000	308
8800000	309	1850000	309
8540000	310	1760000	310
8260000	311	1680000	311
8060000	312	1610000	312
7820000	313	1550000	313
7550000	314	1490000	314
7400000	315	1440000	315
7250000	316	1390000	316
7090000	317	1330000	317
6960000	318	1200000	318
6840000	319	1130000	319
6740000	320	1050000	320
6620000	321	1000000	321
6560000	322	937000	322
6480000	323	882000	323

Figure D.12: Numerical data for figure 8.16 (on the left) & 8.17 (on the right).

At P=17.5kbar		in DAC					
T (K)	1/T	R (Ohm)	ρ (Ohm*cm)	S (S/cm)	Log conduct	Energy Ga	Band Gap
294	0.003401	21300000	685223.13	1.4594E-06	-13.4375	0.325455	0.6509104
295	0.00339	20000000	643402	1.5542E-06	-13.374525		
296	0.003378	18200000	585495.82	1.708E-06	-13.280214		
297	0.003367	16600000	534023.66	1.8726E-06	-13.188195		
298	0.003356	15500000	498636.55	2.0055E-06	-13.119633		
299	0.003344	14400000	463249.44	2.1587E-06	-13.046021		
300	0.003333	13500000	434296.35	2.3026E-06	-12.981482		
301	0.003322	12700000	408560.27	2.4476E-06	-12.920395		
302	0.003311	12000000	386041.2	2.5904E-06	-12.863699		
303	0.0033	11400000	366739.14	2.7267E-06	-12.812406		
304	0.003289	10800000	347437.08	2.8782E-06	-12.758339		
305	0.003279	10300000	331352.03	3.0179E-06	-12.710937		
306	0.003268	9820000	315910.382	3.1655E-06	-12.663214		
307	0.003257	9390000	302077.239	3.3104E-06	-12.618438		
308	0.003247	9050000	291139.405	3.4348E-06	-12.581557		
309	0.003236	8800000	283096.88	3.5324E-06	-12.553544		
310	0.003226	8540000	274732.654	3.6399E-06	-12.523554		
311	0.003215	8260000	265725.026	3.7633E-06	-12.490217		
312	0.003205	8060000	259291.006	3.8567E-06	-12.465706		
313	0.003195	7820000	251570.182	3.975E-06	-12.435477		
314	0.003185	7550000	242884.255	4.1172E-06	-12.40034		
315	0.003175	7400000	238058.74	4.2006E-06	-12.380273		
316	0.003165	7250000	233233.225	4.2876E-06	-12.359794		
317	0.003155	7090000	228086.009	4.3843E-06	-12.337478		
318	0.003145	6960000	223903.896	4.4662E-06	-12.318972		
319	0.003135	6840000	220043.484	4.5446E-06	-12.30158		
320	0.003125	6740000	216826.474	4.612E-06	-12.286853		
321	0.003115	6620000	212966.062	4.6956E-06	-12.268888		
322	0.003106	6560000	211035.856	4.7385E-06	-12.259783		
323	0.003096	6480000	208462.248	4.797E-06	-12.247513		

At P=28kbar		in DAC					
T (K)	1/T	R (Ohm)	ρ (Ohm*cm)	S (S/cm)	Log conduct	Energy Ga	Band Gap
294	0.003401	5310000	170823.231	5.854E-06	-12.048385	0.450457	0.9009143
295	0.00339	4570000	147017.357	6.8019E-06	-11.898306		
296	0.003378	4150000	133505.915	7.4903E-06	-11.801901		
297	0.003367	3820000	122889.782	8.1374E-06	-11.719043		
298	0.003356	3460000	111308.546	8.984E-06	-11.620061		
299	0.003344	3180000	102300.918	9.7751E-06	-11.535674		
300	0.003333	2980000	95866.898	1.0431E-05	-11.470716		
301	0.003322	2730000	87824.373	1.1386E-05	-11.383094		
302	0.003311	2590000	83320.559	1.2002E-05	-11.330451		
303	0.0033	2490000	80103.549	1.2484E-05	-11.291075		
304	0.003289	2330000	74956.333	1.3341E-05	-11.224661		
305	0.003279	2220000	71417.622	1.4002E-05	-11.1763		
306	0.003268	2140000	68844.014	1.4526E-05	-11.139599		
307	0.003257	2060000	66270.406	1.509E-05	-11.101499		
308	0.003247	1950000	62731.695	1.5941E-05	-11.046622		
309	0.003236	1850000	59514.685	1.6803E-05	-10.993978		
310	0.003226	1760000	56619.376	1.7662E-05	-10.944107		
311	0.003215	1680000	54045.768	1.8503E-05	-10.897587		
312	0.003205	1610000	51793.861	1.9307E-05	-10.855027		
313	0.003195	1550000	49863.655	2.0055E-05	-10.817048		
314	0.003185	1490000	47933.449	2.0862E-05	-10.777569		
315	0.003175	1440000	46324.944	2.1587E-05	-10.743436		
316	0.003165	1390000	44716.439	2.2363E-05	-10.708096		
317	0.003155	1330000	42786.233	2.3372E-05	-10.663972		
318	0.003145	1200000	38604.12	2.5904E-05	-10.561114		
319	0.003135	1130000	36352.213	2.7509E-05	-10.50101		
320	0.003125	1050000	33778.605	2.9605E-05	-10.427583		
321	0.003115	1000000	32170.1	3.1085E-05	-10.378793		
322	0.003106	937000	30143.3837	3.3175E-05	-10.313721		
323	0.003096	882000	28374.0282	3.5243E-05	-10.25323		

Figure D.13: BGs at *Pelevated* in DAC for the $Pt(CH_3NH_2)_4PtCl_4$ complex.

The $Ir(CO)_2(bta)$ complex

DAC		
P (kbar)	R (Ohm)	ρ (Ohm*m)
0	1.07E+10	3442200.7
1.52	1.04E+10	3345690.4
3.27	1.046E+10	3364992.5
5.1	1.039E+10	3342473.4
5.46	1.04E+10	3345690.4
8.11	1.039E+10	3342473.4
11.47	1.04E+10	3345690.4
13.34	1.038E+10	3339256.4
15.78	1.034E+10	3326388.3
19.64	1.03E+10	3313520.3
25.52	1.032E+10	3319954.3
29.38	1.019E+10	3278133.2
30.83	1.014E+10	3262048.1
34.72	1.0135E+10	3260439.6
38.18	9980000000	3210576
39.98	9890000000	3181622.9
42.85	9710000000	3123716.7
44.78	9790000000	3149452.8
47.11	9600000000	3088329.6
49.8	9410000000	3027206.4
52.42	9175000000	2951606.7
55.08	8825000000	2839011.3
59.3	8150000000	2621863.2
65.97	7080000000	2277643.1
71.73	5950000000	1914121
76.14	5010000000	1611722
78.3	4730000000	1521645.7

Figure D.14: Numerical data for figure 8.18.

The Ir(CO)2(tfp) complex

DAC			DAC		
Pressure application			Pressure release		
P (kbar)	R (Ohm)	ρ (Ohm*m)	P (kbar)	R (Ohm)	ρ (Ohm*m)
0	1.2E+10	3860412	48.9	6.8E+08	218756.68
6.4	9.4E+09	3023989.4	42.2	9E+08	289530.9
15.8	8.38E+09	2695854.38	36.5	32000000	10294.432
18.6	7.8E+09	2509267.8	34.8	4.7E+08	151199.47
20.8	7.37E+09	2370936.37	29	1.5E+09	482551.5
25.9	6.06E+09	1949508.06	22.2	3.12E+09	1003707.12
29.8	3.13E+09	1006924.13	17.2	4.7E+09	1511994.7
32.6	1.62E+09	521155.62	7.2	9E+09	2895309
34.6	4.55E+08	146373.955	0	1.19E+10	3828241.9
37.9	2.75E+08	88467.775			
40.5	1.53E+08	49220.253			
43.9	3.7E+08	119029.37			
48.9	6.8E+08	218756.68			

Figure D.15: Numerical data for figure 8.19.

The GDC1 complex

Pamb hot plate	
R (Ohm)	T (K)
238000	295
220000	296
214000	297
210000	298
206000	299
199000	300
192000	301
190000	302
181000	303
178000	304
172000	305
169000	306
167000	307
164000	308
149000	310
144000	311
141000	312
135000	313
133000	314
127000	316
124000	317
122000	318
116000	319
110000	320
105000	321
102000	322
94900	324
91000	325
90100	327
88900	328
84500	329
84000	330
83600	331
82500	332
79100	333
76600	334
74500	335
71400	336
66900	338
63600	339
60400	340
59400	341
56700	342
55600	343
53200	344
51200	345
49400	346
48700	348
46800	349
46200	351
44700	352
43200	353

At P=0kbar		on CPP					
T (K)	1/T	R (Ohm)	ρ (Ohm*cm)	S (S/cm)	Log conduc	Energy Gap	Band Gap
295	0.0034	238000	46370.254	2E-05	-10.7444	0.26259479	0.52519
296	0.0034	220000	42863.26	2E-05	-10.6658		
297	0.0034	214000	41694.262	2E-05	-10.6381		
298	0.0034	210000	40914.93	2E-05	-10.6193		
299	0.0033	206000	40135.598	2E-05	-10.6		
300	0.0033	199000	38771.767	3E-05	-10.5654		
301	0.0033	192000	37407.936	3E-05	-10.5296		
302	0.0033	190000	37018.27	3E-05	-10.5192		
303	0.0033	181000	35264.773	3E-05	-10.4706		
304	0.0033	178000	34680.274	3E-05	-10.4539		
305	0.0033	172000	33511.276	3E-05	-10.4196		
306	0.0033	169000	32926.777	3E-05	-10.402		
307	0.0033	167000	32537.111	3E-05	-10.3901		
308	0.0032	164000	31952.612	3E-05	-10.372		
310	0.0032	149000	29030.117	3E-05	-10.2761		
311	0.0032	144000	28055.952	4E-05	-10.242		
312	0.0032	141000	27471.453	4E-05	-10.2209		
313	0.0032	135000	26302.455	4E-05	-10.1774		
314	0.0032	133000	25912.789	4E-05	-10.1625		
316	0.0032	127000	24743.791	4E-05	-10.1163		
317	0.0032	124000	24159.292	4E-05	-10.0924		
318	0.0031	122000	23769.626	4E-05	-10.0762		
319	0.0031	116000	22600.628	4E-05	-10.0257		
320	0.0031	110000	21431.63	5E-05	-9.97262		
321	0.0031	105000	20457.465	5E-05	-9.9261		
322	0.0031	102000	19872.966	5E-05	-9.89712		
324	0.0031	94900	18489.652	5E-05	-9.82497		
325	0.0031	91000	17729.803	6E-05	-9.783		
327	0.0031	90100	17554.453	6E-05	-9.77306		
328	0.003	88900	17320.654	6E-05	-9.75965		
329	0.003	84500	16463.389	6E-05	-9.70889		
330	0.003	84000	16365.972	6E-05	-9.70296		
331	0.003	83600	16288.039	6E-05	-9.69819		
332	0.003	82500	16073.723	6E-05	-9.68494		
333	0.003	79100	15411.29	6E-05	-9.64286		
334	0.003	76600	14924.208	7E-05	-9.61074		
335	0.003	74500	14515.059	7E-05	-9.58294		
336	0.003	71400	13911.076	7E-05	-9.54044		
338	0.003	66900	13034.328	8E-05	-9.47534		
339	0.0029	63600	12391.379	8E-05	-9.42476		
340	0.0029	60400	11767.913	8E-05	-9.37313		
341	0.0029	59400	11573.08	9E-05	-9.35644		
342	0.0029	56700	11047.031	9E-05	-9.30992		
343	0.0029	55600	10832.715	9E-05	-9.29033		
344	0.0029	53200	10365.116	1E-04	-9.2462		
345	0.0029	51200	9975.4496	0.0001	-9.20788		
346	0.0029	49400	9624.7502	0.0001	-9.17209		
348	0.0029	48700	9488.3671	0.0001	-9.15782		
349	0.0029	46800	9118.1844	0.0001	-9.11803		
351	0.0028	46200	9001.2846	0.0001	-9.10512		
352	0.0028	44700	8709.0351	0.0001	-9.07212		
353	0.0028	43200	8416.7856	0.0001	-9.03798		

Figure D.16: Numerical data for figure 8.20 (on the left) and BG calculations for the GDC1 complex (on the right).

The GDC2 complex

Pamb heat gun	
R (Ohm)	T (K)
64300000	308
53200000	313
47400000	318
41600000	323
38600000	328
32800000	333
23500000	338
21700000	343
21100000	348
20200000	353

Pamb PPMS	
R (Ohm)	T (K)
16800000	300
18400000	295
20600000	290
23400000	285
26900000	280
31200000	275
36200000	270
42700000	265
53600000	260
67800000	255
85100000	250
1.06E+08	245
1.4E+08	240
2.04E+08	235
2.59E+08	230
3.35E+08	225
4.42E+08	220
7.91E+08	215
1.04E+09	210
1.37E+09	205
1.85E+09	200
2.63E+09	195
3.81E+09	190

Figure D.17: Numerical data for figure 8.21 (on the left) & 8.22 (on the right).

PCC			PCC		
P (kbar)	R (Ohm)	ρ (Ohm*m)	P (kbar)	R (Ohm)	ρ (Ohm*m)
0	7970000	15528.1901	11.43472	1210000	2357.4793
2.038895	6620000	12897.9446	11.90451	1060000	2065.2298
2.978477	6010000	11709.4633	12.3743	975000	1899.62175
3.448269	5590000	10891.1647	12.8441	861000	1677.51213
3.91806	5250000	10228.7325	13.31389	760000	1480.7308
4.387851	4960000	9663.7168	13.78368	669000	1303.43277
4.857643	4350000	8475.2355	14.25347	585000	1139.77305
5.327434	3830000	7462.1039	14.72326	518000	1009.23494
5.797226	3390000	6604.8387	15.19305	474000	923.50842
6.267017	3130000	6098.2729	15.66284	415000	808.55695
6.736808	2720000	5299.4576	16.13264	370000	720.8821
7.2066	2360000	4598.0588	16.60243	333000	648.79389
7.676391	2180000	4247.3594	17.07222	301000	586.44733
8.146183	1780000	3468.0274	17.54201	270000	526.0491
8.615974	2110000	4110.9763	18.0118	245000	477.34085
9.085765	1810000	3526.4773	18.48159	220000	428.6326
9.555557	1560000	3039.3948	18.95138	199000	387.71767
10.02535	1430000	2786.1119	19.42118	178000	346.80274
10.49514	1640000	3195.2612	20.17284	160000	311.7328
10.96493	1400000	2727.662			

At P=0kbar		on CPP using heat gun					
T (K)	1/T	R (Ohm)	ρ (Ohm*cm)	S (S/cm)	Log conduct	Energy Gap	Band Gap
308	0.003247	64300000	12527761.9	7.98E-08	-16.343458	0.2580667	0.516133
313	0.003195	53200000	10365115.6	9.65E-08	-16.153956		
318	0.003145	47400000	9235084.2	1.08E-07	-16.03852		
323	0.003096	41600000	8105052.8	1.23E-07	-15.907998		
328	0.003049	38600000	7520553.8	1.33E-07	-15.83315		
333	0.003003	32800000	6390522.4	1.56E-07	-15.670327		
338	0.002959	23500000	4578575.5	2.18E-07	-15.336898		
343	0.002915	21700000	4227876.1	2.37E-07	-15.25721		
348	0.002874	21100000	4110976.3	2.43E-07	-15.229171		
353	0.002833	20200000	3935626.6	2.54E-07	-15.185581		

At P=0kbar		on CPP using PPMS					
T (K)	1/T	R (Ohm)	ρ (Ohm*cm)	S (S/cm)	Log conduct	Energy Gap	Band Gap
300	0.003333	16800000	3273194.4	3.06E-07	-15.001277	0.2536569	0.507314
295	0.00339	18400000	3584927.2	2.79E-07	-15.092249		
290	0.003448	20600000	4013559.8	2.49E-07	-15.205189		
285	0.003509	23400000	4559092.2	2.19E-07	-15.332634		
280	0.003571	26900000	5241007.7	1.91E-07	-15.472024		
275	0.003636	31200000	6078789.6	1.65E-07	-15.620316		
270	0.003704	36200000	7052954.6	1.42E-07	-15.768957		
265	0.003774	42700000	8319369.1	1.2E-07	-15.934097		
260	0.003846	53600000	10443048.8	9.58E-08	-16.161447		
255	0.003922	67800000	13209677.4	7.57E-08	-16.39646		
250	0.004	85100000	16580288.3	6.03E-08	-16.623725		
245	0.004082	106000000	20652298	4.84E-08	-16.843337		
240	0.004167	140000000	27276620	3.67E-08	-17.12154		
235	0.004255	204000000	39745932	2.52E-08	-17.498018		
230	0.004348	259000000	50461747	1.98E-08	-17.736726		
225	0.004444	335000000	65269055	1.53E-08	-17.994029		
220	0.004545	442000000	86116186	1.16E-08	-18.271208		
215	0.004651	791000000	154112903	6.49E-09	-18.853196		
210	0.004762	1040000000	202626320	4.94E-09	-19.126874		
205	0.004878	1370000000	266921210	3.75E-09	-19.402464		
200	0.005	1850000000	360441050	2.77E-09	-19.702839		
195	0.005128	2630000000	512410790	1.95E-09	-20.054637		
190	0.005263	3810000000	742313730	1.35E-09	-20.425283		

Figure D.18: Numerical data for figure 8.23 (on the left) and BG calculations for the GDC2 complex (on the right).

Appendix E

Publications

- Giordano, N. et al., 2019. The Effect of Pressure on Halogen Bonding in 4-Iodobenzonitrile. *Molecules*, 24(10), pp.Molecules, 27 May 2019, Vol.24(10).
- Benjamin, Helen et al., 2020. Pressure-induced non-innocence in bis(1,2-dionedioximato)Pt(ii) complexes: an experimental and theoretical study of their insulatormetal transitions. *Physical Chemistry Chemical Physics*, 22(12), pp.6677–6689.
- Benjamin, Helen et al., 2020. Electrochemical deposition of a semiconducting gold dithiolene complex with NIR absorption. *Dalton Transactions*, *The Royal Society of Chemistry*, 24 Sep 2020.

References

[1] P.A. Kizelev, 2017. Информационные технологии в обществе. [Information technology in society], Achinsk, Russia.

[2] V. A. Gurtov, 2005. Твердотельная электроника. [Solid State Electronics], Moscow, Russia.

[3] Dennard, R. et al., 1999. Design Of Ion-implanted MOSFET's with Very Small Physical Dimensions. *Proceedings of the IEEE*, 87(4), pp.668–678.

[4] Moore, G.E., 2006. IEEE Solid-State Circuits Society. *Newsletter*, 11(3), pp.36–37.

[5] Advanced Micro Devices, Inc. Available at: https://www.amd.com/en/products/cpu/amd-ryzen-9-3950x

[6] Anon, 2015. More from Moore. *Nature*, 520(7548), p.408.

[7] Waldrop, M.M.M., 2016. More Than Moore. *Nature*, 530(7589), pp.144–147.

[8] Theis, T.N. & Solomon, P.M., 2010. It's time to reinvent the transistor! *Science* (New York, N.Y.), 327(5973), pp.1600–1601.

[9] Theis, T.N. & Solomon, P.M., 2010. In Quest of the "Next Switch": Prospects for Greatly Reduced Power Dissipation in a Successor to the Silicon Field-Effect Transistor. *Proceedings of the IEEE*, 98(12), pp.2005–2014.

[10] Haensch, W. et al., 2006. Silicon CMOS devices beyond scaling. *IBM Journal of Research and Development*, 50(4-5), pp.339–361.

[11] Baccarani, G., Wordeman, M.R. & Dennard, R.H., 1984. Generalized scaling theory and its application to a ¼ micrometer MOSFET design. *IEEE Transactions on Electron Devices*, 31(4), pp.452–462.

[12] Haensch, W. et al., 2006. Silicon CMOS devices beyond scaling. *IBM Journal Of Research And Development*, 50(4-5), pp.339–361.

[13] Waldrop, M.M., 2016. The chips are down for Moore's law. *Nature*, 530(7589), pp.144–7.

[14] Huang, X. et al., 1999. Technical Digest - *International Electron Devices Meeting*, pp.67–70.

[15] Fossum, J.G.G. & Trivedi, V.P.P., 2011. Fundamentals of ultra–thin–body MOSFETs and finFETs, *Cambridge University Press*.

[16] Taiwan Semiconductor Manufacturing Company Limited. Available at: https://www.tsmc.com

[17] SK HYNIX INC. Available at: https://www.skhynix.com

[18] SK HYNIX INC. Available at: https://www.skhynix.com/eng/about/history2010.jsp

[19] Taiwan Semiconductor Manufacturing Company Limited. Available at: https://www.tsmc.com/english/dedicatedFoundry/technology/16nm.htm

[20] Togatov, V. & Ternovskii, D., 2013. Metal-oxide-semiconductor field-effect transistor (MOSFET) ultrafast switching research and its applications. *Instruments and Experimental Techniques*, 56(1), pp.59–65.

[21] Kenny, R., Watt, J. The Breakthrough Advantage for FPGAs with Tri-Gate Technology. 2016. *Intel Corporation*. Available at: https://www.intel.com/content/dam/www/programmable/us/en/pdfs/literature/wp/wp-01201-fpga-tri-gate-technology.pdf

[22] Bhole, M. et al., 2013. FinFET- Benefits, Drawbacks and Challenges. *INTERNATIONAL JOURNAL OF ENGINEERING SCIENCES & RESEARCH TECHNOLOGY*, pp.3219-3222.

[23] Ali Javey et al., 2003. Ballistic carbon nanotube field-effect transistors. *Nature*, 424(6949), pp.654–657.

[24] He Tian et al., 2014. Novel Field-Effect Schottky Barrier Transistors Based on Graphene-MoS2 Heterojunctions. *Scientific Reports*, 4(1), p.5951.

[25] Mathew, L. et al., 2006. ITFET: Inverted T Channel FET, A Novel Device architecture and circuits based on the ITFET. 2006. *IEEE International Conference on IC Design and Technology*, pp.1–4.

[26] Horowitz, G., 1998. Organic Field-Effect Transistors. *Advanced Materials*, 10(5), pp.365–377.

[27] Rupp, K. Available at: https://www.karlrupp.net/2018/02/42-years-of-microprocessor-trend-data/

[28] David Altavilla and Hot Hardware, Inc. Available at: https://hothardware.com/news/amd-breaks-frequency-record-with-upcoming-fx-processor

[29] Martin Rodbell, 1980. The role of hormone receptors and GTP-regulatory proteins in membrane transduction. *Nature*, 284(5751), pp.17–22.

[30] Solomon et al., 2015. Pathway to the piezoelectronic transduction logic device. *Nano letters*, 15(4), pp.2391–2395.

[31] Datta, S. & Das, 1990. Electronic analog of the electro-optic modulator. *Applied Physics Letters*, 56(7), pp.665–667.

[32] Chen, I.-R., 2014. Novel Material Integration for Reliable and Energy-Efficient NEM Relay Technology.

[33] Baek, S. H. et al., 2011. Giant Piezoelectronicity on Si for Hyperactive MEMS. *Science*, 334, 958–961.

[34] Newns, D. et al., 2012. The piezoelectronic transistor: A nanoactuator-based post-CMOS digital switch with high speed and low power. *MRS Bulletin*, 37(11), pp.1071–1076.

[35] Uchino, K., 2003. Introduction to Piezoelectronic Actuators and Transducers. International Center for Actuators and Transducers, *Penn State University*.

[36] Chang, J. B. et al., 2015. First realization of the piezoelectronic stress-based transduction device. *Nanotechnology*, 26.

[37] Park, S. & Shrout, T.R., 1997. Ultrahigh strain and piezoelectronic behavior in relaxor based ferroelectric single crystals. *Journal of Applied Physics*, 82(4), pp.1804–1811.

[38] Copel, M. et al., 2013. Giant piezoresistive on/off ratios in rare-earth chalcogenide thin films enabling nanomechanical switching. *Nano letters*, 13(10), pp.4650–4653.

[39] Tichì, J., 2010. Fundamentals of piezoelectronic sensorics. Mechanical, dielectric and thermodynamical properties of piezoelectronic materials, Berlin; London: *Springer*.

[40] Moheimani, S.O.R., Fleming, A.J. & SpringerLink, 2006. Piezoelectronic transducers for vibration control and damping, London: *Springer*.

[41] Douglas A. S. et al., 2007. *Principles of Instrumental Analysis*, 6th Edition. Wadsworth publishing company.

[42] Newns, D.M. et al., 2012. High Response Piezoelectronic and Piezoresistive Materials for Fast, Low Voltage Switching: Simulation and Theory of Transduction Physics at the Nanometer-Scale. *Advanced Materials*, 24(27), pp.3672–3677.

[43] Tybell, T., Ahn, C.H. & Triscone, J.-M., 1999. Ferroelectricity in thin perovskite films. *Applied Physics Letters*, 75(6), pp.856–858.

[44] Lin, A. et al., 2001. Epitaxial growth of Pb(Zr0.2Ti0.8)O3 on Si and its nanoscale piezoelectronic properties. *Applied Physics Letters*, 78(14), pp.2034–2036.

[45] Li, F. et al., 2010. Composition and phase dependence of the intrinsic and extrinsic piezoelectronic activity of domain engineered (1 − x) Pb (Mg 1/3 Nb 2/3) O 3 − x PbTiO 3 crystals. *Journal of Applied Physics*, 108(3), pp. *Journal of Applied Physics*, 01 August 2010, Vol.108(3).

[46] Jayaraman, A. & Maines, R., 1979. Study of the valence transition in Eu-, Yb-, and Ca-substituted SmS under high pressure and some comments on other substitutions. *Physical Review B*, 19(8), pp.4154–4161.

[47] Jayaraman, A. et al., 1970. Continuous and discontinuous semiconductor-metal transition in samarium monochalcogenides under pressure. *Physical Review Letters*, 25(20), pp.1430–1433.

[48] Valade, L. & Tanaka, H., 2010. Molecular Inorganic Conductors and Superconductors. In *Molecular Materials*. John Wiley and Sons, pp. 211–280.

[49] Baldo, M., Grasser, T. & Meller, G., 2010. Organic electronics, Heidelberg ; New York: *Springer*.

[50] Lee, Jiun-Haw et al., 2008. Efficiency improvement and image quality of organic light-emitting display by attaching cylindrical microlens arrays. *Optics express*, 16(26), pp.21184–21190.

[51] Anon, 2012. Organic Electronics for a Better Tomorrow: Innovation, Accessibility, Sustainability. *A White Paper from Chemical Sciences and Society Summit*, San Francisco, California, United States.

[52] Schwoerer, M.C. & Wolf, H.C., 2008. Organic Molecular Solids, *John Wiley and Sons*.

[53] Eremets, M.I., 1995. *High pressure experimental methods*, Oxford, [England]; New York, N.Y.: Oxford University.

[54] Recio, J., Menendez, A. & Otero de La Roza, 2016. *An Introduction to High-Pressure Science and Technology 1st ed.*, CRC Press.

[55] Eisenberg, D et al., 2005. The Structure and Properties of Water, *Oxford University Press.*

[56] Jiang, S.F. et al., 2018. Metallization and molecular dissociation of dense fluid nitrogen. *Nature Communications*, 9(1), pp.1–6.

[57] Williams, J.M. et al., 1992. Organic Superconductors (Including Fullerenes): Synthesis, Structure, Properties, and Theory. *Prentice Hall*.

[58] Shirota, Y. & Kageyama, H., 2007. Charge carrier transporting molecular materials and their applications in devices. *Chemical reviews*, 107(4), pp.953–1010.

[59] Benjamin, Helen et al., 2020. Pressure-induced non-innocence in bis(1,2-dionedioximato)Pt(ii) complexes: an experimental and theoretical study of their insulator-metal transitions. *Physical chemistry chemical physics*, 11 March 2020.

[60] Natali et al., 2013. Rare-earth mononitrides. *Progress in Materials Science*, 58(8), pp.1316–1360.

[61] Yasuzuka, S. & Murata, K., 2009. Recent progress in high-pressure studies on organic conductors. *Science and Technology of Advanced Materials*, 10(2), p.024307.

[62] Okuhata et al., 2006. High-pressure study of a doped-type organic superconductor, κ-(BEDT-TTF) 4 Hg 2.89 Br 8. *Journal of Low Temperature Physics*, 142(3), pp.547–550.

[63] Thurmond, J., 1997. Design and synthesis of potentially superconducting organic polymers incorporating tetrathiafulvalene (TTF) moieties, pp.*ProQuest Dissertations and Theses.*

[64] Brown, T.L. et al, 2006. Chemistry: the central science. 10th edition, Upper Saddle River, N.J.: *Pearson Prentice Hall*.

[65] P. Atkins., 1980. Физическая химия. [Physical chemistry], 1st volume. *Издательство «Мир»*, Moscow, USSR.

[66] Frolov, V.V., 1986. Учебное пособие для машиностроительных специальностей вузов. [Textbook for machine building university professions]. Volume 3. *Vysshaya Shkola*, Moscow, Russia.

[67] V.V. Parfenov, R.H. Zakirof, 2001. Физика полупроводников. [*Semiconductor Physics*], Kazan, Russia.

[68] E.M. Averbah, 1981. Введение в физику твердого тела. [Introduction to solid state physics], Voronezh, Russia.

[69] M.P. Sarina, 2017. Физика твердого тела. [Solid state physics], Novosibirsk, Russia.

[70] A.A. Tager, 1963. Физико-зимия полимеров. [Physical chemistry of polymers.], Moscow, USSR.

[71] V.V. Parfenov, R.H. Zakirof, 2001. Физика полупроводников. [Semiconductor Physics.], Kazan, Russia.

[72] U.A.Yakov, 1984. Общая химия. [General chemistry], Volume 2. *Vysshaya Shkola*, Moscow, USSR.

[73] Tsidilkovski, I.M., 1982. Band structure of semiconductors. International Series in the Science of the Solid State. Volume 19. *Pergamon Press*, Sverdlovsk, USSR.

[74] Butterfield, A.J. & Szymanski, J., 2018. Arrhenius equation. A Dictionary of Electronics and Electrical Engineering, pp.A Dictionary of Electronics and Electrical Engineering.

[75] Lowrie, W., 2007. Fundamentals of geophysics Second., Cambridge: *Cambridge University Press*.

[76] Sudha L. K., Sukumar Roy, and K. Uma Rao, 2014. Evaluation of Activation Energy (Ea) Profiles of Nanostructured Alumina Polycarbonate Composite Insulation Materials. *International Journal of Materials, Mechanics and Manufacturing*, Vol. 2, No. 1, pp.96–100.

[77] O.S. Zajcev, 1990. Общая химия. Состояние веществ и химические реакции. [General chemistry. The state of substances and chemical reactions.], Moscow, USSR.

[78] Sze, S.M., Ng, K.K. & MyiLibrary, 2007. Physics of semiconductor devices. Third edition / S.M. Sze and Kwok K Ng.., Hoboken, N.J.: *Wiley-Interscience*.

[79] Frey, H. & Khan, H.R., 2015. Handbook of thin film technology, Berlin: *Springer*.

[80] S.V. Antonenko, 2008. Технология тонких пленок. [Thin film technology], Moscow, Russia.

[81] Edwards Ltd., (2016). PRODUCT DATA SHEET: ACTIVE INVERTED MAGNETRON (AIM) GAUGE. Available at: https://www.edwardsvacuum.com/en/our-products/measurement-control-leak-detection/instrumentation

[82] Shirotani, I.; Kawamura, A.; Suzuki, K.; Utsumi, W.; Yagi, T. Insulator-to-Metal-to-Semiconductor Transitions of One-Dimensional Bis(1,2-Dione Dioximato)Pt(II) Complexes at High Pressures. *Bull. Chem. Soc. Jpn*. 1991, 64 (5), 1607–1612.

[83] Takeda, K.; Shirotani, I.; Sekine, C.; Yakushi, K. Metal to Insulator Transition of One-Dimensional Bis(1,2-Benzoquinonedioximato)-Platinum(II), Pt(Bqd) 2 , at Low Temperatures and High Pressures. *J. Phys. Condens. Matter* 2000, 12 (30), L483–L488.

[84] Takeda, K.; Shirotani, I.; Yakushi, K. Insulator to Metal Transition and Electronic Spectra of Bis(1,2-Benzoquinonedioximato)Platinum(II), Pt(Bqd)2 at High Pressure. *Synth. Met*. 2003, 133–134, 415–416.

[85] Mégnamisi-Bélomeé, M., 1979. Crystal and molecular structure of the linear metal-chain semiconductor bis(1,2-benzoquinonedioximato)platinum(II), Pt(bqd) 2. *Journal of Solid State Chemistry*, 27(3), pp.389–396.

[86] Frasson, E., Panattoni, C. & Zannetti, R., 1959. X-ray studies on the metal complexes with the glyoximes. II. Structure of the Pt-dimethylglyoxime. *Acta Crystallographica*, 12(12), pp.1027–1031.

[87] Takeda, K.; Shirotani, I.; Yakushi, K. Pressure-Induced Insulator-to-Metal-to-Insulator Transitions in One-Dimensional Bis(Dimethylglyoximato)Platinum(II), Pt(Dmg) 2. *Chem. Mater*. 2000, 12 (4), 912–916.

[88] Shirotani, I. et al., 1991. Pressure-sensitive absorption spectra of thin films of bis(diphenylglyoximato)platinum(II), Pt(dpg) 2 : potential application as an indicator of pressure. *Journal of Materials Chemistry*, 1(6), pp.1041–1043.

[89] Metzger, R.M., 2012. Unimolecular and Supramolecular Electronics I Chemistry and Physics Meet at Metal-Molecule Interfaces. Topics in current chemistry. *Springer*. 312, pp.IX-X.

[90] Anderson, B. M.; Hurst, S. K. Platinum Stacking Interactions in Homoleptic Platinum Polymers. *Eur. J. Inorg. Chem.* 2009, 2009 (21), 3041–3054.

[91] Phelps, D.W.W., Little, W.F.F. & Hodgson, D.J.J., 1976. Linear Metal Chain Complexes. Structural Characterization of Bis(pyridine-2-methylcarboxaldoximinato)platinum(II). *Inorganic Chemistry*, 15(9), pp.2263–2266.

[92] Xie, Y. et al., 2013. Synthesis, optical properties and charge transport characteristics of a series of novel thiophene-fused phenazine derivatives. *Journal of Materials Chemistry* C, 1(21), pp.3467–3481.

[93] Dell, E.J.J. & Campos, L.M.M., 2012. The preparation of thiophene-S,S-dioxides and their role in organic electronics. *Journal of Materials Chemistry*, 22(26), pp.12945–12952.

[94] Perepichka, I.F., 2009. Handbook of thiophene-based materials : applications in organic electronics and photonics, Chichester, U.K.: *Wiley*.

[95] Kim, E.G. et al., 2006. Magnus' Green Salt Revisited: Impact of Platinum–Platinum Interactions on Electronic Structure and Carrier Mobilities. *Advanced Materials*, 18(15), pp.2039–2043.

[96] L. Atkinson, P. Day & R. J. P. Williams, 1968. Semiconductivity of Magnus' Green Salt Analogues. *Nature*, 218(5142), pp.668–669.

[97] Interrante, L.V.V. & Bundy, F.P.P., 1971. Studies of Intermolecular Interactions in Square-Planar d 8 Metal Complexes. I. The Physical Properties of Magnus' Green Salt and Some Related Complexes at High Pressures. *Inorganic Chemistry*, 10(6), pp.1169–1174.

[98] Ballard, L. & Wortman, 1970. Piezoresistance in Organometallic Crystals. *Journal of Applied Physics*, 41(10), pp.4232–4236.

[99] Bonati & Ugo, 1968. Iridium dicarbonyl β-diketonates. *Journal of Organometallic Chemistry*, 11(C), pp.341–352.

[100] Eizagirre Barker, S. 2019, Towards low pressure piezoresistivity in iridium based molecular semiconductors, Chemical Physics 5MX Project Report, *University of Edinburgh*, Edinburgh.

[101] Mcguire, J. et al., 2019. Enabling single qubit addressability in a molecular semiconductor comprising gold-supported organic radicals. *Chemical Science*, 10(5), pp.1483–1491.

[102] Stoliar, P. et al., 2015. Resistive switching induced by electric pulses in a single-component molecular Mott insulator. *Journal of Physical Chemistry* C, 119(6), pp.2983–2988.

[103] Mizuno, A.M. et al., 2019. High Ambipolar Mobility in a Neutral Radical Gold Dithiolene Complex. *Advanced Functional Materials*, pp.

[104] Leander Müller, M. 2019, Synthesis, Characterisation and Thin Film Fabrication of a Gold Dithiolene Complex, Chemistry 5MX Research Report, *University of Edinburgh*, Edinburgh.

[105] Tenn, N. et al., 2009. A single-component molecular metal based on a thiazole dithiolate gold complex. *Journal of the American Chemical Society*, 131(46), pp.16961–16967.

[106] Fazekas, P., 1999. Lecture notes on electron correlation and magnetism, Singapore ; London: *World Scientific*.

[107] Qinglei Meng, Q., 2010. Metal Insulator Transition, *University of Illinois*, USA.

[108] Cuniberti, G. et al., 2005. Introducing Molecular Electronics 1st ed. 2005.., Berlin, Heidelberg: Springer Berlin Heidelberg : Imprint: *Springer*.

[109] David B. Newell and Eite Tiesinga, 2019. *The International System of Units (SI).* Ninth edition., National Institute of Standards and Technology Special Publication 330. https://doi.org/10.6028/NIST.SP.330-2019

[110] Sophocleous, Marios. (2017). Electrical Resistivity Sensing Methods & Implications. 10.5772/67748.

[111] Afonskij A.A., Djakonov V.P., 2011. Электронные измерения в нанотехнологиях и микроэлектронике. [Electronic Measurements in Nanotechnology and Microelectronics.], Moscow, Russia.

[112] Keithley Instruments, Inc. (2003). Model 2002 Multimeter: User manual. Available at: https://uk.tek.com/digital-multimeter/high-resolution-digital-multimeters-manual-3

[113] Keithley Instruments, Inc. (2003). Model 6517A Electrometer: User's manual. Available at: https://uk.tek.com/manual/model-6517a-electrometer-users-manual-rev-d-manual

[114] Jerry Janesch., 2013. Two-Wire vs. Four-Wire Resistance Measurements: Which Configuration Makes sense for Your Application?. Tektronix Inc. Available at: *download.tek.com/document/2Wire_4Wire* Resistance *Article.pdf*

[115] Keithley Instruments, Inc., 2004. Low Level Measurements Handbook. Sixth Edition. Available at: http://web.mit.edu/8.13/8.13d/manuals/LowLevMsHandbk.pdf

[116] Keithley Instruments, Inc., 2005. High Resistance Measurements. Application note series number 312.

[117] Waremra Richard S & Betaubun Philipus, 2018. Analysis of Electrical Properties Using the four point Probe Method. *E3S Web of Conferences*, 73, p.13019.

[118] Van Der Pauw, L., 1958. A method of measuring resistivity and Hall effect of lamellae of arbitrary shape. *Philips Tech Rev*, 20(I), 220–224.

[119] Montgomery, H.C., 1971. Method for Measuring Electrical Resistivity of Anisotropic Materials. *Journal of Applied Physics*, 42(7), pp.2971–2975.

[120] Singh, Y., 2013. ELECTRICAL RESISTIVITY MEASUREMENTS: A REVIEW. *International Journal of Modern Physics*: Conference Series, 22, pp.745–756.

[121] Jayaraman, A., 1983. Diamond anvil cell and high-pressure physical investigations. *Reviews of Modern Physics*, 55(1), pp.65–108.

[122] Bassett, W.A., 2009. Diamond anvil cell, 50th birthday. *High Pressure Research*, 29(2), pp.163–186.

[123] Dubrovinsky et al., 2015. The most incompressible metal osmium at static pressures above 750 gigapascals. *Nature*, 525(7568), pp.226–229.

[124] Kaminsky, F.V., 2017. *The Earth's Lower Mantle Composition and Structure* 1st ed. 2017.., Cham: Springer International Publishing : Imprint: *Springer*.

[125] Naoki Fujiwara et al 2014., A NiCrAl pressure cell up to 4.6 GPa and its application to cuprate and pnictide superconductors., *J. Phys.*: Conf. Ser.

[126] Ishii, T. et al., 2017. Pressure generation to 65 GPa in a Kawai-type multi-anvil apparatus with tungsten carbide anvils. *High Pressure Research*, 37(4), pp.507–515.

[127] Hattori, T. et al., 2019. Development of a technique for high pressure neutron diffraction at 40 GPa with a Paris-Edinburgh press. *High Pressure Research*, 39(3), pp.417–425.

[128] J. M. Besson, G. Hamel, T. Grima, R. J. Nelmes, J. S. Loveday, S. Hull & D. Häusermann, 1992. A large volume pressure cell for high temperatures, *High Pressure Research*, 8:5-6, 625-630

[129] Wang, X., 2015. Development of novel high pressure instrumentation, pp.*PQDT* - UK & Ireland.

[130] Zabaleta, J. et al., 2017. Electrical transport measurements of thin film samples under high hydrostatic pressure. *Review of Scientific Instruments*, 88(3), pp.033901/1–033901/7.

[131] Cui, H. et al., 2014. Pressure-Induced Metallic Conductivity in the Single-Component Molecular Crystal [Ni(dmit) 2]. *European Journal of Inorganic Chemistry*, 2014(24), pp.3837–3840.

[132] Rotundu, C. et al., 2013. High-pressure resistivity technique for quasi-hydrostatic compression experiments. *Review of Scientific Instruments*, 84(6), p.063903.

[133] Walker, I.R., 1999. Nonmagnetic piston–cylinder pressure cell for use at 35 kbar and above. *Review of Scientific Instruments*, 70(8), pp.3402–3412.

[134] Taniguchi, Hiromi et al., 2010. Short piston-cylinder pressure cells based on Ni–Cr–Al cylinders and their application to fragile materials. *Review of Scientific Instruments*, 81(3), p.033903.

[135] Guo, H. & Keppler, H., 2019. Electrical Conductivity of NaCl-Bearing Aqueous Fluids to 900 °C and 5 GPa. *Journal of Geophysical Research: Solid Earth*, 124(2), pp.1397–1411.

[136] Kepa, M. et al., 2016. Piston cylinder cell for high pressure ultrasonic pulse echo measurements. *Review of Scientific Instruments*, 87(8), pp.085103/1–085103/6.

[137] Adams, D. M. *Journal of Physics D : Applied Physics*; A computer-aided design study of the behaviour of diamond anvils under stress. (1982).

[138] Lorenzana, H. et al., 1994. Producing diamond anvil cell gaskets for ultrahigh-pressure applications using an inexpensive electric discharge machine. *Review of Scientific Instruments*, 65(11), pp.3540–3543.

[139] Winter, R., Jonas, J., & NATO Advanced Study Institute on High Pressure Chemistry, Biochemistry, Materials Science. (1993). High pressure chemistry, biochemistry, and materials science (NATO ASI series. Series C, Mathematical and physical sciences ; no. 401). Dordrecht ; London: *Kluwer Academic*.

[140] Feng, Y., Silevitch & Rosenbaum, 2014. A compact bellows-driven diamond anvil cell for high-pressure, low-temperature magnetic measurements. *Review of Scientific Instruments*, 85(3), p.033901.

[141] Giriat, G et al., 2010. Turnbuckle diamond anvil cell for high-pressure measurements in a superconducting quantum interference device magnetometer. *Review of Scientific Instruments*, vol. 81, no. 7, 073905.

[142] Binns, J. et al., 2016. Use of a miniature diamond-anvil cell in high-pressure single-crystal neutron Laue diffraction. , 3(Pt 3), pp.168–179.

[143] Komatsu, K. et al., 2011. A design of backing seat and gasket assembly in diamond anvil cell for accurate single crystal x-ray diffraction to 5 GPa. *Review of Scientific Instruments*, 82(10), p.105107.

[144] Lawson, A. & Tang, 1950. A Diamond Bomb for Obtaining Powder Pictures at High Pressures. *Review of Scientific Instruments*, 21(9), p.815.

[145] Li, Bing et al., 2018. Diamond anvil cell behavior up to 4 Mbar. *Proceedings of the National Academy of Sciences of the United States of America*, 115(8), pp.1713–1717.

[146] Jin, H. et al., 2017. A novel diamond anvil cell for x-ray diffraction at cryogenic temperatures manufactured by 3D printing. *Review of Scientific Instruments*, 88(3), pp.035103/1–035103/8.

[147] Giordano, N. et al., 2019. The Effect of Pressure on Halogen Bonding in 4-Iodobenzonitrile. Molecules, 24(10), pp.*Molecules*, 27 May 2019, Vol.24(10).

[148] Kuzovnikov, M.A. et al., 2017. Pressure-induced metallization in Erbium trihydride. *Solid State Communications*, 263, pp.23–26.

[149] Zeto, R. & Vanfleet, 1969. Pressure Calibration to 60 kbar Based on the Resistance Change of a Manganin Coil under Hydrostatic Pressure. *Journal of Applied Physics*, 40(5), pp.2227–2231.

[150] L H Dmowski, 1999. The variation of the pressure coefficient of manganin sensors at low temperatures. *Measurement Science and Technology*, 10(5), pp.343–347.

[151] G. Yiannakopoulos, “A review of manganin gauge technology for measurements in the gigapascal range,” tech. rep., *Materials Research Labs Ascot Vale (Australia)*, 1990.

[152] Weiss, J., Decker & Vanfleet, 1976. Behavior of a manganin coil at elevated temperatures and pressures. *Journal of Applied Physics*, 47(9), pp.4188–4189.

[153] J Sanchez-Benitez et al., 2008. High-pressure cell for a SQUID magnetometer with a plug for in situ pressure measurements. *J. Phys.: Conf. Ser*. 121 122001.

[154] Forman, R.A. et al., 1972. Pressure measurement made by the utilization of ruby sharp-line luminescence. *Science* (New York, N.Y.), 176(4032), pp.284–285.

[155] Barnett, J., Block & Piermarini, 1973. An Optical Fluorescence System for Quantitative Pressure Measurement in the Diamond-Anvil Cell. *Review of Scientific Instruments*, 44(1), pp.1–9.

[156] King, H. & Prewitt, 1980. Improved pressure calibration system using the ruby R 1 fluorescence. *Review of Scientific Instruments*, 51(8), pp.1037–1039.

[157] Hemley, R. et al., 1989. X-ray diffraction and equation of state of solid neon to 110 GPa. *Physical Review* B, 39(16), pp.11820–11827.

[158] Grasset, O., 2001. Calibration of the R ruby fluorescence lines in the pressure range [0-1 GPa] and the temperature range [250-300 K]. *High Pressure Research*, 21(3-4), pp.139–157.

[159] Mao, H.K., 1978. High-pressure physics: sustained static generation of 1.36 to 1.72 megabars. *Science* (New York, N.Y.), 200(4346), pp.1145–1147.

[160] Ragan, D., Gustavsen & Schiferl, 1992. Calibration of the ruby R 1 and R 2 fluorescence shifts as a function of temperature from 0 to 600 K. *Journal of Applied Physics*, 72(12), pp.5539–5544.

[161] Nakano, K. et al., 2000. Ruby scale at low temperatures calibrated by the NaCl gauge: Wavelength shift of ruby R1 fluorescence line at high pressure and low temperature. *Japanese Journal of Applied Physics*, Part 1: Regular Papers and Short Notes and Review Papers, 39(3A), pp.1249–1251.

[162] Chervin, J.C., Canny, B. & Mancinelli, M., 2001. Ruby-spheres as pressure gauge for optically transparent high pressure cells. *High Pressure Research*, 21(6), pp.305–314.

[163] Takemura, K., 2007. Pressure scales and hydrostaticity. *High Pressure Research*, 27(4), pp.465–472.

[164] Yokogawa, K. et al., 2007. Solidification of High-Pressure Medium Daphne 7373. *Japanese Journal of Applied Physics*, 46(6A), pp.3636–3639.

[165] N. Tateiwa and Y. Haga, Evaluations of pressure-transmitting media for cryogenic experiments with diamond anvil cell, *Review of Scientific Instruments*, vol. 80, p. 123901, 2009.

[166] Klotz, S. et al., 2009. Hydrostatic limits of 11 pressure transmitting media. *Journal of Physics D: Applied Physics*, 42(7), p.7.

[167] Murata, K. et al., 2008. Pressure transmitting medium Daphne 7474 solidifying at 3.7 GPa at room temperature. *Review of Scientific Instruments*, 79(8), p.085101.

[168] Sidorov, V.A. & Sadykov, R.A., 2005. Hydrostatic limits of Fluorinert liquids used for neutron and transport studies at high pressure. *Journal of Physics: Condensed Matter*, 17(40), pp.S3005–S3008.

[169] Piermarini, G., Block & Barnett, 1973. Hydrostatic limits in liquids and solids to 100 kbar. *Journal of Applied Physics*, 44(12), pp.5377–5382.

[170] Developed by Prof. Keizo Murata and Idemitsu Kosan Co., Ltd. Available at: http://www.idemitsu.com/

[171] Torikachvili, M. et al., 2015. Solidification and loss of hydrostaticity in liquid media used for pressure measurements. *Review of Scientific Instruments*, 86(12), pp.123904/1–123904/7.

[172] - Merrill, L. & Bassett, 1974. Miniature diamond anvil pressure cell for single crystal x-ray diffraction studies. *Review of Scientific Instruments*, 45(2), pp.290–294.

[173] Jha, R., Tiwari, B. & Awana, V., 2014. Hydrostatic Pressure Studies on Parent Phase SrFBiS2 of BiS2-Based Superconducting Family. *Journal of the Physical Society of Japan*, 83(10), pp.

[174] Jordan, B., 1969. The development of an improved non-magnetic alloy based on the copper-beryllium system. *Journal of Materials Science*, 4(12), pp.1097–1105.

[175] Ekin, J.W., 2007. Experimental techniques for low-temperature measurements: cryostat design, material properties, and superconductor critical-current testing Reprinted 2007 (with corr.)., Oxford; New York: *Oxford University Press.*

[176] Henkel Corporation. Available at: https://www.henkel-adhesives.com/us/en/product/potting-compounds/loctite_stycast_2850ft.html

[177] Logitech Ltd. Available at: https://uk.store.logitech.uk.com/index.php?route=product/product&product_id=69

[178] NGK BERYLCO. Available at: http://www.ngk-alloys.com

[179] Yoshiya Uwatoko, 2002. Material properties of NiCrAl alloy and design of a 4 GPa class non-magnetic high-pressure cell. *Journal of Physics: Condensed Matter*, 14(44), pp.11291–11296.

[180] ILL Neutrons for Society. Available at: https://www.ill.eu/fr/users/support-labs-infrastructure/sample-environment/equipment/high-pressures/clamped-cells/04pcl150cb5/

[181] Shermadini, Z. et al., 2017. A low-background piston-cylinder-type hybrid high pressure cell for muon-spin rotation/relaxation experiments. High Pressure Research, 37(4), pp.449–464.

[182] Lamé, M.G., 1866. Lecons sur la théorie mathématique de l'élasticité des corps solides, *Gauthier-Villars*.

[183] Vullo V., 2014. Circular Cylinders and Pressure Vessels. Springer Series in Solid and Structural Mechanics, vol 3. *Springer*, Cham.

[184] Tooley M. & Dingle L., 2012. Engineering science: For Foundation Degree and Higher National. New York: *Elsevier Science*.

[185] Rao, J.S., 2017. Simulation Based Engineering in Solid Mechanics, Cham: *Springer International Publishing*.

[186] ANSYS, Inc. Available at: http://www.ansys.com/

[187] Moatamedi, M. & Khawaja, H.A., 2018. Finite Element Analysis 1st ed., *CRC Press*.

[188] Budynas, R.G. & Nisbett, J.K., 2011. Shigley's mechanical engineering design Ninth edition in SI units., Singapore; London: *McGraw-Hill*.

[189] ANSYS, Inc. Available at: https://www.ansys.com/products/platform/ansys-designxplorer

[190] D. M. Adam and A. C. Shaw, "A computer-aided design study of the behaviour of diamond anvils under stres," *Journal of Physics D: Applied Physics*, vol. 15, pp. 1609–1635, 1982.

[191] Moss, W. et al., 1986. Finite element analysis of the diamond anvil cell: Achieving 4.6 Mbar. *Applied Physics Letters*, 48(19), pp.1258–1260.

[192] D M Adams, 1993. Optimization of diamond anvil cell performance by finite element analysis. *Measurement Science and Technology*, 4(3), pp.422–430.

[193] Fang, J. et al., 2012. Strength analysis and optimisation of double-toroidal anvils for high-pressure research. *Review of Scientific Instruments*, 83(9), p.093902.

[194] Wang, W. et al., 2011. Large volume high-pressure cell for inelastic neutron scattering. *The Review of scientific instruments*, 82(7), p.073903.

[195] ANSYS, Inc. Available at: https://www.ansys.com/services/training-center/fluids/introduction-to-ansys-designmodeler

[196] Besson, J.-M., 1997. High-pressure techniques in chemistry and physics: a practical approach. Oxford. *Oxford University Press*.

[197] Almax easyLab Inc. Available at: https://www.almax-easylab.com

[198] Li, Bing et al., 2018. Diamond anvil cell behavior up to 4 Mbar. *Proceedings of the National Academy of Sciences of the United States of America*, 115(8), pp.1713–1717.

[199] Fang, J. et al., 2010. A rotator for single-crystal neutron diffraction at high pressure. *Review of Scientific Instruments*, 81(11), p.113901.

[200] Boehler, R. & De Hantsetters, K., 2004. New anvil designs in diamond-cells. *High Pressure Research*, 24(3), pp.391–396.

[201] Dymet Alloys. Available at: http://www.dymetalloys.co.uk/tungsten-carbide-grade-chart/

[202] Erskine, D., Yu & Martinez, 1987. Technique for high-pressure electrical conductivity measurement in diamond anvil cells at cryogenic temperatures. *Review of Scientific Instruments*, 58(3), pp.406–411.

[203] Graf, D.E. et al., 2011. Nonmetallic gasket and miniature plastic turnbuckle diamond anvil cell for pulsed magnetic field studies at cryogenic temperatures. *High Pressure Research*, 31(4), pp.533–543.

[204] Solli, D. & Jeanloz, 2001. Nonmetallic gaskets for ultrahigh pressure diamond-cell experiments. *Review of Scientific Instruments*, 72(4), pp.2110–2113.

[205] V. A. Sputnikov & B.M. Bulichev, 2012. ВЫСОКИЕ ДАВЛЕНИЯ В ХИМИИ. АЛМАЗ И АЛМАЗОПОДОБНЫЕ МАТЕРИАЛЫ, технические и синтетические аспекты. [HIGH PRESSURES IN CHEMISTRY. DIAMOND AND DIAMOND-LIKE MATERIALS, technical and synthetic aspects.] Moscow, Russia.

[206] MOHAMMAD, Y., & K GOVINDA RAJAN, 1982. Principle of massive support in the opposed anvil high pressure apparatus. *Reactor Research Centre*, Kalpakkam 603 102, India.

[207] Anonymous. Available at: https://shodhganga.inflibnet.ac.in/bitstream/10603/73991/9/09_chapter%202.pdf

[208] D M Adams, 1982. A computer-aided design study of the behaviour of diamond anvils under stress. *Journal of Physics D: Applied Physics*, 15(9), pp.1609–1635.

[209] D M Adams, 1993. Optimization of diamond anvil cell performance by finite element analysis. *Measurement Science and Technology*, 4(3), pp.422–430.

[210] Go-Araldite. Available at: http://go-araldite.com/

[211] Giordano, N.L. et al., 2019. The effect of pressure on halogen bonding in 4-iodobenzonitrile. *Molecules*, 24(10), pp.Molecules, 2019, Vol.24(10).

[212] Physik Instrumente Ltd. (2020). Available at: https://www.physikinstrumente.co.uk/fileadmin/user_upload/physik_instrumente/files/datasheets/P-840-Datasheet.pdf

[213] Dejay Distribution Ltd., 2011. Available at: http://www.dejaydistribution.co.uk/

[214] AEP transducers, 2020. Available at: http://www.aeptransducers.com/load-cells/75-c2s.html

[215] Quorum Technologies Ltd. (2011). *SC7620 Mini Sputter Coater Operating Manual.* Available at: http://www.iitk.ac.in/meesa/SEM/coater_manual.pdf

[216] Bostic Ltd. Available at: https://blu-tack.co.uk/en-UK

[217] SHI Cryogenics Group., 2021. Available at: https://www.shicryogenics.com/

[218] Quantum Design, Inc. Available at: https://www.qdusa.com/

[219] Quantum Design, Inc., 1999. Physical Property Measurement System. Resistivity Option User's Manual. Second Edition. Available at: https://www.mrl.ucsb.edu/sites/default/files/mrl_docs/instruments/resPPMS.pdf

[220] SINOMAS, 2018. Polyimide (Kapton) Heater. Available at: https://www.flexheaters.com/polyimide-kapton-heater

[221] OMEGA ENGINEERING, Inc. (2010). *RDXL4SD 4-Channel Datalogger Thermometer: User's Guide.* Available at: https://www.manualslib.com/manual/928701/Omega-Rdxl4sd.html#manual

[222] Farnell Instruments Limited, (1978). E30 BENCH POWER SUPPLIES: INSTRUCTION BOOK. Available at: http://mirror.thelifeofkenneth.com/lib/electronics_archive/FarnellE30Psu_text.pdf

[223] Benjamin, Helen et al., 2020. Electrochemical deposition of a semiconducting gold dithiolene complex with NIR absorption. *Dalton Transactions, The Royal Society of Chemistry*, 24 Sep 2020.